Spin and Magnetization Dynamics Studied by Spin-Resolved Photoemission

Im Fachbereich Physik der Freien Universität Berlin eingereichte Dissertation

Beatrice Andres

Berlin, 2016

Betreuer:	Prof. Dr. Martin Weinelt
Zweitgutachter:	Prof. Dr. Paul Fumagalli

Datum der Disputation: 13. September 2016

Contents

Chapter 1

Introduction

Imagine a life with the advantages of magnetism and electronics combined in the same material. This is hard to conceive, because we use so little of the benefits the electron spin could give us. The way electrons interact with each other and with their surroundings determines the electrical – and many other – properties of a material. These interactions of electrons depend on their spin direction, which leads to measurable effects in a lot of materials but is only used in few. The most famous effect is the giant magnetoresistance (GMR)[1], implemented in read heads of hard drives. The GMR can also be utilized to inject a spin-polarized current into a non-magnetic material. Despite of much more magnetic-field effects[2] capable of modifying electrical properties, the utilization of the spin polarization in an electric current is up to now hindered by spin-relaxation processes. These spin-relaxation processes[3] are driven by spin-dependent and spin-flip scattering mechanisms, which are the topic of this thesis. A detailed knowledge of these processes is crucial for spin applications.

This thesis investigates spin-dependent scattering processes by means of spin-, time-, and angle-resolved direct photoemission and two-photon photoemission (STARPES). These techniques add information about the spin degree of freedom to the conventional measurement of the electronic band structure in photoemission. By a laser excitation (pump pulse) preceding the actual measurement (by a probe pulse) we are able to resolve the dynamic behavior of excited electrons in the spin-dependent band structure and learn more about the spin dependence of electronic scattering processes. In STARPES, we use the photoeffect to excite electrons out of their equilibrium states to higher energies where they immediately start to return back to the ground state transferring their energy to every possible absorber. This energy relaxation is mediated by the same basic scattering processes that limit the electrical conductivity or also the switching of the magnetization in a ferromagnet. Thus, investigating the energy relaxation of excited electrons by photoemission with a second

[1] This effect causes a higher electrical resistance through two ferromagnetic layers, if they are magnetized antiparallel instead of parallel.

[2] Further effects, in which the application of a magnetic field changes the resistance of non-magnetic materials are the conventional magnetoresistance, different versions of the Hall effect, the Aharanov-Bohm effect, and the Shubnikov-de-Haas effect.

[3] The three main mechanisms that have been proposed to cause spin relaxation or spin dephasing, are Elliott-Yafet scattering, the D'yakonov-Perel' mechanism, and the Bir-Aronov-Pikus mechanism.

photon, we learn about the processes limiting conduction and magnetization in technology. In spin-resolved photoemission, spin dependencies observed in the lifetimes of excited electrons or in the linewidth of electronic states indicate which scattering processes contribute to the decay and dephasing of electrons.

Since energy conservation requires that the energy lost by any laser-excited electron excites either an electron of lower energy or a collective of particles (quasiparticles such as phonons or magnons), the number of occupied and unoccupied electronic states near the Fermi level E_F (also referred to as the phase space) determines the timescale of the relaxation and allows or forbids certain types of scattering processes. A detailed microscopic understanding of the transport and the magnetic properties of a material is thus not possible without knowing the underlying band structure around E_F. The band structure near E_F also determines the magnetic properties of a material. That is why not only spin-dependent scattering but also material-dependent magnetic properties can be studied very effectively in spin- and time-resolved photoelectron spectroscopy: Band mapping gives insights into correlation effects such as magnon emission and band hybridization due to spin-orbit coupling, and the spin polarization and exchange splitting of the bands reflect their role in the exchange interaction.

The samples under investigation in this thesis are ferromagnetic thin films evaporated *in situ* onto a tungsten substrate W(110). The energy range of the lasers used in this work (1.5 to 6 eV) is suited best for the investigation of surface electronic states. These states are of increasing importance due to the proceeding miniaturization of electronic devices. Although most surface states only exist in vacuum, the study of their dependencies on boundary conditions, such as potential barriers or the influence of the bulk band structure, can also be applied to interface states, which also exist in air – as in topological insulators – and could thus be used in daily life applications.

This work investigates the spin dependence of electronic scattering processes and the fundamental magnetic properties in the surface electronic band structure in three STARPES experiments, which show very different effects on magnetic surface states.

In the first experiment, described in Chapter 4, the laser-induced demagnetization of a Gd(0001) thin film on W(110) is studied. Laser-induced demagnetization is another beautiful way to study the fundamental magnetic interactions. This is done by exciting a huge amount of electrons and investigating the response in the band structure. The energy relaxation of the excited electrons leads to a transfer of energy to the lattice and the magnetic system resulting in a transition from the ferro- to the paramagnetic phase. This is particularly interesting from a scientific point of view. By distinctly exciting the electronic system we are able to create entirely new states of matter that don't exist naturally in thermal equilibrium. We can thus investigate magnetic phase transitions from a completely new point of view. When we use this opportunity to investigate the responses of the distinct systems of electrons, spins, and lattice to the excitation, this might offer clues valuable to disentangle the mysteries of magnetism.

Especially in the case of Gd, the phenomenon of laser-induced demagnetization is controversially discussed. This is due to the fascinating fact, that different experimental methods found different demagnetization timescales. While the temperature-dependent

behavior of the signals in MOKE, XMCD, SHG, and MLD is the same during the magnetic phase transition of Gd, the responses of these techniques differ in the laser-triggered phase transition. It is thus not clear, which of these results reflects the true magnetization and which processes lead to the differences.

The only shortcoming of STARPES is that it suffers from low count rates, since several orders of magnitude are lost in the spin-detection process. For this reason, it was not possible to resolve the spin-dependent band structure during laser-induced demagnetization until now – because this process requires a huge power in the laser pulse, which is only possible at low repetition rates of the laser leading to low count rates in photoemission. The laser-induced demagnetization experiments performed so far, were total yield experiments [Scholl et al., 1997; Weber et al., 2011; Fognini et al., 2014a], in which the spin polarization of the total amount of photoemitted electrons was measured without energy and angular resolution. Thus, the impact of laser excitation on the spin-dependent band structure could not be resolved until now. That is why there is an ongoing debate about the microscopic processes driving the demagnetization. The spin relaxation mechanism of Elliott-Yafet scattering is in discussion to cause such a demagnetization after laser excitation. But also spin-dependent transport and other spin-dependent scattering mechanisms have been proposed.

In our setup, spin-resolved measurements of the band-structure dynamics are now possible thanks to a new spin detector based on exchange interaction instead of spin-orbit interaction as usually used. Making use of the time-, energy-, and spin-resolution of our experiment, we can differentiate between responses in the electron temperature (reflected in the Fermi function), the band energies, and the spin. Thus, we are able to answer present questions like: How does laser-excitation influence the magnetic properties – namely exchange splitting and spin polarization – of the electronic band structure? Why do experimental techniques with the same temperature-dependent behavior show responses on different timescales in the laser-induced demagnetization of Gd? Is there a difference in the influence of hot electrons and a heated lattice? Do electrons of opposite spin directions have different Fermi distributions and thus different electronic temperatures?

The second experiment in Chapter 5 investigates the surface band-structure of Fe(110) around E_F with the focus on the interaction between electrons and the collective excitations of the solid, *i.e.* phonons, magnons, plasmons, etc. It is well-established that electron-phonon interaction can modify the band dispersion of the involved electrons significantly. Just a single reference [Schäfer et al., 2004] reported on a similar change of the dispersion induced by electron-magnon interaction. In this reference, only a weak electron-magnon coupling was found in a surface band on Fe(110). With the advantage of spin sensitivity, we have the means to confirm this result and address the question: Does electron-magnon interaction influence the surface electronic band structure in the same manner as electron-phonon interaction?

Besides the interaction with magnons, the surface band-structure of iron itself is particularly interesting. Fe has the largest magnetic moment of the $3d$ transition metal ferromagnets Fe, Co, and Ni. This leads to a large exchange splitting in the band structure. In addition to that, spin-orbit coupling induces hybridizations of different bands. It is thus questionable, if surface states in a system like this still appear in exchange-split pairs or whether there are

single majority- and minority-spin states.

In the third experiment (Chapter 6), the occupied and unoccupied surface states of Ni(111) are studied as well as the energy relaxation and dephasing of electrons excited in an unoccupied state. The broad bulk bands of nickel compromised the investigation of surface states around the Fermi level for a long time. It is thus not clear, which of the postulated surface states exist and if they appear at the proposed energies. We utilize the surface sensitivity of two-photon photoemission (2PPE) to disentangle surface from bulk states and are thus able to resolve the puzzling preceding observations.

A special class of surface states are image-potential states. These are unoccupied states in front of the surface where electrons are trapped by the surface barrier. In two-photon photoemission experiments, electrons are excited into these unoccupied states by one photon before a second photon photoemits the electrons. The image-potential states are also called barrier-induced surface states. On ferromagnets, the image-potential states are spin-polarized and exchange split in their binding energy. The magnitude of these properties is partly influenced by the bulk band structure and partly by the potential landscape at the surface. The image states are thus also a model system for the fundamentals of magnetism lying in the interaction of electrons in dependence on their spin.

Studying the binding energies of the exchange-split image-potential states, we can complete the current model view of the formation of image-potential states on ferromagnetic surfaces. In additional time-dependent measurements, we investigate the elastic and inelastic scattering rates of excited electrons in those states and how these processes depend on the spin direction. Since nickel has a low atomic magnetic moment, it is not clear why high spin polarizations have been observed in tunneling from a nickel tip or in secondary electron emission from graphene on Ni(111). That is why we address the question: Which processes can lead to a spin dependence in the scattering rates on nickel?

Before going into the details of these STARPES experiments, some of the concepts of magnetism and the physics of solid state surfaces are repeated in Chapter 2. The experimental technique of STARPES is introduced along with a detailed description of the setup in Chapter 3.

Chapter 2

Magnetism, Spins, and Thermodynamics

> I think the problem, to be quite honest with you, is that you've never actually known what the question is.
>
> *The Hitchhiker's Guide to the Galaxy*
> Douglas Adams

In Douglas Adams' novel, the answer to the ultimate question of life, the universe, and everything is 42. Unfortunately, nobody tried to formulate an appropriate question before the seven and a half million years had passed, that it took to calculate this answer. In my opinion, we have arrived at a similar point concerning our knowledge about magnetism. Magnetism is one of the oldest phenomena studied by mankind. Yet, we are far from understanding it. This has never been more obvious than in the last 20 years, in which the research field of ultrafast magnetization dynamics has developed. No theory is capable of fully explaining the microscopic processes underlying ultrafast magnetization dynamics triggered by a laser. Nevertheless, we are eager to study these non-equilibrium phenomena without even having a proper theory to describe magnetism in thermal equilibrium. Such ultrafast laser-induced phenomena will be the subject of Chapter 4. In contrast, this chapter repeats some of the basics of equilibrium magnetism aiming to approach the formulation of the ultimate question of magnetism, spins, and thermodynamics.

After a quick review of the concept of exchange interaction in Section 2.1, the basics of magnetic phase transitions are introduced in Section 2.2. The section repeats the commonly accepted models explaining the temperature dependence of magnetism. This is a necessary prerequisite to discuss what we observe when gadolinium is heated by an ultrafast laser pulse later in Chapter 4. The magnetism in gadolinium, being a rare earth, differs from that of the transition metals iron and nickel. In contrast to the transition metals, in the rare earths the magnetic moment originates from other electronic states than those mediating the exchange interaction. This is described in Section 2.3. Finally, the signatures of magnetism in the surface electronic structure is introduced in Section 2.4. Surface states are not just

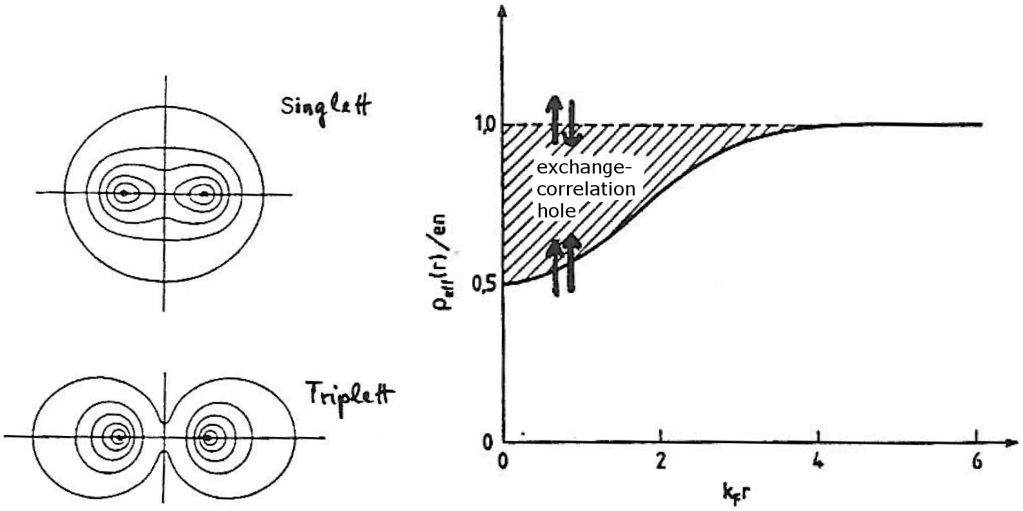

Figure 2.1: Two examples to visualize the concept of exchange interaction. On the left panel the probability density of the electrons in a hydrogen molecule is shown (reprinted from Ref. [Schroeder, 1999]). In the singlet state, where the electron spins are aligned antiparallel, the probability density between the two atom cores is higher than in the triplet state with parallel spin. Thus, the singlet state reduces the Coulomb repulsion between the cores. In case of the hydrogen molecule, an antiparallel spin alignment is favored. The right panel shows the effective charge density an electron in a free electron gas – taking into account the Pauli principle – experiences (reprinted from Ref. [Madelung, 1972]). For electrons of parallel spin the charge density is reduced as compared to antiparallel spin alignment. A parallel spin alignment reduces the electron density and thus the Coulomb repulsion between the electrons.

sensitive to the magnetization by their spin polarization and exchange splitting, but also contribute to the magnetic moment at the surface.

2.1 The Concept of Exchange Interaction

Since the development of quantum mechanics in the beginning of the 20th century, magnetism is obtained from to the concept of electron spin and angular momentum, which both contribute to the magnetic moment of an atom. The alignment of electronic spins in one atom is in turn lead back to the concept of exchange interaction. This interaction is also made responsible for the alignment of atomic magnetic momenta, which finally leads to the formation of magnetically ordered phases, *i.e.* ferromagnetism, ferrimagnetism, antiferromagnetism, *etc.*.

Two examples are very popular to visualize the concept of exchange interaction. The first is the hydrogen molecule (depicted in Fig. 2.1, left panel), where an antiparallel alignment of the spins of both electrons leads to a minimization of Coulomb energy. This is due to Pauli's principle. It states that an antisymmetric[1] wave function is required to describe a set of

[1] antisymmetric upon exchange of the electrons

electrons. Thus the antiparallel spin alignment leads to a symmetric spatial part of the wave function. In this state (singlet) the probability to find the electrons between the two atomic cores is higher than with an antisymmetric spatial wave function (triplet state). The former reduces the Coulomb repulsion of the ionic cores and leads to a bound state. In the case of the hydrogen molecule, the exchange contribution to the total energy is negative favoring an antiparallel spin configuration. The second famous example for exchange interaction is the exchange correlation hole (Fig. 2.1, right panel). This means that an electron is surrounded by a reduced density of electrons with the same spin. The Coulomb repulsion is thus again reduced, now for electrons of parallel spin.

2.2 Temperature Dependence of Magnetism

To understand magnetism, it seems crucial to understand the concept of exchange interaction. It might even be the key question. Two different approaches have been developed by Weiss and Stoner. Both were working on theories to explain ferromagnetism in solids. It was observed by Pierre Curie in 1896 that ferromagnetism is a temperature-dependent phenomenon. He found a phase transition from the ferro- to the paramagnetic phase at a certain temperature, the Curie temperature T_C. Based on this observation, in 1907 Pierre Weiss developed a model that became suitable to describe this temperature dependence in combination with the theory developed by Paul Langevin in 1905, who had been a student of Curie. Weiss postulated the existence of a molecular field H_W of unknown origin, which stabilizes the alignment of atomic magnetic moments against thermal motion[2]:

$$\frac{M(T)}{M(0)} = \tanh\left(\frac{-\mu_B(H + H_W)}{k_B T}\right). \tag{2.1}$$

The molecular field $H_W = \lambda M(T)$ is proportional to the magnetization $M(T)$ with the molecular field constant λ. H may be an additional external magnetic field. The energy gain of a dipole aligned parallel to such a field $E = -\mu_B H$ is working against the thermal energy $k_B T$. The molecular field determines the phase transition and the Curie temperature.

Weiss also assumed that the magnetization of the solid is split up into domains magnetized in different directions, which is common knowledge today and has been proven by numerous imaging techniques. The molecular field had of course also been a revolutionary approach by Weiss and it is still the basis for today's mean field theory.

In the time between the Weiss and the Stoner model, a lot of progress has been made in the microscopic description of solid matter. The existence of the electron spin had been discovered and band theory for electronic states in solids was established. Since the early years of the 20th century, band theory is used to describe the fundamental properties of metals and semiconductors. In the 1930s, Stoner [1936, 1938] and Slater [1936a,b] started to develop also a description of ferromagnetism based on the band theory.

[2] Eq. 2.1 corresponds to the Brillouin function for a spin $s = 1/2$.

2.2.1 Interlude: Band Theory

Stoner's model had been modified and adapted by numerous great thinkers and is reoccurring as a limiting case in several current theories of magnetism. It is identical to the molecular field approximation of the Hubbard model in many-body theory and can equally be treated in the local spin density approximation (LSDA) of density functional theory (DFT). This section shall give a quick overview of band theory and Stoner's model. To adopt a more modern view, a few analogies to the Hubbard model will be mentioned.

2.2.1.1 Tight Binding

In a solid, the valence electrons of neighboring atoms may have a finite spatial overlap, which then leads to the formation of energy bands. These bands can be modeled from various approaches. The most suitable approach for the transition metals Fe, Co, and Ni is the tight-binding model, since it already contains the localized nature of the d electrons.

In the tight-binding model, similar to the linear combination of atomic orbitals, the wavefunctions are composed from the single atomic orbital wavefunctions $\phi(\mathbf{r})$:

$$\Psi_{\mathbf{k}}(\mathbf{r}) = \frac{1}{\sqrt{N}} \sum_i \; e^{i\mathbf{k}\cdot\mathbf{R_i}} \; \phi_n(\mathbf{r} - \mathbf{R_i}). \tag{2.2}$$

Thus, we obtain Bloch functions oscillating in the periodic lattice of the solid. Using an appropriate Hamiltonian

$$H = -\frac{\hbar^2\nabla^2}{2m} + V_{\mathrm{A}}(\mathbf{r} - \mathbf{r_i}) + V(\mathbf{r} - \mathbf{r_i}) \tag{2.3}$$

$$= H_{\mathrm{A}} + V(\mathbf{r} - \mathbf{r_i}), \tag{2.4}$$

accounting for the potential V_{A} of each atom itself and the perturbation potential V of the other atoms. The single atom Hamiltonian H_{A} has the eigenvalues E_n and the eigenfunctions ϕ_n. So we find the eigenvalues for H by

$$\langle\Psi|H|\Psi\rangle = \langle\Psi|H_{\mathrm{A}}|\Psi\rangle + \langle\Psi|V(\mathbf{r} - \mathbf{r_i})|\Psi\rangle \tag{2.5}$$

$$= E_n \, {}_i\langle\phi|\phi\rangle_i + \; {}_i\langle\phi|V(\mathbf{r} - \mathbf{r_i})|\phi\rangle_i$$

$$+ \sum_{i\neq j} \; e^{i\mathbf{k}\cdot(\mathbf{r_i}-\mathbf{r_j})} \int \phi_n^*(\mathbf{r} - \mathbf{r_i}) V(\mathbf{r} - \mathbf{r_i}) \phi_n(\mathbf{r} - \mathbf{r_j}) d\mathbf{r} \tag{2.6}$$

$$= E_n - A - B \sum_{i\neq j} \; e^{i\mathbf{k}\cdot(\mathbf{r_i}-\mathbf{r_j})}. \tag{2.7}$$

We substituted the overlap integrals A and B. The meaning of both is illustrated in Figure 2.2. A leads to a lowering of the electronic binding energies in the solid compared to the energy in the atom. The overlap B between wave functions of neighboring atoms determines the width of the bands. Thus localized states with a low overlap between neighboring atoms will have a small bandwidth and show low dispersion.

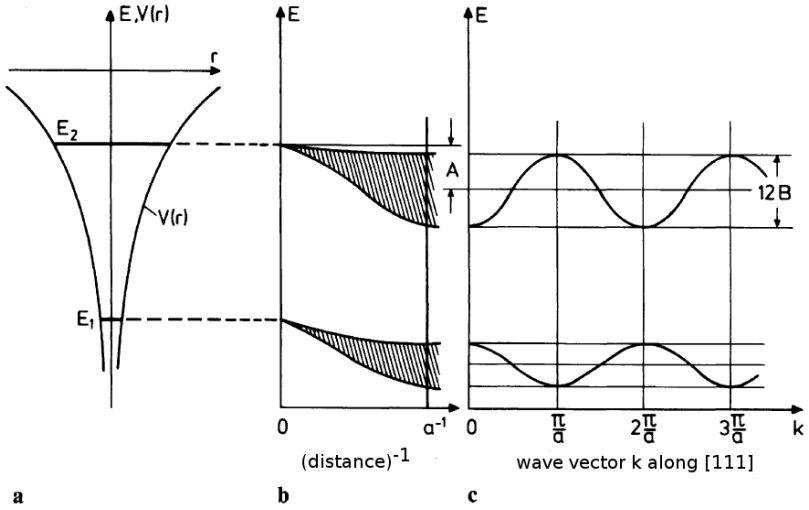

Figure 2.2: Illustration of the band structure obtained from the tight-binding model (reprinted from Ref. [Ibach and Lüth, 2009]). (a) shows where the energy levels lie in the single atomic potential $V(r)$. (b) illustrates the lowering of the center of gravity in the energy levels dependent on the reciprocal atomic distance. (c) the resulting lowering is A and the width of the band is $12B$ for s electrons in a simple cubic lattice with atomic distance a.

2.2.1.2 The Hubbard Model

In the Hubbard model, the single atom Hamiltonian H_{A} in Equation (2.4) is replaced by the so called hopping integrals T_{ij}, when written in the second quantized form. They describe the motion of electrons between neighboring atoms at different lattice sites $\mathbf{R}_i$ and $\mathbf{R}_j$. While the Coulomb interaction of electrons expressed in the perturbation potential, V gives rise to the intra-atomic Coulomb matrix element U. These are the two ingredients of the Hubbard Hamiltonian[3]:

$$H = \sum_{i,j,\sigma} T_{i,j} c^{\dagger}_{i,\sigma} c_{j,\sigma} + \frac{1}{2} U \sum_{i,\sigma} n_{i,\sigma} n_{i,-\sigma}, \tag{2.8}$$

with σ indexing the spin, $c^{\dagger}_{i,\sigma}$ and $c_{i,\sigma}$ being the creation and annihilation operators, and $n_{i,\sigma} = c^{\dagger}_{i,\sigma} c_{i,\sigma}$ the occupation number operator.

In general, a molecular field approximation neglects fluctuations from the mean values of the observables, which are the band occupation numbers $n_{i,\sigma}$ in the case of the Hubbard model. By using this mean field approach and defining the quantities: spin polarization $m = n_{\uparrow} - n_{\downarrow}$ and electron density $n = n_{\uparrow} + n_{\downarrow}$, one finds the electronic band energies to be:

$$\epsilon_{\uparrow/\downarrow}(\mathbf{k}) = \left(\epsilon(\mathbf{k}) + \frac{1}{2} U n\right) \mp \frac{1}{2} U m. \tag{2.9}$$

The band is exchange-split by $\Delta E_{ex} = Um$. From this splitting we can define an exchange field $B^{ex}_{\uparrow/\downarrow} = \frac{U}{2\mu_B}(n \mp m)$.

2.2.2 The Stoner Model

Stoner's model was a great step forward. While Weiss' mean field theory was a purely phenomenological concept, Stoner attempted to solve the problem of temperature-induced

[3] which is the special case for the limit of s bands

magnetic phase transitions by a first principles calculation. Unfortunately, the Stoner model overestimates Curie temperatures by almost one order of magnitude and a first principles theory for the temperature dependence of magnetism is still missing today. Nevertheless, Stoner's theory was a great success, since it was suitable to answer several open questions. First, it explained the puzzling fact about the magnetic moments of the band ferromagnets Fe, Co, and Ni. Their magnetic moments are far below the values predicted by Hund's rules. This was done by the simple statement, that the magnetic moment is determined by the number of holes in the d band. Second, it gave reasons why Fe, Co, and Ni are ferromagnetic while other materials are not. Stoner derived a simple relation, which has to be fulfilled in order to obtain ferromagnetism, known today as the Stoner criterion:

$$IN(E_F) \geq 1. \tag{2.10}$$

It states that for the existence of ferromagnetism (at $T = 0\,\mathrm{K}$) in a material, there has to be a sufficiently high exchange interaction, given by the exchange integral[4] I, accompanied by a large density of states $N(E_F)$ at the Fermi level E_F.

The Stoner criterion can be interpreted as a competition of exchange interaction and kinetic energy of the electrons. On the one hand, the exchange interaction ensures that Coulomb energy is gained in the case of parallel aligned spins. On the other hand, the parallel alignment of electron spins means that the same number of electrons has to occupy higher energetic states since every state can be occupied by only one electron. This increases the kinetic energy of the system, which can outweigh the energy gained by exchange interaction. This is the case for completely delocalized free electrons. We thus need a certain degree of localization to obtain magnetism. Localized states in relatively narrow bands (small parameter B in Fig. 2.2 meaning a low dispersion of the band) lead to high values in the density of states. Thus upon a higher occupation, the kinetic energy increases less than for more delocalized states in broader bands (large B, high dispersion) with a low density of states.

Stoner developed the concept of including the exchange interaction as an energetic splitting in the band structure between electrons having their spin parallel or antiparallel to an effective internal field [Wohlfahrt, 1967]. He wrote the exchange splitting as

$$\Delta E_{ex} = 2k\Theta'\zeta \tag{2.11}$$

with ζ being the temperature-dependent magnetization and $k\Theta'$ an interaction energy coefficient.

Stoner assumed that the temperature dependence, leading to changes in the density of states near the Fermi level and thus also to ΔE_{ex}, was completely determined by the changing Fermi distribution function $f(E,T) = (e^{(E-\mu)/k_BT} + 1)^{-1}$. He calculated values

[4] In the original work of Stoner, there was the term $\frac{2k\theta'}{n}$ instead of the exchange integral I, with n being the number of particles (or holes) contributing to the magnetic moment. He found that Θ' was a material-specific characteristic temperature, which is several times larger than the Curie temperature T_C. The ratio Θ'/T_C was found to be 3 for nickel and 8 for iron [Wohlfahrt, 1967].

for the Curie temperature from the condition that the susceptibility he derived

$$\chi(T) = \frac{\chi_0(T)}{1 - \frac{k\theta'}{n\mu_B^2}\chi_0(T)} \quad \text{with} \quad \chi_0(T) = 2\mu_B^2 \int_0^\infty N(E) \left| \frac{\partial f}{\partial E} \right| dE \tag{2.12}$$

goes to infinity when the magnetization vanishes. $N(E)$ is the density of states. This condition can be reformulated to

$$\frac{1}{\chi_0(T)} = \frac{k\theta'}{n\mu_B^2} \tag{2.13}$$

which finally leads to

$$\frac{2k\theta'}{n} \int_0^\infty N(E) \left| \frac{\partial f(T_C)}{\partial E} \right| dE = 1. \tag{2.14}$$

This is the temperature-dependent equivalent to the Stoner criterion $\frac{2k\theta'}{n} N(E_F) \geq 1$ for ferromagnetism. When the temperature increases, the changing Fermi function leads to a decrease of the integral until the left side becomes equal to 1 at T_C.

Unfortunately, the resulting values for T_C are nearly one order of magnitude larger than measured values. This is a significant shortcoming of the Stoner model. We know today that the main reason for that is the interpretation of the exchange splitting as the cause for a long-range magnetization. The energy difference ΔE_{ex} between the majority- and minority-spin bands is huge. It is the energy needed to reverse a single spin in one atom and is thus a measure for the local intra-atomic formation of magnetic moments. Therefore local moments can persist up to temperatures above T_C. Pickel et al. [2010] showed in a spin-resolved photoemission experiment, that the electronic states of iron can still be exchange-split as well as spin-polarized above T_C on short length scales. An attempt to correct Stoner's model came up in the 1970s, which will be discussed in the following subsection.

2.2.3 Spin Mixing or Fluctuating Local-Band Theory

In the 1970 years, there was increasing experimental evidence for the persistence of exchange splittings [Eastman et al., 1978; Petersson et al., 1976] and short-range magnetic order [Mook et al., 1973] above the Curie temperature. It was now challenging to develop a theory that includes a persisting spin splitting in the paramagnetic state above T_C. It was recognized that the excitation of spin waves (magnons) plays an important role for the low-temperature behavior of magnetization and probably also in the high-temperature regime. Spin waves had been neglected in the theory of Stoner.

A lot of work had been done to describe the temperature dependence of magnetism in a framework beyond mean-field theories like the Stoner model. The idea that was discussed the most and is continuously recurring is the spin-mixing model, formerly known as fluctuating local-band theory or fluctuating mean-field theory. This model had been developed by several authors in different theoretical frameworks. A few early versions were published

by Capellmann, who started from the Hubbard model and developed the term for the exchange splitting ΔE_{ex} in Equation (2.9) until he got a Hamiltonian of the Heisenberg form ($H = \sum_{ij} J_{ij} \boldsymbol{\sigma}_i \boldsymbol{\sigma}_j$). He assumed that the splitting ΔE_{ex} has the meaning of a local moment. This is the fundamental assumption of the spin-mixing model.

Korenman and Prange developed this idea in a series of publications. They assumed the existence of a local mean field with a direction that is fluctuating in time and space. These fluctuations play the role of spin wave excitations. In the ferromagnetic state, the local moments have parallel order. Since only the average macroscopic magnetization has to vanish above T_C, a local magnetization can remain in this model. Further, they explicitly allow the existence of exchange-split energy bands above T_C.

2.2.4 Vocabulary: Stoner *vs.* Spin-Mixing Behavior

To conclude this section, the vocabulary shall be clarified, that has been derived from the above-mentioned theoretical models. What is usually referred to as "Stoner behavior" is the observation of a decreasing exchange splitting in electronic bands when the temperature is increased. The term may be used in particular to describe a changing exchange splitting in combination with a constant spin polarization[5] in the same band. In contrast, "spin-mixing behavior" describes a lowering of the spin polarization accompanied by a persisting exchange splitting especially when heating across the Curie temperature.

A lot of progress in the description of temperature-dependent effects has been made through the transition from Stoner's mean-field theory to spin-mixing models [Sandratskii and Kübler, 1993]. While in Stoner's theory, only the value of the net magnetization is important, spin mixing accounts for fluctuations of the direction of the local magnetization. This ansatz is particularly interesting for the description of local-moment magnets as discussed in the following section.

2.3 Localized Magnetic Moments

All the approaches mentioned so far have been made to describe itinerant or band ferromagnetism. In itinerant ferromagnets, magnetism is caused by the same sort of electrons which is responsible for electrical conduction. It is thus the ferromagnetism of metals with delocalized magnetic moments. The prototypes are the transition metals Fe, Co, and Ni. They have got a direct exchange interaction, which is the type described in Section 2.1.

A second type of ferromagnetic metals are local-moment magnets, for which Gd is the prototypical example. In that type of magnets, the exchange interaction between the localized moments is mediated indirectly by the conduction electrons. It can be described by a Heisenberg Hamiltonian[6] with an indirect exchange interaction, in the case of Gd the Ruderman-Kittel-Kasuya-Yosida (RKKY) interaction. The idea for this interaction

[5] From here on, the term spin polarization addresses a macroscopic scale averaging over several local moments in terms of the fluctuating local-band theory.

[6] The prototypes of a simple Heisenberg model for magnetism are insulators like EuO. There also exist magnetic insulators with itinerant moments. These are called Mott-Hubbard insulators (*e.g.* NiO). The magnetic moments in Mott-Hubbard insulators stem from broad fully occupied bands below the Fermi level.

was developed by Ruderman and Kittel [1954] to describe the coupling of nuclear spins by a hyperfine interaction with s conduction electrons. Kasuya [1956] and Yosida [1957] recognized that an analogous mechanism can induce an exchange coupling between localized electrons in ferromagnetic metals. In Gd, the localized $4f$ electrons have no spatial overlap between neighboring atoms but with the delocalized ($5d6s$) conduction electrons. This induces a spin polarization in conduction electrons, which leads to a transmission of the spin information to the $4f$ electrons of the neighboring atom.

The localized nature of the magnetic moments in Gd has caused several debates about the correct description of the band structure and the magnetic properties of Gd. In an extensive study on the applicability of different models, Kurz et al. [2002] came to the conclusion that the measured band structure is best reproduced within the LDA+U method. This method uses the "Hubbard U" to induce strong intra-atomic interactions between the localized states. Otherwise, false binding energies are obtained in LDA where the $4f$ states are usually treated as valence states. If not corrected, one obtains an incorrect antiferromagnetic ground state of Gd. Alternatively, the $4f$ states can be declared as core states without hybridization with states of neighboring atoms. Regarding the temperature dependence, LDA+U also provides an estimate for the Curie temperature of $T_C = 263\,\mathrm{K}$, which is closest to the experimentally obtained value of $T_C = 293\,\mathrm{K}$.

Even better results have been obtained by Nolting et al. [1997] [Rex et al., 1999; Santos et al., 2004], who used a many-body approach to the Kondo-lattice (or s-f) model combined with LDA-DFT calculations. In this framework, the Hamiltonian consists of the two well-defined parts:

$$H = H_{dd} + H_{df}. \tag{2.15}$$

The $4f$ electrons with flat dispersions do not contribute to the kinetic energy. Therefore, the hopping integrals T_{ij} in the noninteracting part of the Hamiltonian are solely determined by the itinerant ($5d6s$) electrons.

$$H_{dd} = \sum_{ij\sigma} T_{ij} c^\dagger_{i\sigma} c_{j\sigma} = \sum_{k\sigma} \epsilon(\mathbf{k}) c^\dagger_{\mathbf{k}\sigma} c_{\mathbf{k}\sigma} \tag{2.16}$$

The hopping integrals T_{ij} have been Fourier-transformed into the band energies $\epsilon(\mathbf{k})$ – with $\mathbf{k}$ being the wave vector in the first Brillouin zone – by

$$T_{ij} = \frac{1}{N} \sum_{k} \epsilon(\mathbf{k}) e^{ik(\mathbf{R}_i - \mathbf{R}_j)}. \tag{2.17}$$

The Coulomb interaction term is determined by the intra-atomic interaction between the overlapping ($5d6s$) and $4f$ electrons.

$$H_{df} = -J \sum_i \boldsymbol{\sigma}_i \mathbf{S}_i \tag{2.18}$$

$\mathbf{S}_i$ is the spin operator of the localized $4f$ electrons and $\boldsymbol{\sigma}_i$ that of the ($5d6s$) valence electrons. If the coupling constant J is positive, a ferromagnetic exchange coupling is obtained as in

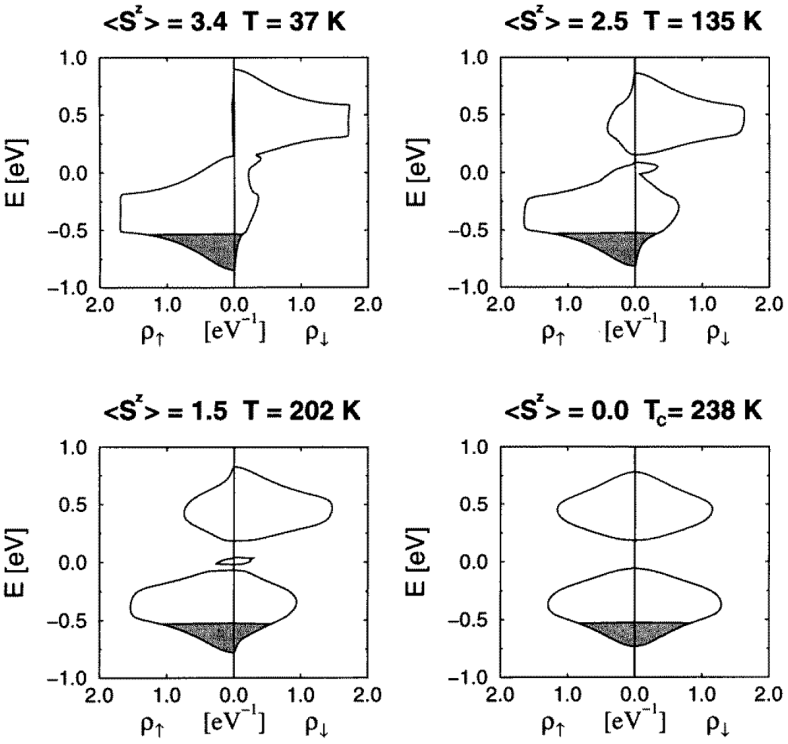

Figure 2.3: Energy-dependent quasiparticle density of states (QDOS) for majority- (left) and minority-spin (right) electrons (reprinted from Ref. [Nolting et al., 1997]). The gray shaded region indicates the occupied part of the QDOS. The four panels show scenarios for increasing temperatures (from left top to right bottom) and the decreasing $4f$ magnetization $\langle S_z \rangle$ according to Eq. (2.19). The QDOS equalize at high temperatures, because of an increasing probability for magnon absorption and emission.

the case of Gd. The case of $J < 0$ is that of the Kondo lattice. This is usually applied for the intra-atomic (antiferromagnetic) exchange coupling of magnetic impurities with conduction electrons in metals, which leads to a rising electrical resistance at low temperatures *i.e.* the Kondo effect. The screening of such a magnetic impurity by the spin polarization of the conduction electrons oscillates with the distance to the impurity (Friedel oscillations). The exchange coupling of RKKY-coupled magnets is found to oscillate in the same way between ferro- and antiferromagnetic coupling with the inter-atomic distance. It is shown in Reference [Nolting et al., 1997], that (2.18) can be transformed into the Heisenberg form $H_f = -\sum_{ij} J_{ij} \mathbf{S}_i \mathbf{S}_j$ with the effective exchange integrals J_{ij}, which can be Fourier transformed analogous to Equation (2.17) into $J(q)$. In first order, $J(q)$ shows the typical oscillatory behavior of an RKKY interaction.

The most important aspect of the approach of Nolting et al. [1997] is, that it is a spin-mixing approach. The magnetization $\langle S^z \rangle$ of the $4f$ moments is calculated according to Ref. [Callen, 1963] as:

$$\langle S^z \rangle = \hbar \frac{(S-\phi)(1+\phi)^{2S+1} + (S+1+\phi)\phi^{2S+1}}{(1+\phi)^{2S+1} - \phi^{2S+1}} \tag{2.19}$$

with ϕ being interpretable as an average number of magnons. In the ferromagnetic case $\langle S^z \rangle = S$. So $\langle S^z \rangle$ decreases from $\frac{7}{2}\hbar$ to 0 with increasing spin mixing.

Nolting et al. [1997] find that strongly temperature-dependent spin-exchange processes dominate the temperature behavior of the band structure in Gd. These spin-exchange

processes occur in two different forms: One by continuous emission and reabsorption (and *vice versa*) of magnons by a propagating electron. This case can be considered as a dressing of the electron by a virtual cloud of magnons, which Nolting calls a magnetic polaron. The second possibility of spin exchange is the simple emission or absorption of a magnon. This process is only possible, if there is an appropriate state of the opposite spin direction, since the electrons flip their spin in this process. In Figure 2.3, the resulting quasiparticle density of states (QDOS) $\rho_{\uparrow/\downarrow}(E)$ is shown. At low temperatures, minority-spin electrons (right side) can emit magnons, which leads to the low energy tail in $\rho_\downarrow$ at energies where $\rho_\uparrow \neq 0$. With increasing temperatures, the majority-spin electrons can absorb thermally excited magnons. This causes the majority- and minority-spin QDOS to equalize.

To conclude this section, it shall be mentioned that Sandratskii and Kübler [1993] also applied the concept of spin hybridization (spin mixing) to Gd using a density-functional-based theory. In this approach, temperature-induced effects are simulated by a disorder of the $4f$ magnetic moments. It is further explained in Chapter 4.2.5 regarding its applicability to ultrafast laser-induced demagnetization. They find, in accordance with Nolting, that a description in the Stoner picture is inadequate for Gd.

2.4 Magnetism in the Surface Band Structure

The reduced dimensionality at the surface affects the magnetic moment as well as the band structure. After it has first been debated in the 1970s, that the surface might be magnetically "dead" [Liebermann et al., 1970], it has been shown in the 1980s that to the contrary, there often is a higher magnetic moment at the surface [Plummer and Eberhardt, 1979]. A discussion about enhanced magnetism and even enhanced Curie temperatures at the surface followed.

Regarding the Stoner criterion, we find a higher affinity towards ferromagnetism induced by a higher density of states at the surface. Due to the lower number of neighboring atoms, the electrons have a reduced probability to hop to another lattice site. This leads to a lowering of the bandwidth and thus to an increasing density of states. This increased density of states does usually outweigh the lowered exchange interaction caused by the missing neighboring atoms. Thus, most surfaces show larger magnetic moments than bulk materials.

In the surface band structure, magnetism is reflected in the exchange splitting and spin polarization of surface states. Surface states are electronic states with a high probability density at the surface. They arise from the finite width of the potential barrier at the surface. We will derive their existence in the following subsection.

2.4.1 The Nearly-Free-Electron Model

We introduce a lattice-periodic potential $V(\mathbf{r}+\mathbf{R}) = V(\mathbf{r})$ and lattice-periodic Bloch waves $\psi_\mathbf{k} = e^{i\mathbf{kr}}u_\mathbf{k}(\mathbf{r})$ with coefficients $u_\mathbf{k}(\mathbf{r}+\mathbf{R}) = u_\mathbf{k}(\mathbf{r})$. We write both in form of a Fourier series:

$$V(\mathbf{r}) = \sum_{\mathbf{g}'} V_{\mathbf{g}'} e^{i\mathbf{g}'\mathbf{r}} \qquad \text{and} \qquad \psi_\mathbf{k} = e^{i\mathbf{kr}} \sum_\mathbf{g} u_\mathbf{g} e^{i\mathbf{gr}}. \tag{2.20}$$

The periodic potential of the lattice can be modeled for example by $V(z) = V_0 + 2V_g cos(gz)$ in the z direction perpendicular to the surface.

We solve the Schrödinger equation $\left(-\frac{\hbar^2}{2m}\nabla^2 + V(\mathbf{r})\right)\psi = E\psi$ for the coefficients $u_{\mathbf{g}}(\mathbf{k})$:

$$\sum_{\mathbf{g}} \left[-\frac{\hbar^2}{2m}(\mathbf{k}+\mathbf{g})^2 - E\right] u_{\mathbf{g}} e^{i\mathbf{g}\mathbf{r}} + \sum_{\mathbf{g}'\mathbf{g}} V_{\mathbf{g}'} u_{\mathbf{g}} e^{i(\mathbf{g}'+\mathbf{g})\mathbf{r}} = 0. \tag{2.21}$$

By shifting the index in the potential part, we can factor out $e^{i\mathbf{g}\mathbf{r}}$ and solve the equation for each summand:

$$\left[-\frac{\hbar^2}{2m}(\mathbf{k}+\mathbf{g})^2 - E\right] u_{\mathbf{g}} + \sum_{\mathbf{g}'} V_{\mathbf{g}'} u_{\mathbf{g}-\mathbf{g}'} = 0. \tag{2.22}$$

Solutions only exist for certain energies $E(\mathbf{k})$, from which we obtain our band structure.

We want to investigate these solutions within the two band approximation, which means that we take two reciprocal lattice vectors $\mathbf{g}_1 = \mathbf{0}$ and $\mathbf{g}_2 = -\mathbf{g}$ into account. Then (2.22) is a system of two linear equations, which we can write in matrix form and obtain a solution from zeroing the determinant. This will at first provide us with an equation that is quadratic in the energy E, so that we end up with two solutions:

$$E(\mathbf{k}) = V_0 + \frac{1}{2}\frac{\hbar^2}{2m}\left(\mathbf{k}^2 + (\mathbf{k}-\mathbf{g})^2\right) \pm \sqrt{\frac{1}{4}\left(\frac{\hbar^2}{2m}(\mathbf{k}^2 - (\mathbf{k}-\mathbf{g})^2)\right)^2 + V_g^2}. \tag{2.23}$$

The two-band approximation is valid for small coefficients $V_g \ll \hbar^2 g^2/2m$. $E(\mathbf{k})$ is shown in Figure 2.4(a). The periodicity of the potential induces a gap of $2V_g$ in the energy dispersion relation. This gap emerges at the Brillouin zone boundaries $\mathbf{k} = g/2$.

$$E(\mathbf{k}) = V_0 + \frac{\hbar^2\,(\mathbf{g}/2)^2}{2m} \pm V_g. \tag{2.24}$$

For the solutions outside the band gap, $\mathbf{k}$ is real with $\Im(\mathbf{k}) = 0$, as indicated by the solid line in Figure 2.4(a). Inside the gap, solutions still exist for complex wave vectors $\mathbf{k}$, which induce an exponential behavior. For an infinite crystal, this exponential behavior leads to no normalizable wave functions, due to the exponential rise in one direction. At a surface, we can normalize the waves that are exponentially decaying in the crystal, since their wave functions on the other side of the surface are not determined by the crystal anymore. This exponential damping is illustrated in Figure 2.4(b). Due to the damping of the wave functions in the crystal, the states are localized at the surface. The wave function outside the crystal is determined by the surface potential. In the case of metals this surface potential is given by the vacuum barrier arising from a dipole, which is induced by the changing charge density at the suddenly terminated periodic crystal structure.

Surface states can be classified in two categories: crystal- and barrier-induced states (see Fig. 2.5). While crystal-induced surface states derive from the electronic bands that also exist in the bulk, barrier-induced states arise solely from the form of the potential barrier

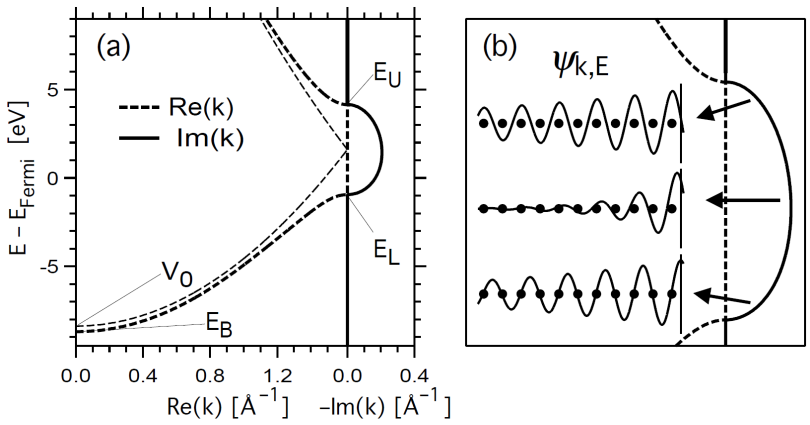

Figure 2.4: Solutions of the two-band approximation for the Cu(111) surface, reprinted from Ref. [Hotzel, 1999]. Panel (a) illustrates the real (dashed thick line) and imaginary part (solid line) of the wave vector $\mathbf{k}$ in relation to the energy $E(\mathbf{k})$. Note the two abscissa axises. The dashed thin line corresponds to the dispersion of a free electron inverted at the Brillouin zone boundary, where the periodicity of the lattice induces an energy gap. In the gap between E_L and E_U, solutions exist for complex $\mathbf{k}$. Corresponding wave functions inside the gap are shown in (b). The finite imaginary part of $\mathbf{k}$ induces a damping of the wave function into the crystal. Possible electronic states, existing inside the bulk band gap, are thus localized at the surface. The strength of the damping is energy-dependent. There is also an energy-dependent phase shift δ, since the wave function character on Cu(111) changes from s near E_U to p near E_L (Shockley-inverted). The black dots indicate the position of the atoms.

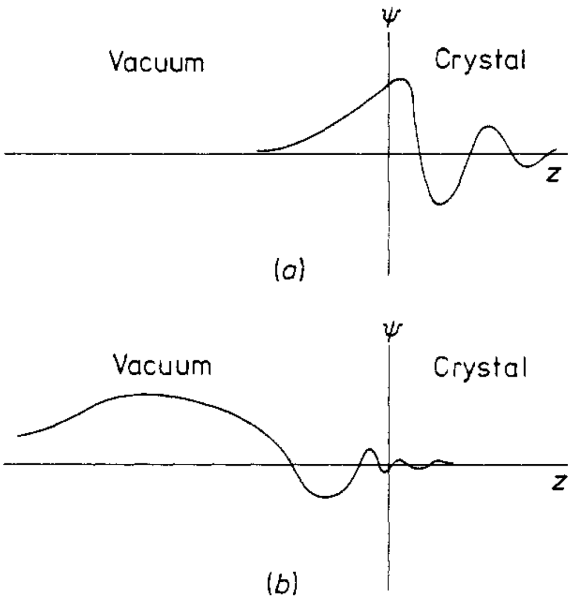

Figure 2.5: Schematic wave function of (a) a crystal-induced and (b) a barrier-induced surface state, from Ref. [Echenique and Pendry, 1978]. The maximum amplitude shifts from being localized at the surface in (a) away from the surface in (b).

at the surface and have no bulk pendant. The common example is the Rydberg series of image-potential states, that will be introduced in the following subsection.

The magnetic properties – such as spin splitting and spin polarization – of crystal-induced surface states can be extremely complex. A nice example for this is iron. The large exchange splitting in the iron bulk bands compared to the bandwidth leads to different hybridization of s, p, and d bands for opposite spin directions. Thus in iron, majority- and minority-spin surface states have different conditions to form and do not necessarily appear in pairs anymore [Braun et al., 2002]. A different situation holds for image-potential states. They constitute a nearly textbook-like model system with very little changes induced by a small wave function overlap with the underlying band structure. As such, the image-potential states provide a unique opportunity to study electronic correlation effects such as exchange interaction.

2.4.2 Image-Potential States

The existence of image-potential states was confirmed in 1984 by inverse photoemission experiments [Straub and Himpsel, 1984; Dose et al., 1984] and a year later by two-photon photoemission (2PPE) [Giesen et al., 1985]. The states had already been proposed 6 years earlier by Echenique and Pendry [1978]. Echenique and coworkers continued to study the topic for many years and produced wonderful review articles on the theoretical description [Echenique et al., 2002; Chulkov et al., 1999; Echenique et al., 2004]. A nice overview on image-potential states observed in 2PPE has also been written by Fauster and Steinmann [1995]. More information on 2PPE investigations of image-potential states can be found in Weinelt [2002].

The investigation of image-potential states on ferromagnetic thin films began in the early 90s, as nicely summarized by Donath et al. [2007]. The first spin-resolved two-photon photoemission studies on image-potential states were performed by Schmidt et al. [2005] and Pickel et al. [2006]. They investigated the open surfaces (001) of the ferromagnetic[7] transition metals Fe and Co.[8] Besides the image-potential states' exchange splitting, they studied the spin-dependent decay and scattering rates of electrons in these states. We will continue these studies on the close-packed surfaces Ni(111) and Fe(110) in Chapter 6.

Electrons in image-potential states are trapped a few Ångstrøms in front of the surface in a potential well that is induced by the electrons own image charge. In this picture, the concept of image charges is that known from classical electrodynamics, where an electron at a distance z in front of a metal induces a rearrangement of the charges inside the metal leading to a field perpendicular to the surface. The potential several Ångstrøms outside of the metal may then be described by the Coulomb potential of a positive charge at $-z$

[7] The samples in these works had been grown epitaxially on a Cu(001) substrate. Although under these conditions, Fe grows in the face-centered cubic (fcc) phase, the films had been found to be ferromagnetic [Donath et al., 2009].

[8] More of these studies can be found in the following references: [Schmidt et al., 2007; Weinelt et al., 2007; Pickel et al., 2008; Schmidt et al., 2008; Pickel et al., 2010; Schmidt, 2007; Pickel, 2007].

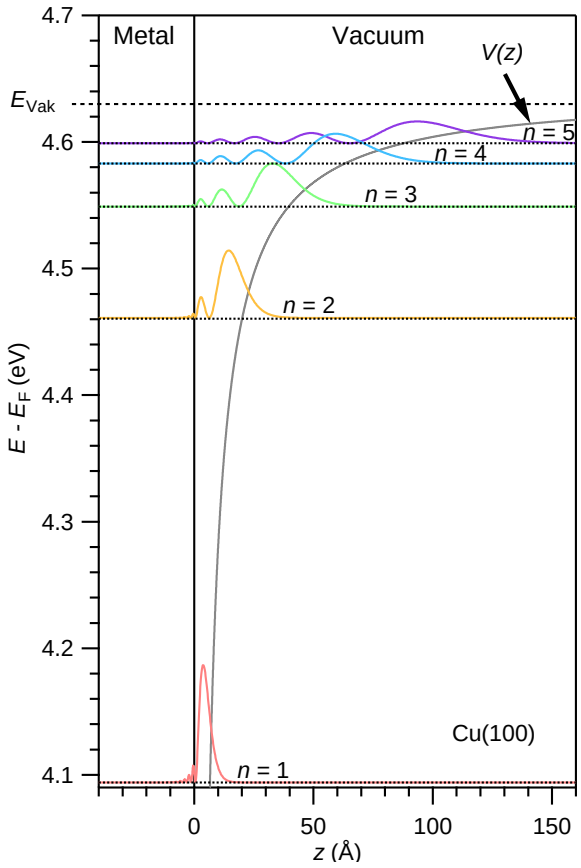

Figure 2.6: Image-potential states on Cu(100), reprinted from Ref. [Peev, 2013], calculated using a script by Cornelius Gahl based on Refs. [Hotzel, 1999] and [Fauster and Steinmann, 1995]. Colored lines represent the square of the electronic wave functions (probability density) in arbitrary units. The gray line resembles the Coulomb potential of the vacuum barrier converging to E_{vac}. The abscissa indicates the distance from the surface in Ångstrøms. The ordinate shows the binding energies to which the zero line of the probability density curves (colored lines with black dotted zero line) has been set.
The maximum probability density shifts away from the surface for higher quantum number n and higher energy. The number of minima on the vacuum side is always equal to n and the probability density inside the metal decreases with n^{-3}.

converging towards the vacuum energy of the metal.

$$V(z) = E_{vac} - \frac{e}{4\pi\epsilon_0}\frac{1}{4z} \tag{2.25}$$

In analogy to the hydrogen atom, this Coulomb-like potential causes a Rydberg series of electronic states, the image-potential states (Fig. 2.6) with binding energies

$$E_n = E_{vac} - \frac{0.85\,\mathrm{eV}}{(n + a^{\uparrow/\downarrow})^2}, \tag{2.26}$$

with the quantum number n and 0.85 eV=Ry/16 evolving from the distance $2z$ between image charge and electron.

The quantum defect a accounts for variations from the ideal Coulomb potential. Since there usually is no infinitely repulsive barrier at the metal surface, a correction has to be made at smaller distances z. A simple way to do this correction is the phase analysis model developed by Echenique and Pendry [1978]. They considered an electronic wave propagating freely between crystal surface and vacuum barrier and being reflected at both. The reflections change the waves phase by a value Φ_B and a value Φ_C at the barrier and crystal, respectively. Standing waves are obtained when $\Phi_B + \Phi_C = 2\pi n$ with $n = 1, 2, 3, \ldots$.

The quantum defect is then given by the crystal-induced phase $a = \frac{1}{2}(1 - \Phi_C/\pi)$, which is dependent on the band structure and differs for majority- ($\uparrow$) and minority-spin ($\downarrow$) electrons. Thus from this simple model, one already obtains different binding energies for majority- and minority-spin image states, since they see a different position of the band gap.

Today, accurate LDA calculations on the energetic and dynamic behavior of image-potential states are performed by Chulkov et al. [1999] [Chulkov et al., 1997, 1998; Echenique et al., 2002; Chulkov et al., 2006], who assume a model potential varying only in z direction and consisting of three parts [Echenique et al., 2004]: i) A $\cos(z)$ potential in the bulk region, which is chosen to reproduce the experimentally observed energy band gap. ii) A further cosine-like function in the solid-vacuum interface, which is chosen to reproduce the experimental energy of the crystal-induced surface states. iii) The long-range image potential. High-quality LDA calculations for the electron and hole dynamics in surface states are possible by using this model potential.

A simple approximation of the image-potential-state binding-energies and wave functions can already be obtained by combining the phase analysis model with the two-band approximation as suggested by Smith [1985]. In this approach, the wave function is obtained by matching the wave function outside the metal to a damped Bloch wave inside. The model potential used in this approach is thus similar to that of Chulkov et al. [1999] with the simplification that the image potential is directly matched to the muffin-tin potential inside the crystal at the image plane ($z = 0$). The image plane is usually set to half an atomic layer distance outside the crystal [Hotzel, 1999; Fauster and Steinmann, 1995]. The crystal-induced phase Φ_C can then be derived from the boundary condition of a continuous matching of the wave functions and their derivatives at the surface. This yields the relation

$$k \tan(\frac{\Phi_C}{2}) = \frac{g}{2} \tan(\frac{\pi}{2} + \delta) \tag{2.27}$$

between Φ_C and the phase shift δ obtained in the two band model (*cf.* Fig. 2.4(b)). Hence, in an *sp*-inverted band gap, where δ varies from $-\frac{\pi}{2}$ at the bottom to 0 at the top, Φ_C goes from 0 to π and thus a from $\frac{1}{2}$ to 0 (*cf.* Fig. 2.7). The energy-dependent (with respect to the *sp* band gap) phase and damping lead to an energy dependence of the probability densities inside the crystal, which influence binding energy, exchange splitting, lifetimes, and dephasing.

The exchange splitting arising from the different band-gap situation for majority- and minority-spin electrons has been studied by Peev [2013]. He applied the ansatz of Smith [1985] in a script[9] based on calculations developed by Hotzel [1999]. Starting from the binding energy of an $n = 1$ image-potential state, one finds a different band gap for majority- and minority-spin electrons due to the exchange splitting of the bulk bands (displayed in Fig. 2.8). This leads to a different crystal-induced phase Φ_C and quantum defect a for majority and minority spin, which in turn changes the image-potential-state binding-energy according to Equation (2.26).

The arising exchange splitting of the image-potential states can be observed in spin-resolved experiments[10]. Measured values for the exchange splitting of the $n = 1$ image-

[9] implemented by Cornelius Gahl

[10] Without spin resolution, the energy difference is too small – compared to the linewidth – to be resolved.

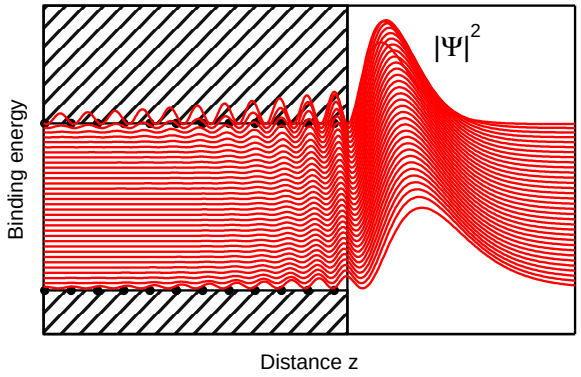

Figure 2.7: $n = 1$ image-potential state in dependence on the binding energy relative to the bulk band gap, reprinted from Ref. [Peev, 2013], calculated using a script by Cornelius Gahl based on Refs. [Hotzel, 1999] and [Fauster and Steinmann, 1995]. To obtain the different binding energies shifting across the whole band gap, the vacuum energy has been adjusted with respect to the fixed band edges. The figure illustrates that the maximum probability density shifts to larger z for a lower energy in the band gap, which happens to minority-spin electrons compared to majority-spin electrons in the $n = 1$ IPS. The character of the wave function and damping inside the metal changes as shown in Fig. 2.4(b).

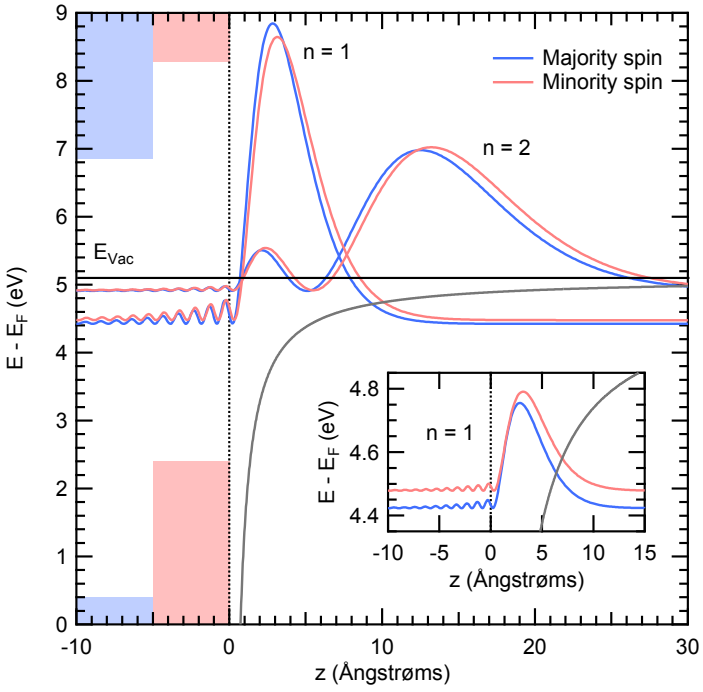

Figure 2.8: $n = 1$ and $n = 2$ image-potential states for Fe(110), reprinted from Ref. [Christ, 2014], calculated as described in Figs. 2.6 and 2.7. Compared to the majority image-potential states (blue lines), the minority image-potential states (red lines) are situated at a lower energy with respect to the band gap. Therefore, they behave as the lower lying states in Fig. 2.7 having their maximum probability density at larger z and showing a more p-like character of the wave function. The inset shows the $n = 1$ states in detail. The band-gap edges (indicated by the areas filled in light blue and red) correspond to values given in Ref. [Nekovee and Inglesfield, 1995].

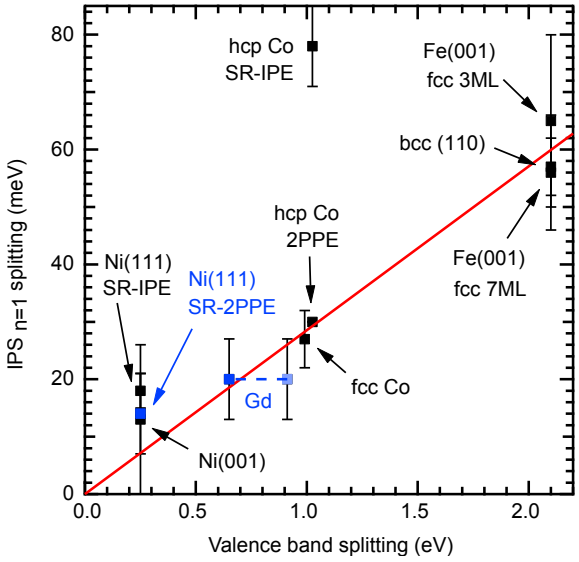

Figure 2.9: Measured values for the exchange splitting of the $n = 1$ image-potential state for different materials in dependence on the valence-band exchange-splitting. Black data points correspond to values cited in Ref. [Donath et al., 2007]. The figure is reprinted from Ref. [Andres, 2010], in which the values for Gd (blue) have been added. The blue data point for Ni(111) has been determined in this work. The red line displays a scaling with a factor of 3 %.

potential state are summarized in Figure 2.9. We find that the exchange splitting of the image-potential states scales with that of the valence bands [Andres, 2010], which is reasonable since this effects Φ_C. In contrast to our findings, Thomann et al. [1999] assumed that the exchange splitting in the image-potential states depends on the atomic magnetic moment similar to the exchange splitting in the valence bands as shown by Himpsel [1991]. Starting from the findings of Himpsel [1991] showing a valence band splitting of 1 eV per μ_B, Thomann et al. [1999] estimated a probability density of 3 % inside the crystal for the $n = 1$ image-potential state on Fe/Cu(001) and found a proportionality of 30 meV per μ_B. While this scaling with the atomic magnetic moment works fine for the $3d$ transition metal magnets, it would predict a far too large exchange splitting for the $n = 1$ image-potential state on Gd(0001). Thus, we suggest a scaling with the valence band exchange splitting, which describes the transition metals as well as the lanthanides[11]. It is, however, surprising that a scaling of 3 % (red line in Fig. 2.9) appears to fit nicely, since the calculations by Peev [2013] yield larger values of up to 6 % for the probability density inside the crystal.

[11] Weschke and Kaindl [2001] showed for the lanthanides, that the exchange splitting of the valence bands also scales with the atomic magnetic moment. The proportionality is lower by a factor of seven than in the $3d$ transition metals.

Chapter 3

Spin- and Time-Resolved Photoelectron Spectroscopy: Setup & Theory

Spin-resolved photoelectron spectroscopy is an excellent technique to study not only magnetism but also spin-dependent electronic processes like excitation, transport, and scattering. Having all benefits of simple photoemission, energy and momentum sensitivity, it completes the measurement of electronic degrees of freedom by adding spin resolution. Energy, momentum, and spin detection are experimentally realized by different components of the ultrahigh-vacuum chamber specified in Section 3.1. Time resolution is achieved by the laser setup explained in Section 3.2. Section 3.3 will introduce the necessary prerequisites for a deeper analysis of photoemission spectra concerning lineshapes and selection rules. Finally, to move on to the experiments, in Section 3.4 the basics of preparation and characterization of our samples are provided.

3.1 UHV Setup for Spin-Resolved Photoemission

Figure 3.1(a) shows a schematic overview of our photoemission setup. The basic principle is that of the photoeffect, which has been described by Einstein and observed by Hertz: When light (laser pulses sketched in red and blue) of sufficient photon energy $h\nu$ is incident on a sample, it can lead to the emission of electrons. This happens through absorption of photons, so the electrons of initial binding energy E_B can overcome the work function Φ_S of the sample and have a distinct resulting kinetic energy:

$$E_{kin} = E_B + h\nu - \Phi_S. \tag{3.1}$$

This energy relation is sketched in Figure 3.2(a). The energy is detected by a cylindrical sector analyzer (CSA 300, Focus). This is done by the application of a cylindrically symmetric electrical field, in which the electrons are deflected by 90° (Fig. 3.1(b)). Only electrons of a certain kinetic energy (pass energy) can pass the exit slit S_2 of the analyzer. After passing

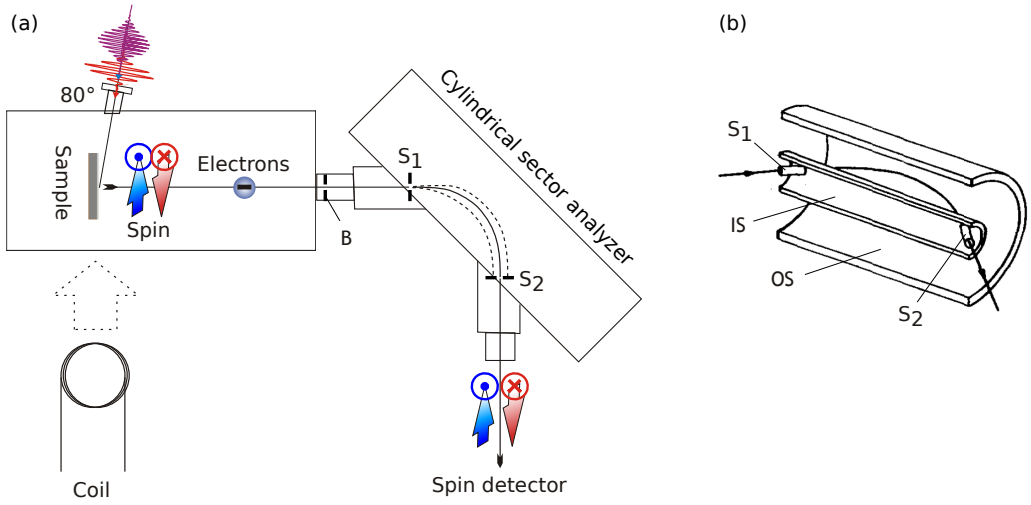

Figure 3.1: (a) Schematic drawing of our UHV setup for spin- and time-resolved photoemission, from Ref. [Andres, 2010] in the style of Ref. [Schmidt, 2007], incident at 80°). Energy resolution is realized by a spin-conserving deflection in a cylindrical sector analyzer before the electrons enter a spin detector, where they are scattered and then detected by a channeltron to obtain spin resolution. Rotating the sample allows for momentum resolution. The entrance aperture B restricts the range of accepted emission angles to $\pm 2.5°$. (b) Visualizes the parts and electron trajectories in a cylindrical mirror analyzer with the inner sector IS and the outer sector OS. Figure (b) is adapted from Ref. [Risley, 1972].

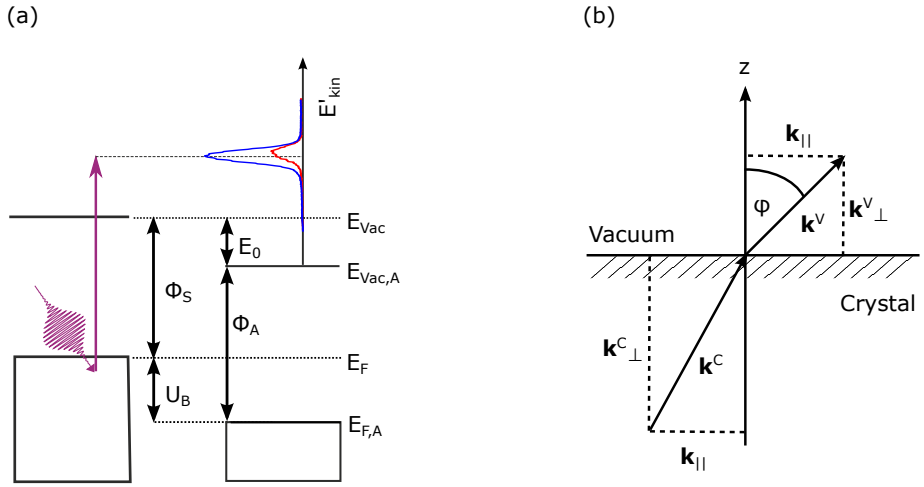

Figure 3.2: Schematic drawing of the energy (a) and momentum (b) conservation in the photoemission process, from Ref. [Andres, 2010]. (a) visualizes the difference between the kinetic energy E'_{kin} measured by the analyzer and the kinetic energy relative to the sample as given in Eq. (3.2). (b) illustrates the difference between the electron's momentum inside the crystal $\mathbf{k}_C$ before photoemission and in the vacuum $\mathbf{k}_V$ after being photoemitted. The momentum component parallel to the surface $\mathbf{k}_{||}$ is conserved, while a part of the momentum perpendicular to the surface $\mathbf{k}_\perp$ is reduced by the work function the electron has to overcome.

the entrance aperture B, the electrons are decelerated / accelerated to the pass energy E_{pass} by a system of grids and lenses before they enter the analyzer through the entrance slit S_1. By variation of the decelerating / accelerating retarding voltage U_{ret}, a range of kinetic energies can be scanned. The potential of the inner sector IS (Fig. 3.1(b)) of the CSA is thereby equally varied, which is important since it determines the potential of the entrance and exit slit S_1 and S_2 and is thus the reference potential for every voltage applied to our spin detectors.

To pass the analyzer, the electrons need to have a certain minimum of kinetic energy, which is called the analyzer's work function $\Phi_A = 4.22 \pm 0.01\,\mathrm{eV}$. The kinetic energy measured in the analyzer is thus not determined by the sample's vacuum level but by Φ_A. Since the sample and analyzer are usually grounded, their Fermi levels E_F are aligned to the same potential. The measured kinetic energy is thus (*cf.* Fig. 3.2(a)):

$$E_{kin'} = E_B + h\nu - \Phi_A + U_B = E_{kin} + E_0, \tag{3.2}$$

where we define E_0 as the difference between measured kinetic energy and kinetic energy relative to the sample:

$$E_0 = \Phi_S - \Phi_A + U_B. \tag{3.3}$$

U_B may be an additional bias voltage applied between sample and analyzer.

Momentum resolution is realized by a rotation of the sample. The entrance aperture B restricts the accepted angular range of emitted electrons to $\pm 2.5°$. The emission angle φ can be varied by rotating the sample. Since in photoemission the electron's momentum parallel to the surface $k_{||}$ is conserved (Fig. 3.2(b)), the rotation enables us to scan through the reciprocal space along this direction.

$$k_{||} = \sqrt{\frac{2m}{\hbar^2} E_{kin}} \sin\varphi \tag{3.4}$$

After having passed the analyzer, the electrons enter the spin detector where they are scattered before being detected by a channeltron. The spin detector is situated in an extra part of the vacuum chamber having its own ion and titanium-sublimation pump – and in the case of the exchange-scattering detector also an extra turbomolecular pump.

3.1.1 Spin Detection: Spin-Orbit *vs.* Exchange Interaction

Since the first realization [Shull et al., 1943] of the double-scattering experiment predicted by Mott [Mott, 1929, 1932], spin-polarization detection for a beam of free electrons is realized using spin-dependent scattering methods. The following Hamiltonian $\mathcal{H}$ describes the scattering of an electron at a surface composed of atoms sitting at the positions $\mathbf{r_i}$ having spins $\mathbf{S_i}$ [Reihl, 1981]:

$$\mathcal{H} = \underbrace{\sum_i V(\mathbf{r} - \mathbf{r_i})}_{\text{Coulomb interaction}} + \underbrace{\frac{1}{2m^2c^2} \sum_i \frac{1}{|\mathbf{r} - \mathbf{r_i}|} \frac{d}{dr} V(\mathbf{r} - \mathbf{r_i}) \cdot \mathbf{s} \cdot \mathbf{l}}_{\text{spin-orbit coupling}} + \underbrace{\sum_i J(\mathbf{r} - \mathbf{r_i}) \cdot \mathbf{s} \cdot \mathbf{S_i}}_{\text{exchange interaction}} \tag{3.5}$$

where $V(\mathbf{r}-\mathbf{r_i})$ is the Coulomb and $J(\mathbf{r}-\mathbf{r_i})$ the exchange potential that the electron with position $\mathbf{r}$, spin $\mathbf{s}$ and orbital momentum $\mathbf{l}$ experiences. The Coulomb interaction term does not depend on the electron's spin. The exchange interaction term only exists for ferromagnetic scattering targets and is the basis for the so-called exchange scattering. For non-ferromagnetic materials the spin-orbit coupling term can lead to spin resolution, which is the working principle of spin-dependent low-energy electron diffraction (SPLEED) detectors.

Two spin detectors were used to acquire the data underlying this thesis: a commercial SPLEED detector built by FOCUS GmbH and a home-built exchange-scattering detector which has been constructed and initially characterized [Winkelmann et al., 2008] by Jürgen Kirschner and coworkers of the Max Planck Institute of Microstructure Physics in Halle. The SPLEED detector was replaced by the exchange-scattering detector during the preparation of this thesis. The characterization and commissioning of the detector thus became a significant part of this work and is described likewise in the Master Thesis of Marc Christ [Christ, 2014].

Using the principle of exchange scattering for spin detection yields certain advantages compared to spin-orbit coupling. The spin-orbit-coupling energy is low compared to the Coulomb interaction constituting the main part of the scattered intensity. Therefore, to obtain a significant spin resolution, one has to select scattering conditions, which reduce the Coulomb interaction. This leads to low scattering intensities and thus low count rates. There is usually a loss of three orders of magnitude as will be described in the following.

In the SPLEED detector, the incoming electrons are accelerated to a scattering energy of 104.5 eV. Due to the spin-orbit-coupling term in Equation (3.5), electrons with $\mathbf{s}$ parallel to $\mathbf{l}$ have a higher scattering cross section. For an antiparallel alignment the scattering cross section is lowered. This results in a spin-dependent asymmetry A between opposite scattering angles:

$$A = \frac{N_l - N_r}{N_l + N_r} \tag{3.6}$$

with the count rates N_l and N_r measured left and right of the incident electron beam. Figure 3.3(a) shows a sketch of the scattering symmetry in our SPLEED detector. The intensity of scattered electrons is measured in the peaks of the low-energy electron diffraction pattern (LEED spots of index (0,2) and $(0,\overline{2})$). It has been found by Kirschner [1986], that the intensity scattered $N_{l/r}$ in these LEED spots is highest when the incoming electrons have a kinetic energy of 110 eV. At the same time, a comparably large value for the spin asymmetry A is measured in this energy region. To minimize the uncertainty of the measured spin polarization, both values have to be maximized. They are therefore combined in a new quantity, the relative figure of merit (relative FoM).

$$\text{relative FoM} = A^2 \cdot \frac{N_{l/r}}{N_0} \tag{3.7}$$

To take the statistical uncertainty into account, which is proportional to $\sqrt{N_{l/r}}$, the asymmetry A is squared in Equation (3.7). A maximum of the relative FoM is found at 104.5 eV, which is therefore chosen as the "working point" (point of optimum operation) of the SPLEED detector. At this energy, the number of electrons scattered into one of the LEED spots is

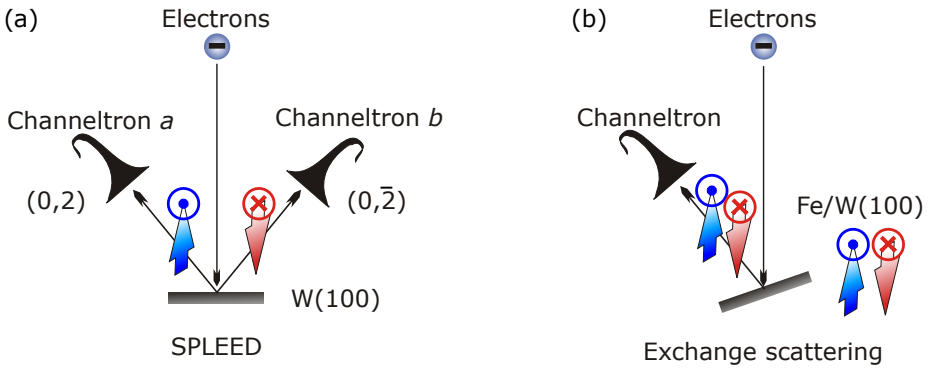

Figure 3.3: Sketch of the scattering geometry in our spin detectors: (a) SPLEED and (b) exchange-scattering detector. In the SPLEED detector, electrons are scattered at a W(100) target in normal incidence using spin-orbit coupling to generate a spin-dependence in the scattering probabilities to the left (Channeltron *a*) and to the right (Channeltron *b*). The exchange-scattering detector relies on the spin-dependent reflectivity of an oxidized Fe/W(100) target. This allows to use the specular reflex at an incidence (and emission) angle of 15°. Fig. (a) is reprinted from Ref. [Andres, 2010].

0.1 % of the incident electron beam [Foc, 2003]. Thus, the SPLEED detector looses a factor of 1000 in count rate.

$$\frac{N_{l/r}}{N_0} = 2 \cdot 10^{-3} \tag{3.8}$$

The count rate can be improved using the specular reflex (index (0,0)) as it is done in the exchange-scattering detector (shown in Fig. 3.3(b)). The electron beam comes in at an incidence angle of 15° off normal. At low scattering energies, nearly all scattered intensity is gathered in the specular reflex because no diffracted beams are created by the periodic lattice. We now use the exchange-induced asymmetry that is present for ferromagnetic scattering targets – in our case an Fe film on W(100).

Exchange scattering relies on the presence of a spin-split band gap in the scattering target (*cf.* Fig. 3.6). Electrons with energies and momenta matching the band gap, can not occupy any states and are thus reflected with higher intensities. If the band gap is spin-split, scattering energies near the band gap edges can lead to huge differences in the reflectivity of electrons of opposite spin directions. A spin-dependent asymmetry can thus be achieved by magnetization reversal of the sample or scattering target.

$$A = \frac{N_{\uparrow\uparrow} - N_{\uparrow\downarrow}}{N_{\uparrow\uparrow} + N_{\uparrow\downarrow}} \tag{3.9}$$

$N_{\uparrow\uparrow}$ / $N_{\uparrow\downarrow}$ means sample and target are magnetized parallel / antiparallel.

The measured spin-dependent asymmetry A is still different from the spin polarization $P = \frac{I^{\uparrow} - I^{\downarrow}}{I^{\uparrow} + I^{\downarrow}}$, which is a property of the sample describing the ratio between majority- and minority-spin electrons. This difference is caused by the finite spin-dependence of the

scattering process. We can account for it by adding a factor S to equations (3.6) and (3.9).

$$A = S \cdot P \tag{3.10}$$

$$P = \frac{1}{S}\frac{N_l - N_r}{N_l + N_r} \tag{3.11}$$

Note that the count rates $N_{l/r}$ in Equation (3.11) are in the notation of Equation (3.6) for the SPLEED detector. Relation (3.10) is the same for the exchange-scattering detector when the asymmetry A from Equation (3.9) is used.

The factor S is called the Sherman function. It is a measure for the detector's spin resolution and depends on scattering energies, scattering angles, and on the quality of the scattering target. For the SPLEED detector, we found that S increased from 0.23 [Pickel, 2007] to 0.28 [Andres, 2010] with the repetitive cleaning of the W(001) scattering target, which is in line with the findings of Yu et al. [2007]. The newly installed exchange-scattering detector exhibits a Sherman function of $S = 0.24$ at our preferred operating point specified in the following section. We determined the Sherman function of the new detector by measuring the highly spin-polarized Gd(0001) surface state. S was then adjusted to obtain the same spin polarization from Equation (3.11) as when using the SPLEED detector [Andres, 2010].

We can calculate our majority- and minority-spin intensities from:

$$I^{\uparrow} = \frac{1+P}{2}(N_l + N_r) \tag{3.12}$$

$$I^{\downarrow} = \frac{1-P}{2}(N_l + N_r) \tag{3.13}$$

In fact, for the data measured using the SPLEED detector, we took the geometric mean values of two measurements with opposite magnetization direction instead of the count rates N_l and N_r in the equations above. This is done to cancel out false asymmetries, that are not caused by the spin dependence of the scattering process but by a different geometry of the electronic beam trajectories. When we name the channeltrons a and b, we obtain the count rates $N_l = \sqrt{N_{a1}N_{b2}}$ and $N_r = \sqrt{N_{b1}N_{a2}}$ of measurement 1 and 2.

Such a geometry-induced false asymmetry is not present in the scattering geometry of the exchange-scattering detector (see Fig. 3.3). The only false asymmetry possible in this scattering geometry is an asymmetry induced by magnetic stray fields surrounding the target. To avoid stray fields emitted by the target, we prepare a thin Fe film instead of using a bulk crystal. In the following section, the exchange-scattering detector is described in more detail including preparation of the target films, optimization of the electron-beam trajectories, and determination of the optimum operation point as well as the Sherman function.

3.1.2 Commissioning of the New Exchange-Scattering Detector

Figure 3.4 shows a drawing of the exchange-scattering detector. The incoming electron beam is scattered with an incidence angle of 15° at an Fe target W (indicated by the dashed blue line) before being detected by the channeltron $Ch\ B$. The target W is mounted onto a crystal holder H, which includes an electromagnet M. This magnet is a ferrite ring wrapped

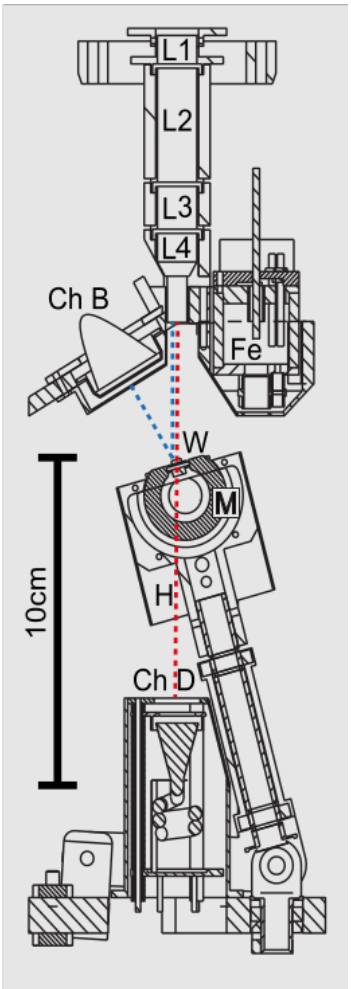

Figure 3.4: Drawing of the main parts of the exchange-sattering detector, from Ref. [Winkelmann et al., 2008]. The electrons enter the detector through the four lenses $L1$ to $L4$ and are scattered at the target W into the channeltron $Ch\ B$ (B standing for back scattering) as indicated by the dashed blue line. The target W is mounted on a crystal holder H, which includes an electromagnet M. The crystal holder H can be moved from the measurement position behind the four lenses into a preparation position in front of an Fe evaporator Fe. In this constellation, the incoming electrons can be directly detected by the channeltron $Ch\ D$ (D for direct) as indicated by the dashed red line.

with a coil, which has been carefully designed to show a negligible remanent magnetic field [Winkelmann et al., 2008]. The complete holder H – including electromagnet M and target W – is rotatable by 360° allowing for spin resolution in every possible direction parallel to the target surface. Furthermore, H can be moved in front of the iron evaporator Fe to grow a new target. In this position, the incoming electrons can be directly detected by the channeltron $Ch\ D$ (dashed red line). Additional spin-integrated measurements without any loss in count rate can be performed in this constellation.

3.1.2.1 Voltages at the Lenses

As shown in Figures 3.4 and 3.5, there is a significant difference (7.5 cm) in the electron's trajectories between spin-resolved and spin-integrated measurement modes. Since the scattering target is 3.5 cm behind the lenses, it is easy to focus all the electrons onto the target by simply optimizing the lenses to maximum count rate, while direct channeltron $Ch\ D$ is easily missed by most of the electrons. We therefore used the ray tracing software

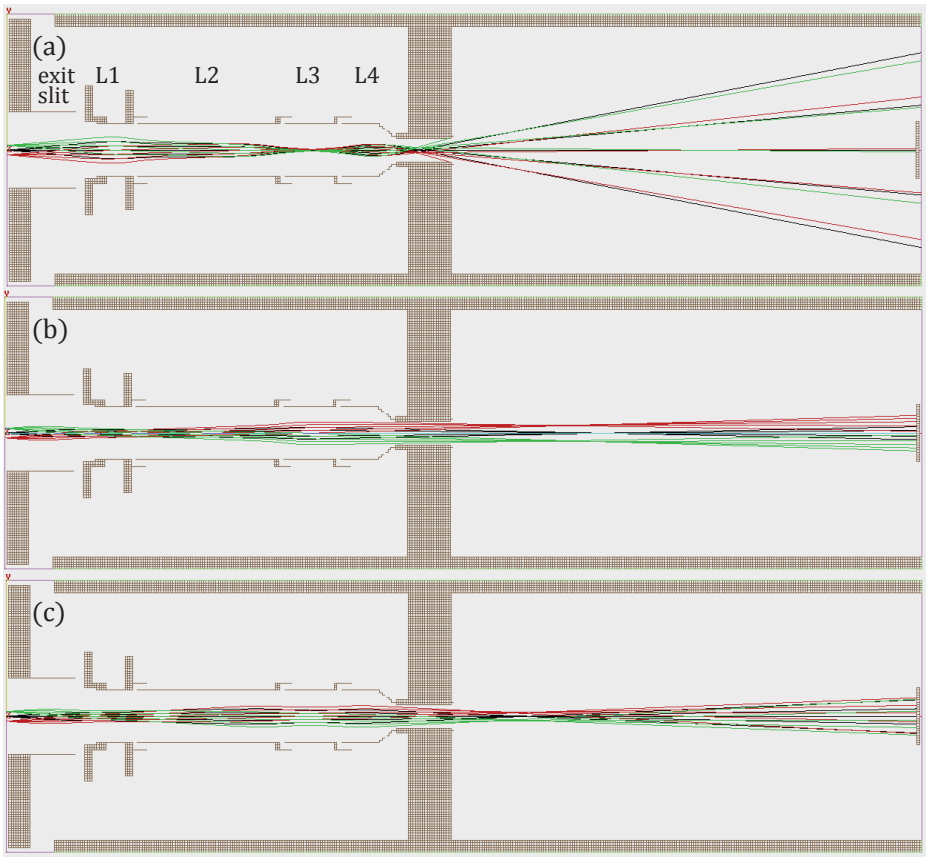

Figure 3.5: Electron trajectories simulated with the ray tracing software "SIMION" (Scientific Instruments Services, Inc.), reprinted from Ref. [Christ, 2014]. The exit slit of the CSA (shown in Fig. 3.1) is the reference potential for every voltage applied to the detector. $L1$ to $L4$ denote the lenses of the electron optics. $L4$ is electrically connected to the detector housing, which is set to the same potential as the scattering target. The direct channeltron $Ch\ D$ is drawn as a metal plate on the right side of the detector. (a) illustrates a typical unwanted situation of a highly dispersive electron beam with the voltage set $L1 = 0$, $L2 = 5.3$, $L3 = 100$, and $L4 = 0\,\mathrm{V}$. (b) shows the trajectories for a lens setting optimized for $E_{pass} = 1\,\mathrm{eV}$ using $L1 = 10$, $L2 = 5$, $L3 = 15$, and $L4 = 5\,\mathrm{V}$. (c) has been optimized for $E_{pass} = 4\,\mathrm{eV}$ using $L1 = 30$, $L2 = 20$, $L3 = 70$, and $L4 = 20\,\mathrm{V}$.

"SIMION" (Scientific Instruments Services, Inc.) to simulate the electron trajectories from the CSA's exit slit into the direct channeltron $Ch\ D$.

Figure 3.5(a) illustrates the trajectories simulated for a set of lens voltages, which we found by maximizing the count rates in $Ch\ B$. It is hardly possible to find a set of voltages, which simultaneously maximizes the counts in $Ch\ B$ and $Ch\ D$. The panels (b) and (c) show simulations for two different pass energies $E_{pass} = 1$ and $4\,\mathrm{eV}$. It turned out that the most critical point is lens 4, which is connected to the potential of the detector housing and scattering target. In the spin-resolved mode, this potential has to be set to accelerate the electrons to a certain kinetic energy. This is the scattering energy of the electrons,

the optimum of which is determined in Figure 3.6. It is the sum of the pass energy E_{pass} and the scattering potential accelerating the electrons. To obtain a better focusing in the spin-integrated mode, we use this potential as an extra lens, since no scattering potential is needed. With this, it is possible to focus the full electron beam into the direct channeltron *Ch D*.

In the spin-resolved mode, we can not afford to use lens 4, since we need to put it on the scattering potential. The lens voltages in the spin-resolved experiments are thus different from that obtained in the simulations in Figure 3.5. The lens voltages were to be optimized for every scattering potential measured in Figure 3.6, since lens 4 changes with the scattering potential.

3.1.2.2 Target Preparation

The target is a thin Fe film evaporated onto a W(001) substrate. Beforehand, the substrate needs to be cleaned from carbon impurities using the same procedure as for the W(110) substrate described in Section 3.4.1. The cleaning is achieved by heating the tungsten for several hours to temperatures between 1,400 and 1,800 K in an oxygen atmosphere of at least 2×10^{-7} mbar oxygen partial pressure. To protect the detector from melting, evaporation, and oxidation of sensitive parts, the W(001) crystal has once been cleaned by the procedure described in Section 3.4.1 before it was mounted in the detector. Additionally, the crystal is cleaned inside the detector by repetitive flashing in oxygen atmosphere as described by Zakeri et al. [2010a]. This procedure is more gentle, since each flash is done during a few seconds, which prevents the manipulator parts from reaching high temperatures. The oxygen atmosphere was created by the use of the oxygen doser included in the SPLEED setup (described in [Foc, 2003]). It comprises a heated silver tube, which exhibits an enhanced oxygen diffusion at higher temperatures.

The crystal holder can be moved from the measurement position behind the four lenses into a preparation position in front of an Fe evaporator. Here Fe is evaporated from a 2.0 mm-thick rod(/wire) of 99.999% purity (Alfa Aesar) by electron bombardment from a filament. A flux monitor is used to control the deposition rate. We calibrated the flux monitor by the use of a quartz micro-balance introduced from the side into the detector. This has been done in a separate vacuum chamber with the μ-metal shielding removed from the detector. The resulting deposition rate obtained with our standard evaporation procedure using 8 W electron-beam heating power at a voltage of 1,100 V is 3 ML of Fe per minute at a flux of 50 nA. Scattering targets of ≈ 6 ML were used for the measurements in Chapter 4 and Chapter 5. They have been deposited for 2 minutes using the just described parameters. Subsequent to the deposition, the Fe films were oxidized for 2 minutes at a partial pressure of $3 \cdot 10^{-8}$ mbar O_2.[1] This is equivalent to a dose of ≈ 3 L O_2 at which a $p(1 \times 1)$ oxygen super structure is expected [Legg et al., 1977]. This passivates the film against contaminations without losing spin asymmetry as has been shown in References [Winkelmann et al., 2008; Bertacco et al., 1999; Okuda et al., 2008]. It has even been reported, that the oxygen

[1] The base pressure in the detector chamber was typically $1 \cdot 10^{-10}$ mbar and $2 \cdot 10^{-10}$ mbar during evaporation.

superstructure increases the magnetic exchange splitting and spin-dependent scattering asymmetry [Bertacco and Ciccacci, 1999]. Subsequent to the oxidation, the film is annealed to about 600 K (measured by a pyrometer) by e-beam heating at 7 W for 10 seconds to desorb excess oxygen and produce a smooth surface.

3.1.2.3 Point of Optimum Operation

Our target film is very thin compared to those used in other detectors of the same type [Bertacco et al., 1999; Okuda et al., 2008; Winkelmann et al., 2008]. The advantage of a thinner film is the large magnetic shape anisotropy. This usually causes the easy magnetization axis of thin films to lie in the film plane to minimize magnetic stray fields. Often there is a critical thickness at which a phase transition (spin-reorientation transition) to an out-of-plane direction occurs, when the shape anisotropy is outweighed by the magneto-crystalline anisotropy. At a thickness of 6 ML, we are well below a spin-reorientation transition. Thus stray fields are minimal, which could otherwise lead to a false asymmetry contribution A_f to the scattered intensity I_μ^σ according to Ref. [Bertacco et al., 1999].

$$I_\mu^\sigma = \alpha I_0(1 + \mu\sigma P_0 A_{ex} + \sigma P_0 A_{so})(1 + \mu A_f) \tag{3.14}$$

I_0 is the initial unscattered intensity. The indices μ and σ describe the orientation of the target's magnetization direction and the spin polarization P_0 of the incoming electron beam, respectively. They are usually defined with respect to the normal $\mathbf{n}$ of the scattering plane. $\mu = +/-$ stands for magnetization parallel/antiparallel to $\mathbf{n}$. Besides the false asymmetry contribution A_f, there is the exchange-induced asymmetry A_{ex} and the spin-orbit-induced asymmetry A_{so} contributing to changes in the scattered intensity. The asymmetry contributions can be extracted from Equation (3.14) by a smart combination of intensities measured with different constellations of μ and σ [Alvarado et al., 1982].

$$A_{ex} = \frac{I^{\uparrow\uparrow} - I^{\uparrow\downarrow} - I^{\downarrow\uparrow} + I^{\downarrow\downarrow}}{I^{\uparrow\uparrow} + I^{\uparrow\downarrow} + I^{\downarrow\uparrow} + I^{\downarrow\downarrow}} \tag{3.15}$$

$$A_{so} = \frac{I^{\uparrow\uparrow} - I^{\uparrow\downarrow} + I^{\downarrow\uparrow} - I^{\downarrow\downarrow}}{I^{\uparrow\uparrow} + I^{\uparrow\downarrow} + I^{\downarrow\uparrow} + I^{\downarrow\downarrow}} \tag{3.16}$$

Figure 3.6 shows the resulting asymmetries for our detector for different values of the scattering potential applied to the Fe target. The highly spin-polarized Gd(0001) surface state[2] (investigated in Chap. 4) was used as electron source. We measured the magnetization-dependent count rates for different scattering energies of the electron beam in the detector. The incoming electrons had a pass energy of $E_{pass} = 1\,\text{eV}$. This energy is added to the scattering potential to obtain the kinetic energy of the electrons at the Fe target.

For comparison, the topmost panel of Figure 3.6 shows a band structure calculation [Tamura and Feder, 1986] for the energy range above E_F in the $\overline{\Gamma H}$ direction perpendicular

[2] At 100 K, the spin polarization of the majority-spin surface state in an in-plane-magnetized Gd thin film is $P \approx 0.63$ with the magnetization parallel to the $\overline{\Gamma\text{K}}$ direction [Andres, 2010]. The spectra shown in the present work were measured with spin resolution along the $\overline{\Gamma\text{M}}$ direction of Gd, which reduces the measured spin polarization to $P \approx 0.4$.

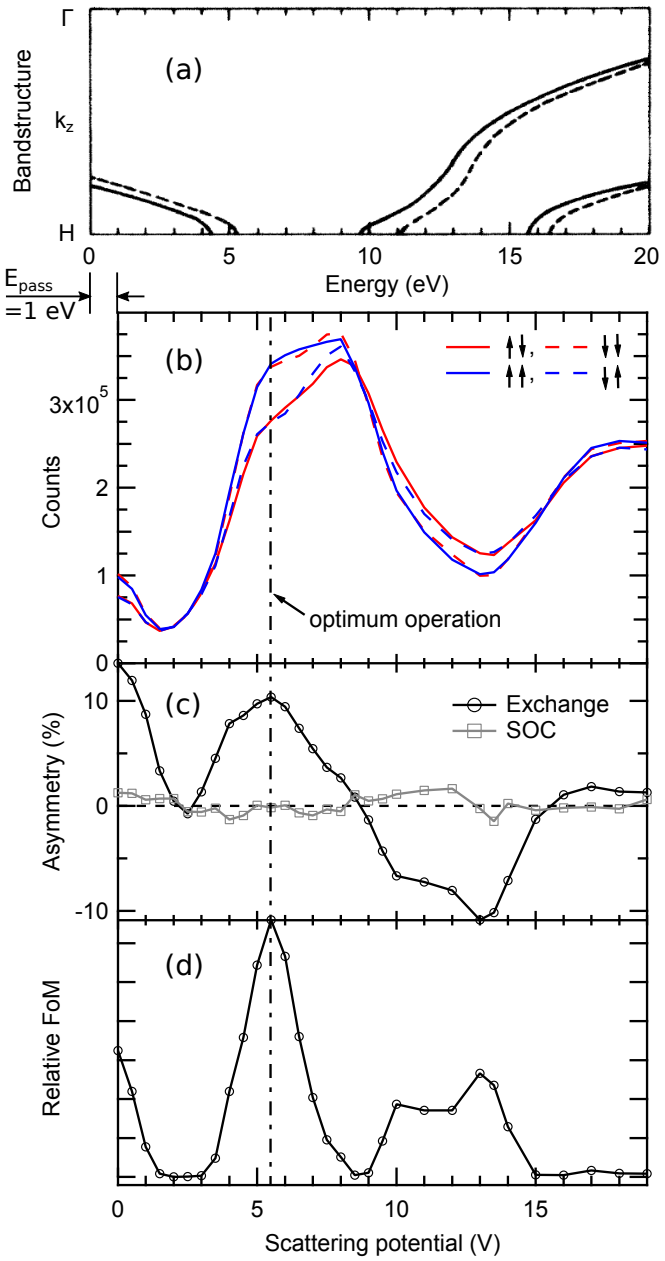

Figure 3.6: Magnetization-dependent count rates (b), resulting spin asymmetries (c), and figure of merit (FoM) (d) for different scattering potentials. Panel (a) shows a band structure calculation from Ref. [Tamura and Feder, 1986]. Solid (dashed) lines are majority- (minority-) spin bands. (b) The arrows denote the direction of detector (first arrow) and sample (last arrow) magnetization direction. A parallel alignment leads to higher (lower) count rates with respect to antiparallel magnetization near 5 V (13 V) scattering energy. The exchange- and spin-orbit-induced (SOC) asymmetries (c) have been calculated using Eqs. (3.15) and (3.16). The exchange asymmetry shows a positive and negative peak corresponding to the difference in (b). The SOC-induced asymmetry is negligible. The figure of merit (FoM) shown in (d) is given in Eq. (3.7). We find the point of optimum operation at a scattering potential of 5.5 V, where count rates and exchange asymmetry are high. The count-rate value for each scattering energy has been obtained from the total area of the Gd(0001) surface-state peak, measured in direct photoemission using the frequency-tripled of the Ti:Sa laser oscillator.

to the Fe(001) surface. There is a band gap between 5 and 10 eV kinetic energy. This is the energy range in which we find the most intensity (counts) of scattered electrons. There are no unoccupied states available, in which the electrons could reside. Thus, the reflectivity is highest. Near the edges of the band gap, the reflectivity differs for electrons with spin parallel ($\uparrow\uparrow$ or $\downarrow\downarrow$) or antiparallel ($\uparrow\downarrow$ or $\uparrow\downarrow$) to the magnetization direction of the Fe target. This is a result of the exchange splitting, which leads to the occurrence of available minority-spin states (dashed lines) at an energy, where the majority-spin band structure (solid lines) already has a band gap and *vice versa*. Thus, at the lower edge of the band gap, the reflectivity is higher for electrons with spin parallel to the target's magnetization direction ($\uparrow\uparrow$ or $\downarrow\downarrow$), while at the upper edge of the band gap, there is a larger reflectivity for an antiparallel configuration ($\uparrow\downarrow$ or $\uparrow\downarrow$).

Figure 3.6(c) shows the asymmetry values calculated from the count rates using Equations (3.15) and (3.16). The spin-orbit-induced asymmetry turns out to be very low (<1 %) in this measurement, we will therefore neglect its contribution to the spin resolution of our detector as has been done in References [Winkelmann et al., 2008] and [Okuda et al., 2008]. Using Equation (3.15) to obtain spin-resolved photoemission spectra, additional spin-orbit-induced asymmetries are ruled out.[3] The exchange-induced asymmetry (black circles) reflects the above-described behavior. It has a positive peak near the lower band-gap edge, indicating a higher reflectivity for parallel alignment of incoming spin and target magnetization. The second peak of negative asymmetry near the upper band-gap edge in turn shows the higher reflectivity for antiparallel alignment. In Figure 3.6(d), we calculated the relative figure of merit (Eq. (3.7)) from the exchange asymmetry. This yields a significant peak at 5.5 V scattering potential ($E_{kin} = 6.5$ eV) marking the point of optimum operation. All spin-resolved measurements shown in Chapters 4 and 5 have been performed at this scattering potential.

It is quite remarkable that we find the point of optimum operation at 5.5 V, while Winkelmann et al. [2008] determined a value of 13.5 V at the upper edge of the band gap for the same detector construction. Comparing our count rates with that of Winkelmann et al. [2008], we find significantly increased intensities in the low-energy regime in our setup, while the spin asymmetry shows a behavior similar to that found by Winkelmann et al. [2008]. The increased figure of merit at low energies is thus caused by the difference in count rate. We ascribe the superior low-energy operation of our detector to an additional shielding from magnetic fields. We designed a new UHV chamber for our detector exclusively comprised of μ-metal. Small magnetic fields remaining despite the integrated μ-metal shielding in the detector deflect electrons of low kinetic energies much more than those in the higher energy regime. These remaining fields are shielded by our μ-metal chamber leading to higher count rates and thus a better figure of merit at 5.5 V scattering potential.

[3] A detailed investigation of additional asymmetries occurring in the spin-detection process is given in appendix A.

Table 3.1: Performance parameters of the SPLEED and exchange scattering detector in comparison. I/I_0 for the SPLEED is taken from Ref. [Foc, 2003]. The other values have been measured in our setup and calculated accordingly. The absolute figure of merit (FoM) for the exchange-scattering detector is half of the value $S^2 \cdot I/I_0$, since each scan has to be measured twice. Once with parallel and once with antiparallel magnetization of sample and detector.

spin detector	Sherman function	I/I_0	FoM
SPLEED	0.28	$2 \cdot 10^{-3}$	$1.6 \cdot 10^{-4}$
exchange scattering	0.24	$5.5 \cdot 10^{-2}$	$1.6 \cdot 10^{-3}$

3.1.2.4 Sherman Function

We intended to reach the low-energy point of optimum operation with the additional μ-metal shielding, because other spin detection systems based on Fe(001)-p(1 × 1)-O (oxidized Fe(001)) [Okuda et al., 2008; Bertacco et al., 1999] found far larger spin asymmetries at low scattering energies $\leq 6\,\text{eV}$. Okuda et al. [2008] derived a value of 0.40 for the Sherman function at the point of optimum operation of their detector. According to Bertacco et al. [1999] and Escher et al. [2011] even larger values for the spin asymmetry are possible in the low-energy regime. Using the highly spin-polarized Gd(0001) surface state for calibration, we find a Sherman function of $S = 0.24$ at the point of optimum operation of the exchange scattering detector. This value coincides with the values determined by Winkelmann et al. [2008].

In the following, we will review the performance of our former SPLEED and the new exchange scattering detector.

3.1.2.5 Performance Overview

In summary, we find an improved performance of the exchange-scattering detector compared to our SPLEED detector. The most important parameters are summarized in Table 3.1. The exchange-scattering detector has the great advantage of an increased count rate I/I_0, which now allows measurements with an amplified laser system of a lower repetition rate (described in Sec. 3.2). The Sherman function of $S = 0.24$ of the exchange scattering detector is slightly lower than that of the SPLEED detector ($S = 0.28$). Nevertheless, when we regard the figure of merit (FoM), this lowering is more than outweighed by the increase in count rate.

Another merit of the exchange-scattering over the SPLEED detector is the possibility of switching on the fly to a spin-integrated measurement mode. This allows for quick spin-integrated scans of high intensity with energy and angular resolution, while valuable spin information can be obtained in thorough measurements at selected points in k space.

The principle of exchange scattering can be exploited to measure also non-magnetic samples or systems in which a magnetic dichroism occurs, since the magnetization of the scattering target in the detector can be reversed to obtain spin resolution. In contrast to spin-orbit coupling used in the SPLEED detector, the electron trajectories are now the same for opposite spin directions. No geometric asymmetry compromises the spin resolution anymore.

3.2 Laser

To do time-resolved photoelectron spectroscopy, a pulsed light source is necessary. In a table-top experiment as ours, this is usually a pulsed laser. A comparably simple way of creating a pulsed laser source is the principle of self (or Kerr-lens) mode-locking, which is exploited in Ti:Sapphire (titanium-doped sapphire) lasers. Two different laser setups have been used for the preparation of this thesis. Both comprising Ti:Sapphire oscillators followed by different types of frequency conversion or amplification.

The first laser has been set up by Anke B. Schmidt as the light source for the above described spin- and time-resolved photoemission setup. The laser setup has been extensively described in Refs. [Weinelt et al., 2007; Schmidt, 2007]. The pulses emitted by the Ti:Sapphire oscillator are frequency doubled and tripled. Both steps of frequency conversion can be used for two-photon photoemission (2PPE) together with the fundamental frequency. This laser system had been used for the investigation of image-potential states on ferromagnetic surfaces ever since it was build. It also has been used to investigate the energetics and electron dynamics in the image states in front of Ni(111) in Chapter 6 in this thesis. Further details on this system can be found in Section 3.2.1.

The second laser became accessible as a second light source for the same experiment through the moving of the group's laboratories from the Max-Born-Institut to the Freie Universität Berlin during the preparation of this thesis. The laser has initially been set up by Christian Eickhoff, Jens Kopprasch, and Cornelius Gahl and was rebuilt in the laboratory next to the spin-resolved experiment by Kristof Zielke, Thomas Kunze, Dominic Lawrenz, and Cornelius Gahl. It is a multi-colored source applying a regenerative Ti:Sapphire amplifier to produce pulses intense enough for either frequency conversion in two optical-parametric amplifiers (OPA) each followed by second-harmonic generation or for frequency quadrupling in a series of nonlinear optical crystals. The fundamental and the quadrupled frequency of this laser have been used for the laser-induced demagnetization experiment in Chapter 4 and the investigation of the surface band structure of Fe in Chapter 5. The details of this setup are described in Section 3.2.2.

3.2.1 Ti:Sapphire-Oscillator System

The pulsed mode of Ti:Sapphire lasers relies on the optical Kerr effect. This is a non-linear process that occurs when light intensities as high as in a laser pulse are reached. Due to the intensity dependence of the refractive index, an intensity-dependent lens – a Kerr lens – forms in a medium. Light of higher intensity experiences a larger refractive index and is thus focused harder. In our oscillators, the Kerr medium is the Ti:Sapphire crystal itself. The crystals in both systems are pumped by cw (continuous wave) light of 532 nm wavelength. The simple oscillator is pumped by a Nd:YVO_4 laser "Verdi V6" (Coherent, Inc.)[4] at a power of 5.2 W. In the amplified laser system, the beam emitted by a "Verdi G18" (Coherent,

[4]The "Verdi V6" is a neodymium-doped solid state laser emitting at a single wavelength of 1064 nm. The output is frequency doubled to 532 nm.

Inc.)[5] is split in two branches of 30 and 70 % power. It pumps the seed oscillator at a power of 4.1 W and the regenerative amplifier at 9.5 W.

The oscillators emit light of a broad spectral range from 740 to 830 nm with still more than half of the maximum possible power (this is for the central wavelength of 790 nm). This broad spectral profile carries a large number of laser modes that can oscillate simultaneously in the resonator. The modes can be superimposed by an external perturbation to form a pulse. In our cases this is done by nudging a prism or a mirror in the oscillator. The pulse then has a higher intensity than the cw mode and thus focuses itself to reach a smaller beam waist inside the Ti:Sapphire crystal. We can now prefer the pulsed mode over the cw mode by focusing the pump beam onto the area of the pulse's beam waist in the crystal. This way, the population inversion is created in the crystal only at the area of the focused pulse. The pulse is thus amplified in every cycle through the resonator, while the cw modes are more and more suppressed. This is called a soft aperture, since the cw beam is not cut off by a mechanical aperture but it is simply not amplified as much as the pulse. The pulsed mode of operation is further supported by tuning the cavity's focusing mirrors (see Fig. 3.7) to be less stable towards cw operation.

The periodic amplification of the pulse induces a modulation of the laser intensity at a frequency corresponding to the inverse of the resonator's round trip time $\frac{c}{2L}$, with L being the resonator length. Such a modulation leads to the formation of side bands at exactly the inter-mode spacing of the resonator. Thus, the side bands coincide with possible resonator modes. The modes are phase-locked to each other by the modulation and excite more and more neighboring modes. This self mode-locking stabilizes the pulse and broadens its spectrum. Having a certain spectral width, the pulse can reach a short temporal resolution of several femtoseconds.

The pulse experiences a high group-velocity dispersion (gvd) when it passes the Ti:Sapphire crystal. In the amplified laser system, this is compensated by the use of chirped mirrors. The simple oscillator shown in Figure 3.7 applies a prism compression path, which has the advantage that a desired part of the spectrum can be selected by placing a slit S in front of the output coupler OC (a 90 %-reflecting beam splitter) at the high-dispersive end of the prism compressor. Moving the slit S and the prism in front provides a certain wavelength tunability in the range from 740 to 830 nm with a spectral width of 25 to 35 nm at pulse lengths of down to 23 fs. The latter parameters can be monitored directly by a spectrometer and an autocorrelator ("Wavescan" and "Micro", APE Angewandte Physik und Elektronik GmbH) by placing an optional mirror behind the second half of the prism compression path (dashed red line).

The pulses generated by the oscillator have a power up to 1 W (for 790 nm) at a repetition rate of 88 MHz. Following the red path in Figure 3.7, we split the beam at $BS1$ in two paths having 30 % and 70 % of the original power. The 70 % are used to create pulses of the doubled or tripled frequency with enough photon energy for 2PPE when combined with the

[5] The "Verdi G18" is an optically pumped semiconductor laser (OPSL). The laser medium is a semiconductor chip comprising GaAs absorption layers with InGaAs quantum well structures. Carriers are excited in the absorption layers and recombine in the quantum well layers, leading to the emission of near infrared light. The emitted wavelength can be tuned by the stoichiometry and dimension of the layers.

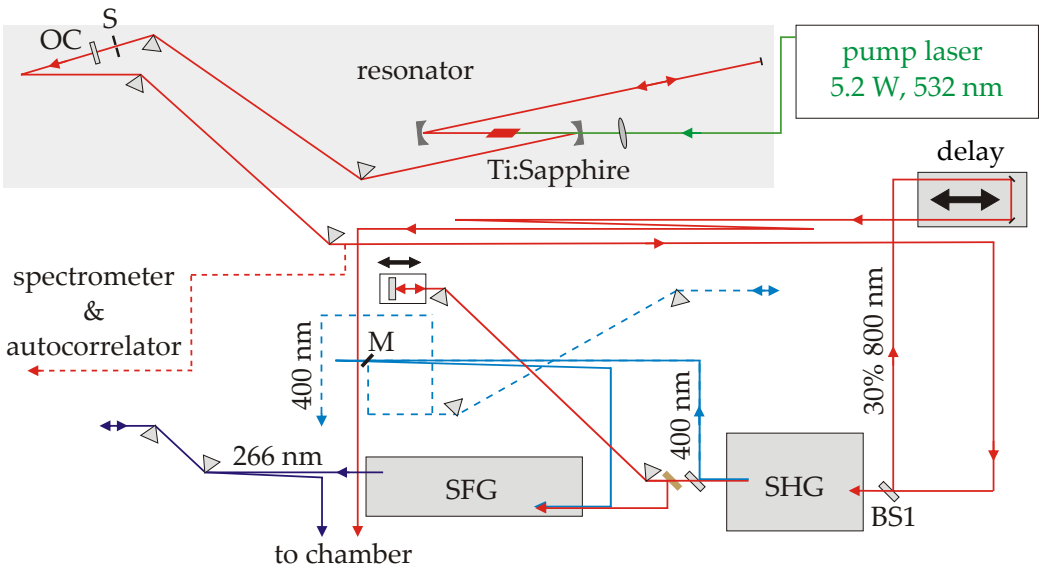

Figure 3.7: Ti:Sapphire oscillator system with second and third harmonic generation as used in Chap. 6, reprinted from Ref. [Andres, 2010] in the style of Ref. [Schmidt, 2007]. A movable slit S in the prism compression path of the resonator allows to tune the wavelength of the pulse reaching the output coupler OC in a range from 740 to 830 nm (800^{+30}_{-60} nm). The beam is then divided by a beam splitter $BS1$ into a 30 % portion going to the delay stage and a 70 % portion that is frequency doubled (second harmonic generation SHG) to 400^{+15}_{-30} nm. The 400 nm beam can either be directly guided into the vacuum chamber along the dashed blue path by placing mirror M or be used to generate the third harmonic (266^{+10}_{-20} nm) by sum-frequency generation (SFG) with the fundamental.

30 % part of the fundamental. For temporal resolution, the 30 % part is guided onto a delay stage allowing to adjust the length of the beam path relative to that of the other pulse.

The second harmonic is generated (SHG) in a 1 mm-thick lithium triborate (LBO) crystal, into which the beam is focused using curved mirrors. LBO and BBO (β barium borate) are birefringent materials that are both well suited for frequency conversion to the relatively short wavelengths in the UV regime. They have a large band gap and are not damaged by UV light. A 200 μm-thick BBO is used to generate the third harmonic by sum frequency generation (SFG). Both frequency conversion processes apply a type I phase matching. The generated beam is thus polarized perpendicular to the original beam(s). The frequency-doubled (400 nm, blue line) and -tripled (266 nm, violet line) beams are therefore rotated by polarizing periscopes shortly after their generation. A part of the fundamental beam (red) escapes the SHG and is used again in the SFG. Since a large gvd is induced in the 1 mm-thick LBO crystal, the pulses need to be shortened again in a prism-compression path before being overlayed with the second harmonic in the SFG. Alternative to SFG, the SHG pulses can be used directly for 2PPE if the optional mirror M is set into the beam path (dashed blue line). In this case, a thinner LBO crystal (0.5 mm) is used to generate shorter pulses (of lower output power). The remaining gvd is then compressed by a prism path as well. When the second harmonic is used to generate the third harmonic, a higher

intensity is favored over a shorter pulse length. The pulse is then compressed by a prism compressor in the path of the third harmonic.

3.2.2 Amplified Ti:Sapphire-Laser System

The idea on which our amplified Ti:Sapphire laser system has been founded, was to access an even wider range of photon energies than available in the oscillator and its harmonics themselves. This is done by the generation of white light in three different optical parametric amplifiers (OPAs). For the white-light generation process, higher pulse energies are required than those created in the Ti:Sapphire oscillator ($\approx 0.01\,\mu$J per pulse). For this purpose, the pulses were amplified in a commercially available chirped-pulse amplification system by Coherent Inc. ("RegA 9050" in combination with the stretcher/compressor unit of a "Legend-F" amplifier).

In this thesis, the amplified pulses were used directly to trigger ferro- to paramagnetic phase transitions, for which high laser intensities are required as well. Our amplified pulses reach energies of $\approx 6\,\mu$J. At our short pulse lengths on the order of a few tens of femtoseconds, peak powers of several thousand GW/cm^2 would be reached in the self-focusing Ti:Sapphire crystal of the regenerative amplifier (RegA). This would cause severe damage. It is suggested to keep the intensity present in Ti:Sapphire amplifiers $< 10\,$GW/cm^2 [Coh, 2006]. That is why the pulses are temporally stretched by a factor of 10,000 before they enter the RegA. The different wavelengths within the pulse spectrum are delayed to obtain a large positive gvd by the use of a single diffraction grating, which the pulse passes in four cycles. The pulse is thus chirped when it enters the RegA. After the amplification, the pulses are compressed again to a few tens of femtoseconds (48 fs pump pulses were used in this work) by another grating. The temporal stretching and compression of the pulses is done in the sole stretcher and compressor unit of the "Legend F" amplifier system (Coherent Inc.). The large optics used in this system ensure a large spectral bandwidth and thus short pulse times. A different number of lines in the grids in this system leads to reduction of third order chirps.

A scheme of the laser system is shown in Figure 3.8. After generation in the Ti:Sapphire oscillator and temporal broadening in the stretcher, the pulses are introduced to the RegA system. The RegA is another Ti:Sapphire oscillator. Its crystal is pumped by 70% of the Verdi G18 pump laser power (9.5 W), while the other 30% (4.1 W) pump the seed oscillator. The length of the cavities in the RegA and seed oscillator are matched to a round trip time of $(76\,\text{MHz})^{-1}$. For the amplification, a single pulse is injected into the RegA. It is then gradually amplified by passing the Ti:Sapphire crystal in about 28 round trips (setting-dependent) before being ejected again. After the ejection, there is a time of $3\,\mu$s to regenerate an inversion population in the Ti:Sapphire crystal before the next pulse is injected. Now, you may already guess that the RegA is a small miracle of accurate timing technology. It is realized by two acousto-optic components: A Q-switch and a cavity dumper. Both diffract incident light (otherwise transmitted) at the presence of an acoustic wave. The Q-switch is a TeO_2 crystal reducing the quality Q of the cavity, when it is driven at an acoustic wave of 80 MHz frequency. This is vital to keep the RegA from lasing by spontaneous emission, so the pump power can be stored in the Ti:Sapphire crystal during the regeneration time. The cavity dumper is a SiO_2 crystal that injects and ejects the pulses

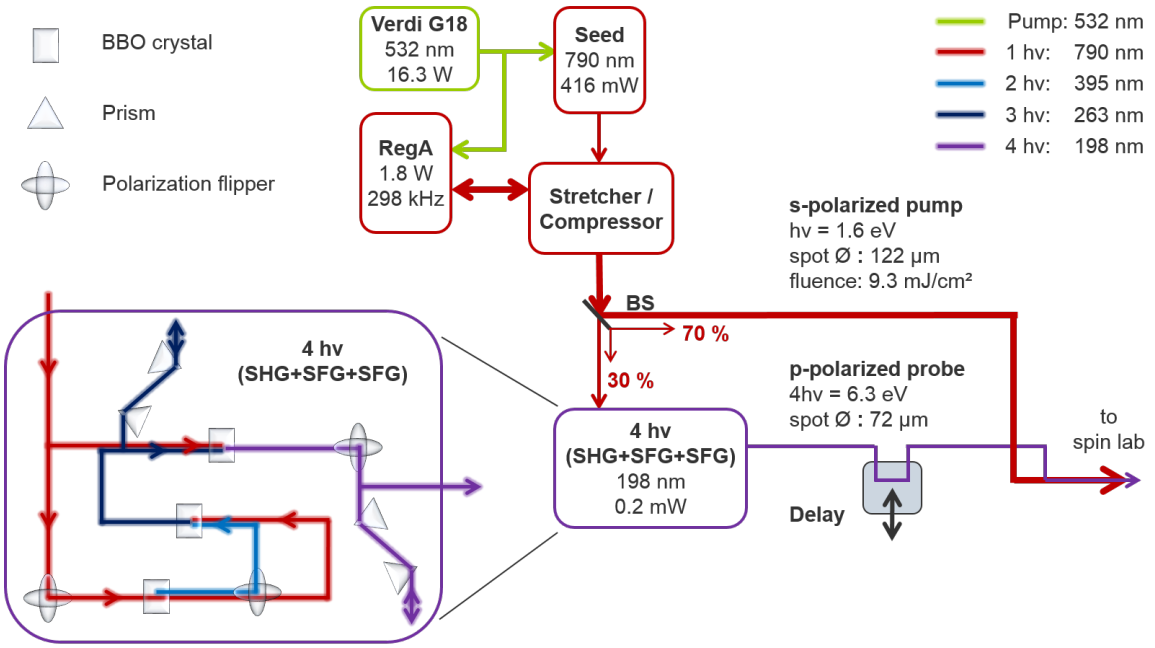

Figure 3.8: Schematic drawing of the components in the amplified Ti:Sapphire-laser system in the configuration used in this work. The seeding oscillator (Seed) and the regenerative amplifier (RegA) are pumped by the Verdi G18 (Coherent Inc.). A stretcher / compressor system is used to prevent damage of the RegA laser crystal. For the demagnetization experiment in Chapter 4, 70 % of the amplified fundamental frequency ($1h\nu$) component are used as s-polarized pump beam. To generate a probe beam, the remaining 30 % are frequency-quadrupled (as used in chapters 4 and 5). The inset shows the stages of frequency conversion from $1h\nu$ to $4h\nu$.

driven by two short 380 MHz radio frequency pulses. Triggered by the seed oscillator via a photodiode, the Q-Switch is stopped shortly before the injection of the pulse to allow for lasing in the RegA cavity. The radio frequency pulses, triggering the cavity dumper are sufficiently short to inject only one pulse out of the 76 MHz train coming from the seed oscillator. After the desired time of round trips, the cavity dumper ejects the pulse and the Q-switch is started again. The pulse is now temporally compressed at the compressor grating before it is split up into a pump (70 %) and a probe (30 %) beam (*cf.* Fig. 3.8). The beam profile of the pump beam is controlled by a telescope (not shown) for low divergence across the large distance to the vacuum chamber. Its polarization is rotated from p to s in order to avoid photoemission from the pump beam.

For probe, we used the largest photon energy available in our laser system (6.3 eV) to perform direct photoemission experiments and gain as much information on the band structure as possible. This probe beam is the fourth harmonic of the remaining 30 % of the amplified beam. The fourth harmonic is generated very similar to the third harmonic in Section 3.2.1. It is a series of nonlinear processes (*cf.* Fig. 3.8, inset) starting with the generation of the second harmonic (SHG). Different from Section 3.2.1, this is now also done in a BBO crystal of 100 μm thickness. We use again type I phase matching,

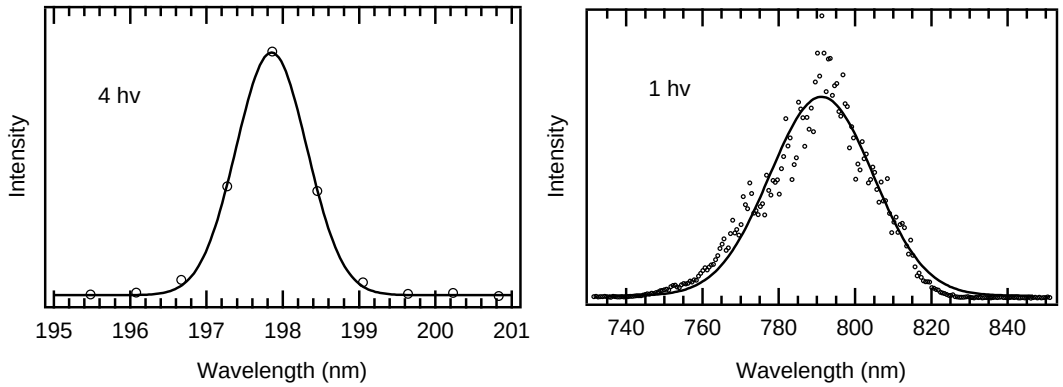

Figure 3.9: Spectra of the frequency-quadrupled (left) and amplified fundamental (right) of the Ti:Sapphire laser.

Table 3.2: Wavelengths and photon energies of the frequency-quadrupled and amplified fundamental laser beam derived from Fig. 3.9.

harmonic	central wavelength	FWHM (nm)	photon energy	FWHM (meV)
$1h\nu$	$791 \pm 2\,\mathrm{nm}$	$32 \pm 3\,\mathrm{nm}$	$1576 \pm 4\,\mathrm{meV}$	$64 \pm 6\,\mathrm{meV}$
$4h\nu$	$197.85 \pm 0.05\,\mathrm{nm}$	$1.1 \pm 0.2\,\mathrm{nm}$	$6267 \pm 2\,\mathrm{meV}$	$35 \pm 6\,\mathrm{meV}$

so the polarization has to be rotated either for the incoming or the generated beam in order to finally obtain p polarization (with respect to our sample) in all beams. In this setup, the polarization of the incoming beam is rotated by 90°. The same is done with the second harmonic. So we now have the transmitted fundamental and the second harmonic in s-polarized configuration, when we perform sum frequency generation (SFG) in another BBO crystal ($100\,\mu$m) yielding a p-polarized third harmonic. This is now guided into another BBO ($50\,\mu$m) overlayed with a part of the initial beam, that has been split off from the fundamental before the polarization was rotated. The last BBO emits the fourth harmonic as the sum of the third harmonic and the fundamental. The polarization is again rotated by a periscope.

Figure 3.9 shows spectra of the frequency-quadrupled and the amplified fundamental laser beam. Table 3.2 summarizes the photon energies derived from Figure 3.9.

3.2.3 Pump Fluence

For the demagnetization experiment in Chapter 4, the fluence of the pumping laser pulse is of great importance. A given value for the laser fluence depends on multiple measured properties that are not uniformly defined. Therefore, this section shall capture our method of calculating the laser fluence.

The incident pump fluence F was calculated from two values:

1. The pump beam power P measured in a powermeter (Melles Griot) as close as possible

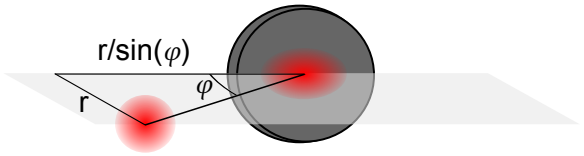

Figure 3.10: The laser spot is distorted by the angle of incidence.

(two Al-coated mirrors in between) to the vacuum chamber.

2. From the pump beams spot profile recorded by a camera (The Imaging Source) placed in the focusing point of the laser outside the vacuum chamber at a position equivalent to that of the sample.

The incident fluence is the power per pulse (therefore divided through the lasers repetition rate of 298 kHz) per cm^2:

$$F = \frac{P}{289\,\mathrm{kHz} \cdot \mathrm{A}},$$

with A being the area of the laser spot. While in that calculation the laser pump spot is assumed to be circular with a radius r that equals the half width at $\frac{\max}{e}$ of a Gaussian fitted to the spot profile.[6] This circular spot is distorted by the sine of angle φ of incidence on the sample as shown in Figure 3.10. The spot area A is thus elliptic:

$$A = \frac{\pi r^2}{\sin\varphi}.$$

Since not all of the incident laser light is absorbed but part of it is reflected, to get the absorbed fluence, we have to multiply with (1− reflectivity). The reflectivities relevant for the experiments in this work are summarized in Table 3.3.

With the knowledge of our absorbed fluence, we can now calculate how many electrons per atom are excited by the laser pulse. This is our excitation density. First, we get the number of absorbed photons by dividing through the photon energy of 1.5 eV. Second, we need to transform the area illuminated by the laser spot into a volume. We do that when we take into account the absorption profile. Having some incident light with the electric field:

$$E_{xI} = E_{x0}\, e^{i(kz-\omega t)},$$

we obtain the light in a medium with a modified velocity $\frac{c}{\tilde{n}}$. $\tilde{n}$ being the complex refractive index $\tilde{n} = n + i\kappa$. So instead of $k = \frac{\omega}{c}$, we have now $\tilde{n}k = \omega\frac{\tilde{n}}{c} = (n + i\kappa)k$ and thus find the modified electric field:

$$E_{xT} = E_{x0}\, e^{i[(n+i\kappa)kz-\omega t]} \tag{3.17}$$

$$= E_{x0}\, e^{-\kappa kz} e^{i(nkz-\omega t)}. \tag{3.18}$$

[6] This is the definition of the American National Standard Z136.1-2007 for Safe Use of Lasers.

Table 3.3: The reflectivities relevant for the experiments in this work.

material	angle of incidence	polarization	reflectivity
10 nm Gd film	45 °	s	0.58
	80 °	p	0.06

Having a look at the intensity of this light in our medium, we find

$$I_{xT} = E^*_{xT} E_{xT} = I_{x0}\ e^{-2\kappa k z}, \tag{3.19}$$

which is the Lambert-Beer law describing an exponential decay into our sample. Usually, $2\kappa k$ is summarized as one attenuation coefficient. A detailed discussion of the complex refractive index of Gd has been done by Lisowski [2005]. The value he obtained for infrared light is $\tilde{n} = 2.21 + i2.49$, which is corroborated by the measurements in Ref. [Petrakian et al., 1977]. With this $\kappa = 2.49$ and $k = \frac{2\pi}{\lambda} = \frac{2\pi}{790\,\mathrm{nm}}$, we find that 36 % of our absorbed pump fluence is absorbed in the 10 nm-thick Gd film, which is $36\,\% \cdot 42\,\% = 15\,\%$ of the incident pump fluence (reflectivity $R = 0.58$). 0.5 % of the incident fluence are absorbed in the topmost layer. Assuming that every absorbed photon excites an electron, we expect an excitation density of

$$\frac{P \cdot 0.5\,\%}{f\ A\ h\nu} = 0.03 \text{ electrons/Å}^2 \tag{3.20}$$

at the surface, with laser power $P = 470\,\mathrm{mW}$, repetition rate $f = 298\,\mathrm{kHz}$, and beam radius $r = 61\,\mu\mathrm{m}$. For Gd having a lattice constant of $a = 3.64\,\mathrm{Å}$, we find about 0.3 excited electrons per surface atom. This means there is one electron excited at every third or forth atom of the surface.

3.3 Theoretical Background of Photoemission

Finally, a few more details on photoelectron spectroscopy have to be mentioned. In Section 3.1, the energy and momentum conservation in photoemission was introduced. These allow to map the band energies onto k space and thus to determine the band structure. Echenique et al. [2004] point out that "Band mapping, however, represents only the lower level of photoelectron spectroscopy. The higher level is to derive the dynamical information from the interpretation of lineshapes, linewidths and peak intensities." The basic knowledge, that is required for such an interpretation, shall be provided in this section.

The intensity for the photoemission process can be derived from Fermi's golden rule to [Hüfner, 2003]

$$I(E) \propto \sum_{i,f} A(\mathbf{k}_i, E)\ \left|M_{i,f}\right|^2\ f(E,T)\ \delta(E_f - E_i - h\nu)\ \delta(\mathbf{k}_f - \mathbf{k}_i + \mathbf{G}). \tag{3.21}$$

The indexes i and f indicate the initial and final state. Energy and momentum conservation is fulfilled by the δ functions. $f(E,T)$ is the Fermi-Dirac distribution function. The spectral

function $A(\mathbf{k}_i, E)$ accounts for electronic correlations, scattering processes and quasiparticle interactions, which will be discussed in Sections 3.3.3, 3.3.4, and 3.3.5. The transition matrix element $M_{i,f}$ contains the dipole selection rules, which will be addressed in Sections 3.3.1 and 3.3.2.

3.3.1 Dipole Selection Rules

Dipole selection rules define whether a transition from an initial state $|i\rangle$ into a final state $|f\rangle$ can be performed in the optical excitation with light of a certain polarization (vector potential $\mathbf{A}$). The dipole selection rules can be derived by regarding the symmetry of the electronic states and that of the dipole operator responsible for the excitation. This is usually done in the framework of group theory.

An arrangement of atoms of a certain symmetry can be described by a point group that includes all symmetry operations that lead to the arrangement again. For the Ni(111) and the Gd(0001) surfaces (when regarded as 2D) this point group is C_{3v}, since they have a three-fold symmetry. The bcc Fe(110) surface has a two-fold symmetry. Its point group is C_{2v}. Every point group has a certain number of irreducible representations. These irreducible representations form a complete set of eigenfunctions to a systems Hamilton operator, if the Hamiltonian commutes with the symmetry operations. Thus, electronic wave functions can be described by a sum of irreducible representations of a system's point group. The states along the [111] direction of Ni are named Λ. In Gd [0001] direction, we find Δ states.[7] The states along the Fe[110] direction are denoted by Σ. The symmetry of each state is given by an index i in the corresponding irreducible representation. For example total symmetric states ($\equiv$ symmetric character[8] upon every symmetry operation of the group) are indexed $i = 1$ (in our cases Λ_1, Δ_1, Σ_1).

To get to selection rules, we have to regard the symmetry of our experiment. To obtain a transition matrix element unequal to zero, we need a total symmetric product of the initial state, the photons vector potential and the final state:

$$\Psi_i \times \vec{A} \times \Psi_f \mathrel{\widehat{=}} \Lambda_1,\ \Delta_1,\ \text{or}\ \Sigma_1 \tag{3.22}$$

For normal emission, the only possible final-state wave-function is a total symmetric one (Λ_1, Δ_1, or Σ_1). In this case, the product $\Psi_i \times \vec{A}$ must be total symmetric as well. Thus the direction of light polarization $\mathbf{A}$ determines the symmetry of the available initial states Ψ_i. The selection rules arising from that are shown in Figure 3.11 for the example of normal photoemission from the Fe(110) surface. When $\mathbf{A}$ is perpendicular to our scattering plane (s-polarized), electrons from initial states of Σ_4 symmetry can be emitted. P-polarized light ($\mathbf{A}$ lying in the mirror plane) has two components: $\mathbf{A}_{||}$ parallel and $\mathbf{A}_{\perp}$ perpendicular to the surface. $\mathbf{A}_{\perp}$ emits electrons out of the total symmetric initial state Σ_1. In our configuration, $\mathbf{A}_{||}$ is suitable to emit electrons from Σ_3 states. Very helpful collections of lookup tables for the dipole selection rules in various symmetries are given in Refs. [Eberhardt and Himpsel, 1980; Himpsel and Eastman, 1980; Benbow, 1980; Hermanson, 1977].

[7] The symmetry group of a 3D hcp crystal is D^4_{6h}.

[8] The characters of the representation tell, whether it is symmetric (1) or antisymmetric (-1) under the corresponding symmetry operation or if there are degenerate wave functions (2, 3, ...).

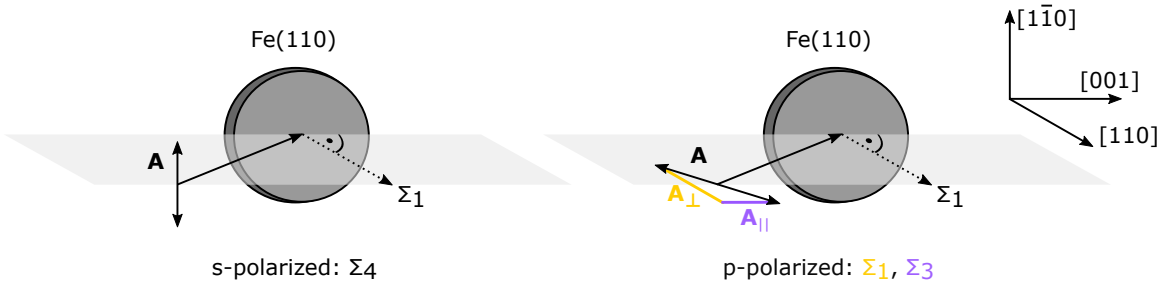

Figure 3.11: Photoemission from the Fe(110) surface using s- and p-polarized light. In normal emission (indicated by the dashed line), the final state has Σ_1 symmetry. S-polarized light (with vector field **A** perpendicular to the mirror plane indicated in gray) can only induce transitions from states of Σ_4 symmetry into Σ_1 states. P-polarized light (polarization in the mirror plane) consists of two components: One perpendicular (orange) and one parallel (violet) to the surface. The field component perpendicular to the surface can emit electrons from states of Σ_1 symmetry. The component parallel to the surface emits electrons out of Σ_3 states.

3.3.2 Magnetic Linear Dichroism

In general, magnetic dichroism means that there is a change of intensity when the magnetization is reversed. In photoemission, the intensity is caused by the interaction of light with matter and a magnetic dichroism can occur when using circularly (MCD) or linearly polarized light (MLD). Since light doesn't interact with the electron's spin but only with the orbital part of the wavefunction, a coupling of the spin to the crystal lattice is a necessary precondition for the observation of magnetic dichroism.

The selection rules introduced in the previous section are referred to as the non-relativistic selection rules. They are solely based on the spatial symmetry character of the electronic wave functions. In contrast, in the relativistic selection rules, the spin polarization is included as well. Spin-orbit coupling or magnetization reduces the symmetry of the electronic system. This can be taken into account by using double groups. A double group is obtained by multiplication of the single group with the rotational group SU_2 accounting for the spin. Energetic degeneracies are lifted in the transition from the single group to the double group and a spin-orbit splitting is obtained in the corresponding states. The double group has less irreducible representations. Thus, there are a lot more states with the same symmetry (irreducible representation). For the example of Fe(110), the four spatial symmetry representations $\Sigma_1, \Sigma_2, \Sigma_3, \Sigma_4$ each having two possible spin directions $\uparrow$ / $\downarrow$ transform into the two representations [Kuch and Schneider, 2001]:

$$\begin{aligned} \Sigma_1^{\uparrow}, \Sigma_2^{\downarrow}, \Sigma_3^{\uparrow}, \Sigma_4^{\downarrow} &\rightarrow \gamma_+ \\ \Sigma_1^{\downarrow}, \Sigma_2^{\uparrow}, \Sigma_3^{\downarrow}, \Sigma_4^{\uparrow} &\rightarrow \gamma_-. \end{aligned} \tag{3.23}$$

The corresponding band structure is shown in Figure 3.12. Since crossings between bands of the same symmetry are forbidden, hybridization gaps form at the non-relativistic crossing points (indicated by circles labeled *A*-*D*). Such hybridization points give rise to the occurrence of magnetic linear dichroism (MLD) in photoemission spectra as has, *e.g.*,

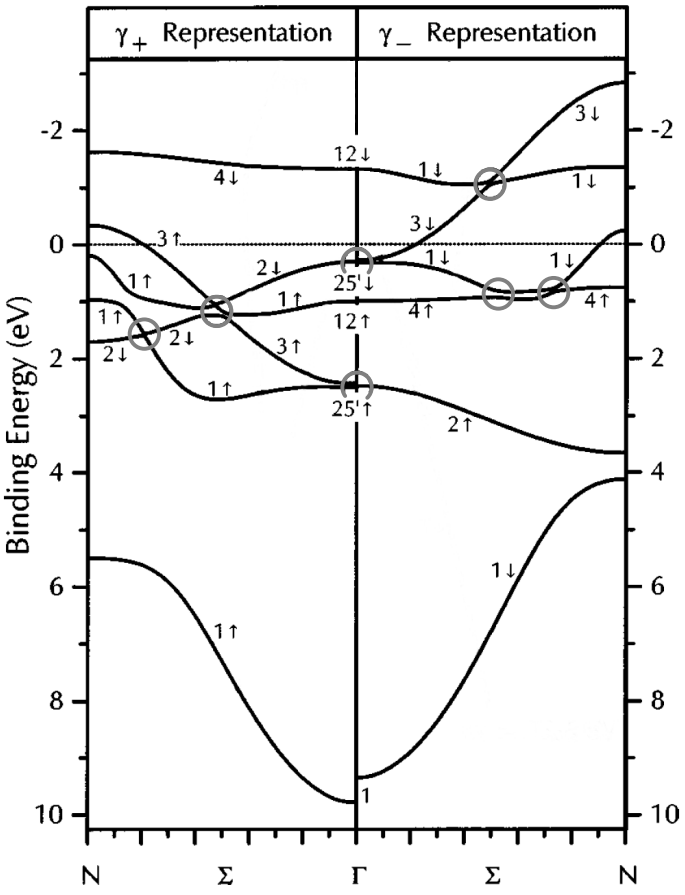

Figure 3.12: Fully relativistic band structure of Fe, reprinted from Ref. [Rampe et al., 1998]. The left and right panels show bands of the two different double-group symmetries γ_+ and γ_- induced by spin-orbit coupling according to Eq. (3.23). The numbers labeling the bands indicate the spatial single-group-symmetry characters. The arrows stand for the spin direction. The circles indicate band gaps arising to lift energetic degeneracies between bands of the same symmetry in the relativistic band structure. At these band gaps the states of different spatial symmetry hybridize to avoid a crossing of the bands.

been observed by Pickel et al. [2008] in 2PPE from Co/Cu(001) and by Rampe et al. [1998] in direct photoemission from Fe/W(110). The latter example, was measured in the same geometry as we use in Chapter 5 (*cf.* Fig. 3.11). It shall therefore be reviewed here. For readers interested in MLD in valence-band photoemission in this and other symmetries, I also recommend the references [Kuch and Schneider, 2001; Henk et al., 1996].

Rampe et al. [1998] identify the microscopic origin of the MLD to be "an interference effect induced by hybridization of initial states of different spatial symmetry at band gaps arising from spin-orbit coupling". The photoemission intensities $I(M_\pm)$ for the geometry specified in Figure 3.11 using p-polarized light have been derived by Henk et al. [1996] as:

$$\begin{aligned} I(M_\pm) =& (\sin^2\theta)\left(\left|M^{1++}\right|^2 + \left|M^{1--}\right|^2\right) + (\cos^2\theta)\left(\left|M^{3++}\right|^2 + \left|M^{3--}\right|^2\right) \\ & \pm (\sin\theta)(\cos\theta)\; Im\left(M^{1++*}M^{3++} - M^{1--*}M^{3--}\right), \end{aligned} \tag{3.24}$$

with θ being the angle of incidence (with respect to the surface normal), M_+ and M_- being the magnetization direction, and M^{1++} the transition matrix elements. In the superscript, the number indicates the spatial representation of the initial-state symmetry (*e.g.* Σ_1), the

first sign is the corresponding double group representation (*e.g.* γ_+), and the last sign is the double group representation of the final state (*e.g.* γ_+). As visualized in Figure 3.11, using *p*-polarized light, we can induce transitions from Σ_1 and Σ_3 initial states. For normal incidence ($\theta = 0°$), $\mathbf{A}_\perp$ vanishes and the light is polarized entirely parallel to the surface. According to Equation (3.24) ($\sin\theta = 0$), only Σ_3 transitions are allowed. The opposite is the case for ideal grazing incidence ($\theta = 90°$), when $\cos\theta = 0$ and only transitions from Σ_1 states remain. For all incidence angles in between, transitions from states of both symmetries are allowed, which leads to the third term in Equation (3.24), the interference term. This additional contribution to the intensity is the only part depending on the magnetization direction and thus giving rise to a magnetic-linear-dichroic effect. At the hybridization points shown in Figure 3.12, the bands change their spatial symmetry character instead of crossing. At these points, there can be a mixture of different spatial symmetries in one energy band. The interference term in Equation (3.24) can thus reach significantly large values to show a measurable dichroic effect. For example, at the Γ point, at hybridization gap *B*, both bands show Σ_1 as well as Σ_3 character. This leads to linear-dichroic effects in both bands as demonstrated in Ref. [Rampe et al., 1998].

Although the symmetry-selection rules used by Rampe et al. [1998] provide a qualitative explanation of the measured linear-dichroic effects, the selection rules may not be applicable in our case. As pointed out by Kuch and Schneider [2001], the selection rules assume inversion symmetry, which is broken at the surface. We might thus find a different situation in photoemission from surface states. Further possible origins for dichroism will be discussed in Chapter 5. A general rule to predict the existence of MLD – but not the magnitude – is given by the symmetry operations of the system: If there is no symmetry operation that reverses the magnetization and simultaneously leaves the light polarization invariant, there should be MLD. For Fe(110), the symmetry operations are the identity E, a rotation of π along the surface normal C_2, and two reflection operations at the planes perpendicular to the surface m_x and m_y. In the geometry specified in Figure 3.11, it is easy to see that reflection at the scattering plane (m_y) doesn't change the electric field of the light and leaves the pseudo vector of the magnetization invariant. So does of course the identity E. The opposite happens upon rotation C_2 and reflection m_x (at the plane between $[1\bar{1}0]$ and [110]). These operations reverse both, the magnetization and the light polarization. MLD is thus in principle possible in this geometry.

3.3.3 Electronic Correlations, Scattering Processes, Quasiparticles

Correlations between electrons or interactions of electrons with the lattice, the spins, and other systems can modify the photoemission spectrum in several ways. First of all, the intrinsic properties like electron binding energy or lifetime differ from those of noninteracting electrons. Second, the interactions can also change the effectivity of the photoemission process. Since such interacting systems of many particles are much too complex to be solved exactly, the interaction of the electron with the residual system can be summarized as an interacting quasiparticle. The self energy $\Sigma_{\mathbf{k}}(E) = \epsilon_{QP}(\mathbf{k}) - \epsilon_{\mathbf{k}}$ is the difference in energy between the non-interacting and the interacting particles. $\Sigma_{\mathbf{k}}(E)$ determines the shape of the spectral function $A(\mathbf{k}, E)$, which had been introduced in Equation (3.21):

$$A(\mathbf{k}, E) \approx -\frac{\hbar}{\pi} \frac{Im(\Sigma_{\mathbf{k}}(E))}{(E - \epsilon_{\mathbf{k}} - Re(\Sigma_{\mathbf{k}}(E)))^2 + Im(\Sigma_{\mathbf{k}}(E))^2}. \tag{3.25}$$

It has a Lorentzian structure for a fixed $\mathbf{k}$. It can easily be seen from (3.25) that the real part of the self energy renormalizes the dispersion relation of the noninteracting electron. The imaginary part determines the linewidth $\Gamma = 2\ Im(\Sigma)$ in the spectrum, which is related to the lifetime $\tau \propto \frac{\hbar}{2\ Im(\Sigma)}$ of the quasiparticle.

A common approximation for the self energy within the framework of density functional theory (DFT) is the GW approximation (GWA), in which the contributions to the self energy are restricted to the Coulomb interaction, the exchange interaction and the polarization. The name is derived from the integral:

$$\Sigma(\mathbf{r}, \mathbf{r}'; \omega) = \frac{i}{2\pi} \int d\omega' e^{-i\omega'\eta} G(\mathbf{r}, \mathbf{r}'; \omega + \omega') W_{\text{eff}}(\mathbf{r}, \mathbf{r}'; \omega'), \tag{3.26}$$

which contains the one-particle Green's function G and the screened Coulomb potential W_{eff}. The GWA is a good approach for systems with long-range screening, while the results deviate from the observations for strongly correlated systems with short-range interaction. The GWA also fails to describe systems with spin-polarized states, since it does not include spin-flip processes. W_{eff} shows no spin dependence and G describes a single electron traveling from $\mathbf{r}$ to $\mathbf{r}'$ thereby keeping the same spin state. To account for spin flips and also for short-range interactions, the GWA formalism can be extended by another matrix T to include higher-order scattering processes. This GW+T method has been applied to calculate the lifetimes and mean free paths of hot electrons in ferromagnets by Zhukov, Chulkov, and Echenique [Zhukov et al., 2004, 2005, 2006; Zhukov and Chulkov, 2009].

Considering electron-electron interaction, the screening of the Coulomb potential of the "naked" electron arises from a polarization of the surrounding electrons, which creates a cloud of polarization weakening the electron's potential. In the presence of this cloud, it is also spoken of a "dressed" particle or a quasiparticle dressing the electron. In a similar way, the electron can be dressed by a phonon cloud when electron-lattice interaction is considered or a magnon cloud in the case of electron-spin interaction.

Photoemission is a beautiful technique to study the effects of quasiparticle interactions on the electronic structure. We will use the concept of the self energy in Chapter 5 to identify the difference between two surface features in the photoemission spectrum of an Fe/W(110) thin film. Since for quasiparticles like phonons and magnons we can also assign energy dispersion relations, we find kinks in the electronic band structure at points, where the quasiparticle interaction is switched off. This happens when the energy in the electronic band structure exceeds the energy of the quasiparticle band, that renormalized the electronic energy. At such kinks, we also find a changing behavior of the linewidth, since $Re(\Sigma)$ and $Im(\Sigma)$ are Kramers-Kronig-related. This relation leads to a constant linewidth $Im(\Sigma(E)) = \text{constant}$, when there is no energy renormalization $Re(\Sigma(E)) = 0$. When there is energy renormalization, the linewidth changes. This shall be the topic of the following section.

3.3.4 Linewidth Analysis in Photoemission

For interactions with bosonic quasiparticles, the linewidth can be described by

$$\Gamma_B(E) = 2\pi \int_0^{\hbar\omega_{\max}} \alpha^2 F(\epsilon)\ (1 - f(E-\epsilon) + 2n(\epsilon) + f(E+\epsilon))\ d\epsilon. \tag{3.27}$$

Here $f(\epsilon)$ stands for the Fermi-Dirac and $n(\epsilon)$ for the Bose-Einstein distribution. $\alpha^2 F(\epsilon)$ is called the Eliashberg function. It describes the coupling between electron and quasiparticle. Using the Debye approximation, we find

$$\alpha^2 F(\epsilon) = \lambda \left(\frac{\epsilon}{\hbar\omega_D}\right), \text{ if } \epsilon \leq \hbar\omega_D \quad \text{and otherwise } \alpha^2 F(\epsilon) = 0. \tag{3.28}$$

λ is the mass enhancement parameter describing the strength of the coupling and ω_D is the Debye frequency of the quasiparticle system under investigation. From the temperature-dependent distribution functions in Equation (3.27), one obtains the following temperature-dependent behavior for the bosonic linewidth:

$$\Gamma_B \approx 2\pi\lambda k_B T. \tag{3.29}$$

There is of course also a contribution to the linewidth in the case of electron-electron interaction. Here the commonly used approximation is the Fermi-liquid theory. The linewidth

$$\Gamma_e = \beta \left[(\pi k_B T)^2 + (E - E_F)^2\right] \tag{3.30}$$

contains a temperature-dependent and an energy-dependent part. The former accounts for thermal broadening of the Fermi edge and the resulting gain of scattering phase space. The latter contains the energy distance from the Fermi level, which is a measure of phase space as well. The temperature-dependent part is negligible unless $(E - E_F) < k_B T$, which only holds for very large temperatures and binding energies E close to the Fermi level. We will see an example for this case in Chapter 4, when we directly heat the electron gas with a high power laser pulse to temperatures of $\sim 2,000\,\mathrm{K}$.

The different contributions to the linewidth may be added up according to Matthiessen's rule $\Gamma_{\mathrm{tot}} = \Gamma_e + \Gamma_B + \ldots$.

3.3.5 Linewidth Analysis in 2PPE: Scattering Processes

In Chapter 6, we will apply two-photon photoemission (2PPE) to determine the spin-dependent scattering processes occurring in the image-potential states of Ni(111) contributing to the lifetime and the linewidth of these states. The linewidth of an electronic state usually has a dephasing part, which compromises the determination of a lifetime from a measured linewidth. 2PPE is the only technique [Echenique et al., 2004] able to study the decay of an excited population of electrons and thus measure true lifetimes.

The underlying principle of 2PPE is very similar to direct photoemission with the distinction that unoccupied states are populated by a first laser pulse before electrons from these states can be measured by a second pulse. The process is illustrated in Figure 3.13

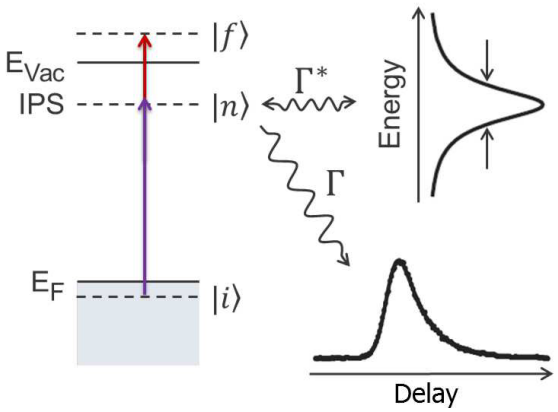

Figure 3.13: Illustration of the contributions to the linewidth measured in 2PPE, in the style of Ref. [Weinelt, 2002]. Part of the linewidth is determined by the lifetime of the electrons in the intermediate state $|n\rangle$, which is determined by energy decay through inelastic scattering processes. Another major contribution arises from the dephasing of the excited electron wave packet. Such a dephasing originates from quasi-elastic scattering processes, which induce only marginal changes in the electronic energy but shift the phase of the electron's wave function.

for the example of an image-potential state IPS close to the vacuum level E_{Vac}. In this case, electrons from an occupied initial state $|i\rangle$ are photo-excited (violet arrow) into an unoccupied image-potential state IPS, which serves as intermediate state $|n\rangle$. The photon energy is usually chosen to be lower than the work function to suppress direct photoemission, which would overlay the 2PPE signal by several orders of magnitude higher intensity. Thus, a second laser pulse (red arrow) is necessary to emit electrons from the intermediate state $|n\rangle$ into the final state $|f\rangle$. The introduction of a time delay between the two photons allows us to access the lifetime of electrons in the intermediate state $|n\rangle$.

In the intermediate state $|n\rangle$, the electrons undergo elastic and inelastic scattering leading to decay and dephasing contributions to the 2PPE spectrum with a rate of Γ and Γ^*, respectively. These contributions are illustrated to the right side of Figure 3.13. When electrons are excited coherently (for example by a laser pulse), the system does not occupy only one state anymore, but a superposition of initial $|i\rangle$, intermediate $|n\rangle$, and final state $|f\rangle$. A wave packet is created, which consists of electrons in these three states. These electronic waves scatter elastically. Thus, the electrons do not lose energy (do not decay) but change their phase while they are scattered away from the intermediate state into energetically degenerate states with different momentum and back again. This change of phases leads to a dispersion of the electronic wave packet and thus an energetic broadening. This process is called dephasing. Dephasing thus provides us with a tool to distinguish elastic and quasi-elastic scattering processes from inelastic processes leading to a decay.

The contributions to the linewidth measured in 2PPE have nicely been separated by Boger et al. [2002]. It is much more complex to describe 2PPE compared to direct photoemission. This is due to a number of additional processes happening in the intermediate state. The dynamics of the mixture of quantum states can be described in the density matrix formalism using the Liouville-von-Neumann equation

$$\dot{\rho} = \frac{1}{i\hbar}[H, \rho] - \Gamma\rho. \tag{3.31}$$

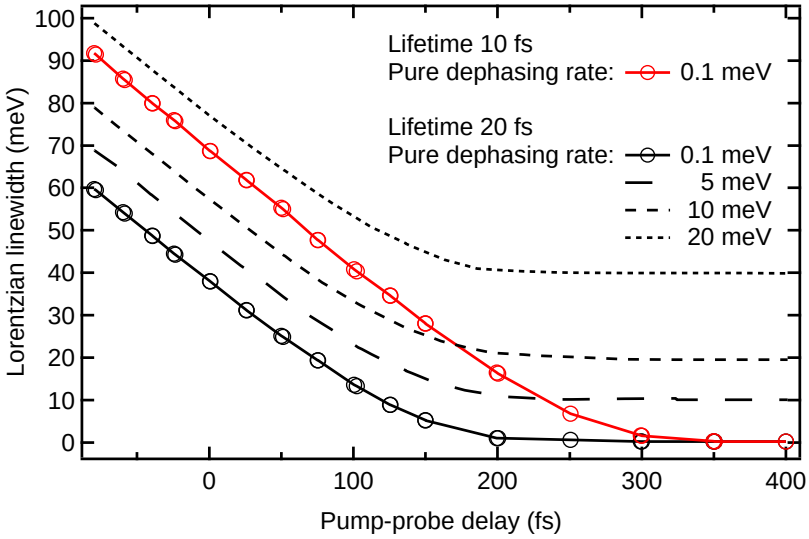

Figure 3.14: Calculated Lorentzian part of the linewidth in a 2PPE experiment, data reprinted from Ref. [Boger et al., 2002]. There are two basic contributions to the Lorentzian part of the linewidth: the lifetime and the pure dephasing rate. The lifetime contribution decreases with increasing pump-probe delays. Thus, at large pump-probe delays, the pure dephasing part can be determined.

It contains the damping matrix:

$$\Gamma = \begin{pmatrix} 0 & \frac{\Gamma_n}{2} + \Gamma_n^* + \Gamma_i^* & \Gamma_i^* + \Gamma_f^* \\ \frac{\Gamma_n}{2} + \Gamma_n^* + \Gamma_i^* & \Gamma_n & \frac{\Gamma_n}{2} + \Gamma_n^* + \Gamma_f^* \\ \Gamma_i^* + \Gamma_f^* & \frac{\Gamma_n}{2} + \Gamma_n^* + \Gamma_f^* & 0 \end{pmatrix}, \tag{3.32}$$

in which Γ_n are the decay and Γ_n^* are the dephasing rates in state $|n\rangle$ (and Γ_i^* and Γ_f^* in $|i\rangle$ and $|f\rangle$ accordingly). Using this formalism, Boger et al. [2002] find a temporal evolution of the linewidth of the intermediate-state peak during the pump-probe process. This is shown in Figure 3.14 for the Lorentzian part of the linewidth. A convolution with the Gaussian shape of the pump and probe pulses adds an offset to the total linewidth, that increases in the direction of negative pump-probe delays. Figure 3.14 shows that the lifetime contribution to the linewidth decreases with rising pump-probe delay and vanishes for large pump-probe delays. There, the pure dephasing rate remains as the only linewidth contribution. The linewidth is then twice the pure dephasing rate. Thus measuring the linewidth at large delays allows to measure the sole contribution of the pure dephasing rate. This is particularly interesting in spin-resolved experiments, since a spin dependence in the quasi-elastic scattering processes is very likely to be caused by electron-magnon interactions with low energy transfer.

3.4 Samples

All samples investigated in this thesis were grown *in situ* on a W(110) substrate. The body-centered-cubic lattice (bcc) of W results in a pseudo-hexagonal structure of the sites on the W(110) surface. Fe, Ni, and Gd films grow in equally hexagonal or pseudo-hexagonal structure on W(110). We can thus investigate the close-packed surfaces of the ferromagnets. Using W(110) as a substrate has even more benefits. Due to its high melting point, it can be cleaned from almost every kind of impurity by a flash to a high temperature close to the melting point. Even the deposited films can be removed by a high temperature flash. The only known impurity, that can not be desorbed by simple flashing, is carbon. In order to remove carbon impurities, the carbon has to be oxidized first. It is therefore a common procedure to clean a W single crystal by cycles of heating in oxygen atmosphere and subsequent high-temperature flashing in order to eliminate tungsten oxide. All temperatures were measured with a thermocouple (type C) directly attached to the tungsten crystal. The thermocouple was calibrated in Reference [Andres, 2010].

3.4.1 Preparation of the W(110) Substrate for the Deposition of Thin Films

There are different methods of oxygen heating applicable to clean W from carbon impurities. The choice of the method strongly depends on the shape of the crystal, the surroundings of the sample holder, and the vacuum chamber. Since we use a crystal of 2 mm thickness it is nearly impossible to purify the whole bulk of the crystal from carbon. Instead, we created a zone of carbon depletion at the surface, which needs to be refreshed after several high-temperature flashes, since carbon keeps segregating from the bulk to the surface layers, when the crystal is heated. This segregation is much more efficient at higher temperatures. We performed a neat study comparing the commonly used cleaning temperatures of 1400 and 1800 K in the master thesis of Paul Weiss [Weiss, 2013]. Therein, we demonstrated by heating the W crystal without oxygen atmosphere, that far more carbon segregates from the bulk to the surface, when the crystal is kept at 1,800 K for only 10 minutes than at 1,400 K for half an hour. Therefore, we applied the following two cleaning procedures.

In order to prepare a freshly grown W single crystal for the use as a substrate, we heated the crystal to a temperature of 1,800 K at an oxygen partial pressure of 2×10^{-7} mbar for 60 hours with repetitive flashes[9] to 2,300 K every 8 hours. Since these are usually unfavorable conditions for a vacuum chamber housing evaporators and for a sample holder with a good thermal contact designed for cooling to low temperatures during a measurement, this procedure was performed in an extra chamber, which we set up solely for the purpose of tungsten cleaning. After this treatment, the crystal has the desired zone of carbon depletion in the outer layers. It can now be mounted in the measurement chamber, where carbon impurities segregating to the surface during film preparation need to be removed every few weeks. This has been done as described in the following.

[9] To flash the crystal means to heat to the specified temperature within 10 seconds and to decrease the temperature immediately afterwards.

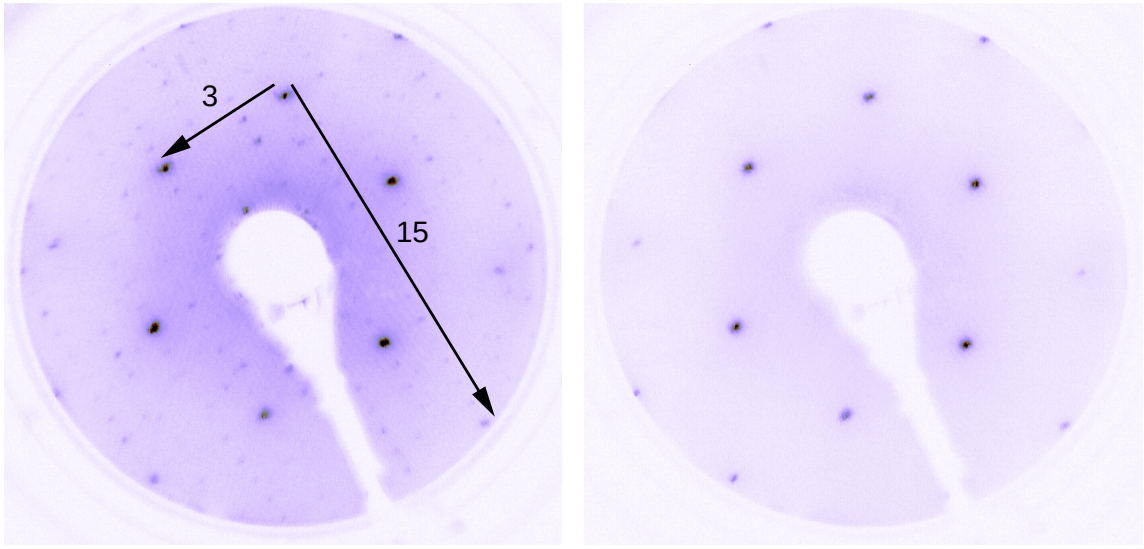

Figure 3.15: LEED pictures of the W(110) substrate at 165 eV and room temperature. The left panel shows the W(110) crystal after 30 times flashing to 2,300 K (from the last cleaning). The carbon impurities form the typical 3×15 superstructure on the surface. The right panel shows a clean W(110) surface without any superstructure. The surface was cleaned by three cycles of heating to 1,800 K in $5 \cdot 10^{-8}$ mbar O_2 partial pressure for 4 minutes and one flash to 2,300 K in order to remove tungsten oxide. Subsequent to these cycles, the crystal was heated to 1,400 K in $3 \cdot 10^{-8}$ mbar O_2 for one hour followed by another flash to 2,300 K.

In order to clean only the surface and avoid more segregation of carbon from the bulk to the surface, the crystal was kept at a temperature of 1,400 K at a low oxygen partial pressure of $5 \cdot 10^{-8}$ mbar for 1 hour followed by one flash to 2,300 K. The left panel of figure 3.15 shows the R(3×15) superstructure induced on the W(110) surface by carbon impurities after the deposition and removal of several Gd-films. To clean the W substrate from such contaminations and reestablish the carbon depletion of the surface without exposing the sample holder to high temperatures for too long, we heated the crystal to 1,800 K at $5 \cdot 10^{-8}$ mbar O_2 for only a few minutes. This procedure was repeated with intermediate high-temperature flashs (to 2,300 K). The cleaning was then finished by an hour of heating to 1,400 K at $3 \cdot 10^{-8}$ mbar O_2 and another high-temperature flash. Afterwards, we obtained low-energy electron diffraction (LEED) pictures free from any sign of impurities as shown in the right panel of Figure 3.15.

3.4.2 Deposition of Thin Films

We evaporated Fe and Ni in a commercial UHV evaporator (EFM3, Focus) each from a 2.0 mm-thick rod(/wire) of 99.999% purity (Alfa Aesar). We replaced the evaporator's original filament (usually 0.125 mm W wire) by a more robust self-made filament made of 0.15 mm-thick thoriated W wire. The filament was run at a current of ~ 2.6 A with a high voltage applied to the rod for electron-beam heating. Electron-beam heating was performed

in constant-power mode driven by a high-voltage supply (Heinziger)[10] at 9 W for Fe and 11 W for Ni, respectively.

Gd was evaporated from a tungsten crucible in a home-built evaporator that is shown in Reference [Döbrich, 2007]. The crucible was heated by electron bombardment as well. A tantalum filament was used in this case. The applied heating power was 49 W. We installed an extra tantalum shielding (shown in [Christ, 2014]) to prevent our Cu(111) reference sample from contamination with gadolinium during the evaporation.

We monitored the sample quality by LEED and directly in our photoemission studies. Further information on the growth and characterization of the samples is included in the corresponding chapters. The film thickness was determined via a quartz micro-balance and temperature programmed desorption spectroscopy.

3.4.3 Temperature-Programmed Desorption

For thin films of only a few monolayers, it is desirable to crosscheck the film thicknesses besides monitoring the deposition rate by a quartz micro-balance. To determine the thickness of our *in situ* grown films with a higher accuracy, we performed temperature programmed desorption (TPD). In TPD the temperature of the substrate is gradually increased until the previously deposited structures desorb. The amount of desorbed material is monitored in a quadrupole mass spectrometer (QMS200, Pfeiffer). Figure 3.16 shows a set of TPD spectra for different coverages of Ni on W(110). Since the adsorption energy between Ni and Ni differs from that between Ni and W, the first layer will desorb at a temperature different from that of the desorption of additional layers. We can thus take advantage of the different desorption temperatures to determine the amount of material desorbed in the multilayers by calibrating its TPD peak to that of the first monolayer. This results in the equation:

$$\#\mathrm{ML} = \frac{A_{\mathrm{multi}}}{A_{\mathrm{mono}}/x} + 1, \tag{3.33}$$

with the A_{multi} being the area under the multilayer and A_{mono} for the monolayer peak, respectively. The factor x accounts for a difference in the number of atoms, which can arise from a pseudomorphic growth of the first monolayer. In the case of Ni/W(110), the monolayer grows pseudomorphically with a density of 1.43×10^{15} atoms/cm^2 equal to that of the W(110) surface. The subsequently deposited multilayers have a density of 1.81×10^{15} atoms/cm^2. So for Ni/W(110), $x = 0.78$.

The peak areas A_{multi} and A_{mono} are evaluated from solving the temperature-dependent Polanyi-Wigner equation [Malte 35] for the deposition rate:

$$r(T) = -\frac{d\Theta(T)}{dT} = \frac{v_n}{\beta} e^{\frac{-E_{\mathrm{des},n}}{RT}} \Theta^n(T), \tag{3.34}$$

with the temperature ramp $T(t) = T_0 + \beta t$. $E_{\mathrm{des},n}$ is the energy needed for desorption, v_n is called frequency factor, and R is the universal gas constant. $\Theta = N_{\mathrm{ads}}/N_{\mathrm{surf}}$ describes the coverage of adsorption sites N_{surf} on the surface with adsorbed atoms N_{ads}. The exponent n

[10] The electron-beam voltage was typically $\approx 1,000$ V and the emission current ≈ 10 mA.

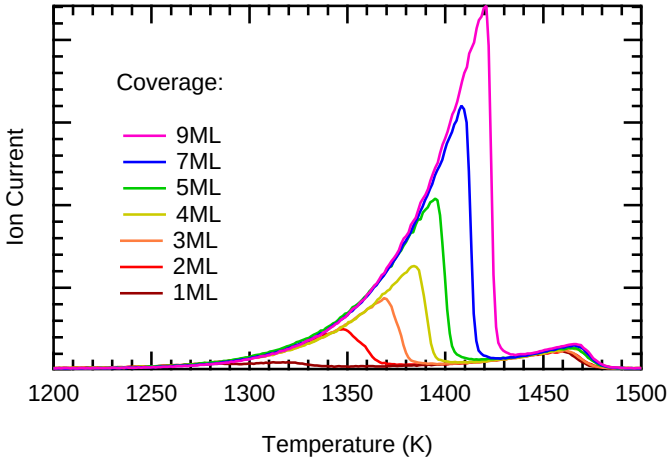

Figure 3.16: TPD spectra for different coverages of Ni on W(110), reprinted from Ref. [Weiss, 2013]. The monolayer shows a first order ($n = 1$) desorbtion with a peak temperature of $\approx 1,470\,\mathrm{K}$. The peak temperature of the multilayer desorbtion (zero order $n = 0$) gradually changes with coverage. The film thickness can be determined by comparison of the area under the multilayer peak to that under the monolayer peak.

denotes the order of the desorption. The multilayer peak commonly shows a prototypical zero-order desorption ($n = 0$). The temperature dependence placed in the factor Θ^n cancels for the zero-order desorption, meaning that this process does not depend on the coverage. This is intuitive, since the surface stays covered as long as the monolayer resides. The multilayer desorption can thus be described by a simple exponential behavior:

$$\Theta_0(T) = v_0 e^{\frac{-E_{\mathrm{des},0}}{RT}} \cdot \frac{1}{2}\left(1 + \mathrm{erf}\left(\frac{T_0 - T}{\sqrt{2}w_0}\right)\right). \tag{3.35}$$

The brackets including the error function account for the break down of the signal, which occurs at temperature T_0 when all material except for the first monolayer is desorbed. This break down occurs with a certain variation w_0.

The desorption order of the monolayer is $n = 1$, which makes the description of the instantly desorbed coverage Θ_1 rather complicated. To obtain reliable coefficients for the desorption energy $E_{\mathrm{des},1}$ or the frequency factor v_1, one could either perform a numeric recursion or include an integration in the fitting function. Nevertheless, for our purpose, which is a decomposition of the monolayer and multilayer peak area, it is a sufficient approximation to use Equation (3.35) for the desorption of the monolayer as well.

Note that in Figure 3.16 the temperature of the maximum peak intensity changes with the coverage in the multilayer, but stays constant for the monolayer. This can be derived from $\frac{dr(T)}{dT} = 0$ at $T = T_{\mathrm{max}}$, where the coverage independence is shifted from $n = 0$ to $n = 1$ by the differentiation.

Chapter 4

Ultrafast Laser-Induced Demagnetization of Gadolinium

Part of this chapter has already been published in the author's work "Separating Exchange Splitting from Spin Mixing in Gadolinium by Femtosecond Laser Excitation" in Physical Review Letters ***115****, 207404 (2015) [I].*

Laser pulses of high power can lead to significant changes in the material, which are then reflected in the band structure [Carley et al., 2012; Teichmann et al., 2015] or the inter-atomic distance revealed in X-ray diffraction [von Reppert and Koc, 2015]. In a magnetically ordered material (*e.g.* a ferro- or ferrimagnet), it can cause a decrease of the magnetic moment and lead to a laser-induced phase transition *i.e.* a demagnetization or a switching of the magnetization.

What motivates me to investigate laser-induced demagnetization is that it provides a whole new view on magnetism. Since a laser pulse predominantly excites electrons, the resulting non-equilibrium state between electrons, lattice, and spins may cause transient states that do not exist in the natural thermal equilibrium – such as a ferromagnetic state in the ferrimagnetic compound GdFeCo [Radu et al., 2011]. In this chapter, we investigate the laser-induced demagnetization of a gadolinium (Gd) film grown epitaxially on a W(110) substrate (described in Sec. 4.3.1). We too find a response quite different from the equilibrium phase transition, which allows us to separate different contributions to the demagnetization. Until now, these contributions caused severe confusion, since they led to different observations depending on the experimental technique of the measurement.

A short overview of these preliminary works on the laser-induced demagnetization of Gd is given in Section 4.1. Section 4.2 introduces the recent approaches towards a theoretical description of the non-equilibrium demagnetization. After a short introduction to the surface state on the Gd(0001) surface, Section 4.3 gives an overview of our results obtained from a spin-resolved photoemission experiment, which monitors the response of the majority-spin component of the surface state to laser-excitation. The timescales observed in the demagnetization process allow to separate different contributions to magnetic order. A deeper investigation of these contributions is given in Section 4.4, where the recent

demagnetization theories are discussed in comparison to our experimental observations. Some final concluding remarks are made in Section 4.5, where we also compare the behavior found in the equilibrium and in the non-equilibrium phase transition.

4.1 State of the Art - Experimental Work

Gadolinium was the first material demagnetized by a laser pulse in 1991 [Vaterlaus et al., 1991]. This demagnetization experiment by Vaterlaus et al. [1991] was in fact the first and up to now the only demagnetization experiment by the means of spin-resolved photoemission on Gd. A 10 ns laser pulse at a photon energy of 2.15 eV was applied for pump and a 60 ps pulse for probe with an energy of 3.2 eV.[1] A decrease of spin polarization within 2 ns was observed in the total yield of photoemitted electrons, which could solely be explained by spin-lattice equilibration at a characteristic time of $\tau_{sl} = 100 \pm 80$ ps. This result was corroborated in 2008 by measurements of the magnetic linear dichroism (MLD) observed in photoemission from the $4f$ core levels [Melnikov et al., 2008a].

Studies on ever shorter timescales followed showing that magnetic figures like X-ray magnetic circular dichroism (XMCD) [Wietstruk et al., 2011], Kerr rotation and ellipticity [Sultan et al., 2011, 2012], and exchange splitting [Carley et al., 2012; Teichmann et al., 2015] can be reduced by a laser pulse in less than 1 ps. This sub-picosecond demagnetization can not be induced by thermal equilibration between spins and lattice but is a new startling phenomenon. In addition to that, there are significant deviations between the results of the afore-mentioned experiments.

To provide a better overview, Table 4.1 summarizes the timescales found by different experimental techniques for the laser-induced demagnetization of Gd. Although, in the thermally-induced equilibrium phase transition all these techniques show the same temperature dependence, when the phase transition is driven by a laser pulse they can roughly be divided into three temporal regimes. We find the slow (100 ± 80 ps) response observed in the spin-resolved photoemission experiment of Vaterlaus et al. [1991] as well as in the MLD in photoemission from the $4f$ core levels [Melnikov et al., 2008a]. A recent MLD study by Frietsch et al. [2015] using the high harmonics of a Ti:Sapphire laser to probe the $4f$ core levels, determined the response of the $4f$ magnetic moment to be on a timescale of 14 ± 3 ps. An XMCD experiment by Wietstruk et al. [2011] performed at the M_5 absorption edge also reveals a slow component decreasing within several tens of picoseconds (40 ± 10 ps) and an additional faster timescale in the sub-ps regime (0.76 ± 0.25 ps). A response on a similar timescale has been observed in measurements by Sultan et al. [2011] exploiting the magneto-optical Kerr effect (MOKE). The decrease of the MOKE[2] signal may be explained by a reduction of the magnetic exchange splitting, which has later been observed to occur for the ($5d6s$) valence bands on a timescale of the same order of magnitude (0.86 ± 0.1 ps) [Carley et al., 2012; Teichmann et al., 2015]. The magnetic component of second-harmonic generation (SHG) at the Gd surface reveals an even faster response. In the studies performed

[1] The investigated sample was a Gd film on a polycrystalline iron substrate with a work function of 3 eV, which is significantly lower than 3.73 ± 0.02 eV for a freshly prepared Gd/W(110) film [Andres, 2010].

[2] MOKE is sensitive to optical transitions between all electronic states in the Brillouin zone.

Table 4.1: Overview of previous studies of the ultrafast laser-indunced demagnetization of gadolinium using different experimental techniques. The results of the different techniques can roughly be assigned to three timescales. While second harmonic generation (SHG) finds an ultrafast decrease of its magnetic component within the laser pulse duration of $< 100\,\mathrm{fs}$, a timescale close to 1 ps is observed in X-ray magnetic circular dichroism (XMCD) and magneto-optical Kerr effect (MOKE). The exchange splitting ΔE_{Ex} of the valence bands is found to decrease within an equally short time in photoemission spectroscopy (PES), whereas spin-resolved photoemission (srPES) and the magnetic linear dichroism (MLD) in the $4f$ core levels in PES reveal a much slower demagnetization taking several tens of picoseconds.

technique	timescale			reference
	ultrafast	sub-picosecond	picosecond	
SHG	$< 100\,\mathrm{fs}$	–	–	[Melnikov et al., 2003]
XMCD	–	$0.76 \pm 0.25\,\mathrm{ps}$	$40 \pm 10\,\mathrm{ps}$	[Wietstruk et al., 2011]
MOKE	–	similar	–	[Sultan et al., 2011]
PES (ΔE_{Ex})	–	$0.86 \pm 0.1\,\mathrm{ps}$	–	[Carley et al., 2012]
srPES	–	–	$100 \pm 80\,\mathrm{ps}$	[Vaterlaus et al., 1991]
MLD	–	–	similar	[Melnikov et al., 2008a]
MLD	–	–	$14 \pm 3\,\mathrm{ps}$	[Frietsch et al., 2015]

in References [Melnikov et al., 2003, 2008b; Lisowski et al., 2005] the total SHG signal was decomposed into an even and odd signal component with respect to reversal of the sample magnetization. They find an oscillation in both signals, which is triggered by the pumping laser pulse and was interpreted as a coherent phonon-magnon mode. Furthermore, the signal of the odd component – which is dependent on the magnetization – is significantly decreased within the duration of the pumping laser pulse ($< 100\,\mathrm{fs}$). In Reference [Melnikov et al., 2008b], it is assumed that the surface state plays a dominant role in the second-harmonic-generation process. We can thus expect to find the cause of this ultrafast decrease in our photoemission study on the surface state.

4.2 State of the Art - Theoretical Work

Until now, the approaches towards a theoretical description of laser-induced ultrafast demagnetization are mostly phenomenological, describing the process as a whole without detailed characterization of the microscopic changes. The two models that are discussed the most, are based on spin-dependent transport [Battiato et al., 2010] and electron-phonon spin-flip scattering [Koopmans et al., 2010]. Both provide a full description of known XMCD data measured in nickel. They are introduced in Sections 4.2.1 and 4.2.3. Further models describe laser-induced ultrafast demagnetization on the basis of other spin-flip scattering processes such as electron-electron scattering [Krauß et al., 2009] and electron-magnon scattering [Carpene et al., 2008; Haag et al., 2014]. Even a direct interaction with the laser photons has been suggested [Zhang and Hübner, 2000; Zhang et al., 2009; Bigot et al., 2009].

A nice overview has been put together by Illg et al. [2013], who conclude that combinations of such two-particle spin-flip scattering processes could provide a better explanation of the ultrafast demagnetization.

Besides these, there are a few more theories, some of which aim to explain not only the phenomenon of ultrafast laser-induced demagnetization but also predict microscopic changes of energy and spin polarization in the underlying band structure. This is particularly interesting in the case of Gd, where we have the RKKY-coupled localized magnetic moments in the $4f$ core levels *vs.* the delocalized ($5d6s$) valence electrons, which mediate the exchange interaction. The recent approaches, regarding the distinctions between $4f$ and ($5d6s$) spin moments, are mentioned in Sections 4.2.4 and 4.2.5.

4.2.1 Spin-Dependent Transport Effects

More and more experiments provide strong evidence for transport effects subsequent to laser excitation: Kampfrath et al. [2013] found laser-induced spin currents in iron to cause the emission of a terahertz electromagnetic wave due to the inverse spin hall effect. Eschenlohr et al. [2013] discovered that an ultrafast demagnetization in Ni can be triggered by laser heating an adjacent Au capping layer. Also the concept of spin-transfer torque, where spin currents can cause a precession of the magnetization, is well established [Choi et al., 2014; Schellekens et al., 2014].

Of course, transport effects should play a significant role in the demagnetization process, since the laser-excited electrons have high velocities[3] ($\sim 1\,\mathrm{nm/fs}$) and different mean free paths depending on their spin direction. A corresponding theory was developed by Battiato et al. [2010, 2012]. They describe the electronic motion as a superdiffusive process, which means that the motion starts in a ballistic regime after the excitation and goes to normal diffusion for times larger than 100 fs. It is a necessary prerequisite that the transport is in the superdiffusive regime, since a simple diffusive transport would be too slow to cause the experimentally-observed effects, while ballistic transport wouldn't show any spin dependence, since there would be no scattering (without an interface). The model successfully describes XMCD data on the laser-induced demagnetization of nickel without the need of any ultrafast spin flips. It calculates the magnetization-dynamics as [Battiato et al., 2010]

$$M(E,z,t) = 2\mu_B(n(\uparrow,E,z,t) - n(\downarrow,E,z,t)) \tag{4.1}$$

from the different electronic densities $n(\uparrow\ /\ \downarrow, E, z, t)$ for majority- and minority-spin electrons, which are described by a set of coupled transport equations [$\frac{\partial n}{\partial t} = \ldots$]. Here z is the position of the electrons inside the material, E the energy, μ_B the Bohr magneton and t the traveling time ($\equiv$ time delay to pump laser pulse). The electron densities evolve from an electron source term $S(\uparrow\ /\ \downarrow, E, z, t)$, which is initially generated by the laser excitation and then changes iteratively with a second, third and nth generation of electrons

[3] According to Ref. [Knorren et al., 2002] the average transport velocity is about half of the Fermi velocity, which is 1.5 nm/fs in copper [Knorren et al., 2002], 0.28 nm/fs in nickel [Petrovykh et al., 1998]. For Gd, the relation $v_\mathrm{F} = \hbar k_\mathrm{F}/m$ yields a Fermi velocity of 0.46 nm/fs taking a Fermi wave vector of $k_\mathrm{F} = 0.4\,\text{Å}^{-1}$ obtained from the ferromagnetic Fermi surface in Ref. [Döbrich, 2007].

gradually created by electronic scattering. This cascade-like process of electron scattering after laser-excitation will be further explained in Section 4.4.1. Therein, we find that the excited electrons thermalize predominantly through exchange scattering processes, which equalize the excited majority- and minority-spin population. This should quickly reduce the influence of spin-dependent transport effects. The population of thermalized electrons is then again distributed in the form of a Fermi function. The temperature of this Fermi distribution reaches very high values of several thousand Kelvins before it starts to cool down by transferring energy to the lattice as described by the two-temperature model.

4.2.2 Two-Temperature Model

The dissipation of energy from the laser-excited electrons to the lattice is well established and used in laser ablation. A model to describe the electronic and lattice temperature after laser heating has been developed by Anisimov et al. [1974]. It is known as the two-temperature model (2TM). The 2TM describes the change in electronic temperature T_e and lattice temperature T_l as follows [according to Anisimov et al. [1974]]:

$$C_e(T_e)\frac{dT_e}{dt} = S(t) - G_{el}\left(T_e - T_l\right) - \frac{\partial}{\partial z}\left(\kappa\frac{\partial T_e}{\partial z}\right) \tag{4.2}$$

$$C_l(T_l)\frac{dT_l}{dt} = \quad - G_{el}\left(T_l - T_e\right), \tag{4.3}$$

with the specific heat capacities C_e and C_l, $S(t)$ the heating induced by the laser pulse and a coupling constant G_{el} between the electronic and phononic heat bath. The last term in Equation (4.2) describes the recooling by the transport of heat into the deeper layers ($z < 0$) of the bulk and substrate with a thermal conductivity κ. For a metal, this heat transport is predominantly carried by the electrons. As an approximation of the 2TM (Eqs. (4.2) and (4.3)), the pump-probe spectra are commonly fitted by a set of exponentially decaying functions. These yield the frequently discussed time constants for the exponentials, that can be found in most of the literature [Beaurepaire et al., 1996; Rhie et al., 2003; Frietsch et al., 2015; Carley et al., 2012; Teichmann et al., 2015; Stamm et al., 2007; Weber et al., 2011]. A set of relations relying on the 2TM, will be derived in Section 4.4.2 to describe the temporal evolution of our spectra.

4.2.3 Elliott-Yafet Spin-Flip Scattering

When Beaurepaire et al. [1996] observed the laser-induced ultrafast demagnetization of nickel, they extended the two-temperature model (Eqs. (4.2) and (4.3)) to a three-temperature model (scheme illustrated in Fig. 4.1). They added a spin reservoir coupled to the electronic and lattice reservoir in the same manner as the latter are coupled in Equations (4.2) and (4.3). Koopmans et al. [2010] pointed out later that the phenomenological model of Beaurepaire et al. [1996] lacked an explanation for the transfer of angular momentum, since a changing temperature of the spin reservoir would mean a loss of angular momentum. Koopmans et al. [2010] introduced a change of angular momentum by a spin-flip scattering mechanism discovered by Elliott [1954] and Yafet [1963]. In this Elliott-Yafet scattering mechanism,

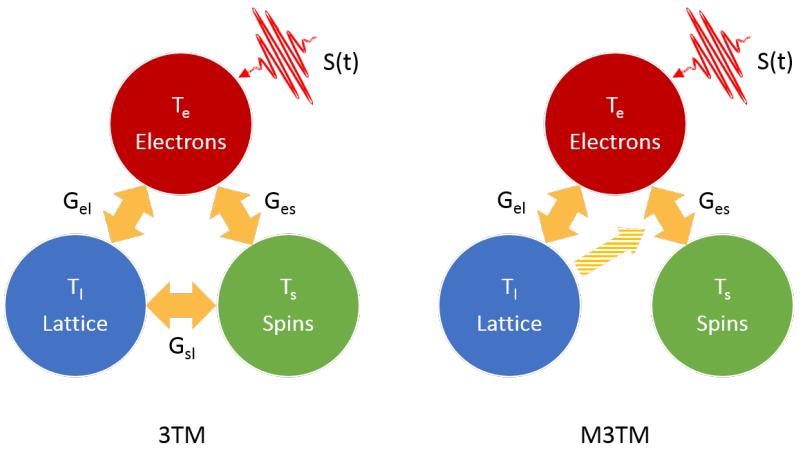

Figure 4.1: Illustration of the two variants of the three-temperature model (3TM) as introduced by Beaurepaire et al. [1996] and the microscopic three-tempertaure model (M3TM) as used by Koopmans et al. [2010]. Instead of a direct spin-lattice interaction, the M3TM uses the mechanism of Elliott-Yafet scattering to induce a change of angular momentum mediated by electron-phonon scattering.

an electron can change its spin by transferring angular momentum to the lattice in an electron-phonon scattering process. The model by Koopmans et al. [2010] thus does not include a direct spin-lattice coupling instead a spin can only be flipped upon absorption or emission of a phonon (*cf.* Fig. 4.1, right panel). In a set of Boltzmann rate equations for the three subsystems they obtain a microscopic expression for the spin-flip rate, which is finally rewritten as a differential equation for the normalized magnetic moment ($m = M/M_0$) [Koopmans et al., 2010]:

$$\frac{dm}{dt} = R\ m\ \frac{T_l}{T_C}\left(1 - m\ \coth\left(\frac{m\ T_C}{T_e}\right)\right). \tag{4.4}$$

Together with Equations (4.2) and (4.3) for the transient electronic (T_e) and lattice temperature (T_l) this constitutes the microscopic three-temperature model (M3TM) which is also known as the Koopmans model. Besides the Curie temperature T_C, the parameter [Koopmans et al., 2010]

$$R = \frac{8 a_{\mathrm{sf}} G_{el} k_B T_C^2 V_{\mathrm{at}}}{E_D^2 \mu_{\mathrm{at}} / \mu_B} \tag{4.5}$$

contains material-dependent parameters, *i.e.* the atomic magnetic moment μ_{at}, the spin-flip probability a_{sf}, the electron-lattice coupling constant G_{el}, the Debye energy E_D and the atomic volume V_{at}.

A few interesting consequences arise from Equations (4.4) and (4.5). The Koopmans model is capable of reproducing two timescales for the demagnetization in gadolinium as it has been observed in XMCD by Wietstruk et al. [2011]. The model predicts an initial drop of the magnetization on the timescale of electron-lattice equilibration.[4] After the electrons

[4]For gadolinium, which has a low Curie temperature T_C and a large magnetic moment per atom μ_{at}, the parameter R is lower than the electron-lattice relaxation rate τ_{E0}^{-1} at $T = T_C$. Gadolinium is thus demagnetized on the timescale of the electron-lattice equilibration, while for $R > \tau_{E0}^{-1}$, as in the $3d$ transition metals, demagnetization times faster than the electron-lattice equilibration are possible.

equilibrated with the lattice, the electronic temperature T_e is also much closer to T_C and due to the last term in Equation (4.4) the demagnetization rate drops significantly giving rise to the emergence of a second timescale. We will discuss this occurrence of two timescales in Section 4.4.3.

The spin-flip probability a_{sf} is a key ingredient in the Koopmans model. It caused several debates on the applicability of the model during the last years. The spin-flip probability in the Elliott-Yafet framework is $a_{sf} = p\langle b^2 \rangle$. p is a dimensionless material-specific parameter varying from 1 to 10 [Koopmans et al., 2010]. $\langle b^2 \rangle$ is the so-called spin-mixing parameter denoting the contribution of the opposite spin to a spin-mixed Bloch state, *e.g.* $\Psi_{\mathbf{k},\uparrow}(\mathbf{r}) = (a_{\mathbf{k}}(\mathbf{r})\,|\uparrow\rangle + b_{\mathbf{k}}(\mathbf{r})\,|\downarrow\rangle)e^{i\mathbf{kr}}$ [Steiauf and Fähnle, 2009]. $\langle b^2 \rangle$ can thus be determined from first-principle calculations. Koopmans et al. [2010] used a_{sf} as a fit parameter and compared the so-determined values to *ab initio* calculations based on the band structure. Such calculations had also been performed in previous publications by [Koopmans et al., 2005a]. They found that the fitted parameters for a_{sf} match the calculated values for $\langle b^2 \rangle$ with p ranging from 1 to 10.

Carva et al. [2011] pointed out later, that the model by Koopmans et al. [2010] in the approximation of Elliott [1954] neglects important properties such as the electron-phonon matrix elements and the phonon dispersion. Carva et al. [2011] included the latter properties by using a generalized Eliashberg function to obtain the electron-phonon spin-flip rate. They concluded that the so-obtained demagnetization rate is too small to account for femtosecond demagnetization.

It has in turn been noticed by Mueller et al. [2013] that the preceding calculations [Carva et al., 2011; Koopmans et al., 2010] were based on the band structure of the ground state, which should be changed during the demagnetization experiment. Mueller et al. [2013] extended the M3TM to account for a dynamic exchange splitting of the band structure. Their so-called μT model [Mueller and Rethfeld, 2014] includes a spin dependence in electron temperatures, chemical potentials, and scattering processes. It distinguishes majority- and minority-spin distribution functions $f_{\Delta}^{\uparrow/\downarrow}(E, T, \mu)$, which are shifted by the dynamic exchange splitting $\Delta(t)$ on the paramagnetic density of states. As introduced in the Hubbard model in Equation (2.9), $\Delta(t) = U_{\text{eff}}\, m(t)$ with the effective Coulomb interaction and the time-dependent normalized magnetization $m(t)$.

The assumption of a dynamic exchange splitting is of course a useful addition to the M3TM and the separate treatment of electrons of opposite spin directions is also adequate. Nevertheless, the calculations for nickel by Mueller and Rethfeld [2014] result in huge differences between the spin-dependent electronic temperatures of a factor of 1.7 to 1.8, while we observe at least for gadolinium no difference in the majority- and minority-spin Fermi distribution (see Sec. 4.4.1).

4.2.4 Landau-Lifshitz-Gilbert Equation

It has been shown by Koopmans et al. [2005b] that the demagnetization rate obtained in the Elliott-Yafet scattering framework can be related to the Gilbert-damping parameter in the Landau-Lifshitz-Gilbert (LLG) equation. This equation had up to then been used exclusively

for the description of switching and damping of the magnetization in an external magnetic field and was not connected to laser-induced ultrafast demagnetization. It describes the change in the angular momentum $\mathbf{M}$ [Koopmans et al., 2005b]

$$\frac{\partial \mathbf{M}}{\partial t} = \gamma \mu_0 \mathbf{M} \times \mathbf{H}^{\text{eff}} + \frac{\alpha}{m} \mathbf{M} \times \frac{\partial \mathbf{M}}{\partial t}, \tag{4.6}$$

which consists of the torque that $\mathbf{M}$ experiences in a magnetic field $\mathbf{H}^{\text{eff}}$ and a damping term with the damping constant α. $\gamma = g\mu_B/\hbar$, with the Bohr magneton μ_B and the vacuum permeability μ_0. $\mathbf{H}^{\text{eff}}$ contains the sum of magnetic fields affecting $\mathbf{M}$, namely the magneto-crystalline anisotropy, the shape anisotropy, the magnetic dipole-dipole interaction, etc. and of course all external magnetic fields.

A model based on the LLG equation has recently been developed by Wienholdt et al. [2013] to describe the demagnetization of the ferrimagnet GdFeCo. They derived an orbital-resolved model treating the $4f$ and $5d$ moments separately. This model has been applied to the laser-induced demagnetization of gadolinium [Frietsch et al., 2015]. They use an effective field $\mathbf{H}^{\text{eff}} = -\frac{\partial \mathcal{H}}{\partial \mathbf{M}} + \zeta(t)$ consisting of the Hamiltonian $\mathcal{H}$ and a thermal noise term $\zeta(t)$. $\mathcal{H}$ distinguishes $4f$ and $5d$ spins similar to Equation (2.15) but in the Heisenberg model. The term $\zeta(t)$ accounts for thermal fluctuations and depends on the transient temperatures that are in turn calculated from an extended version of the 2TM. This includes the spin contribution to the heat capacity by adding to Equations (4.2) and (4.3) the energy flow into the spin systems [Frietsch et al., 2015]. They thereby assume the laser-excited hot electrons to transfer energy directly to the $5d$ spin subsystem, while the $4f$ spin system is predominantly coupled to the phonon heat bath.

With this distinction between the intra-atomic spin subsystems, Frietsch et al. [2015] obtain distinct dynamics for the demagnetization of the $5d$ valence bands and the $4f$ core levels, which are in excellent agreement with the exchange splitting measured for the ($5d6s$) bands and the MLD contrast in photoemission from the $4f$ levels.

4.2.5 Non-Collinearity of the $4f$ Spin Moments

Sandratskii [2014] questions the applicability of the model suggested by Wienholdt et al. [2013]. He argues that the separate treatment of the $5d$ and $4f$ spins coupled in a Heisenberg Hamiltonian $\mathcal{H} = J\mathbf{S}_{5d6s} \cdot \mathbf{S}_{4f}$ is not justified, because the ($5d6s$) valence electrons do not form a rigid entity. To estimate the exchange parameter J from the energy difference between parallel and antiparallel $5d$-$4f$-spin configuration as realized by Wienholdt et al. [2013], the energy of the system as a function of the ($5d6s$) spin moment must have a second minimum for an excited state with antiparallel $5d$-$4f$-spin configuration. Sandratskii [2014] shows that this is not the case for gadolinium and therefore the ($5d6s$) moments may not be treated as separate degrees of freedom. He further refers to XMCD measurements of Wietstruk et al. [2011] corroborating the $4f$ and $5d$ spin moments as one rigid entity.

Following his previous publication [Sandratskii and Kübler, 1993], Sandratskii [2014] performs calculations using the local-spin-density approximation (LSDA) of the density-functional theory (DFT) to obtain the band structure for a particular non-collinear configuration of the $4f$ magnetic moments. He utilizes such a disordering of the $4f$ moments

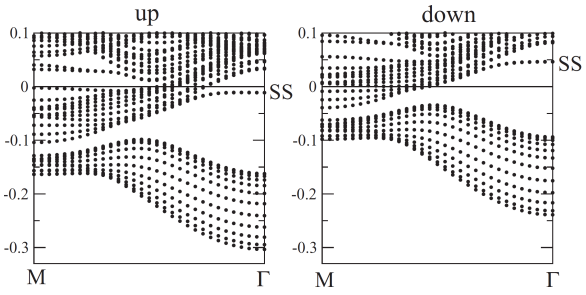

Figure 4.2: Slab calculation of the spin-resolved 2D band structure of ferromagnetic Gd, reprinted from Ref. [Sandratskii, 2014]. Left: spin-up projection. Right: spin-down. The surface-state band is labeled SS. Calculations were performed using the local spin density approximation (LSDA) combined with the augmented spherical wave method (ASW). The ordinate axis shows the energy scaled in Ry. The abscissa displays the ΓM direction of the 2D Brillouin zone.

as the driving force for a laser-induced demagnetization. This disordering is supposed to be induced by fast spin-flip processes during the energy decay of the hot electrons. He finds that the direction of the ($5d6s$) moments does not follow that of the $4f$ moments directly but also depends on the atomic layer and the hybridization of each band with states of neighboring atoms. The calculations corroborate a difference in the energetic shifts of the minority- and majority-spin bulk bands as has been observed by Carley et al. [2012]. The calculations appear to be a beautiful reproduction of the behavior observed in the equilibrium phase transition. Yet, the dependence on the $4f$ spin alignment does not resemble the time dependence after laser excitation. Carley et al. [2012] find differently delayed responses for the minority- and majority-spin states, which is not compatible with any $4f$ spin configuration in the results of Sandratskii [2014] as discussed by the author himself.

Furthermore, Sandratskii [2014] proposes an evolution of energy and spin of the surface state during a magnetic phase transition as discussed in the following section.

4.3 Studying the Gd(0001) Majority-Spin Surface State

The surface state on Gd(0001) provides great opportunities to study magnetism. This is first of all due to its binding energy very close to the Fermi energy E_F. Figure 4.2 shows a slab calculation performed by Sandratskii [2014] for the ferromagnetic band structure of Gd in the ΓM direction of the 2D Brillouin zone. The surface-state band (labeled SS) lies in a gap formed by the ($5d6s$) valence bands at the Γ point. It is proven that this surface state exists on the (0001) surfaces of all heavy lanthanides as well as on lanthanum [Wegner et al., 2006] and yttrium [Stolwijk et al., 2010]. For the heavy lanthanides, which exhibit different exotic magnetic phases, the surface state is exchange-split with the majority-spin part energetically situated below E_F and the minority-spin part above E_F [Bode et al., 1998b]. Thus, the majority part is occupied and can be observed in photoemission experiments[5], while the unoccupied minority part is observed in inverse photoemission [Donath et al., 1996]. This energetic situation makes it easy to distinguish majority- and minority-spin part even in non-spin-resolved experiments.

[5]Studies of the Gd(0001) surface state using photoelectron spectroscopy can be found in References [Fedorov et al., 2002; Weschke et al., 1996; Krupin, 2004; Lisowski et al., 2005; Andres, 2010].

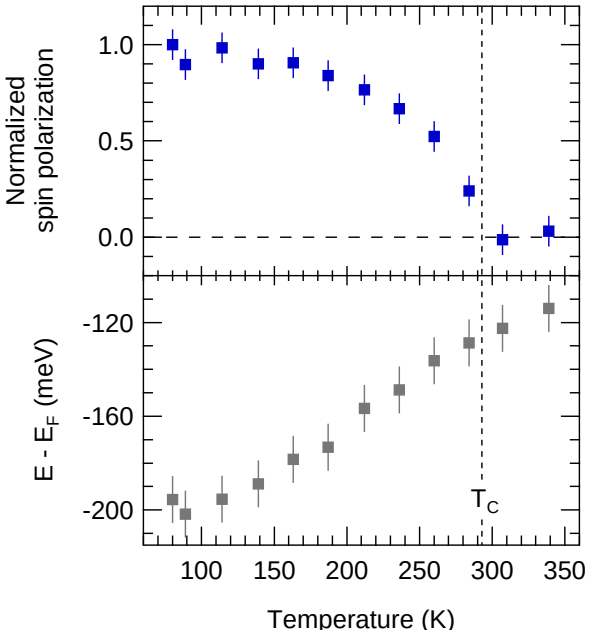

Figure 4.3: Temperature dependence of the spin polarization and binding energy of the majority-spin surface state, reprinted from Ref. [I]. A decreasing exchange splitting shifts the binding energy towards the Fermi level E_F. While the spin polarization breaks down at the Curie temperature T_C, the exchange splitting persists with the majority-spin component of the surface state below and the minority-spin component above E_F.

Owing to this energetic situation, the existence of a finite exchange splitting in the paramagnetic phase[6] ($T > T_C$) of Gd has been found for the Gd(0001) surface state [Bode et al., 1998a]. This was part of a long standing debate about seemingly contradictory observations predicting either Stoner-like [Weschke et al., 1996] or spin-mixing behavior [Li et al., 1995] for the surface state of Gd. Figure 4.3 shows the temperature-dependent spin polarization and binding energy of the majority-spin component of the surface state during the equilibrium phase transition [Andres, 2010], [III]. The spin polarization collapses at T_C. The binding energy shifts closer to the Fermi level indicating a lowering of the surface state's exchange splitting. The exchange splitting remains finite even above T_C with the majority component below and the minority component above E_F [Bode et al., 1998a]. Sandratskii [2014] obtains such a behavior in his calculations. For a non-collinear $4f$ configuration with perpendicular neighboring moments, 70 % of the spin moments in the surface state stay aligned to their local $4f$ moments. Due to the non-collinearity of the $4f$ moments this results in the breakdown of the measured spin polarization. The exchange splitting persists in the spin-dependent atomic potential but decreases since the potential is influenced by the changing ($5d6s$) moments as well.

During the 90s, the observed temperature dependence also gave rise to the question whether the Gd(0001) surface shows a magnetic behavior with strong distinctions from bulk Gd. Later, Maiti et al. [2002] also found evidence for an equally persisting exchange splitting in the ($5d6s$) valence bands, from which the surface state is derived[7]. A persisting exchange splitting in the ($5d6s$) valence bands is corroborated in the calculations of Sandratskii [2014]

[6]Such an exchange splitting can hardly be resolved when both spin components of a band are occupied or unoccupied, since their occurrence in the same experiment leads to signals overlaying each other.

[7]The orbital wave function of the surface state has been found to show a $5d_{z^2}$ symmetry

as well.

Overall, the magnetic properties of the surface state and the ($5d6s$) valence bands are quite similar. The surface state's exchange splitting of 660 ± 10 meV [Wegner et al., 2006] is slightly lower than the bulk exchange splitting of 850 meV [Teichmann et al., 2015] to 900 meV [Maiti et al., 2002; Weschke and Kaindl, 2001] in the ($5d6s$) band (or Δ_2 band). Nevertheless, the exchange splittings of both vary for different lanthanides scaling with the number of electrons in the $4f$ shell [Weschke and Kaindl, 2001; Wegner et al., 2006]. Also the spin polarization observed near 100 K in photoemission has the same value of $\sim 60\,\%$ in Gd [Maiti et al., 2002]. We can thus assume that the magnetic properties of the valence bands are reflected in the surface state at least for the topmost layers within the probing depth of photoemission. Nevertheless, in a laser-induced demagnetization experiment, there may be distinctions occurring between surface and bulk, since the diffusion of heat plays an important role. Also transport effects, which shall be discussed in Section 4.2.1, might lead to a different demagnetization of bulk and surface.

The behavior of the surface state upon laser-induced demagnetization has already been investigated in a non-spin-resolved photoemission experiment by Lisowski et al. [2005] [Loukakos et al., 2007; Bovensiepen, 2007]. They observed a shift in the surface state's binding energy, which was slower than the ultrafast decrease of the SHG signal (mentioned above in Sec. 4.1). This difference in time scales ruled out that the magnetic SHG signal was reflecting the exchange splitting of the surface state. The only remaining magnetic quantity of the surface state, that could cause the response of the magnetic SHG signal, was thus the spin polarization. Which lead to the conclusion, that the surface state must show a strong spin-mixing behavior (*cf.* Chapter 2.2.4) upon laser-driven demagnetization. Meaning the spin polarization breaks down immediately, while the exchange-split binding energy changes much slower. The validity of this interpretation could up to now never be confirmed, since a spin-resolved study was still pending. In the following, we want to catch up on this.

4.3.1 Experimental Details

To trigger a magnetic phase transition, a laser fluence of several $\mathrm{mJ/cm^2}$ is required, which can not be provided by a simple Ti:Sapphire oscillator. Thus, the experiment had to be postponed until the amplified laser system became available through the moving of the laboratories from the Max-Born-Institute to the Free University. Using the 300-kHz Ti:Sapphire regenerative amplifier (*cf.* Chapter 3.2), we were able to obtain a pump fluence of $9.3\,\mathrm{mJ/cm^2}$ while still having enough power per pulse left over to generate the fourth harmonic of the fundamental oscillator frequency as probe beam. At a repetition rate of 300 kHz, spin-resolved measurements with the SPLEED detector would hardly have been possible. The intensity loss of three orders of magnitude in the spin-dependent scattering process is easily overcome by using the 88-MHz Ti:Sapphire oscillator, but not with the 300-kHz amplifier. It was therefore also necessary to set up the new exchange-scattering spin-detector, which loses only two orders of magnitude in count rate to spin resolution, in order to perform the experiments shown in this chapter. A further advantage of the exchange-scattering detector is the possibility of doing spin-integrated measurements as well without the loss of count rate we have in the spin-resolved measurements. We could thus on

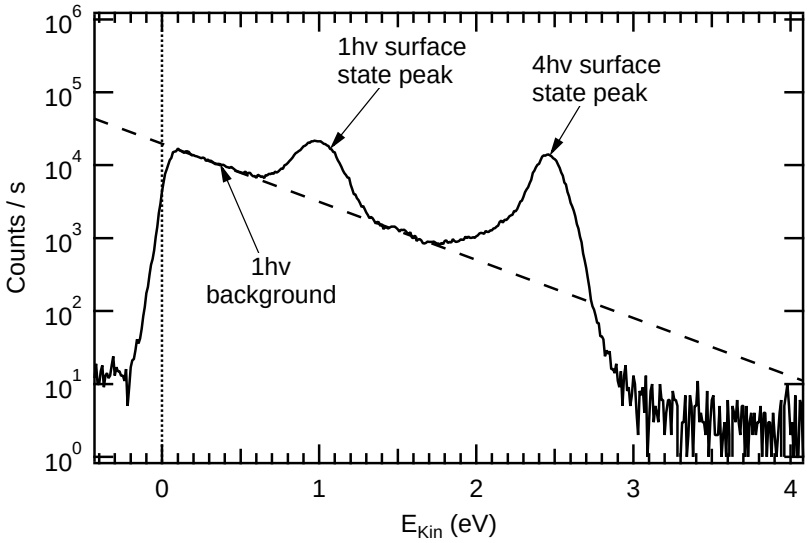

Figure 4.4: Whole photoemission spectrum (on a logarithmic scale) measured at negative pump-probe delay with the infrared ($1h\nu = 1.6\,\mathrm{eV}$) pump and its fourth harmonic ($4h\nu = 6.3\,\mathrm{eV}$) as probe pulse. The infrared pump pulse creates an exponential background (dashed line) as well as a duplication of the probe spectrum including a surface-state peak at 1.6 eV lower kinetic energy. The measured kinetic energy E_{Kin} is determined by the sum of photon energies involved in the emission process minus the work function $\Phi = 3.7\,\mathrm{eV}$ (*cf.* Eq. (3.1)). A decomposition of the $4h\nu$ spectrum is shown in Fig. 4.5.

the one hand acquire high-intensity spin-integrated data on the energetic behavior and on the other hand track the dynamics of the spin polarization. The whole setup is described in further detail in Chapter 3.

The Gd films were evaporated from a W crucible heated at 49 W by electron bombardment from a Ta filament. The evaporation rate at that heating power was determined to be 5 Å/min by a quartz microbalance. Beforehand, the W(110) substrate was cleaned from carbon impurities by heating in oxygen atmosphere as described in Chapter 3.4. We started evaporating Gd while the W crystal was cooling down from a 2200 K flash. For the 20 minutes evaporation process the substrate was kept at a temperature of 300 K. To obtain a smooth and contaminant-free surface, the Gd films were annealed for 1 minute at 780 K. The growth of smooth Gd/W(110) thin films as well as their work function and surface states have already been studied extensively in Andres [2010] using the MHz oscillator as light source and the SPLEED detector for spin-resolved direct and two-photon photoemission.

We magnetized the films remanently by applying a field pulse of 20 mT via a freestanding coil along the Gd[1100] direction. All spectra were taken under normal emission at a base temperature of 90 K kept by liquid nitrogen cooling. The measurements have been performed at a pressure of 2×10^{-11} mbar.

The polarization of the infrared (IR) pump beam (1.6 eV) was turned perpendicular to the scattering plane at the sample (s-polarized). The fourth harmonic at a photon energy of 6.3 eV, provided p-polarized probe pulses (parallel to the scattering plane).

Figure 4.4 shows a complete photoemission spectrum measured at negative pump-probe delays. The peak around 2.5 eV kinetic energy stems from the surface state photoemitted by 6.3-eV photons ($4h\nu$). The large exponential background (indicated by the dashed line) and the peak at 1 eV kinetic energy are caused by photoemission via processes involving three 1.6-eV photons[8] ($1h\nu$). Although the s polarization of the IR beam decreases the probability of photoemission from the surface state, there is still enough intensity to photoemit a comparably large amount of electrons in such a three-photon process. The peak at 1 eV is thus a duplication of our probe ($4h\nu$) spectrum at 1.6 eV less kinetic energy.[9] Thanks to this 1.6 eV difference in kinetic energy, the background spectrum of the pump pulse can nicely be separated from the probe spectrum in which we are interested. The IR spectrum is cut by the Fermi function at ≈ 1.2 eV. At $E_{kin} \geq 2$ eV, there is only a small background remaining from the IR pump beam, while the probe spectrum starts to gain intensity. In the following, we will focus on the $4h\nu$ probe spectrum.

4.3.2 Data Evaluation

Before we start to interpret the data, the different features must be identified, of which the $4h\nu$ probe spectrum is composed. As a basis for our desciption, two measured spectra at pump-probe delays of 0.2 and 10 ps in the energy range of our interest are shown again in Figure 4.5 (circles drawn in light grey). This is the part of the spectrum photoemitted by the ultraviolet $4h\nu$ probe pulse (*cf.* Fig. 4.4). Please note the logarithmic scale of the intensity axis. The function that was fitted to the data is shown as a black solid line. The individual components are represented by the colored and grey lines.

Besides the dominant contribution of the majority-spin surface-state peak (blue), we find a decreasing background from the IR spectrum (violet) (*cf.* Fig. 4.4), a further linear increasing background (gray) from the probe pulse itself [Weschke and Kaindl, 2001], and another peak (red) situated above the Fermi energy. All components are of course cut off by the Fermi function, which complicates the determination of the second peak. For a useful visualization of the Fermi function on the logarithmic scale in Figure 4.5, the linear background (gray) was multiplied by the Fermi function and offset by an additional three-counts offset, that we also find in our spectra. As always done in photoemission, the whole spectrum needs to be convolved with a Gaussian function to account for two energetic broadenings: one caused by the laser pulses finite spectral width, the other one is the energy

[8] For photoemission from the Gd(0001) surface, an overall photon energy > 3.7 eV (the work function) is required, which can not be provided by one or two 1.6-eV photons.

[9] The IR spectrum is broadened in comparison to the $4h\nu$ spectrum. This broadening is a consequence of the laser heating up the electronic system, as we will see in the following sections. In the monochromatic (IR) three-photon photoemission, all photons reach the sample at the same time. Thus, regarding the temporal evolution of the spectral parameters, the IR background mirrors the probe spectrum at zero pump-probe delay.

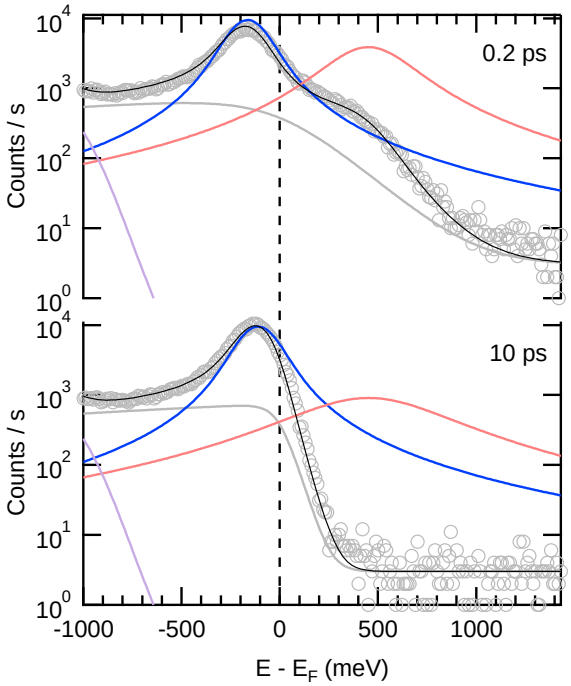

Figure 4.5: Decomposition of the function fitted to the photoemission spectra at 0.2 ps and 10 ps pump-probe delay, reprinted from Ref. [I]. The function consists of two Voigt peaks (blue and red solid lines) and a linear background all multiplied by a Fermi function. The fitting function is shown as a thin black line in the data points (circles). The gray line resembles the linear background multiplied by the Fermi function on a constant offset. The blue (red) Voigt peak corresponds to the majority- (minority-)spin component of the surface state. Additionally, below -600 meV the tail (violet) of the Fermi edge photoemitted by the infrared pump pulse in a three-photon process still has a noticable contribution to the spectrum.

resolution ΔE of our analyzer. The resulting total energy-dependent intensity is thus:

$$I_{\mathrm{UV}}(E) = I_{\mathrm{IR}}(E) + c + \left(\frac{a \cdot E + b + A_1 \frac{\Gamma_1(t)/2}{(E-E_1(t))^2+(\Gamma_1(t)/2)^2} + A_2 \frac{\Gamma_2/2}{(E-E_2)^2+(\Gamma_2/2)^2}}{e^{\frac{E-E_{\mathrm{F,UV}}}{k_{\mathrm{B}}T_{\mathrm{UV}}(t)}} + 1} \right) \star e^{-\frac{1}{2}\left(\frac{E}{\sqrt{(\Delta E)^2+(\text{UV width})^2}}\right)^2}, \tag{4.7}$$

with c being the three-counts offset and $a \cdot E + b$ the linear increasing background. The two peaks are resembled by Lorentzian lines (*cf.* Sec. 3.3) with amplitude $A_{1/2}$, natural linewidth $\Gamma_{1/2}$ and peak position $E_{1/2}$. The intensity of the IR background is composed of the same spectral features with an exponential background instead of a linear one. The high intensity arising at the low-energy side is cut off by a Gaussian-convolved step function that is attributed to the work function of the sample.

$$I_{\mathrm{IR}}(E) = \left(\left(\frac{A_{\mathrm{Exp}} e^{-\frac{E}{\text{decay}}} + A_{1,\mathrm{IR}} \frac{\Gamma_{1,\mathrm{IR}}/2}{(E-E_{1,\mathrm{IR}})^2+(\Gamma_{1,\mathrm{IR}}/2)^2} + A_{2,\mathrm{IR}} \frac{\Gamma_{2,\mathrm{IR}}/2}{(E-E_{2,\mathrm{IR}})^2+(\Gamma_{2,\mathrm{IR}}/2)^2}}{e^{\frac{E-E_{\mathrm{F,IR}}}{k_{\mathrm{B}}T_{\mathrm{IR}}}} + 1} \right) \star e^{-\frac{1}{2}\left(\frac{E}{\sqrt{(\Delta E)^2+(\text{IR width})^2}}\right)^2} \right) \times \sqrt{\frac{\pi}{2}} \Delta E \ \mathrm{Erf}\left(\frac{E_{\mathrm{Cutoff}} - E}{\sqrt{2}\Delta E} \right) \tag{4.8}$$

The error function already resembles the convolution of the cutoff with the Gaussian broadening by the energy resolution ΔE. To simplify the fitting functions 4.7 and 4.8, the convolution with the Gaussian function has been replaced in our fit by the use of Voigt peaks

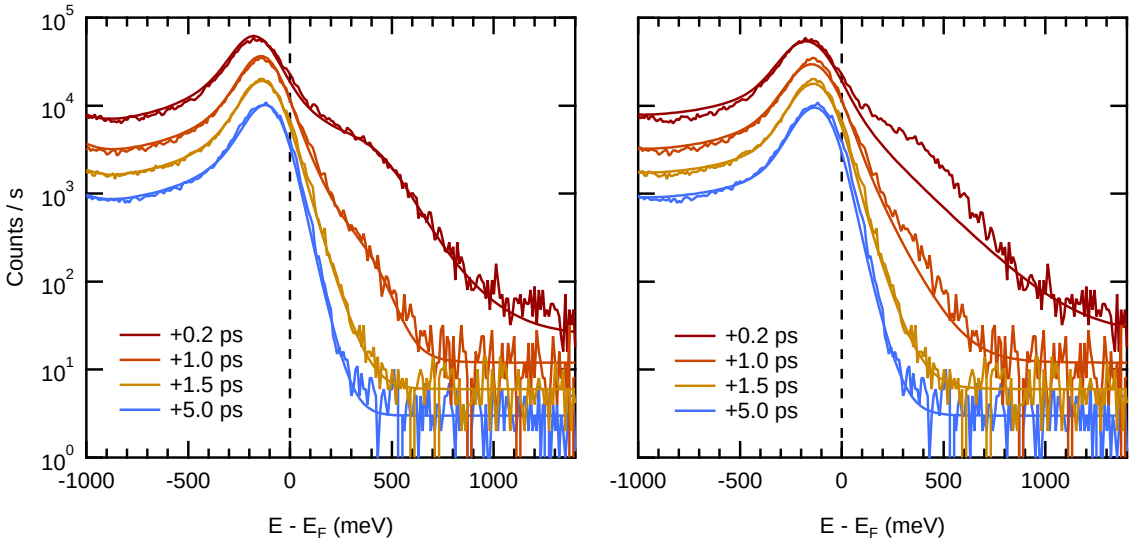

Figure 4.6: Spectra at low pump-probe delays fitted with (left panel) and without (right panel) a second Voigt peak above the Fermi energy. The second peak accounts for the uncoccupied minority-spin component of the surface state on the one hand. In the other hand, also unoccupied bulk states contribute to the additional intensity at $E > E_F$. The spectra at 0.2, 1.0, and 1.5 ps are offset multiplicatively to that at 5.0 ps.

predefined in the data analysis software "Igor Pro 6.3.6.4" (WaveMetrics, Inc.).[10] While the IR background spectrum has constant parameters over all pump-probe delays, there are time-dependent parameters in the UV probe spectrum. The temporal behavior of the electronic temperature $T_{\mathrm{UV}}(t)$, the energy position $E_1(t)$ of the majority-spin surface-state peak, and its linewidth $\Gamma_1(t)$ will be subject of the following sections.

The second peak is necessary to obtain a suitable fit at small pump-probe delays ≤ 1 ps after the excitation. This is visualized in Figure 4.6. The left and right panel display spectra at representative delays fitted with and without the second Voigt peak, respectively. The high electron temperatures at pump-probe delays ≤ 1 ps lead to an extremely broad Fermi function. Nevertheless, the enhanced intensity at $E > E_{\mathrm{F}}$ and $t = 0.2$ and 1.0 ps can not be described by the additional occupation of the high energy tail of the majority surface state or by an increased linear background. The observed intensity can only be explained by the inclusion of a second Voigt peak near 500 meV. At this energy the exchange-split minority-spin component of the surface state has been found in inverse photoemission [Donath et al., 1996], scanning tunneling spectroscopy [Bode et al., 1998a; Getzlaff et al., 1998] and even in photoemission [Lisowski et al., 2005; Bovensiepen, 2007]. This component is initially unoccupied but becomes thermally populated at small pump-probe delays. At delays > 1 ps, the recooling of the electrons leads to a resharpening of the Fermi edge. As

[10] This is legitimate, since the convolution of a Fermi function with a Gaussian yields again a broader Fermi function. The Gaussian broadening has been removed from the fitted temperatures to obtain the true electronic temperature.

a consequence of this, the peak at $E > E_F$ looses intensity and can hardly be determined anymore. We therefore used a globally constant energy position for this peak at every pump-probe delay, which is in line with the findings of Lisowski et al. [2005]. Due to the low count rates at energies above E_F, it is hardly possible to discuss the temporal behavior of the minority-spin surface state. A further argument for neglecting a discussion of the second peak is, that unoccupied bulk states have also been found in inverse photoemission [Donath et al., 1996] and scanning tunneling spectroscopy [Bode et al., 1998a; Getzlaff et al., 1998]. The appearance of these in our spectrum would strongly compromise a temperature behavior determined for our second peak. This is also corroborated by our fit to the spectrum photoemitted by the IR pump beam, in which we find the second peak at an energy that differs by 100 meV from those in the UV spectrum.

In the following, we will discuss the behavior we find for the parameters of our fit in dependence on the pump-probe delay. The changes the strong IR pump pulse induces in the population, linewidth, binding energy, and spin polarization of the Gd(0001) majority-spin surface state, will be briefly introduced in Section 4.3.3. In Section 4.4, we will deduce the timescales on which these changes occur. Since, the timescales are good indicators for the underlying interactions driving the demagnetization, we will use the opportunity to connect our work to the recent theoretical models approaching the description of laser-induced ultrafast demagnetization.

4.3.3 The Surface State upon Laser Heating

In Figure 4.7, the results of our spin-, time-, and energy-resolved demagnetization experiment are summarized. Panel (a) displays spin-integrated photoemission intensities near E_F in dependence on energy $E - E_F$ and pump-probe delay. This high-intensity spin-integrated data can be collected within a very short time of two minutes per delay point. From the resulting information, we are able to select essential energy- and delay-points to perform spin-resolved scans as shown in panels (b) and (c). In the spin-resolved measurement mode with a factor of 100 less in count rate, each of these scans takes at least three hours measurement time. Which is why it is important to complement the information with quick spin-integrated measurements.

Before the excitation by the pump pulse at delays < 0 ps, we find the majority-spin component of the surface state at an energy of $E - E_F = -200$ eV (*cf.* Fig. 4.7(c), at -0.5 ps). Along the Gd[1100] direction, the surface state shows a majority spin polarization of 35 % with a partly minority-spin intensity (red shaded areas in Fig. 4.7(c)). The laser excitation at 0 ps is sketched in Figure 4.7(d). From the sharp Fermi distribution at the sample's base temperature of 90 K, the laser pulse excites part of the occupied electrons below E_F to energies above E_F. Immediately after the excitation, the induced non-equilibrium distribution decays leading to a – much broader – Fermi distribution again. The excited electrons thus thermalize resulting in an electron gas of a far higher temperature. A detailed description of this process is given in Section 4.4.1.

The excitation and thermalization of the electronic system pictured in Figure 4.7(d) is faster than our temporal resolution of 70 fs. We find an instantaneous broadening of the Fermi function during the laser excitation at 0 ps. This causes the population of the surface

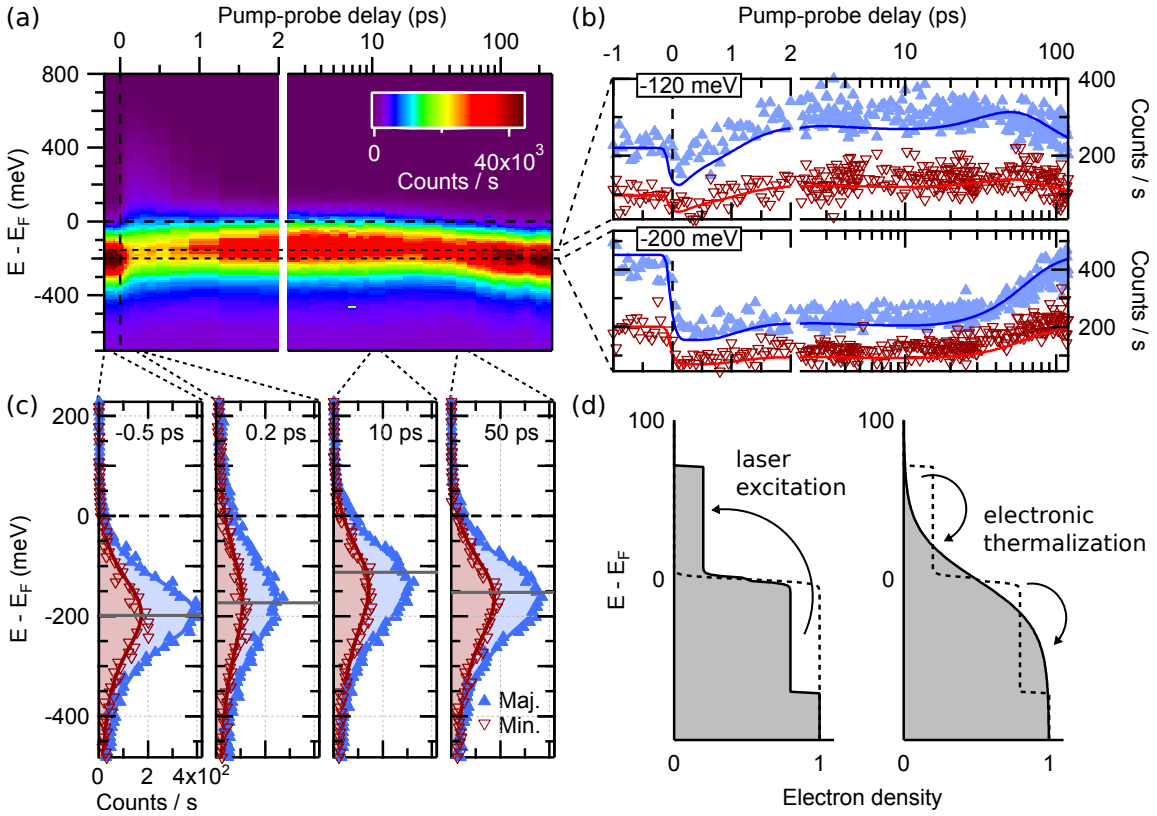

Figure 4.7: Overview of the laser-induced spectral changes in Gd near the Fermi energy. (a): False-color representation of spin-integrated photoemission spectra in dependence on energy $E - E_F$ and pump-probe delay. Corresponding spin-resolved spectra at chosen energies and pump-probe delays are shown in panels (b) and (c), respectively. Panels (a), (b), and (c) are reprinted from Ref. [I]. (d): Excitation and thermalization of the electron gas, in the style of Ref. [Wietstruk, 2010].

state to break down, which is visualized best in Figure 4.7(b). Majority- and minority-spin intensity are reduced in parallel at 0 ps. Figure 4.7(a) and (c) show that at 0.2 ps, the surface state loses half of its population, while electrons are excited above E_F. The line shape of the surface state is broadened by the temperature increase as well. In addition to that, the surface state changes its binding energy to values closer to E_F (indicated by the gray horizontal bars in panel (c)). Directly after the excitation, at a delay of 0.2 ps, the peak position is shifted by 27 meV towards E_F. This shift increases to 90 meV at 10 ps delay. At this delay, the population of the surface state already recovers and most of the laser-excited electrons above E_F are decayed. Nevertheless, the Fermi function is still broader than before the excitation, indicating an elevated temperature of the system. At this temperature a part of the peak is cut by the broad Fermi edge, such that the peak position obtained from a fit to the data (see Sec. 4.3.2) is closer to E_F as the maximum intensity visible in the spectrum. Upon cooling, the surface state binding energy shifts back to the initial value and the broadening of line shape and Fermi edge is reduced further than exemplified by the

spectrum at 50 ps delay (Fig. 4.7(c)).

To summarize the observations, we find three significant features in the temporal evolution of the surface state. The first is a very fast increase of the electronic temperature reflected in the broadening of the Fermi function depopulating the surface state. The second is the shift of the surface state's binding energy that occurs on a somewhat slower timescale, since the population already recovers at 10 ps, while the binding energy is still shifting. The third feature that is important to be mentioned is the surface state's spin polarization. Despite all these changes of occupation, binding energy, linewidth and temperature, the ratio of majority- and minority-spin intensity and thus the spin polarization shows only weak changes for all displayed pump-probe delays.

Note that the first process, the depopulation of the surface state, leads to a demagnetization of the surface already, since the high amount of majority-spin electrons located in the surface state is distributed elsewhere. This may be an effect of spin-dependent transport, as mentioned in Section 4.2.1. With this observation, we can explain the fast decrease of the magnetic signal in SHG observed by Melnikov et al. [2008b] [Lisowski et al., 2005; Bovensiepen, 2007]. It is assumed in Reference [Melnikov et al., 2008b] that the surface state contributes dominantly to the process of second harmonic generation at the Gd(0001) surface. In that case, the depopulation of this highly spin-polarized state will lead to a strong reduction of the magnetic component in the SHG signal.

In the following these features shall be investigated in detail. In Section 4.4.1, we will also have a look at the spin-dependence of the thermalized electrons above E_F, since these are the key elements of some theoretical models like superdiffusive transport [Battiato et al., 2010] and the μT model [Mueller and Rethfeld, 2014] as mentioned in Sections 4.2.1 and 4.2.3, respectively. To analyze the timescale of the binding-energy shift, the spectra shown in Figure 4.7 are decomposed by the fit described in Section 4.3.2. The so-obtained temporal behavior will be subject of Sections 4.4.2 and 4.4.3. Therein, we will discuss the timescales indicating the contributing processes and compare them to the temporal evolution of the spin polarization.

4.4 Timescales and Processes Underlying Ultrafast Demagnetization

4.4.1 Heating the Electronic System

Parts of this section are accepted for publication in the author's work "Spin dependence of relaxation processes in the laser-driven demagnetization of Gd" in Ultrafast Magnetism II (J.-Y. Bigot, W. Hübner, T. Rasing and R. Chantrell, eds.), Springer Proceedings in Physics [III].

It is known that a laser pulse predominantly excites electrons [Beaurepaire et al., 1996]. By absorption of a photon, an electron-hole pair (or exciton) is created, since the excited electron gains the photon energy and is thus lifted above the Fermi level E_F. The pump pulse in our experiment is a 48-fs-long 1.6 eV pulse generated by the regenerative amplifier system described in Section 3.2.2. We find about 0.2 excited electrons per surface atom and

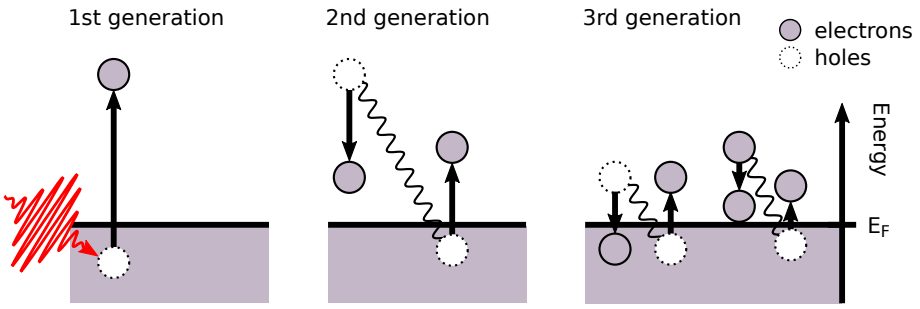

Figure 4.8: Illustration of the decay of directly laser-excited hot electrons to a Fermi distribution of thermalized electrons. The process shown here is electron-electron scattering, in which the equal masses of the scattering partners lead to a high energy transfer. The first generation electron, which was excited directly by the laser pulse, transfers part of its energy to the scattering partner (scattering is indicated by the wiggly line) and thus creates a second generation of excited electrons. The latter undergo the same process. This cascade leads to a Fermi distribution of higher temperature.

an average of 0.15 excited electrons per bulk atom, as we derived in Section 3.2.3. This means there is one electron excited at every fifth atom of the surface and at every seventh atom in the bulk. These electrons undergo scattering processes and relax in energy very fast. A simple approximation of their lifetime is given in the framework of the Fermi-liquid theory, where the lifetime of the electrons is reciprocal to the number of free states and thus to the energy difference $E - E_\mathrm{F}$ of the excited electron to the Fermi level $\tau(E) \propto (E - E_\mathrm{F})^{-2}$. We do not find these directly excited hot electrons in our photoemission spectra which is to be attributed to their high energy and thus short lifetime.[11]

What we do observe in our spectra are thermalized electrons, which are secondarily excited electrons. Their creation is depicted in Figure 4.8. After a certain time, the lifetime of the hot electron,[12] it scatters either with another electron or with a phonon, defect, or magnon. Due to the mass equality in electron-electron scattering, this process is the one with the highest energy transfer between the scattering partners. It therefore leads to the energetic decay of the hot electrons and to the creation of secondarily excited electrons and holes. These secondary electrons scatter again and transfer part of their energy – which is now lower than that of the primarily excited electrons – to a further generation of excited electrons and holes. The result of this cascade is a thermalization of the hot electrons, which leads to a Fermi distribution again, now with a higher temperature.

Energy cuts through this distribution of thermalized electrons are shown in Figure 4.9(b) in dependence on pump-probe delay. We find a majority-spin character close above E_F ($E - E_\mathrm{F} = 0.04\,\mathrm{eV}$ and $0.14\,\mathrm{eV}$), which we attribute to the high-energy tail of the majority-spin surface-state peak (*cf.* Sec. 4.3.3). At higher energies ($E - E_\mathrm{F} \geq 0.2\,\mathrm{eV}$), there is no significant spin polarization observable. Since the occupied part of the band structure

[11] They were observed by Lisowski [2005] [Bovensiepen, 2007] with an s-polarized probe laser pulse (in this chapter, only p-polarized light was used for probe).

[12] Due to shielding of the excited electron and the hole by a cloud of other electrons, which is characteristic in metals, the electron and hole do not feel much of the others Coulomb field. It is thus appropriate to treat them independently.

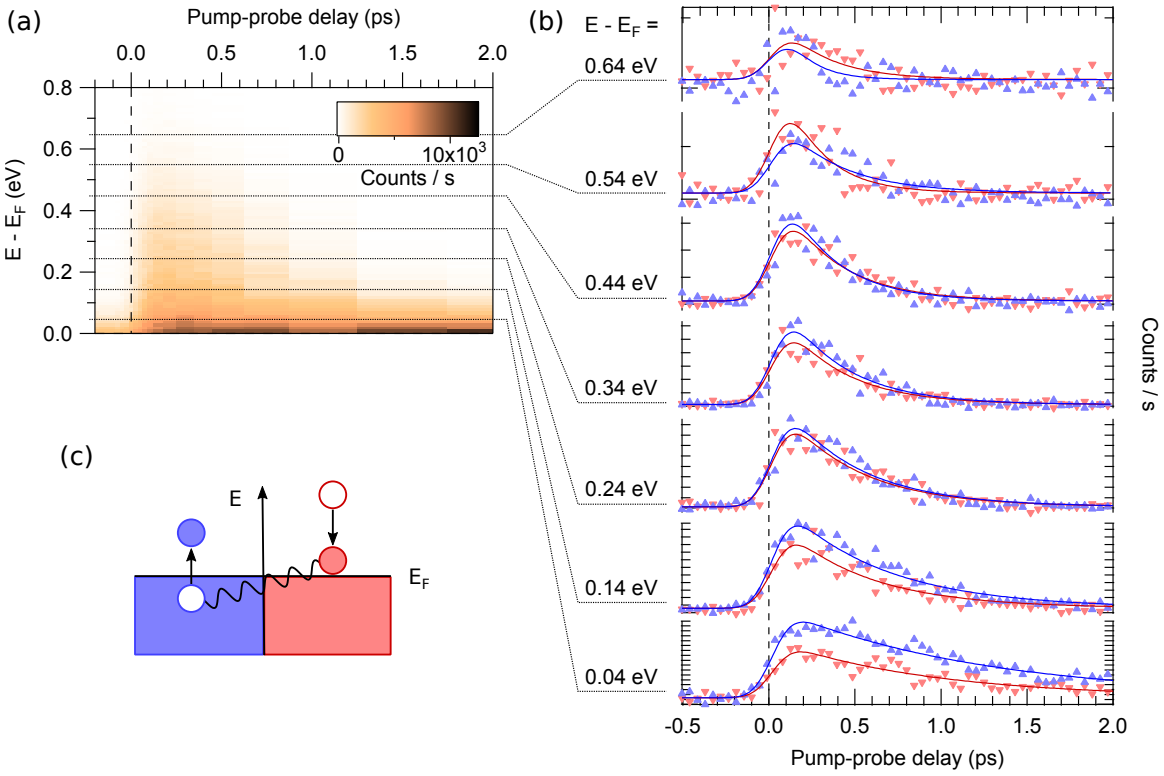

Figure 4.9: Uncoccupied electronic states at $E > E_F$, reprinted from Ref. [III]. (a) shows a spin-integrated overview spectrum in dependence on energy and pump-probe delay. In (b), the spin-resolved photoemission intensities at selected energies are shown in dependence on delay. In the depicted energy range, we find the thermalized electrons constituting the high-energy tail of the Fermi function (generated as shown in Fig. 4.8). The majority character of the spin polarization at 0.04 and 0.14 eV is caused by the high-energy side of the majority-spin surface-state peak ranging above E_F. Note that there is no significant minority-spin polarization detectable in the energy range of the corresponding minority-spin component of the surface state, which is supposed to lie at $E - E_F \sim 0.5$ eV with a much broader lineshape compared to its majority-spin partner (*cf.* Fig. 4.6). The lack of spin polarization in the thermalized electrons also suggests, that the majority- and minority-spin populations are equalized by exchange scattering processes as depicted in (c).

consists of highly spin-polarized states, we may assume that there is some spin-polarization in the first generation of excited electrons. Thus, the missing spin polarization in the thermalized electrons indicates that there is a process involved in the thermalization, which equalizes the amount of excited electrons with opposite spin directions. The equalizing process that has been identified to contribute to the decay of hot electrons is the so-called exchange scattering [Kirschner, 1985]. Exchange scattering describes scattering between electrons of opposite spin. So the energy of a relaxing electron is transfered to an electron of the opposite spin direction (depicted in Fig. 4.9(c)). The higher probability for exchange scattering can be understood from the symmetric wave functions of electrons of opposite spin, which leads to a larger spatial overlap similar to the concept of the exchange hole

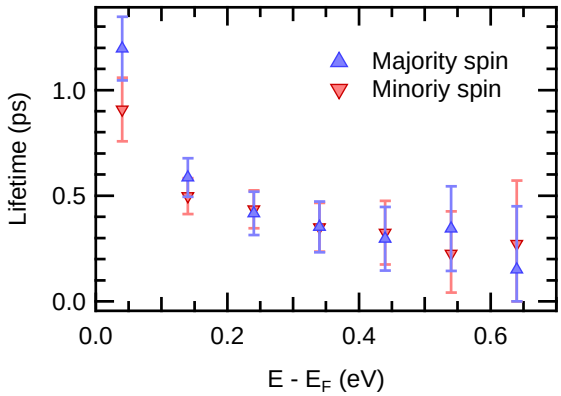

Figure 4.10: Lifetimes obtained from exponential fits to the spectra displayed in Fig. 4.9(b), reprinted from Ref. [III]. The lifetimes found here, reflect the timescale of heat dissipation from the electronic system to the lattice according to the 2TM (*cf.* Sec. 4.2.2). They are not the single electron scattering times. At high excitation densities as in our experiment, the reexcitation by scattering among excited electrons prevents a pure electronic energy relaxation. Energy needs to dissipate into the lattice instead. The equality of the lifetimes found for majority- and minority-spin electrons, suggest that this occurs through the same spin-dependent process for both spin directions.

(*cf.* Section 2.1). It has been shown by Goris et al. [2011] that secondary electrons of majority-spin character are created on the cobalt(001) surface due to exchange scattering with holes excited in a minority-spin surface state. Such exchange-scattering processes would on the one hand transfer a transient electronic population of a distinct spin character into secondary electrons of the opposite spin. On the other hand, exchange scattering in the secondary-electron cascade (as depicted in Fig. 4.8) also equalizes the spin polarization in the secondary electrons. Furthermore, the lifetimes of majority- and minority-spin hot or thermalized electrons are observed to be rather similar in photoemission [Aeschlimann et al., 1997; Goris et al., 2011], since the phase space of both spin directions contributes to scattering in both spin channels.

Figure 4.10 displays the lifetimes we obtain by fitting the time dependence of the intensities shown in Figure 4.9. The equal lifetimes for both spin directions do not necessarily mean, that transport effects induced by the hot or thermalized electrons can not be spin-dependent. As discussed above, the electronic population shown in Figures 4.9 and 4.10 is a thermalized population created by a whole cascade of scattering processes. These are not the lifetimes of the primarily excited electrons and therefore do not reflect the spin dependence of scattering rates that is fundamental for spin-dependent transport. Scattering rates closer to the transport-relevant one-particle lifetimes are observed in measurements with a low excitation density such as Ref. [Goris et al., 2011]. The difference between experiments with low and high excitation densities is that for high excitation densities, as in our experiment, scattering between the already excited electrons is stronger. This leads to a more homogeneous distribution of the excited electrons in k space. We thus find the population of electrons excited in the cascade shown in Figure 4.8 reoccurring in the region of our measurement, while in experiments with low excitation densities the population of thermalized electrons may be excited outside the k range of the measurement. Here, we directly observe that the energy stays in the electron gas and repopulates electrons above the Fermi level. To evoke the decay of the electronic temperature, the energy needs to be transferred to another subsystem – the phononic heat bath. This is subject of the next

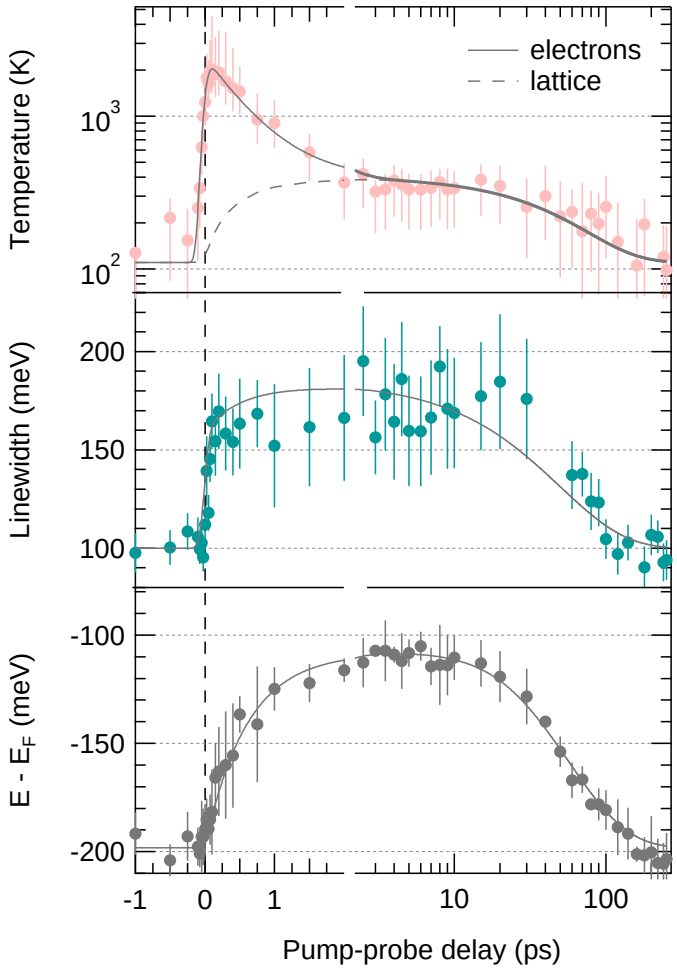

Figure 4.11: Temporal evolution of electronic temperature, surface-state linewidth, and binding energy $E - E_F$, reprinted from Ref. [I]. All three parameters are obtained from a fit to the spectra shown in Fig. 4.7 as described in Sec. 4.3.2. The temperature is determined from the width of the Fermi function. The solid lines correspond to fits of temporal evolutions using Eq. 4.9 for temperature and linewidth, with the dashed line being the contribution of the lattice $T_l(t)$. The temporal evolution of the binding energy is explained in Sec. 4.4.3.

section.

As a conclusion of this section, we can summarize that there is neither a spin polarization observed in the thermalized electrons nor a spin dependence of their lifetimes. We thus find equal electronic temperatures for majority and minority spin electrons. This equalization is supposed to occur through exchange scattering, which appears to be the dominant process in electronic thermalization. The decay of the majority- and minority-spin temperatures must occur through the same spin-independent process, since otherwise a spin dependence at larger time delays would be induced. We shed more light on this temperature decay in a short introduction of the two-temperature model in the next section.

4.4.2 Heating the Lattice - The Two-Temperature Model

Figure 4.11 shows the temporal evolution of the fit parameters electronic temperature and linewidth and peak position of the surface state as obtained from fitting the energy spectra shown in Figure 4.7. The electronic temperature depicted in panel (a) is derived from the

width of the Fermi function. It is raised directly within our time resolution of 70 fs (see also appendix B) through the decay of excited hot electrons as described in the previous section and decreases within 2 ps through dissipation of heat to the lattice.

The dissipation of heat to the lattice is directly reflected in our observed electronic temperature (Fig. 4.11). The temperature does not directly return to the value of 100 K we find for negative pump-probe delays. Instead it equilibrates with the lattice at an elevated temperature of $\approx 350\,\mathrm{K}$. We approximate this equilibration by adding the increasing lattice temperature T_l to the temperature of the electron gas T_e (dashed line in Fig. 4.11). This yields the following fitting functions:

$$T_e(t) = \int S(t)dt \cdot \left(A_{el} \mathrm{e}^{\frac{-t}{\tau_{el}}} + T_l(t) \right) \tag{4.9}$$

$$T_l(t) = A_{le} \left(1 - \mathrm{e}^{\frac{-t}{\tau_{el}}} \right) \cdot \mathrm{e}^{\frac{-t}{\tau_d}}, \tag{4.10}$$

where $A_{el} > A_{le}$. The amplitudes A_{el} and A_{le} account for the different heat capacities C_e and C_l of the electrons and the lattice. The excitation by the laser pulse $S(t)$ was approximated by multiplication with a step function at $t = 0\,\mathrm{ps}$. We can fit Equation (4.9) to the temperature shown in Figure 4.11(a) after convolving with a Gaussian to account for our time resolution given by the time envelope of the laser pulses. The sigmoid function resulting from the convolution of step and Gaussian perfectly resembles the time integral of the Gaussian shaped laser pulse.

Energy is transferred from the electrons to the lattice with the time constant τ_{el}. Since $C_e < C_l$, the temperature loss in the electronic systems is larger than the temperature gain in the lattice. An additional exponential decay term with time constant τ_d was included to account for the cooling of the electrons and lattice through diffusion at large pump-probe delays. This cooling should in principle be driven by the motion of electrons. The term has been included in the relation for T_l in this work to account for the cooling of the lattice as well. This is legitimate, since the equilibration between T_e and T_l is fast compared to the diffusion ($\tau_d \gg \tau_{el}$).

These simple relations provide a good modeling of the measured temperatures as demonstrated by the solid line in Figure 4.11. The temporal evolution of the linewidth and binding energy of the surface state shown in Figure 4.11(b) and (c) can be described by Equations (4.9) and (4.10) as well. The surface state's binding energy shifts closer to the Fermi level. Fitting the binding energy, linewidth, and temperature simultaneously, we find that this energy shift occurs with the same time constant as the lattice temperature increases. It is well described by Equation (4.10) except for a tiny shift at large delays, which will be discussed in the following section. The linewidth is fitted using Equation (4.9) like for T_e. There are electronic and phononic contributions to the linewidth as introduced in Section 3.3.4. The electronic contribution is lower but proportional to T_e^2 and thus increases just like the electronic temperature within the duration of the pump laser pulse.[13] When the

[13] The two in the exponent should of course lead to a steeper increase of the linewidth compared to that of the electronic temperature. This is not resolved in our 70 fs cross correlation. Instead, we fit both parameters with the Gauss-convolved step function mentioned before.

electrons cool down, the decrease of the electronic contribution to the linewidth is outweighed by the larger contribution of the phonons now increasing proportional to T_l. At large delays, we find the relaxation of all three values back to their values in the unpumped state.

The shift of the surface state's binding energy may already be the signature of a demagnetization. A shift of this majority-spin state to lower binding energies is likely to be induced by a decreasing exchange splitting. Nevertheless, as discussed in Section 4.3.2, we have no information on the minority-spin component of the surface state. Bovensiepen took the peak at $\approx 500\,\mathrm{meV}$ for the minority-spin surface state and interpreted that the exchange splitting shows no significant change. Yet, we find no minority-spin character in this energy range, speaking against this interpretation. It has also been observed in MOKE and XMCD experiments that the magnetization is lowered on the timescale on which we observe the shift. A decreasing exchange splitting for the ($5d6s$) valence electrons on this timescale has also been found. We therefore interpret the shift of the majority-spin surface state as a decreasing exchange splitting as well. The spin polarization shows hardly any change at all on this timescale. This distinct temporal behaviors of exchange splitting and spin polarization will be discussed in the following section.

4.4.3 Signatures of Demagnetization - Stoner *vs.* Spin-Mixing Behavior

To trace down any change in the spin polarization of the surface state, we performed spin-resolved measurements through the whole delay range at fixed energies. Although, we find more accurate values for the spin polarization obtained from the full peak, it is more convenient to complement the data by measurements at relevant energies instead of taking full spectra over the whole delay range. This is due to the loss of count rate in the spin-resolved measurements, which is a factor of 10^{-2} compared to the spin-integrated intensity. With a factor of hundred longer measuring times, we could not exclude that the measurements are disturbed by a changing surface quality or laser fluctuations. This scenario is less likely to happen, if we measure the spin polarization at several fixed energy values, which is much faster.

Scans at 200 meV, the binding energy before the pump pulse, and at 120 meV, the energy the surface state reaches through his shift, shown in Figure 4.7(b). The solid lines resemble a constant spin polarization. They roughly fit the data with slight deviations at large pump-probe delays, which finally indicates a lowering of the spin polarization. The spin polarization obtained from the spectra in Figure 4.7(b) is shown in the top panel of Figure 4.12. Despite a very huge error bar arising from the low count rates in this experiment, the center of gravity clearly changes from 1.0 at 0 ps to ≈ 0.85 at 100 ps. By a simultaneous fit of an exponential decay to the two spin-polarization curves, we obtain a time constant of $\tau_S = 15 \pm 8\,\mathrm{ps}$. A few more values with less uncertainty are obtained from the areas of the full spin-resolved spectra at selected time delays. All of the so-obtained values match the two fitted curves very well.

We thus find a slowly (15 ps) decreasing spin polarization, while the peak position, indicating the decreasing exchange splitting, shifts much faster (0.6 ps) towards the Fermi energy E_F showing a typically Stoner-like behavior. This fast shift to E_F can be described with the same exponential as the decreasing lattice temperature. However, the back shift

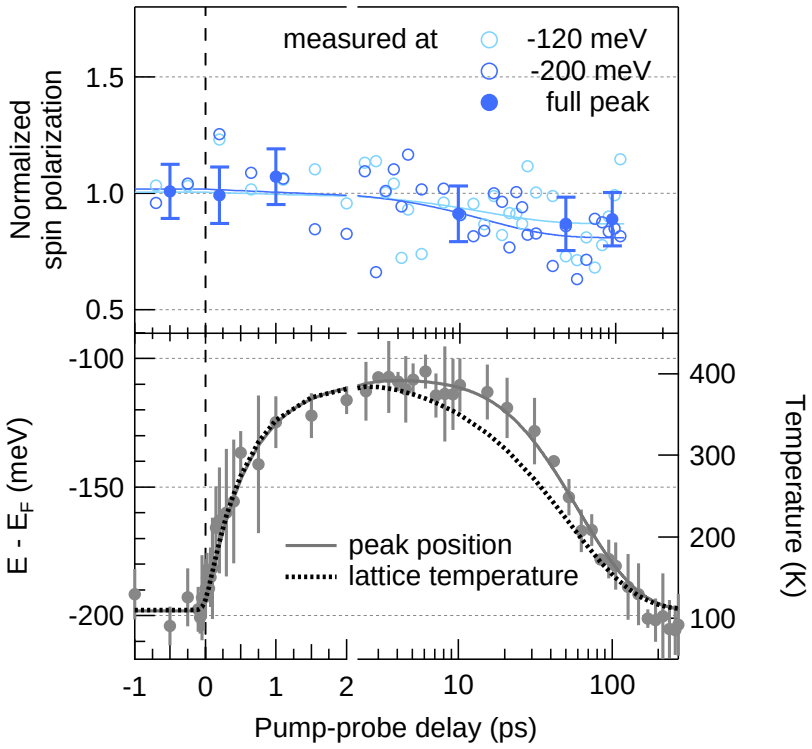

Figure 4.12: Temporal behavior of the spin polarization and binding energy of the majority-spin surface state, reprinted from Ref. [I]. The exchange splitting is decreased on an ultrafast timescale of $\tau_E = 0.6 \pm 0.1$ ps shifting the binding energy towards the Fermi level E_F. The spin polarization decreases much slower with an exponential time constant of $\tau_S = 15 \pm 8$ ps. This time constant is also reflected in a further shift of the surface state towards E_F depicted by the difference to the time evolution of the lattice temperature at large pump-probe delays.

shows deviations from the recooling of the lattice (black dash dotted line in Fig. 4.12). This indicates, that the decreasing spin polarization leads to an additional shift of the peak position towards E_F. Indeed, the back shift of the peak can again be described (grey solid line) with the exponential recooling of the lattice, when a second shift towards E_F is added occurring with τ_S, the time constant of the spin-polarization change.

In the thermally-induced equilibrium phase transition shown in Figure 4.3, spin polarization and exchange splitting are reduced simultaneously. To compare the dynamics found in the laser-induced phase transition to the temperature-induced changes in thermal equilibrium, we plot the spin polarization as a function of the peak position in Figure 4.13. Each pair of values corresponds to the same pump-probe delay or the same temperature for the laser-induced or the thermally-heated experiment, respectively. In the laser-heated experiment (●, ○), we observe a shift from $E - E_F = -200$ meV to -110 meV with almost no decrease of the spin polarization. The latter changes from 1 to 0.9 during the whole shift. In the filament-heated experiment (■), we find a complete breakdown of the spin polarization at a peak shift of the same magnitude as in the laser-heated experiment. At this shift, the Curie temperature is already reached in the equilibrium phase transition. In the laser-heated experiment, the system recools afterwards and the surface state begins to

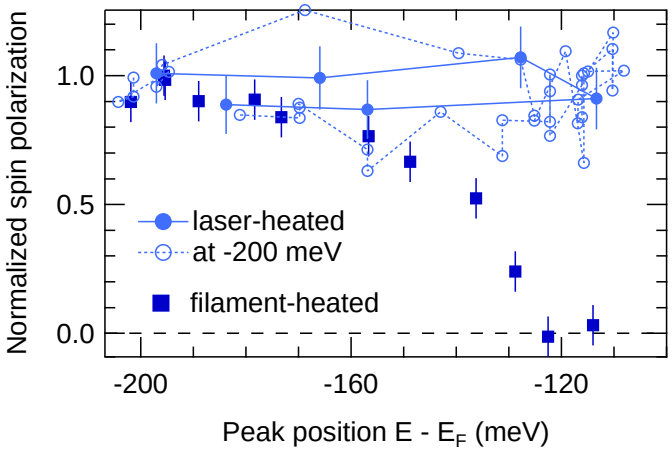

Figure 4.13: Comparison of the laser- and filament-heated phase transition, reprinted from Ref. [I]. Shown is the spin polarization as a function of binding energy each pair of values corresponding to the same pump-probe delay or temperature in the laser-heated and the filament-heated experiment, respectively. The surface state peak shifts from -200 to -110 meV in both experiments. While in the equilibrium phase transition, the spin polarization already breaks down at -120 meV (when T_C is reached), it is only marginally reduced in the laser-heated experiment.

shift back with a lowered spin polarization.[14] So we can conclude that we find the same binding-energy shift in both experiments showing a Stoner-like behavior upon laser-heating, while it is accompanied by spin mixing in the equilibrium phase-transition when the heating is achieved by the use of a filament.

At first, this difference appears to be startling. A possible explanation could be a decay or the emergence of smaller magnetic domains within the area of our probing laser spot, which is several tens of micrometers. If this occurred in the equilibrium phase-transition, our spin sensitivity would break down leading to a decrease of spin polarization as we observe it. Nevertheless, there are time-resolved Fourier transform holography (FTH) experiments revealing that domain wall motion is fast enough to occur in our laser-heated experiment as well [von Korff Schmising et al., 2014]. We can therefore exclude the decay into microdomains as an explanation of the observed differences. Instead we assume, that there are different processes contributing to the demagnetization that occur simultaneously during the equilibrium phase transition and can be separated in the laser-heated experiment.

Since the fast Stoner-like shift happens on the same timescale of the electron-lattice equilibration, it can indeed be induced by Elliott-Yafet scattering as suggested by Koopmans et al. [2010]. Spin flips are needed to decrease the exchange splitting since the occupation changes to more minority- and less majority-spin states. The spin polarization of the particular orbitals does not need to be changed on this timescale, since the decreasing exchange splitting already contributes to the spin-dependent potential and thus stabilizes the new energy position of the states. As calculated by Sandratskii [2014], the spin direction of the surface state is strongly determined by that of the $4f$ electrons. We find that the timescale on which the spin polarization changes, is in line with that found in the MLD in photoemission from the $4f$ levels [Frietsch et al., 2015]. Frietsch et al. [2015] explain the slow response in the $4f$ core levels by the hypothesis of Wienholdt et al. [2013], that the $4f$

[14] The pump-probe delay at which the peak position and spin polarization fully recover lies out of our measurement range. According to Frietsch et al. [2015], this happens near 600 ps. In line with the MLD observed in the $4f$ levels, we expect the spin polarization to show a fast recovering on the last 10 meV of the back shift of the peak.

spin system interacts predominantly with the lattice. The change of spin polarization in the $4f$ electrons leads again to a change of the orbitals binding energy, which is reflected in the second slower peak shift we find in the surface state.

4.5 Summary

In summary, we find three processes during the laser-induced ultrafast demagnetization of gadolinium, which are all reflected in the majority-spin surface state:

1. The ultrafast ($< 70\,\mathrm{fs}$) heating of the electron gas depopulating the surface state and hence leading to a decreasing magnetic moment at the surface.

2. The dissipation of energy from the electrons to lattice at $\tau_E = 0.6 \pm 0.1\,\mathrm{ps}$ inducing a Stoner-like change of the surface state's binding energy and thus a true demagnetization.

3. The subsequent change of the surface state's spin polarization at $\tau_S = 15 \pm 8\,\mathrm{ps}$, which contributes to a further demagnetization.

The slow change of the spin polarization is in line with the change of the $4f$ magnetic moment as observed by Frietsch et al. [2015]. The timescale of $\tau_S = 15 \pm 8\,\mathrm{ps}$ indicates a demagnetization through spin-lattice equilibration, which has been determined by Vaterlaus et al. [1991] to $100 \pm 80\,\mathrm{ps}$. The Stoner-like behavior we find in the surface state at sub-picosecond delays corroborates the findings of Sandratskii [2014], that the spin moment of the surface state stays aligned to that of the $4f$ electrons even upon demagnetization. Nevertheless, the net magnetic moment in the valence states is reduced by the decreasing exchange splitting found in the ($5d6s$) bands [Carley et al., 2012] in line with our Stoner-like shift of the surface state. Such a demagnetization on the timescale of the electron-lattice equilibration corroborates the theory of Koopmans et al. [2010], that Elliott-Yafet scattering is the driving process for the sub-picosecond demagnetization. Although this model also finds that the laser-induced demagnetization of gadolinium occurs on two distinct timescales, it does not distinguish between different processes, which we clearly observe.

The theory developed by Battiato et al. [2010, 2012] of super-diffusive transport contributing to the demagnetization, provides an explanation for the fast depopulation of the surface state. In general, we can expect a minor role of transport effects for the observations in our experiment. It has already been suggested by Knorren et al. [2002] using a semi-empirical theory for noble metal thin films, that excited carriers should be confined to the film, since they are reflected at the interface to the substrate. Strictly spoken, from our measurements we cannot tell, whether the same effect occurs for the directly excited first generation of hot electrons, which are in the super-diffusive regime according to Battiato et al. [2010, 2012]. Yet, due to the ultrashort lifetimes of these hot electrons one would expect transport effects exclusively on the timescale on which we observe the thermalization of the electrons. We find, that exchange scattering processes contribute dominantly to the thermalization. This equalizes the excited majority- and minority-spin population as well as the temperatures of the electron gases of the corresponding spin direction. Spin-dependent transport should thus contribute mostly to the depopulation of the majority-spin surface

state on the ultrafast timescale ($< 70\,\mathrm{ps}$) and explain the magnetic effects found in second harmonic generation [Melnikov et al., 2003].

Our findings finally explain the discrepancies between the timescales found in the different experiments, that have been introduced in Section 4.1. Table 4.1 summarizes them according to the timescales of the three processes. When a technique is sensitive to one of the above-mentioned processes, it shows the corresponding timescale.

This is of course a rough categorization of driving processes, for the exact timescales should depend on experimental details such as the thickness of the Gd film if transport processes are involved. Then also the substrate should play a role or whether the sample is mono- or poly-crystalline. Furthermore, τ_E has been found to be dependent on the pump laser fluence. Thus, the temporal length of the pump pulse should play a role as well as has been investigated by Fognini et al. [2015].

In the thermally-induced equilibrium phase transition, all the experimental techniques mentioned in Section 4.2 show the same behavior, since spin polarization and exchange splitting are reduced in parallel, simultaneously with the broadening of the Fermi distribution. It is the benefit of gadolinium that allows us to separate these contributions to the demagnetization of surface and bulk. The investigation of such transient non-equilibrium states is a unique possibility to finally understand the fundamental processes underlying magnetism.

Chapter 5

A Correlation Effect in the Surface Electronic Structure of Fe(110)

In the last chapter, we found in the magnetic phase transition of gadolinium, that the spin polarization of the surface state can behave different from the state's exchange splitting when the phase transition is driven by an ultrashort laser pulse. This observation is far from all expectations based on measurements in thermal equilibrium and sheds new light on the role of the electronic band structure in cause and effect of magnetism. As a material-dependent property, the band structure can favor certain spin excitations and spin-dependent processes. One example is the increasing probability for spin flips at points, where several bands hybridize due to spin-orbit coupling [Pickel et al., 2008]. Another example is the generation of collective excitations, such as phonons or magnons, which can be enhanced for certain energy ranges of the band structure. In these energy ranges, the behavior of electrons can no longer be described by simple one-electron theories because of the strong correlation between the electrons and their surrounding.

A particularly interesting system with regard to correlation and hybridization effects in the band structure are the surfaces of iron (Fe). Its valence bands are exchange-split by about 2 eV and hybridize due to spin-orbit coupling. The interaction of electrons with collective excitations leads to a renormalization of the electronic band energies. This shows up as a kink, if the band crosses an energy level that exceeds the characteristic energies of the excitations. Thanks to the increasing resolution in photoemission techniques, kinks have been found in the valence bands of Fe, which occur due to electron-electron, electron-phonon, and electron-magnon interactions [Schäfer et al., 2004; Schäfer et al., 2005; Sánchez-Barriga et al., 2012].

In this chapter, we will investigate surface states on Fe/W(110) thin films and their modification due to correlation effects. Since the band structure of Fe as well as the structural and magnetic phase depend very much on the growth mode and substrate, Section 5.1 provides a detailed description of our sample preparation including a study of annealing temperatures. The previous works on the surface band structure of Fe/W(110) and its correlation and hybridization effects are summarized in Section 5.2. The spin-dependent band structure will be the topic of Section 5.3. In Section 5.4, we discuss a magnetic linear dichroism (MLD)

occurring in our spectra along with the dispersion of a minority-spin surface resonance.

5.1 The Growth of Iron Thin Films

The electronic and magnetic properties of iron are known to be very much dependent on the growth mode and layer thickness [Rybicki et al., 2013]. Bulk iron is ferromagnetic at room temperature and has a bcc crystal structure (α-Fe). The ferro- to paramagnetic phase transition at $T_C = 1044\,\mathrm{K}$ is followed by a structural phase transition to the fcc configuration (γ-Fe) at 1183 K [Donath et al., 2009]. Surprisingly, Fe deposited on Cu(001), which grows in the fcc structure for the first 10 ML, happens to be ferromagnetic at room temperature [Donath et al., 2009]. The electronic band structure [Donath et al., 2009] and magnon dispersion [Chuang et al., 2012] vary strongly between the bcc and fcc phase and even within these phases [Zhang et al., 2010; Zakeri et al., 2013].

When iron is deposited onto W(110), it grows in its bcc configuration. Different growth modes can be achieved by adjustment of the substrate temperature.[1] While the first monolayer has been found to grow pseudomorphically in an almost completely closed layer at any temperature [Jensen et al., 1996], the growth of the subsequent layers is very much temperature-dependent. At room temperature, rough layers grow starting in the form of isolated islands [Bethge et al., 1995; Jensen et al., 1996] with a slight tendency to grow along the step edges defined by the W(110) substrate [Kubetzka, 2002]. At elevated temperatures ($\approx 550\,\mathrm{K}$), the higher mobility leads to an increase in this trend. When grown at 550 K, the second layer forms a film, which is closed but exhibits prominent dislocation lines along the [001] direction [Kubetzka, 2002]. The subsequent layers show even more dislocations, forming a 2D network. In contrast, growth on the rougher pseudomorphic double layer (psDL) at room temperature shows little dislocations [Bethge et al., 1995].

Since most STM studies are focused to the growth of the first 1 to 4 layers, reliable receipts to grow thicker Fe films are rare. In several references a growth at temperatures below room temperature is suggested. Atomically smooth films can then be created by annealing after deposition onto a cooled substrate [Rybicki et al., 2013; Nuber, 2011]. At high temperatures it has been found that all Fe material in excess of the psDL ($> 2\,\mathrm{psML}$) agglomerates into clusters (*cf.* Fig. 5.3), giving rise to a change in work function and decreasing the ratio of Fe to W Auger amplitudes [Kołaczkiewicz and Bauer, 2000; Berlowitz et al., 1990]. This process has been found to start between 500 and 600 K Therefore, we used a relatively low annealing temperature of 530 K.

We performed a study on the temperature dependence of iron film growth, which is shown in Figure 5.2. To deposit thin Fe films, we used a commercial UHV beam evaporator (EMF3, FOCUS). Fe was evaporated from a rod by electron bombardment heating. The

[1] The growth modes of Fe on W(110) substrates have *e.g.* been studied in scanning tunneling microscopy (STM) [Kubetzka, 2002; Fruchart et al., 2007; Bethge et al., 1995; Jensen et al., 1996], and by low-energy electron diffraction (LEED) [Rybicki et al., 2013; Gradmann and Waller, 1982], Auger-electron spectroscopy (AES) [Gradmann and Waller, 1982; Berlowitz et al., 1990; Kołaczkiewicz and Bauer, 2000; Nahm and Gomer, 1997a], temperature-programmed desorption spectroscopy (TPD) [Berlowitz et al., 1990], as well as a Kelvin probe method for work function determination [Nahm and Gomer, 1997b].

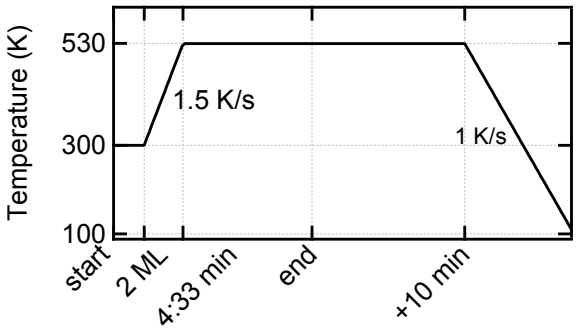

Figure 5.1: Programmed substrate temperature during the growth of the 15 ML-thick Fe films investigated in this thesis. The temperature program was driven by a "Eurotherm 2408" PID controller. The first 2 ML were grown at 300 K. For the subsequent layers the temperature was increased to 530 K at a ramp rate of 1.5 K/s. The temperature was kept at 530 K for the remaining evaporation time plus 10 minutes while moving the manipulator from the preparation to the analyzer chamber. In the measurements position, we cooled the sample down to liquid nitrogen temperature at a rate of 1 K/s.

deposition rate was ~ 2 Å per minute as monitored by a quartz micro balance. With a lattice constant of $a = 2.87$ Å, in [110] direction one monolayer (ML) has a thickness of $\sqrt{2}a/2 = 2.03$ Å.[2] The afore-mentioned in-plane distortions arising at low coverages – from the large lattice mismatch between Fe and W – are considered to be relaxed in films thicker than 10 ML [Nuber, 2011]. Therefore, we chose a thickness of 15 ML for our investigations. To produce films of ~ 15 ML thickness, we deposited 30 Å of Fe. The substrate temperature was set by a PID controller ("Eurotherm 2408") as shown in Figure 5.1. We started deposition at room temperature to prevent the formation of the afore-mentioned dislocation lines in the first two monolayers. After 2 ML were deposited, we gradually increased the substrate temperature by 1.5 K/s until 530 K were reached and kept this temperature for the rest of the deposition process and during the sample transfer into the analyzer chamber. The film was thus annealed in the growth process and possible contaminations during the sample transfer were avoided. Annealing temperatures > 500 K have been reported to be necessary for the formation of large patches with homogeneous thickness [Fruchart et al., 2007]. To verify that annealing to 530 K produces a sufficient sample quality, we grew an Fe film at room temperature and performed post-growth annealing to different temperatures.

Two-photon photoemission (2PPE) spectra of the resulting samples are displayed in Figure 5.2(a). The peaks originate from the $n = 1$ (at $E_{\mathrm{Kin}} < 6$ eV) and $n = 2$ (at $E_{\mathrm{Kin}} > 6$ eV) image-potential states, while the intensity rising to the low-energy side of the spectra is direct photoemission by the UV pulse. The UV photon energy was $3h\nu = 4.73$ eV. Thus, the occurrence of direct photoemission indicates that the film is rather rough with a work function below this energy. From 300 to 500 K the image-potential states shift to higher kinetic energies when annealed at higher temperatures. At 500 K the $n = 2$ image state can no longer be populated, since its binding energy[3] exceeds the UV photon energy. This shift and the vanishing direct photoemission at low energies indicate an improving

[2] A recent LEED study on the near-surface structural properties revealed that the interlayer spacing at the surface differs from this value [Rybicki et al., 2013]. Nevertheless, this does not affect the number of layers specified in our films, since the quartz micro balance determines the deposited mass.

[3] The binding energy of the image-potential states can be determined from the measured kinetic energy subtracting the probe photon energy of $h\nu = 1.577$ eV.

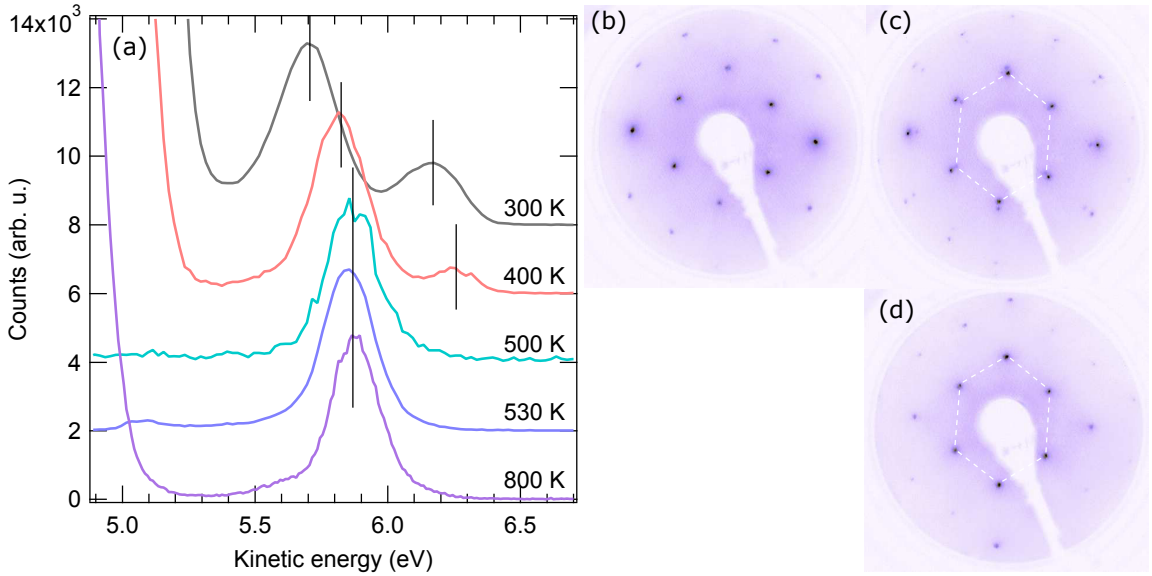

Figure 5.2: (a): 2PPE spectra of a 15 ML Fe film. The film was grown at room temperature and successfully annealed at different temperatures afterwards. The black curve shows the spectra as grown (at 300 K), the orange curve after 30 minutes at 400 K, green after additional 15 minutes at 500 K, blue 5 minutes at 530 K and violet 5 minutes at 800 K. The two peaks shifting to higher kinteic energies from 300 to 500 K are the $n = 1$ and $n = 2$ image-potential states. Their shift indicates an improving sample quality, since their binding energy is pinned to the vacuum level. At 500 K the $n = 2$ image-potential state can no longer be populated, since it reaches an energy larger than the largest photon energy. Below 500 K and at 800 K, direct photoemission occurs giving rise to the high intensities on the low-energy side of the spectra. This indicates a low work function of the sample at these preparation methods. (b), (c), and (d): LEED patterns at 265 eV recorded at room temperature. (b) shows a 15 ML Fe film grown at 530 K by our usual procedure described in the text. In (c) the film is shown after annealing to 800 K for 5 minutes. Here, the Fe film agglomerates into clusters giving rise to the appearance of the LEED patterns of both Fe(110) and W(110). The W pattern is indicated by the white dashed lines, which are identical to those on the right. (d): LEED pattern of the pure W(110) after the Fe film has been desorbed.

sample quality. Since the image-state binding-energy is pinned to the vacuum level, the film appears to smoothen giving rise to an increase in work function Φ. When annealed at temperatures > 500 K, the $n = 1$ peak shows no further significant shifts. Instead, a pronounced secondary cutoff at $\Phi = 5.0$ eV appears when the sample is annealed to 530 K.

Surprisingly at 800 K, the work function is seemingly lowered giving rise to direct photoemission without any back shifting of the image-potential states. According to Kołaczkiewicz and Bauer [2000] and Berlowitz et al. [1990], at this temperature, the afore-mentioned agglomeration of the layers > 2 psML occurs (*cf.* Fig. 5.3). We can thus assume, that the film breaks up into islands (or forms clusters) and only the first 2 psML remain covering the W substrate. The findings of Kołaczkiewicz and Bauer [2000] and Nahm and Gomer [1997a] show that the work function of W shows a minimum at a coverage of 2 psML of Fe. The direct photoemission intensity might thus stem from the W substrate covered with

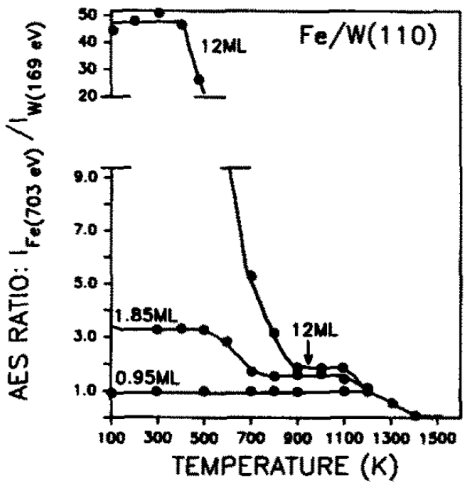

Figure 5.3: Temperature-dependent Auger amplitudes for different coverages of Fe/W(110), reprinted from Ref. [Berlowitz et al., 1990]. The films were deposited at a substrate temperature of 100 K. Note that in this graph 1 ML of Fe is defined as the coverage, which saturates the first order desorption peak in TDS. We find that this coverage actually corresponds to a coverage of 1.6 ML (= 2 psML= 1 psDL) as discussed in detail on page 90.

the 2 remaining Fe layers, while the Fe image-potential states keep their binding energy. This assumption is corroborated by the LEED intensities at a scattering energy of 265 eV shown in Figure 5.2(b), (c), and (d). (b) shows the LEED spots of a smooth 15 ML-thick Fe film as it is grown by our usual procedure described above. The picture in (c) shows the film after annealing to 800 K. Here we find two pseudo-hexagonal structures, of which one is induced by the Fe film (*cf.* Fig. 5.2(b)), while the other is identical to that of the W substrate shown in Figure 5.2(d). This is in line with the findings of Nahm and Gomer [1997a], Berlowitz et al. [1990], and Kołaczkiewicz and Bauer [2000] in AES reprinted in Figure 5.3, which show an increase of the W(NOO) Auger intensity (179 eV) for annealing temperatures in the range of 700 - 900 K. They all find a decreasing ratio of the Fe Auger intensities compared to that of W. Thus, measuring at a scattering energy, which is even higher than that of the W(NOO) line, we have an increased bulk sensitivity and are thus able to see the W substrate in LEED even through a closed Fe film of 2 psML thickness.

Our TPD spectra also give evidence for the agglomeration into nanocrystals and the formation of an underlying Fe double layer. The film thicknesses determined by TPD as described in Chapter 3.4 are consistently half of those determined by our quartz micro balance. The usually deposited amount of 15 ML of Fe constantly results in a TPD spectrum, in which the zeroth order desorption peak is about six times the area of the first order desorption peak, which would result in a film thickness of 7 ML, if only the first monolayer was desorbed with first order kinetics. Since the same evaporation geometry has been used for our Ni(111) films, for which the deposition rate determined by the quartz micro balance and the TPD spectra provide equal film thicknesses, we exclude a bad alignment of sample, quartz, and evaporator as a reason for a seemingly lower deposition rate than determined in the quartz measurement. Instead, we interpret the deviation as the formation of an Fe double layer upon our method of depositing the first two layers at room temperature. Fe grown at elevated temperatures has been found to grow in ordered epitaxial layers on a double layer [Kołaczkiewicz and Bauer, 2000]. The authors find that the first ML grows pseudomorphically at room temperature with the number of atoms corresponding to 0.8 ML in bulk Fe(110) notation. Assuming that the first order peak in our TPD spectra is caused

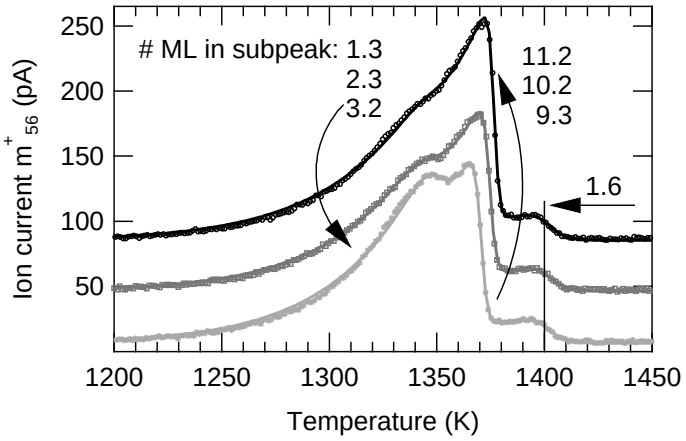

Figure 5.4: Temperature-programmed desorption (TPD) spectra of three 15 ML-thick Fe films all grown by the same procedure as described above on W(110). The zero-order desorption peak exhibits a shoulder of varying intensity for different films. We assign this to the desorption of excess Fe remaining from agglomeration into clusters. The unit of 1 ML corresponds to the amount of Fe atoms in one layer with (110) orientation of bcc bulk iron. We find that the first-order desorption peak is caused by two pseudomorphic monolayers each containing 0.8 ML in Fe(110) notation.

by the desorption of a pseudomorphic double layer with the same structure (corresponding to 1.6 ML Fe(110)), the resulting area of the zeroth order peak (7.8 times the first order peak) would consist of 12.5 additional monolayers. This results in a total thickness of 14.1 layers, which nicely agrees with the quartz measurement. Although not explicitly stated, the simultaneous desorption of the first two pseudomorphic monolayers must have been observed before by Berlowitz et al. [1990]. This is revealed, when the Auger amplitudes measured by Berlowitz et al. [1990] (shown in Fig. 5.3) are compared to those found by Kołaczkiewicz and Bauer [2000]. While Kołaczkiewicz and Bauer [2000] found the nucleation to occur for all layers above a thickness > 2 psML, Berlowitz et al. [1990] found this effect to occur for layers thicker than ≈ 1 ML. Berlowitz et al. [1990] referenced their layer thickness to the first order desorption peak found in TDP. Assuming this peak to contain be 1.6 ML Fe(110) ($= 2$ psML$= 1$ psDL), the temperature-dependence measured by Berlowitz et al. [1990] in AES is the same as that measured by Kołaczkiewicz and Bauer [2000].

The shoulder on the low temperature side had to our knowledge not been observed before. Such a feature could be induced by a structural phase transition from the bcc to the fcc configuration, which occurs at 1183 K shortly below the desorption. It could also be the desorption of some residual amounts of Fe from the nucleation into islands or clusters, which had been found by Berlowitz et al. [1990]. This interpretation appears to be reasonable, since the amount of Fe desorbed in the shoulder varied between different samples with the intensity shifting into the main peak.

5.2 The Surface Band Structure of Fe(110): State of the Art

The surfaces of iron are particularly interesting because of the large exchange splitting in the bulk-band structure. In addition to that, s, p and d states hybridize differently in the majority- and minority-spin band structure creating totally different conditions for surface

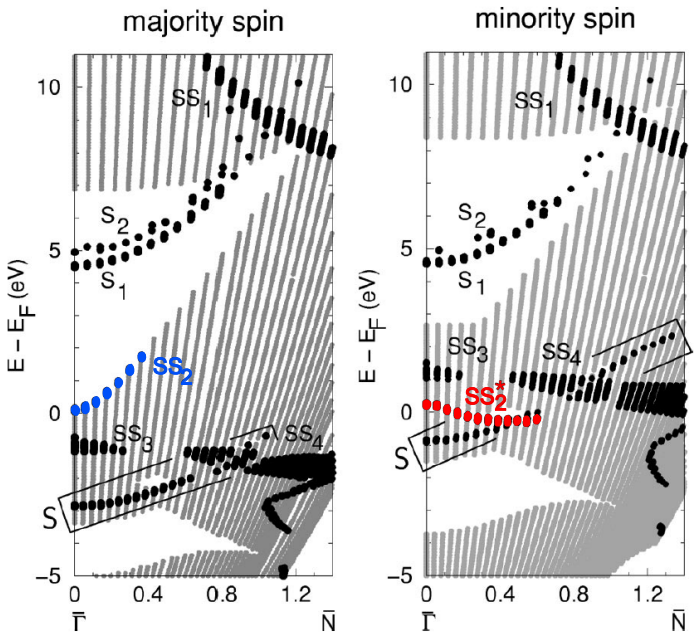

Figure 5.5: Spin-dependent surface-projected band structure of Fe(110) along the $\overline{\Gamma N}$ direction of the surface Brillouin zone, reprinted from Ref. [Braun et al., 2002]. The bulk bands are shown as the gray shaded regions. Surface features are indicated by black circles. Surface and image-potential states are denoted by S and S_1 and S_2, respectively. SS_1, SS_2, SS_3, and SS_4 indicate surface resonances. The resonance SS_2 (highlighted in blue and red in the majority- and minority-spin band structure) shows a particularly interesting dispersion behavior with a positive dispersion in the majority-spin component and a negative dispersion in the minority-spin component.

and interface states of opposite spin to form.

5.2.1 Formation of an Exchange-Split and Correlated Band Structure

The lowest coverage in which signatures of magnetization have been found in the band structure of Fe/W(110) is already in the sub-monolayer regime. Fe deposited on W(110) forms atomic-scale monolayer nanoislands consisting of about 50 iron atoms [Schlenhoff et al., 2012; Herzog et al., 2010; Sonntag et al., 2014]. These nanoislands are found to be ferromagnetic at cryogenic temperatures having an easy magnetization axis in the surface plane along the $[1\bar{1}0]$ direction. The islands exhibit a series of unoccupied field-emission resonance (FER) states [Schlenhoff et al., 2012]. The latter are states into which the system's image-potential states are transformed when an electric field is applied between an STM tip and the islands. The FER states on the nanoislands already exhibit a significant spin splitting.

For film thicknesses of only a few ML, Nuber [2011] studied the formation of quantum-well states. In Reference [Nuber, 2011], these states appear at the Fermi energy and successively shift to higher binding energies – in accordance with the phase-accumulation model – with increasing number of layers in the film. Nuber [2011] assigns a Σ_5^1 symmetry character to the QWS. He further finds the characteristics of electron-phonon coupling in the spectral lineshape with a Debye energy of 25.9 ± 3.7 meV and a coupling constant of 0.44 ± 0.10.

5.2.2 The Surface States

Compared to the amount of publications on the bulk band structure of iron, the Fe(110) surface is widely unexplored. An early photoemission study found a surface state shortly

below E_F at the $\overline{\Gamma}$ point [Sakisaka et al., 1985]. Another photoemission study with spin resolution reported on a minority-spin surface feature emerging below the Fermi level at $0.52 < k_{||} < 1.03\,\text{Å}^{-1}$ along the $\overline{\Gamma\text{H}}$ direction [Vescovo et al., 1993]. A minority-spin surface feature in this E-k region had been predicted before in a tight-binding calculation [Dempsey et al., 1976]. Later, Braun et al. [2002] observed majority- and minority-spin surface features occurring shortly above E_F in spin-resolved inverse photoemission. These features could be explained by the occurrence of several surface-resonance-like structures around the Fermi level in a layer-Korringa-Kohn-Rostoker calculation, the result of which is reprinted in Figure 5.5. By a careful construction of the surface-barrier potential to match the spectroscopic data, this calculation yields a surface-resonance (highlighted in blue and red in Fig. 5.5) showing remarkable differences in the dispersion behavior of the majority- and minority-spin component (SS_2 and SS_2^*). While the minority-spin component disperses downwards from a few meV above E_F at $\overline{\Gamma}$ to energies below E_F for small $k_{||}$ along $\overline{\Gamma\text{N}}$, its majority-spin partner disperses upwards remaining completely unoccupied. The negative dispersion of the minority component has been found to be induced by the existence of degenerate bulk d states in the minority-spin channel, while the majority-spin component is allowed to disperse unhindered along the band gap boundary.

A minority-spin surface resonance has also been observed by Sánchez-Barriga et al. [2009, 2012]. In line with the calculations of Braun et al. [2002], this resonance appears close to the Γ point in $\overline{\Gamma\text{N}}$ direction and vanishes, when the minority Σ_3 bulk band disperses to energies above the Fermi level at $k > 0.5\,\text{Å}^{-1}$ in $\overline{\Gamma\text{N}}$ direction.[4] A $\Sigma_{1,3}$ character is assigned to this surface resonance.

Further minority-spin surface resonances have been found by Schäfer et al. [2004] crossing E_F along the $\overline{\Gamma\text{S}}$ and $\overline{\text{HN}}$ direction. Surprisingly, the surface resonances predicted by Braun et al. [2002] along the $\overline{\Gamma\text{N}}$ direction were not observed in Reference [Schäfer et al., 2005], which is a subsequent and more extensive study of the Fermi surface of Fe(110). Schäfer et al. [2005] compared photoemission spectra at $100 - 140\,\text{eV}$ photon energy with DFT calculations. In this study, exclusively bulk bands with d character have been observed close to the Fermi level around Γ.

Braun et al. [2002] point out, that the surface electronic structure of Fe(110) is dominated by the shape of the surface barrier besides depending on the bulk properties. Thus, the different observations might be explained by differences in the film preparation. The films investigated by Braun et al. [2002] had a thickness $\leq 20\,\text{ML}$ and were grown by a similar as procedure as those in the present work (*cf.* Sec. 5.1). Braun et al. [2002] deposited the first 8 ML at room temperature and then increased the substrate temperature slowly to 550 K. In the spin-resolved photoemission study of Sánchez-Barriga et al. [2012], 20 ML-thick Fe films on W(110) have been investigated. The films were annealed at a more moderate temperature of 400° C. The Fe films grown by Schäfer et al. [2005] had a thickness $> 100\,\text{ML}$ and where annealed to high temperatures of 500° C. As introduced in Section 5.1, at this temperature the film should already agglomerate into clusters leading to the lowering of the work function (*cf.* Fig. 5.2(a) for 800 K). We can thus assume, that the surface barrier on the

[4]Note that the surface resonance itself does not disperse in this study, as here photon energies between 18 and 100 eV have been used to scan through the band structure perpendicular to the surface ($k_\perp$).

films studied by Schäfer et al. [2005] differs significantly from that of a film annealed to lower temperatures. This can explain the absence of surface states along $\overline{\Gamma N}$ in Reference [Schäfer et al., 2005].

5.2.3 Correlation Effects in the Surface Band Structure

An accurate quantitative description of the valence band structure of Fe is compromised by the effects of spin-dependent electronic correlations. Correlation effects lead to the mass renormalization of electronic states, which causes deviations between experimentally obtained band dispersions and those calculated using one-particle-based theories like the local spin-density approximation (LSDA) or the generalized gradient approximation (GGA) in density functional theory (DFT). In addition to that, electrons in states close to the Fermi level may be coupled to bosonic quasiparticle excitations like phonons or magnons. Kinks can be observed in the band dispersion, when the band energy exceeds the characteristic energy range of a quasiparticle with strong coupling to the band.

Such deviations from the one-particle electronic band structure due to correlation effects became accessible to ARPES experiments with the ever improving energy and angular resolution during the last years. Despite Fe being considered as weakly correlated material compared to Ni, the improved experimental resolution led to the observation of such renormalizations due to correlation effects. A first study of Schäfer et al. [2004] revealed a bosonic quasiparticle interaction in the minority-spin surface states. The renormalization appeared close to the Fermi level in the characteristic energy range of the magnon spectrum of Fe and was therefore interpreted as magnonic dressing of the surface-state electrons. This work was followed by studies on electronic Coulomb-interaction-induced renormalizations [Schäfer et al., 2005; Cui et al., 2007; Sánchez-Barriga et al., 2012]. The works have been reviewed in [Walter et al., 2010]. Sánchez-Barriga et al. [2012] showed that the recent approaches (DMFT and 3BS) including many-body effects in the LSDA improve the description of the band structure of Fe significantly but still underestimate modifications of energy and linewidth induced by correlation effects.

5.3 Sampling the Band Structure Near E_F

In this section, we investigate the surface-projected band structure close to E_F from two different viewpoints. First, we project the occupied part of the band structure close to E_F into the unoccupied image-potential states in a two-photon-photoemission (2PPE) process. Second, we discuss the result of direct photoemission along the $\overline{\Gamma H}$ direction in the surface Brillouin zone. The efficiency of the excitation process in 2PPE is of course governed by dipole selection rules. A thorough discussion of the latter thus points out the symmetry character and probability density of the initial-state wave-function.

5.3.1 Experimental Details

All spectra shown in this chapter were measured using the exchange scattering detector described in Chapter 3.1.1. The geometry of the photoemission process is shown in Figure 5.6.

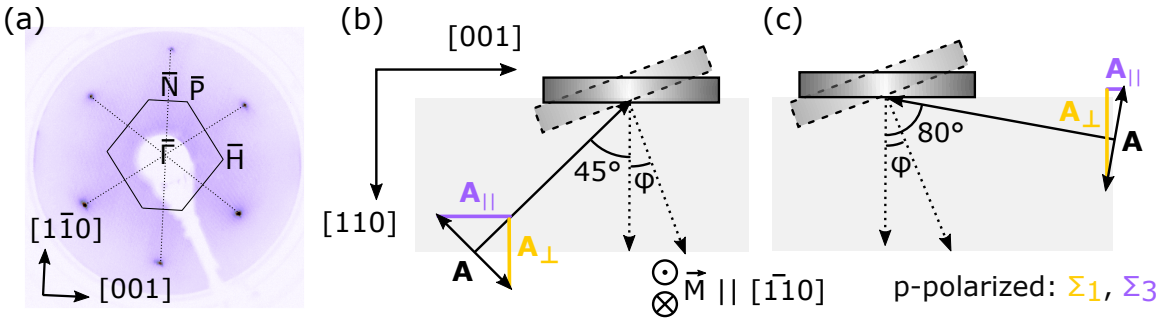

Figure 5.6: (a) LEED pattern of an Fe/W(110) film recorded at 100 eV. The high symmetry points of the surface Brillouin zone are indicated as well as the crystal axes. (b) Measurement geometry in direct photoemission and (c) in two-photon photoemission (2PPE). For angle-resolved measurements, the sample is rotated by an angle φ about the [1$\bar{1}$0] axis, leading to the detection of electrons with a parallel momentum along the $\overline{\Gamma H}$ direction.

The LEED pattern (a) indicates the crystal directions. The surface Brillouin zone has been added with the high symmetry points denoted. The sample is mounted on a manipulator which allows for rotation about the [1$\bar{1}$0] axis. We can thus perform angle-resolved measurements in $\overline{\Gamma H}$ direction.

For Fe films of 15 ML thickness, the easy magnetization axis lies along the [1$\bar{1}$0] direction instead of [100] for bulk Fe. A spin reorientation transition occurs at a certain critical film thickness [Slezak et al., 2013]. This transition appears to depend very much on the preparation conditions. It has been reported to occur in a range from 40 Å for low temperature growth to 140 Å for films grown at elevated temperatures [Gradmann et al., 1986; Przybylski et al., 1987; Albrecht et al., 1992]. At a film thickness of 15 ML, we are far below the reorientation and can thus be sure to have the easy axis in [1$\bar{1}$0] direction.

For the direct photoemission experiments, we used the fourth harmonic generated from the amplified Ti:Sapphire laser described in Chapter 3.2.2. The laser light comes in at an angle of 45° off-normal along the [001] direction (Fig. 5.6(b)). The light is p-polarized and thus contains electric field components parallel to the [001] direction $A_{||}$ and parallel to the [110] direction (perpendicular to the surface $A_{\perp}$) in equal parts.

The 2PPE experiments employ the third harmonic and the fundamental frequency of the Ti:Sapphire oscillator described in Chapter 3.2.1. The experiments are done in nearly grazing incidence (Fig. 5.6(c)). Using an incidence angle of 80° along the [001] direction, we obtain an electric-field vector that is almost purely perpendicular to the surface for p-polarized light. Thus, we mainly excite transitions from Σ_1 into Σ_1 bands and have a very low probability to excite electrons from Σ_3 bands. Using s-polarized light induces transitions from Σ_4 bands exclusively.

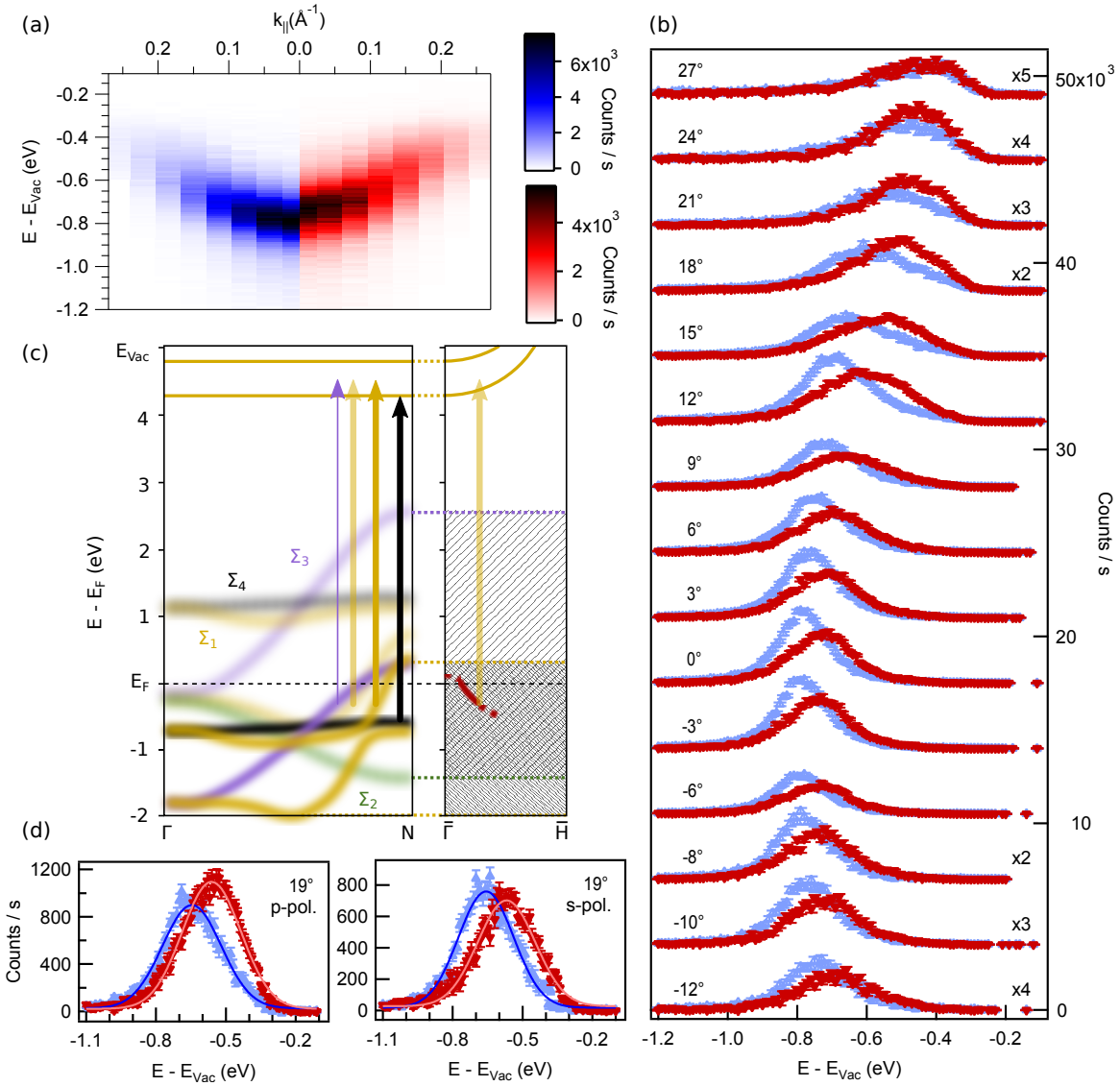

Figure 5.7: Summary of the 2PPE experiment measured with 4.83 eV pump-photon energy and 1.61 eV probe-photon energy at zero pump-probe delay. (a) displays the dispersion of the majority- (blue) and minority-spin (red) $n = 1$ image state in $\overline{\Gamma H}$ direction. (b) shows the corresponding spectra in dependence on the emission angle φ. (c) summarizes the possible excitation processes in a schematic sketch of the band structure. (d) compares two spectra of the $n = 1$ image state excited with p- and s-polarized light. On the left hand of panel (c), the bulk band structure is shown in the direction perpendicular to the surface. The schematic band structure has been drawn in orientation to Ref. [Sánchez-Barriga et al., 2012]. Majority-spin bands are drawn opaque. Minority-spin bands are slightly transparent. The different colors indicate the symmetry of the spatial wave function. On the right hand of panel (c), the bands are projected (strongly simplified) onto the $\overline{\Gamma H}$ direction of momentum $k_{||}$ parallel to the surface. Majority- and minority-spin bands are indicated separately by the differently shaded areas. The parabolic dispersion of the $n = 1$ and $n = 2$ image-potential states is inserted as yellow lines close below the vacuum energy E_{Vac}. An additional surface feature is drawn in red at E_F. The latter will be explained later.

5.3.2 Projecting the Occupied Band Structure onto the Image-Potential States

The outcome of the spin-resolved 2PPE measurements is summarized in Figure 5.7. The spectra shown here, were acquired at zero pump-probe delay using a pump photon-energy of $3h\nu = 4.83\,\mathrm{eV}$ and a probe photon-energy of $h\nu = 1.61\,\mathrm{eV}$. Panel (a) is a false-color plot displaying the energies of the majority- (blue) and minority-spin (red) $n = 1$ image-potential state in dependence on $k_{||}$. The state disperses upwards in a free-electron like parabola. In panel (b) the corresponding spectra are shown in dependence on the emission angle as measured. Panel (c) gives an overview of possible excitation processes and panel (d) shows different spin characters resulting from excitation with p- and s-polarized light.

Since the spin polarization in the 2PPE intensities stems from the occupation in the initial state, a comparison of the majority- and minority-spin intensities in (b) and (d) provides us with the initial-state spin-character. Using p-polarized light for the excitation, we find a strong majority-spin character in the $n = 1$ image-potential state at the $\overline{\Gamma}$ point. At large angles the intensity in the majority-spin component decreases and the minority-spin component becomes dominant. In a spin-integrated 2PPE study Thomann et al. [2000] discovered, that the majority-spin contribution near $\overline{\Gamma}$ upon p-polarized excitation is caused by a Σ_1 majority band (opaque yellow in (c)) crossing the Fermi level E_F near the N point in the perpendicular momentum direction $k_\perp$. The transition is indicated in Figure 5.7(c) by the opaque yellow arrow. The transparent yellow arrow indicates a further possible transition from a Σ_1 minority-spin band. Exciting with p-polarized light at an incidence angle of 80° (*cf.* Fig. 5.6), we also have a small component of the light polarization suitable to excite transitions from the majority-spin Σ_3 band into the image-potential states. This is indicated by the thin violet arrow. The transition from the Σ_3 band contributes even more to the majority-spin character, since the majority-spin part of the Σ_3 band also crosses E_F close to the N point, while the minority-spin part does so near the Γ point, where it has less wave function overlap with the image states. Overall, the majority-spin intensity dominates at $\overline{\Gamma}$.

This situation should in general be the same for other values of $k_{||}$. Nevertheless, we find the dominant minority-spin component when going to off-normal emission angles. This behavior can be explained by the occurrence of an occupied surface resonance of minority-spin character. Since the image-potential states are localized in front of the surface, the spatial overlap of their wave functions is largest with that of surface states. It is thus more probable to excite electrons from surface states into image-potential states rather than from the bulk bands. A resonant transition from an occupied surface state into an image-potential states thus always dominates the 2PPE spectra. As transitions in photoemission occur vertical in the band structure, we can conclude that the minority-spin surface feature does not occur at $\overline{\Gamma}$ but disperses downwards into the region below E_F at higher $k_{||}$.

The excitation by p-polarized light indicates that the minority-spin surface feature must have a Σ_1 or a Σ_3 spatial symmetry. We can verify this by changing the pump light to s polarization. In this case, the transition probability from the majority-spin Σ_4 band (shown in opaque black in Fig. 5.7(c)) to the image states dominates. Figure 5.7(d) shows two spectra at 19° emission angle excited with s- and p-polarized light of the same

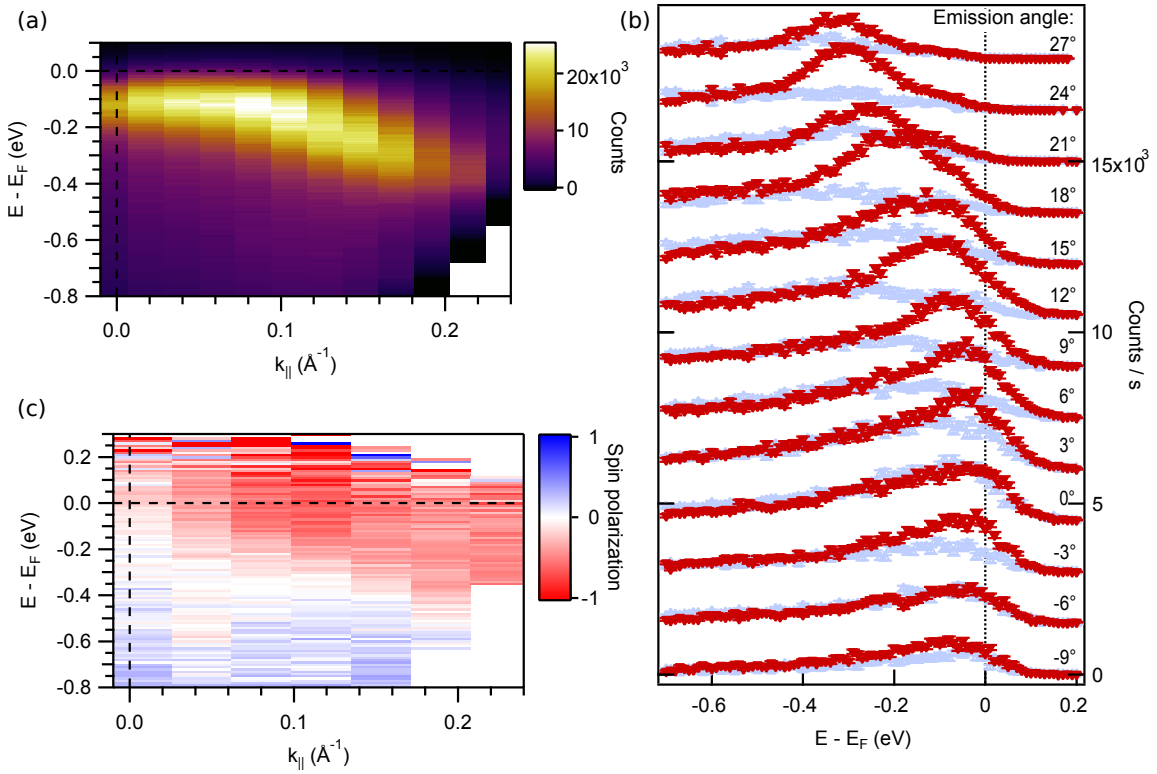

Figure 5.8: Direct photoemission spectra measured with 6.2 eV photon energy along the $\overline{\Gamma H}$ direction. (a) shows spin-integrated spectra of high count rates in dependence of energy and parallel momentum $k_{||}$. (b) shows the corresponding spin-resolved spectra in dependence on emission angle. (c) displays the spin polarization obtained from the spectra in (b) in dependence on energy and $k_{||}$ as well.

photon energy. We find that the minority-spin character vanishes when we use s- instead of p-polarized light for the transition from occupied into unoccupied states. This indicates that the minority-spin surface feature must indeed have a Σ_1 or Σ_3 symmetry in the $\overline{\Gamma H}$ direction. We will investigate its dispersion in the following section.

5.3.3 Direct Photoemission near $\overline{\Gamma}$

An angle-dependent series of direct-photoemission spectra using 6.2 eV photon energy is shown in Figure 5.8. Panel (a) shows a false-color plot of the spin-integrated intensities in dependence on $k_{||}$ along the $\overline{\Gamma H}$ direction. The corresponding spin-resolved spectra are shown in (b) in dependence on the emission angle. For easier comparability to (a), panel (c) shows the spin polarization – as obtained from the spin-resolved measurement in (b) – with the information of angle and kinetic energy again converted to parallel momentum $k_{||}$.

The spectra in (b) show, that the dispersing feature in (a) has a pure minority-spin character. The minority-spin intensity at E_F increases up to an emission angle of 9° (≈

$0.08\,\text{Å}^{-1}$), where the feature disperses below E_F. Tuning to higher values of $k_{||}$, the dispersion shifts the minority-spin peak further down to 300 meV binding energy at $k_{||} = 0.2\,\text{Å}^{-1}$.

All this happens on a non-dispersive and non-spin-polarized background. This can easily be observed when comparing Figure 5.8(a) to (c). We find the strong minority-spin peak with a downward dispersion in the range $0.08 \leq k_{||} \leq 0.2\,\text{Å}^{-1}$. Going to smaller $k_{||}$, at the $\overline{\Gamma}$ point ($k_{||} = 0$), we find a flatly dispersing peak structure, which stems from one or more non-spin-polarized states. In the energy region of this structure ≤ 160 meV below E_F, the formation of quantum well states has been observed for Fe thin films of thicknesses < 24 ML on W(110) [Nuber, 2011]. Although a parabolic dispersion has been found for these quantum well states in $\overline{\Gamma\text{H}}$ direction, at a film thickness of 15 ML, they are not very pronounced and create a rather homogeneous background. In the following, we will regard this feature as background and focus on the second steeply dispersing feature.

The minority-spin feature dispersing downwards along $\overline{\Gamma\text{H}}$ in our Fe(110) thin film explains the minority-spin contribution we also observe for large $k_{||}$ in 2PPE (*cf.* Sec. 5.3.2). Concerning the dipole selection-rules, we find that the wave function of this feature shows the same symmetry characteristics as the minority-spin surface resonance observed by Sánchez-Barriga et al. [2009]. It also occurs close to the $\overline{\Gamma}$ point. Unfortunately, the previous publications address the dispersion along the $\overline{\Gamma\text{N}}$ direction, while our measurement resolves the $\overline{\Gamma\text{H}}$ direction. Nevertheless, the dispersion of the Σ_3 minority band along $\overline{\Gamma\text{H}}$ and $\overline{\Gamma\text{N}}$ is very much alike, so we can assume a similar dispersion of the surface resonance, which is derived from the Σ_3 band. Furthermore, the k range of our measurement is entirely below the value at which the Σ_3 minority band crosses E_F [Schäfer et al., 2005] and where the minority-spin surface resonance disappears in Reference [Sánchez-Barriga et al., 2009]. The dispersion we observe coincides with that predicted by Braun et al. [2002] for the d-derived minority-spin surface resonance SS_2^* (*cf.* Fig. 5.5). We can therefore conclude, that our feature is the minority-spin Σ_3 (d) surface resonance.

Taking a closer look at Figure 5.8(b) and the spin polarization in (c), a weak "shoulder" on the high-energy side of the surface-resonance peak is visible. This "shoulder" gains intensity when the Fe-film is magnetized oppositely. We will investigate this phenomenon in detail in the next chapter.

5.4 Magnetic Linear Dichroism

Figure 5.9 compares the spin-resolved direct photoemission intensities obtained with the sample magnetized parallel and antiparallel to the $[1\bar{1}0]$ direction. For the direction entitled − (left panel), a second peak clearly appears on the low-binding-energy side of the main peak in the minority-spin spectra (red). In + direction (right panel), we also find this peak but with a lower intensity. This leads to a magnetic linear dichroism (MLD) in the spectra.

It is another great advantage of the newly installed exchange-scattering spin detector, that there is no geometric asymmetry in the spin-resolved spectra since the electron's trajectories in the analyzer remain the same for both spin directions. Thus any asymmetries arising when sample and detector are magnetized in the same constellation with respect to each other but differently with respect to the laser polarization must be caused by a

magnetic linear dichroism. While the spin-dependent asymmetry is calculated as introduced in Chapter 3.1.1, the dichroic asymmetries can be distinguished as follows.

The spin-dependent dichroic asymmetry $D^{\uparrow/\downarrow}$ is given by:

$$D^{\uparrow} = \frac{I^{\uparrow\uparrow} - I^{\uparrow\downarrow}}{I^{\uparrow\uparrow} + I^{\uparrow\downarrow}} \tag{5.1}$$

$$D^{\downarrow} = \frac{I^{\downarrow\downarrow} - I^{\downarrow\uparrow}}{I^{\downarrow\downarrow} + I^{\downarrow\uparrow}} \tag{5.2}$$

with $I^{\sigma\mu}$ being the measured intensity for the sample's magnetization direction $\sigma = \uparrow / \downarrow$ and the detector's magnetization direction $\mu = \uparrow / \downarrow$.

To integrate over both spin directions we perform:

$$D = \frac{\sqrt{I^{\uparrow\uparrow} I^{\downarrow\downarrow}} - \sqrt{I^{\uparrow\downarrow} I^{\downarrow\uparrow}}}{\sqrt{I^{\uparrow\uparrow} I^{\downarrow\downarrow}} + \sqrt{I^{\uparrow\downarrow} I^{\downarrow\uparrow}}} \tag{5.3}$$

We calculated D from the spectra shown in Fig. 5.9 and transformed the E-ϕ into an E-$k_{||}$ dependence. The result is shown on the right side of Figure 5.10. The left side compares two minority-spin spectra from Figure 5.9 for 24° emission angle. There is a pronounced change of the sign of the MLD between the main peak (negative asymmetry) and the smaller shoulder (positive asymmetry). This means that upon the change of magnetization not only the intensity of the shoulder increases but also the intensity of the main peak is lowered. It seems as if the magnetization reversal induces a redistribution of intensity from the peak to its high-energy shoulder. The dichroism equally shows up in direct photoemission with 6.2 eV and in the 4.83 eV photoexcitation into the image states in 2PPE as shown in Figure 5.11.[5] In the following, we will discuss possible origins for the observed features and the MLD related to them.

5.4.1 Considering the Well-Known Types of Magnetic Linear Dichroism

We can exclude several sources of dichroism in our measurement. The easiest one to exclude is diffraction dichroism. This kind of magnetic linear dichroism occurs due to interference of emitted electrons due to scattering at different lattice sites. As in our case, the electrons are emitted from a surface state, the probability of this effect is low. Furthermore, diffraction dichroism varies strongly for different emission angles, which is not observed in our case.

Another specific type of dichroism is atomic dichroism. This is caused by the interference of electronic waves created in different transitions that are simultaneously possible. Since we investigate the valence band structure instead of atomic core levels, this type of dichroism transforms to valence-band dichroism as introduced in Chapter 3.3.2. It arises from the interference of photoelectrons from states of different spatial symmetry.

In the case of valence-band dichroism, according to Equation (3.24) our measured intensity would be a mixture of Σ_1 and Σ_3 contributions due to our experimental geometry depicted in Figure 5.6. This is also corroborated by the findings of Sánchez-Barriga et al.

[5] The probe photon energy was 1.61 eV in the 2PPE experiment.

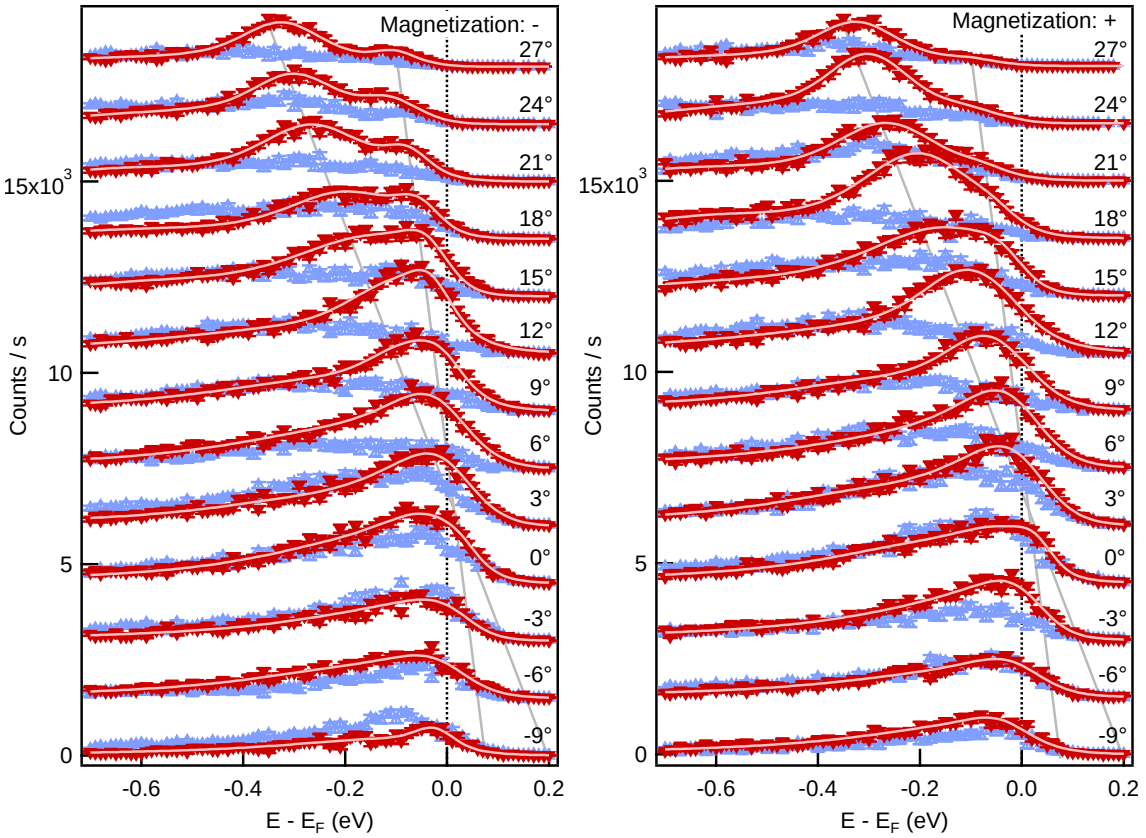

Figure 5.9: Comparison of the spin-resolved photoemission intensities for magnetization directions parallel and antiparallel to the $[1\bar{1}0]$ direction. The spectra shown on the right side (+) are also depicted in Fig. 5.8. They show a weak shoulder on the low-binding-energy side of the minority-spin surface resonance. The feature becomes more prominent on the oppositely magnetized sample (-). The gray lines are a guide to the eye roughly following the dispersion of the two features.

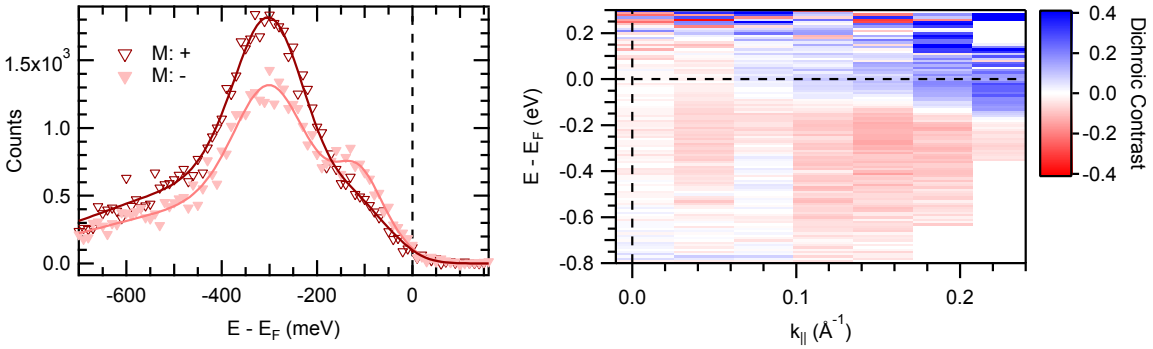

Figure 5.10: Magnetic linear dichroism (MLD) in the minority-spin surface resonance, measured in direct photoemission. Left: Comparison of the minority-spin component of the photoelectron spectra at 24° emission angle for the two antiparallel magnetization directions. Right: MLD calculated from the spectra in Fig. 5.9 using Eq. (5.3).

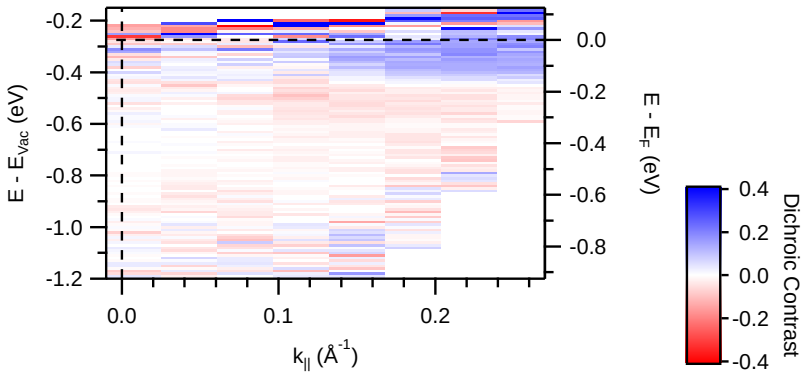

Figure 5.11: Magnetic linear dichroism (MLD) measured in 2PPE. The dichroic contrast is calculated from the spectra shown in Fig. 5.7 using Eq. (5.3).

[2009], who find a $\Sigma_{1,3}$ spatial symmetry for the minority-spin surface resonance. A crossing of a Σ_1 and a Σ_3 minority-spin state wouldn't be allowed, because both bands have the same symmetry in the presence of spin-orbit coupling (*cf.* Eq. (3.23)). The bands would instead hybridize giving rise to a band gap, which is known as hot spot or avoided crossing. A spin-orbit splitting on the order of $\sim 100\,\mathrm{meV}$ would arise between the bands. Such an avoided crossing has been found on Co/Cu(001) exhibiting strong linear magnetic dichroism [Pickel et al., 2008].[6] Although our setup doesn't allow to conveniently resolve a band gap on the order of spin-orbit splitting, the two minority-spin features rather seem to merge instead of splitting up. Nevertheless, we want to discuss possible scenarios of a MLD induced by a spin-orbit hybridization gap in the following paragraphs.

In a mixture of two bands of Σ_1 and Σ_3 symmetry, the photoemitted intensity of the Σ_3 band would decrease and that of the Σ_1 band increase for increasing emission angles. This effect is caused by the rotation of the sample, that is used to realize the angular resolution in our experiment. The rotation changes the light incidence angle and thus also the ratio of parallel and perpendicularly polarized light components. This in turn changes the ratio of photoemitted intensity from Σ_3 and Σ_1 bands. This effect can explain the observed band dispersion, if the flatly dispersing shoulder had Σ_3 symmetry and the steeper dispersing main peak Σ_1 symmetry. Then the maximum of photoemitted intensity would shift from the flatter dispersion at normal emission to the steeper dispersion for large emission angles.

While the observed dispersion can be explained by the changing selection rules for photoemission, the MLD can't. The dichroic asymmetry would change its intensity with variation of the light incidence angle. At an avoided crossing, the spatial symmetry of the bands mixes due to the hybridization. This has been observed to occur on Fe(110) [Rampe et al., 1998]. Thus each of the two features can already generate a dichroic asymmetry on its own [Pickel et al., 2008]. If we observed a transition from predominantly Σ_1 to predominantly Σ_3 character while tuning to larger emission angles, the dichroism would then be stronger in one sign at small angles (caused by the flatly dispersing band of predominantly Σ_1 character) and change towards a dominance of the other sign for large angles (caused by the main peak of predominantly Σ_3 character). In contrast to that, in our spectra the dichroic asymmetry

[6] In Ref. [Pickel et al., 2008] another feature creating MLD is assigned to a minority-spin surface resonance.

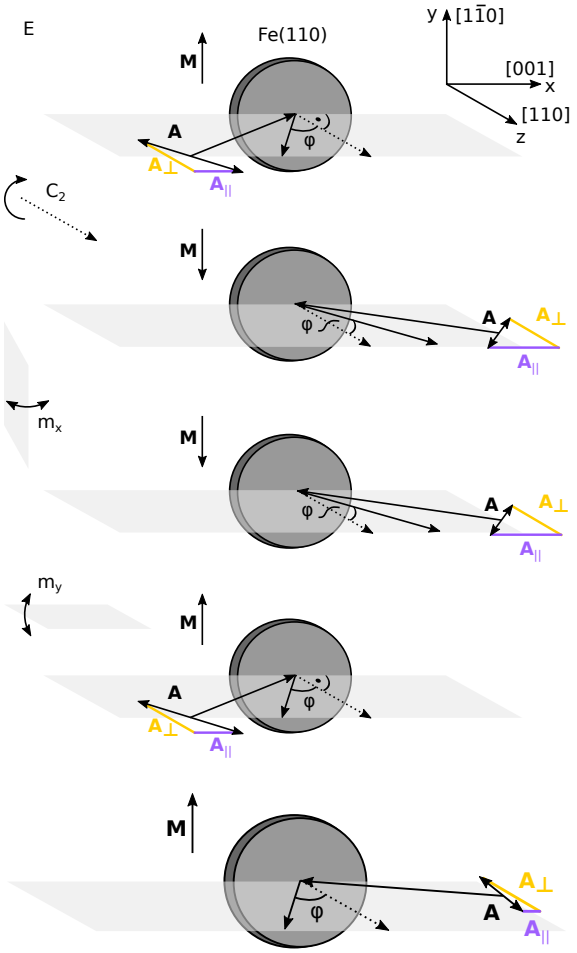

Figure 5.12: Experimental geometry used in the direct photoemission measurements and its transformations in the symmetry group of the Fe(110) surface. The latter is the C_{2v} point group, which is invariant upon rotation by 180° (C_2), the reflection at the y-z plane (m_x), and the reflection at the x-z plane (m_y). The operation E is the identity. All of the operations either reverse the magnetization and the direction of light incidence or keep both. A reversal of the magnetization direction in the experiment without changing the direction of light incidence, can thus give rise to the occurrence of MLD due to the different symmetry situation.

Figure 5.13: Experimental geometry used in 2PPE. Due to the nonzero emission angle, the symmetry differs from the transformations shown in Fig. 5.12 for the measurements performed in direct photoemission.

becomes more intense in both signs for increasing angles, which implies that both states have the same spatial symmetry. Furthermore, we would expect to find the opposite angular dependence in 2PPE, since we use the reverse geometry (*cf.* Fig. 5.6). The light comes in from the opposite direction, while the sample is rotated in the same direction. This leads to an increasing probability for Σ_3 transitions with increasing emission angles, while the probability for Σ_1 transitions decreases. Instead of the opposite angular dependence, we observe the same MLD in direct photoemission and in 2PPE.

In general, we can't exclude the observed dichroism to be induced by the interference of two states of different spatial symmetry or by states, which already have a mixed symmetry character each. Although, we would expect an angular dependence, it might be coincidence that we don't observe much of it. According to symmetry arguments, dichroism is possible in our experimental geometry. Figure 5.12 displays the geometry in direct photoemission and how it is transformed by the C_{2v} symmetry operations, which is the point group of the Fe(110) surface. No transformation can reverse the magnetic field without changing the laser field. This is the common argument for the existence of dichroism. Since we rotate the sample in the same direction in 2PPE, the experiments cannot be transformed into one

another by a C_2 or m_x operation (*cf.* Fig. 5.13). If they could, the dichroic contrast would change sign. In our case, we find the same sign in both geometries, which can't be excluded by the existence of dichroism. Nevertheless, the observed dispersion allows for a different explanation of apparently two states and possibly also for the dichroic contrast as shown in the following section.

5.4.2 Considering Correlation Effects

Apart from the idea of a crossing of two individual states, a much more convincing interpretation of the observed dispersion can be given by an energy renormalization of the main peak by electron-electron correlation or a coupling of the electrons with bosonic excitations as it has already been observed for Fe/W(110). Since the interaction with phonons is the most investigated type of bosonic quasiparticle interactions, we will introduce the effect of phonons on the band structure.

An electron traveling through the lattice interacts with the ion cores via Coulomb interaction. This leads to a deformation of the lattice, which in turn acts back on the electron. The interaction can be described by the continuous emission and reabsorption of phonons[7] leading to slowing down of the electron's velocity and thus to an increased effective mass of the electron. One speaks of a dressing of the electron by a virtual cloud of phonons that the electron carries through the crystal. The difference between the dispersion of the single electron $\epsilon(\mathbf{k})$ and the phonon-dressed electron $E(\mathbf{k})$ is given by the real part of the self energy $\Sigma(E(\mathbf{k}))$:

$$E(\mathbf{k}) = \epsilon(\mathbf{k}) + \mathrm{Re}(\Sigma(E(\mathbf{k}))). \tag{5.4}$$

The imaginary part of the self energy contributes to the linewidth of the spectral function, as introduced in Chapter 3.3.3. Real and imaginary parts can be transformed into each other by the Kramers-Kronig relations. As described in Chapter 3.3.4, the linewidth and thus the imaginary part of $\Sigma(E(\mathbf{k}))$ is given by the Eliashberg function for the interaction. From this we can derive the dependence [Schäfer et al., 2004]:

$$\mathrm{Im}(\Sigma(E(\mathbf{k}))) \propto \lambda \int_0^{\omega} g(\Omega) d\Omega, \tag{5.5}$$

with $g(\omega)$ being the density of states of the bosons, ω corresponds to the energy of the electronic dispersion $E(\mathbf{k}) = \hbar\omega$, and λ is the coupling coefficient[8].

For energies $E(\mathbf{k})$ exceeding the characteristic energy range of the bosons, *i.e.* the Debye energy in the case of phonons, the imaginary part of Σ becomes constant and the real part goes to zero. This leads to a kink in the dispersion as the electron resumes its unperturbed dispersion. Thus, the energy corrections apply close to E_F and become insignificant, when $E - E_\mathrm{F}$ is larger than the maximum phonon energy $\hbar\omega_\mathrm{D}$.

[7] The corresponding quasiparticle is called polaron.

[8] Here we assume that the coupling strength is independent of phonon energy, momentum, and branch.

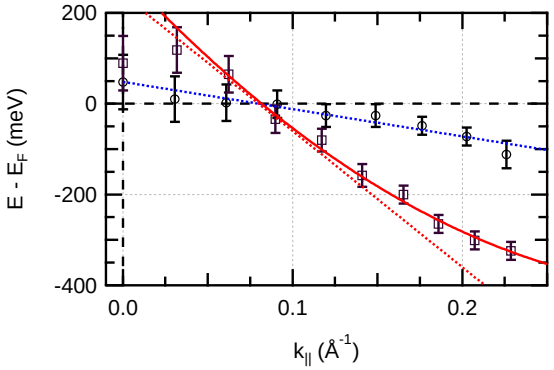

Figure 5.14: Fitted peak energies for the two minority-spin features in the spectra shown in Fig. 5.9. The squares display the dispersion of the main peak, fitted by solid red line. The circles show the dispersion of the smaller shoulder. The dashed lines are tangets visualizing the slope of the dispersions, which corresponds to the Fermi velocity.

The renormalized effective mass m^* and Fermi velocity v^* are then given by:

$$m^* = m_0(1+\lambda) = m_0(1 - \frac{\partial \mathrm{Re}(\Sigma(E(\mathbf{k})))}{\partial \omega}) \tag{5.6}$$

$$\mathbf{v}^* = \frac{\mathbf{v}_0}{1+\lambda}, \tag{5.7}$$

with m_0 and $\mathbf{v}_0$ being the unperturbed effective mass and Fermi velocity, respectively.

In our spectra we find the characteristic dispersion for a renormalization of the electronic self energy by a quasiparticle interaction. The energy positions obtained from a fit to the spectra[9] in Figure 5.9 (pink lines) are shown in Figure 5.14. We find a steep parabolic dispersion of the main peak and a relatively flat almost linear dispersion of the smaller shoulder. The peaks meet exactly at the Fermi level. The energy range of the renormalization coincides not with that of phonons but with that of magnon excitations.

Just like in the dressing of electrons by a virtual cloud of phonons, an electron can also carry a virtual magnon cloud. This concept has already been used by Nolting et al. [1997] to calculate the temperature dependence of the density of states in gadolinium as introduced in Chapter 2.3. Also Schäfer et al. [2004] reported an energy renormalization seen in the two minority-spin surface states of Fe(110), which they assign to electron-magnon interaction.

The dotted lines in Figure 5.14 indicate the slope of the band dispersion at the Fermi level, which is given by the Fermi velocity. The slopes of the main peak (red) and the smaller peak (blue) differ by a factor of five giving rise to a coupling constant of $\lambda = 4.0 \pm 0.8$. This value is slightly larger than renormalizations observed in de-Haas-van-Alphen measurements [Lonzarich, 1984], which range from 0.5 to 2. Other photoemission experiments find renormalizations in the same range for electron-electron correlations [Schäfer et al., 2005; Sánchez-Barriga et al., 2012] but significantly lower coupling constants ($\lambda = 0.20 \pm 0.04$) for electron-magnon interactions [Schäfer et al., 2004]. Compared to Schäfer et al. [2004], the size of λ might be overestimated (by a factor < 2) in our evaluation, because we fit two distinct peaks instead of a single renormalized band. Due to the large angular acceptance of

[9]The spectra for both magnetization directions were fitted simultaneously with the same values for linewidth and peak positions but with different peak amplitudes to account for the dichroism. The fitting function comprises two voigt peaks, one for the main peak and one for the weaker shoulder, a Fermi function, and a broader voigt peak to describe the non-spin-polarized background.

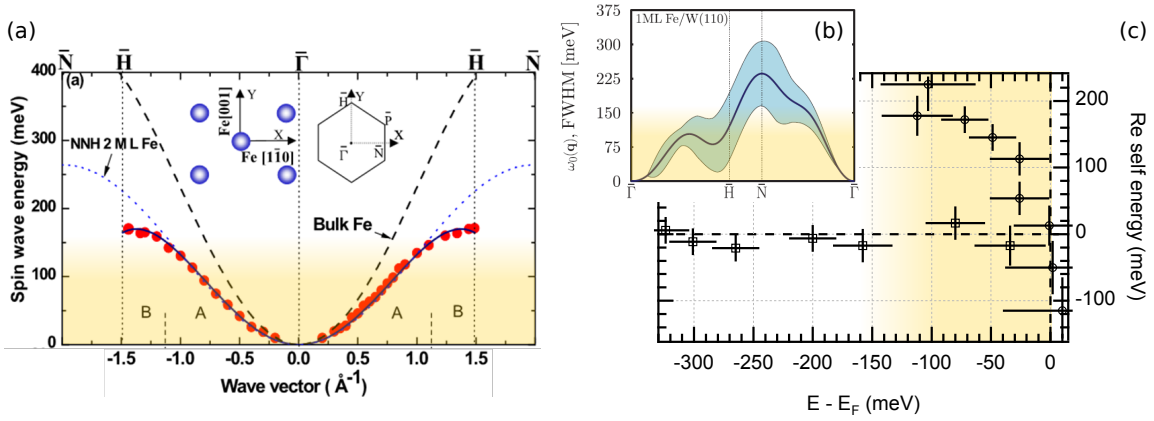

Figure 5.15: Magnon spectrum of Fe/W(110) (panel (a) and (b)) and self energy derived from the fits in Figure 5.14 (panel (c)). (a) shows the magnon dispersion along $\overline{\Gamma}\overline{\mathrm{H}}$ measured in EELS (circles) on a 2 ML-thick Fe film on W(110), reprinted from Ref. [Tang et al., 2007]. The dashed line in (a) is a fit of the dispersion measured for bulk Fe in inelastic neutron scattering (Refs. [Loong et al., 1984; Perring et al., 1991]). The dotted line is a calculation in the nearest neighbor Heisenberg model. (b) is a dispersion calculated in the linear response time dependent density functional theory (LRTDDFT), reprinted from Ref. [Buczek et al., 2011]. The yellow shaded energy range is the one in which we find an energy renormalization. The self energy in (c) has finite values in that range. The energies coincide with that of the magnon dispersion along the $\overline{\Gamma}\overline{\mathrm{H}}$ direction.

$\pm 2.5°$ in our setup, we can assume to detect both the unperturbed and the renormalized peak simultaneously in the whole k range of our measurement. Therefore, we find two peaks in every spectrum. Owing to the angular resolution or not, the appearance of two peaks may further be enhanced by a strong coupling. It has been observed by Lanzara et al. [2001] for strong electron-phonon coupling ($\lambda \approx 2$) that the renormalized and unperturbed peaks both appear in the photoemission spectra.

Figure 5.15(c) displays the values, we derive for the real part of the self energy from the deviation of the fitted peak positions from the parabolic dispersion derived in Figure 5.14. We find that the dispersion is renormalized up to an energy of $E - E_F = -110\,\mathrm{meV}$. Unfortunately, the low photon energies in our experiment do not allow measurements at large $k_{||}$, so we can't follow the dispersion beyond these energies. Nevertheless, the occurrence of the unperturbed peak in all spectra indicates, that the maximum of the renormalized energies will soon be reached. The phonon band structure in Fe has a maximum energy of 30 meV. So the structure, we observe up to binding energies of 110 meV can not be a kink induced by electron-phonon interaction. Figure 5.15(a) and (b) show the magnon dispersion for Fe/W(110). The calculation shown in Figure 5.15(b) predicts that the highest magnon energy is below 300 meV, which is well above our kink structure. So assuming that magnons can contribute to the electronic energy dispersion, the kink we observe may be induced by electron-magnon interaction.

The energy range, in which we find the renormalization (shaded yellow in Fig. 5.15) coincides with that of the renormalization in Reference [Schäfer et al., 2004]. Considering

that the whole magnonic density of states should contribute to the renormalization (*cf.* Eq. (5.5)) and regarding the predicted dispersion for the total k space in Figure 5.15(b), there should be an energy renormalization up to 300 meV.[10] The observed renormalizations in this work and in [Schäfer et al., 2004] rather suggest a k-dependence of the electron-magnon coupling. The renormalization we observe in $\overline{\Gamma H}$ direction coincides nicely with the magnon spectrum in $\overline{\Gamma H}$ direction.

The unforeseen observation in our experiment is the magnetic linear dichroism occurring in line with the renormalized dispersion. There are several reasons, why magnon emission should lead to dichroism. First of all, a magnon being a quasiparticle with explicit dispersion depending on the spatial symmetry directions induces a coupling of the electronic spin to the space and can thus lead to a difference in photoemission intensity for different magnetization directions relative to the incident light. The second even more convincing argument, is that there is already an asymmetry in the dispersion of the magnonic band structure for opposite magnetization directions. This has been predicted by Udvardi and Szunyogh [2009] and observed by Zakeri et al. [2010b], who find a Rashba splitting in the magnon dispersion induced by the asymmetric Dzyaloshinskii-Moriya interaction. This interaction induces an energy difference between magnons of antiparallel momentum or magnetization directions. It also leads to a difference in the magnons' lifetimes [Zakeri, 2014]. This type of interaction might thus as well cause the dichroic effect, we find upon magnetization reversal. Another cause for the MLD could be the formation of steps on the surface. In a recent STM study on the growth of Fe on W(110) steps have been found oriented along the $[1\bar{1}0]$ direction [Schaefer et al., 2016]. Thus, an electron traveling along or against the [001] direction, moves up or down the steps. It has been shown on stepped copper surfaces, that this induces an asymmetry in the lifetime of electrons traveling along these directions [Roth et al., 2003], since there is a higher probability for scattering in the step-upward motion. A mechanism like this could as well lead to an asymmetric coupling of electrons and magnons in opposite magnetization directions.

It is to be noticed that in the 2PPE spectra (Fig. 5.11), the change of sign in the dichroism already appears at an energy of ≈ 160 meV and also remains near this value for the measured $k_{||}$ range. In contrast, in the direct photoemission the MLD seems to appear when the main peak crosses E_F and to follow its dispersion afterwards. The MLD of the positive sign reaches the same energy in both experiments, although in 2PPE, we can access a wider range of $k_{||}$ than in direct photoemission. If the MLD is induced by an electron-magnon interaction, the restriction of the positive MLD asymmetry to energies below 160 meV in 2PPE indicates that this is already the maximum excitation energy for the corresponding magnonic excitations, which nicely agrees with the findings of Schäfer et al. [2004].

5.5 Conclusion

In summary, in our 15 ML-thick Fe films on W(110) we find a minority-spin surface resonance crossing the Fermi level near 0.08 Å^{-1} along the $\overline{\Gamma H}$ direction. We measured the occupied

[10] According to the findings in inelastic neutron scattering experiments, the magnon spectrum in bulk Fe reaches much higher energies as in thin Fe films on W(110) (circles vs. dashed line in Fig. 5.15(a)).

part of this surface resonance in direct photoemission and excited its population into the unoccupied image-potential states in 2PPE.

Although we performed 2PPE measurements with a probe-photon energy ($3h\nu$) high enough to observe direct photoemission at small deviations of the work function, we neither observed the unoccupied region of the minority-spin surface resonance at the $\overline{\Gamma}$ point, nor the upwards-dispersing majority-spin surface resonance SS_2 (*cf.* Fig. 5.5) in 2PPE. Obviously, the pump-photon energy was not sufficient to populate these states. It would be a promising extension of this work, to tune the pump-photon energy to lower values, allowing a resonant transition from the $\Sigma_{1,4}$ majority bands and the $\Sigma_{1,2,3}$ minority bands into the surface resonances. The latter would allow us to measure the different dispersion of the two spin-components of the surface resonance and thus verify the decoupling of majority- and minority-spin band structure.

The minority-spin surface resonance exhibits a strong magnetic linear dichroism (MLD) together with a smaller peak on the low-binding-energy side, which becomes prominent for only one magnetization direction and is only weakly observable when the sample is magnetized in the antiparallel direction. MLD has been observed in photoemission on Fe(110) before, when the intensity comprises several contributions originating from states of different symmetry. In Reference [Rampe et al., 1998], this case occurred at an avoided crossing of two bands having the same symmetry in the total but not in the spatial part of the wave function. In our case, instead of an avoided crossing, the bands rather seem to cross at the Fermi level. Furthermore, we don't find the expected angular dependence of the dichroic asymmetry.

A more suitable explanation for the differently dispersing bands and the positive MLD up to 160 meV below E_F, is the mass renormalization by a quasi-particle interaction. This energy region is that, in which magnon emission has been observed in electron-energy-loss spectroscopy (EELS) [Tang et al., 2007]. Also Schäfer et al. [2004] interpreted kinks found in minority-spin surface states along the $\overline{\Gamma\mathrm{S}}$ and the $\overline{\mathrm{HN}}$ direction, to arise from the electronic dispersion being renormalized by a virtual cloud of magnons. It is thus to be assumed, that the minority-spin surface resonance, we find along the $\overline{\Gamma\mathrm{H}}$ direction, shows a similar mass renormalization.

We find an electron-magnon coupling parameter $\lambda = 4.0 \pm 0.8$. There are several possible explanations for the different strength of the coupling found in our experiment and in the one by Schäfer et al. [2004]. First of all, the experiments were conducted in different crystal directions. Magnons having a k-dependent dispersion may very well interact stronger or weaker with electrons of different momentum direction. Next, there is a large difference in sample preparation between the two experiments. While we investigate 15-ML-thin films annealed to 530 K, Schäfer et al. [2004] grow thick films[11] annealed to 500°C. The variations in band structure already show up in Reference [Schäfer et al., 2005], where the $\Sigma_{3,1}$ minority-spin surface resonance is not observed at all along the $\overline{\Gamma\mathrm{H}}$ direction, where we find it. Thus, a different coupling strength observed in different states on the different samples is not entirely surprising. Furthermore, it has been observed that annealing Fe/W(110) to

[11] A quantitative value for the film thickness in a similar experiment by the same authors is given as > 100 ML in Reference [Schäfer et al., 2005].

more than 600 K leads to the agglomeration of the film into clusters or islands. It is thus possible, that the photoemission signal measured by Schäfer et al. [2004] is an average over several islands of different coupling strength.

Regarding the strong coupling parameter in our spectra, it should be mentioned that there are also photoemission studies on electron-phonon coupling, in which the simultaneous occurrence of a renormalized and an unperturbed dispersion peak has been observed in connection with a strong coupling parameter [Lanzara et al., 2001].

The entirely new observation in this chapter is the MLD occurring along with the dispersion and changing sign between the renormalized and the unperturbed peak. This can be regarded as a further indication for a magnon-induced energy renormalization. Since asymmetries in the magnon spectrum upon magnetization reversal have already been observed in EELS [Zakeri et al., 2010b], the electron-magnon interaction should induce an MLD as well. Otherwise, the phenomenon can be understood as a coupling of the spin direction to the real space induced by the magnon, which leads to a change of the dipole transition-matrix element when the magnetization is reversed with respect to the light field. A full explanation of the magnon-induced MLD requires a thorough examination by many-body theory.

Chapter 6

Spin-Dependent Lifetimes and Exchange Splittings of Surface States on Ni(111)

This chapter is an adaption of the author's work "Spin-Dependent Lifetimes and Exchange Splittings of Surface States on Ni(111)" published in Journal of Physics: Condensed Matter ***27****, 015503 (2015) [II]. Note that part of the data was also presented and discussed by Weiss [2013].*

The exchange splitting of the Ni $3d$ states results in a variety of phenomena interesting for both applications and fundamental science. One example of current interest is the highly spin-polarized tunneling current emitted from a nickel tip [Alvarado and Renaud, 1992], which promises Ni as an efficient material for spin injection. Another observation is a high spin polarization in secondary electron emission from graphene/Ni(111) even under oxygen exposure [Dedkov et al., 2008], which allows for a potential application of the graphene/Ni(111) system in spintronic devices. In Ref. [Dedkov et al., 2008] the microscopic origin of this high spin polarization in secondary electron emission is proposed to be spin-flip scattering between the hot electrons and the $3d$ valence electrons of Ni. However, spin-flip contributions and magnon emission are of low significance to the decay of hot electrons in Ni according to first-principle calculations of Zhukov et al. [2004]. Spin-resolved two-photon-photoemission (2PPE) provides the means to unravel spin-flip and non-spin-flip contributions to electronic scattering as shown in this chapter for the Ni(111) surface.

As already discussed in Chapter 4, the main decay mechanism for excited electrons is inelastic electron-electron scattering whereby the primary electron transfers its energy to a secondary electron-hole pair [Fischer et al., 1990]. Therefore this process is dominated by the occupied and unoccupied electronic states around the Fermi level which closely connects the spin-dependent density of states (DOS) to the lifetime of excited majority and minority spin electrons. To gain a thorough understanding of these scattering processes a detailed knowledge of the spin-split electronic structure around the Fermi level E_F is crucial.

In this chapter, both the electronic structure at E_F and the scattering rates in the

unoccupied image-potential states are investigated. Although the Ni(111) surface has extensively been explored during the last three decades (see Sec. 6.2), the surface electronic band structure is still debated. In direct photoemission, measurements of the surface band structure are often overlayed by bulk band contributions to the photoemission intensity. This can be overcome in 2PPE. Using image-potential states as intermediate states, the probability for excitations from occupied surface states is higher than for bulk states. This is due to the higher probability density at the surface, which results in a large spatial overlap of the surface- and image-state wave-function. The surface sensitivity can thus be increased in 2PPE.

Here, we take advantage of 2PPE to project the occupied part of the surface DOS close below E_{F} onto the intermediate image-potential states [Pickel et al., 2008]. The two-step photoexcitation process allows us to identify the Ni surface states according to their spin character and symmetry. A quick overview of the setup used for this experiment is given in Section 6.1. The surface band structure around E_F is investigated in Section 6.2 in 2PPE. The binding energies and exchange splittings of the image-states are discussed in Section 6.3, where also the spin-dependent decay and dephasing rates of electrons excited into these states are studied.

6.1 Experimental Details

When 2PPE is applied to a ferromagnet, a first laser pump pulse excites electrons from an occupied initial state into an unoccupied intermediate state thereby maintaining the spin polarization of the initial state. For the Ni(111) surface we map the spin polarization of the occupied surface states serving as initial states onto the unoccupied image-potential states serving as intermediate states (illustrated in Fig. 6.1). Using a time-delayed laser probe pulse we can directly access the spin-dependent relaxation times of the excited electrons [Schmidt et al., 2005].

For the 2PPE spectra shown in this chapter, pump and probe pulses were generated by the home-built Ti:Sapphire oscillator, described in Chapter 3.2.1. After excitation by the probe photon (red arrows in Fig. 6.1) the electron trapped in the image potential can overcome the work function Φ of the Ni(111) surface and is photoemitted. For probe we used the laser fundamental ($h\nu$) which was successively tuned from 1.49 to 1.67 eV. The pump pulses were created by frequency tripling the fundamental to $3h\nu = 4.47 - 5.01$ eV. The spin polarization of the photoemitted electrons was detected by the spin-polarized low-energy electron diffraction (SPLEED) detector introduced in Chapter 3.1.1.

During the 2PPE measurements we cooled the sample to a temperature of 90 K with liquid nitrogen. The pressure during data recording was 2×10^{-11} mbar. All spectra were taken for normal electron emission, *i.e.*, at the center of the surface Brillouin zone $\bar{\Gamma}$. Both laser pulses were p-polarized and incident at an angle of 80° off normal along the W[1$\bar{1}$0] direction, corresponding to the Ni[$\overline{11}$2] direction. The advantage of this grazing incidence geometry is that transitions from states of Λ_1 symmetry into the free-electron-like image-potential state [Hermanson, 1977] have the highest probability. While a very small component of the laser field is applicable for transitions from Λ_3 states. Thus we detect

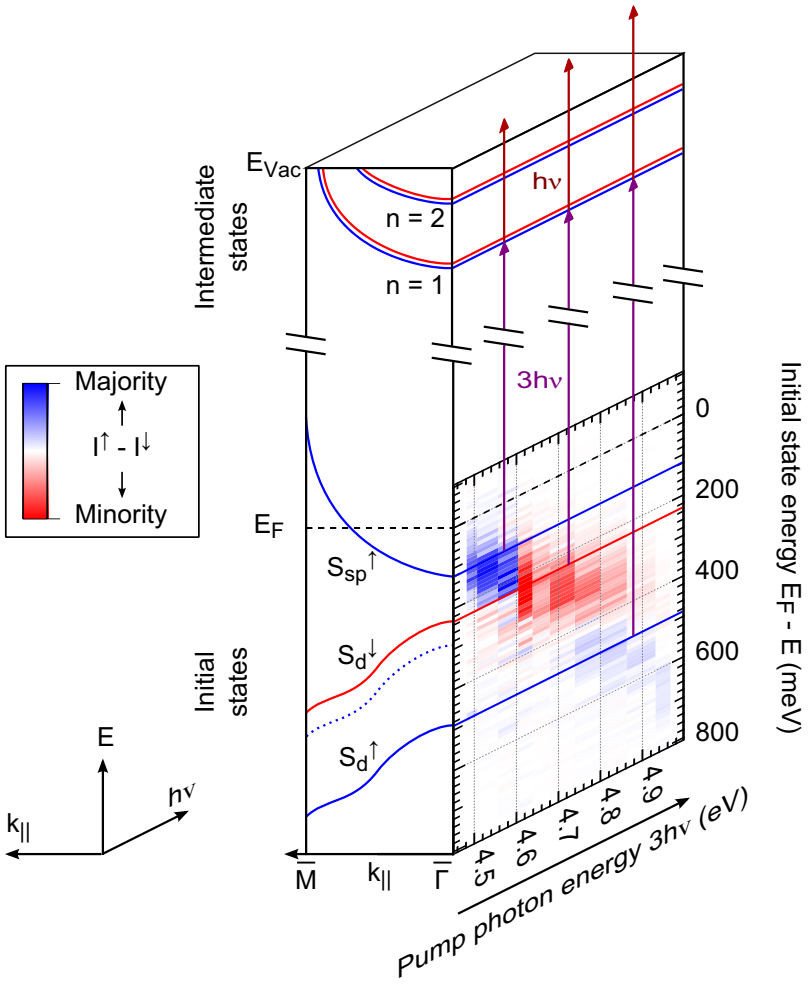

Figure 6.1: Sketch of the 2PPE excitation process for three different pump/probe photon energies, reprinted from Ref. [II]. On the $k_{||}$-E plane (front plane) all states involved in the 2PPE process are displayed in a schematic drawing of the surface band structure. By photon energy variation the $n = 1$ image-potential state is pumped from different initial states ($S^{\uparrow}_{sp}$, $S^{\downarrow}_{d}$, $S^{\uparrow}_{d}$) leading to a varying spin polarization observed in the image-potential state. The intensity difference $I^{\uparrow} - I^{\downarrow}$ between the majority and minority spin spectra (from Fig. 6.2) is shown on the E-$h\nu$ plane (right-hand side) on the energy scale of the initial states. Positive (majority) values are colored in blue, negative (minority) values in red.

the spin polarization of the Λ_1-symmetric surface states close below E_F with hardly any background from the overlapping Λ_3 bulk bands.

The Ni films were magnetized remanently in plane along the Ni[1$\bar{1}$0] direction applying a field pulse of 20 mT via a freestanding coil.

No bias was applied to the samples during the measurements.

6.1.1 Sample Preparation

For the investigations in this chapter thin nickel films from 7 to 14 monolayers (ML) were deposited onto the W(110) substrate using the EFM3 UHV evaporator at an operating pressure of 2×10^{-10} mbar (*cf.* Sec. 3.4). It turned out that from all samples investigated in this thesis, the nickel films were the most sensitive[1] to carbon impurities in the W(110) substrate. It was therefore necessary to develop the careful cleaning procedure described in Section 3.4.1 to be able to perform spin-resolved measurements. We started evaporating Ni at a substrate temperature of 573 K, while the tungsten crystal was cooling down from a 2200 K flash. For the remaining evaporation process the substrate was kept at a temperature of 443 K. To obtain a smooth and contaminant-free surface, the Ni films were annealed for 3 minutes at 573 K after moving to the measurement position. The surface structure of the W(110) substrate and the evaporated Ni(111) film was controlled by LEED. The Ni film-thickness was determined subsequently to the 2PPE measurements by thermal desorption spectroscopy (TPD). Figure 3.16 shows a thickness-dependent series of TPD spectra of Ni films, which we performed for calibration.

Since we deposit our Ni thin films at higher temperatures than in Ref. [Nuber, 2011] to improve the surface quality, it is reasonable that the W/Ni interface is roughened which suppresses the formation of QWS. That is why in the following we conclude that all our observed features are characteristic for the surface of a Ni(111) bulk crystal.

6.2 Surface States near the Fermi Level

During the last three decades the band structure of the Ni(111) surface has been calculated[2] and investigated by means of photoemission[3], inverse photoemission [Donath et al., 1993] and scanning tunneling spectroscopy[4]. The close-packed surface exhibits the well-known Shockley surface state. Its spin splitting and position with respect to the Fermi energy E_F are still subject of controversy. At the center of the Brillouin zone Γ the Shockley surface state was found to be either occupied in both spin components [Braun and Rieder, 2008]

[1] The nickel films grown on a carbon-contaminated tungsten substrate, formed small domains showing no measurable spin polarization and thus no macroscopic magnetization. This already occurred for small amounts of carbon hardly detectable in LEED.

[2] Theoretical studies on the band structure of Ni(111) are contained in References [Dzemiantsova et al., 2011; Lobo-Checa et al., 2008; Borstel et al., 1985; Ohwaki et al., 2006; Braun and Donath, 2002].

[3] Photoemission studies on Ni(111) can be found in the following references [Kutzner et al., 1997; Higashiguchi et al., 2007; Nishimura et al., 2009; Kämper et al., 1988; Rhie et al., 2003].

[4] Scanning-tunneling spectroscopy studies on Ni(111) have been published in the following references [Dzemiantsova et al., 2011; Nishimura et al., 2009; Braun and Rieder, 2008].

or occupied in the majority component and unoccupied in the minority channel [Braun and Donath, 2002; Nishimura et al., 2009; Krönlein et al., 2014] or even unoccupied in both spin parts [Dzemiantsova et al., 2011]. A second surface resonance of d-character was predicted in surface-band-structure calculations [Braun and Donath, 2002] and was observed in the majority of photoemission experiments [Kutzner et al., 1997; Himpsel and Eastman, 1978]. Recently even a third surface resonance was found by Lobo-Checa et al. [2008] with an exchange splitting quantified one year later by Okuda et al. [2009]. In addition, for 1 to 21 monolayer (ML) thick Ni(111) films on W(110) angle-resolved photoemission spectroscopy shows quantum-well states (QWS) close below the Fermi level [Nuber, 2011]. Nevertheless, in our measurements we neither observe QWS signatures in photon-energy-dependent measurements nor a QWS influence to the lifetimes of laser-excited electrons.

By tuning the photon energy $3h\nu$ of the pump pulse we select different initial states from below the Fermi level E_F to populate the unoccupied $n = 1$ image-potential state. Figure 6.1 illustrates the excitation scheme for three different photon energies $3h\nu$ suitable for exitations from the three states $S_{sp}^{\uparrow}$, $S_d^{\downarrow}$ and $S_d^{\uparrow}$. Since the spin is conserved in the optical dipole transitions, the spin character of the initial state determines the spin polarization of the 2PPE final state.

Figure 6.2 displays a series of 2PPE spectra taken at increasing pump photon energies (on a type B sample, see Sec. 6.3.1). Minority and majority spin channels are shown in the left and right panels, respectively. Referencing the 2PPE data to E_F, the initial state energy is fixed in this representation while the intermediate image-potential state shifts with the pump photon-energy variation $\Delta 3h\nu$. As initial states we find the three distinct surface state components, that are shown in the front plane of Fig. 6.1. One can be identified as the occupied part of the Shockley surface state S_{sp} (in Refs. [Lobo-Checa et al., 2008; Ohwaki et al., 2006; Okuda et al., 2009] referred to as S_1) which is discussed in Sec. 6.2.2. The other two belong to d-derived surface resonances S_d (S_2 in Refs. [Lobo-Checa et al., 2008; Ohwaki et al., 2006; Okuda et al., 2009]) as discussed in the following.

6.2.1 d-derived Surface Resonances

Surface-state electrons compared to electrons in bulk states are more likely to be laser-excited into the image potential since both, surface and image-potential states have a high probability density at the surface and thus large spatial overlap. This shows up in a significantly higher 2PPE intensity if the photon energy is resonant to the energy difference between an occupied surface and the image-potential state. Such a resonance is visible in the minority-spin spectra in Figure 6.2 at 4.62 eV pump photon energy (left panel). In addition at lower photon energies the peaks show a clearly asymmetric line shape. This is the manifestation of an initial surface state with significant spectral weight contributing to the 2PPE intensity besides the intermediate image-potential-state peak. Accounting for this we fitted the spectra using the superposition of two Voigt profiles representing the initial and intermediate state contributions to the 2PPE signal. We obtained the best fit results when fixing the initial-state binding energy at 230 meV, the energetic position of a spin-split d-derived minority surface state $S_d^{\downarrow}$ [Okuda et al., 2009]. This state has also been found

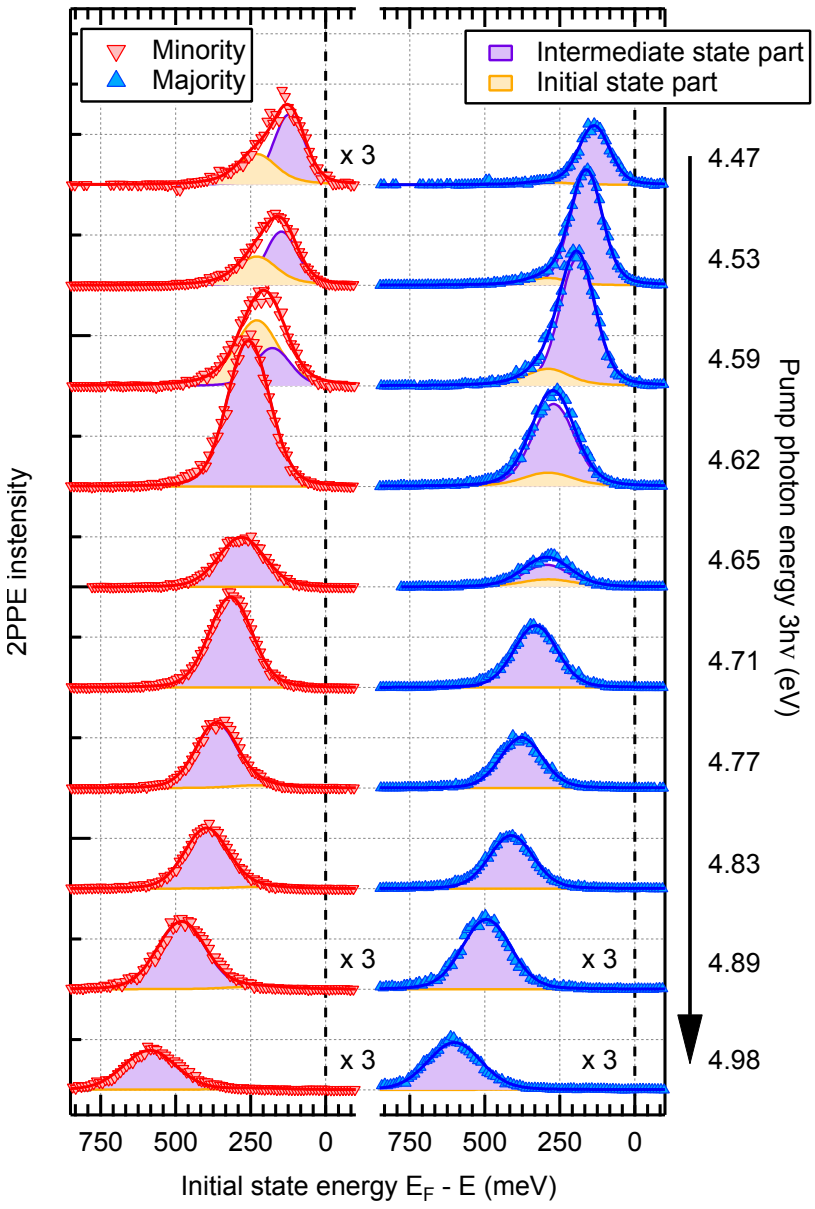

Figure 6.2: 2PPE spectra for minority and majority spins (left and right panels) of a 7 ML Ni/W(110) film (on a type B sample, see Sec. 6.3.1), reprinted from Ref. [II]. The photon energy of the $3h\nu$ pump pulse increases from 4.47 to 4.98 eV. Spectra are recorded in normal emission for zero time delay between pump and probe pulses at a sample temperature of 90 K. The spectra have been fitted (solid lines) using a combination of two Voigt profiles accounting for the initial (solid, light yellow) and intermediate (solid, purple) state contribution to the 2PPE signal.

at 230 meV in spin-integrated 1PPE and 2PPE [Kutzner et al., 1997] measurements. The asymmetry vanishes when going to photon energies higher than the resonance and only the intermediate-state peak remains. Such a behavior is not unusual in 2PPE. It has also been observed on Si(001) and explained by a Fano resonance due to the interference of bulk and surface transitions [Eickhoff et al., 2011].

In Ref. [Okuda et al., 2009] a surface contribution in the majority spin channel of spin-resolved photoemission was found at 289 ± 4 meV and identified as the majority counterpart $S_d^{\uparrow}$ of this d-derived surface state. At this energy we fixed a majority feature in our fits to account for the asymmetric line shape of the majority spin spectra at low photon energies (see Fig. 6.2 right panel). An explanation for the lower intensity of $S_d^{\uparrow}$ as compared to $S_d^{\downarrow}$ is given by DFT [Lobo-Checa et al., 2008] and Green's function calculations [Ohwaki et al., 2006], which predict that the majority component of this d-derived surface state does not contribute to the electronic spectral weight. In contradiction to this assignment the exchange splitting of the d-derived surface resonance is significantly larger according to Refs. [Lobo-Checa et al., 2008; Ohwaki et al., 2006]. They assign a binding energy of around 500 meV to the majority component. Figure 6.1 shows the intensity difference $I^{\uparrow} - I^{\downarrow}$ between minority and majority spin channels extracted from the spectra in Figure 6.2. This reveals a majority-spin intensity rising from 500 meV towards higher binding energies. We can rule out that this feature stems from the exchange split bulk band of Λ_3 symmetry existing in this energy region because of two reasons. First, as mentioned above in Sec. 6.1, using p-polarized light at an incidence angle of 80°, we have a very low transition probability from Λ_3 bulk bands into the Λ_1-symmetric image-potential state. Second, we do not observe a reversal of the spin polarization between 526 ± 2 meV where the minority part is situated [Okuda et al., 2009] and 694 ± 6 meV which is the binding energy of the majority part. Thus we find two majority-spin surface resonances of which one likely constitutes the majority-spin $S_d^{\uparrow}$ partner of the exchange-split d-like surface resonance: A weak majority-spin surface resonance at 289 meV and a second, broad majority-spin surface resonance at around 500 meV (indicated by dashed and solid blue lines in Fig. 6.1, front plane). From our observations we can not distinguish which of these two features is the $S_d^{\uparrow}$.

6.2.2 Shockley Surface State

Lowering the photon energy from $3h\nu = 4.98$ eV to 4.47 eV, *i.e.*, probing initial states closer to E_F, the spin polarization changes from majority to minority and back to majority (see Fig. 6.1). The first reversal at a photon energy of 4.80 eV is caused by a resonance between the dominant minority surface d-resonance and the image-potential state. We assign the second transition at 4.60 eV to a nearing resonance with the majority part of the spin-split Shockley surface state $S_{sp}^{\uparrow}$. The strong majority character close to E_F (see also the spin polarization of the $n = 2$ image-potential state in Fig. 6.5) confirms that the minority component is situated at higher energies above E_F and is thus completely unoccupied corroborating the results of Refs. [Braun and Donath, 2002; Nishimura et al., 2009; Krönlein et al., 2014].

From the rising majority spin polarization in our low-photon-energy spectra we can estimate an energy position $E_\mathrm{F} - E \leq 150$ meV. This value is in between the known results

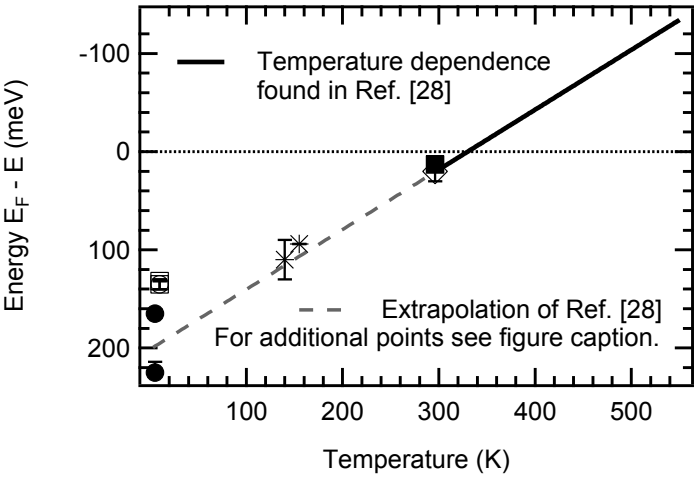

Figure 6.3: Temperature dependence of the majority component of the Shockley surface state, reprinted from Ref. [II]. The solid black line shows the behavior found in Ref. [Auwärter, 2003], the dashed grey line is an extrapolation to lower temperatures that matches the previously known values. Single data points are taken from Refs. [Okuda et al., 2009] (■), [Lobo-Checa et al., 2008] (⋄), [Kutzner et al., 1997] (∗), [Higashiguchi et al., 2007] (○), [Nishimura et al., 2009] (□) and [Braun and Rieder, 2008] (●).

ranging from 94 meV [Kutzner et al., 1997] to 225 meV [Braun and Rieder, 2008] below E_F. To unify the various results, we need to remember that the binding energy of the Shockley surface state on Ni(111) is, as on the noble metal surfaces, strongly temperature-dependent. A shift of 0.61 ± 0.1 meV/K has been observed [Auwärter, 2003] for increasing temperature from 300 K to the Curie temperature of $T_C = 631$ K. As compiled in Figure 6.3 the diversity of known binding energies can be brought onto a line according to this temperature dependence even for temperatures below 300 K [Lobo-Checa et al., 2008; Kutzner et al., 1997; Higashiguchi et al., 2007; Nishimura et al., 2009; Braun and Rieder, 2008; Okuda et al., 2009]. Measured at a temperature of ≈ 90 K the binding energy we find is in accordance with the temperature dependent shift.

6.3 Surface States near the Vacuum Level

The Rydberg-like series of unoccupied image-potential states close below the vacuum energy has been resolved on Ni(111) first by Fischer *et al.* [Fischer et al., 1990] in a 2PPE experiment. An exchange splitting of 18.2 ± 2.5 meV was deduced for the first image-potential state (quantum number $n = 1$) by spin-resolved inverse photoemission (IPE) [Passek and Donath, 1992]. As the binding energy of image-potential states refers to the vacuum level E_{vac}, it is necessary to know the sample work-function to establish their binding energies.

6.3.1 Work Function of Ni(111) Thin Films on W(110)

The work function is derived from the low-energy cutoff in the 2PPE spectrum at normal emission. A distinct low-energy cutoff in the Ni(111) 2PPE spectra can be observed at high photon energies (see Fig. 6.4) stemming from thermally and optically excited electrons above E_F. We deduce two different work functions from this cutoff for Ni films of equal thickness depending on the temperature ramp during annealing: For a ramp rate of 2 K/s (referenced in the following as sample type A) we obtain $\Phi_A = 5.27 \pm 0.03$ eV while for higher ramp rates (sample type B) we find $\Phi_B = 5.11 \pm 0.03$ eV. Both values are close to the work function of

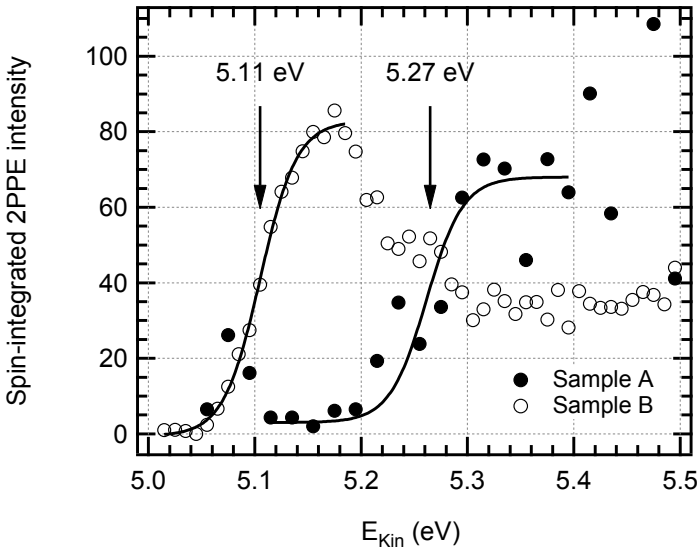

Figure 6.4: The secondary cutoff for type A and type B samples is observed at different kinetic energies, reprinted from Ref. [II]. This difference shows a reduction in the samples work function from $\Phi_A = 5.27 \pm 0.03\,\text{eV}$ to $\Phi_B = 5.11 \pm 0.03\,\text{eV}$ depending on the temperature ramp rate during annealing which is 2 K/s for type A and $> 2\,\text{K/s}$ for type B. The spectrum shown here representative for type A samples has been collected at $3h\nu = 5.01\,\text{eV}$, the type B spectrum at $3h\nu = 4.96\,\text{eV}$. Both samples had a thickness of 7 ML as controlled by TDS.

$\approx 5.22\,\text{eV}$ reported for Ni(111) single crystal surfaces [Fischer et al., 1990; Kutzner et al., 1997; Himpsel and Eastman, 1978; Link et al., 2001].

An explanation for the two different work functions is the well-known Smolouchowski effect [Smoluchowski, 1941]. We expect the Ni films annealed at a faster temperature ramp to show higher surface roughness, *i.e.*, an increased step density than those annealed slower. This increased step density can lead to the lowered work function Φ_B. Additionally, electrons emitted from lower terraces between higher islands can lead to the observation of a lower cutoff at a nominal thickness of 7 ML, since thinner Ni/W(110) films exhibit smaller work functions [Leung et al., 2003; Wortelen, 2011].

6.3.2 Binding Energies of the Image-Potential States

The binding energies of the image-potential states relative to E_{vac} do not change from type A to type B samples. Figure 6.5 shows a spin-resolved 2PPE spectrum recorded on a type A sample at $h\nu = 1.67\,\text{eV}$ and $3h\nu = 5.01\,\text{eV}$. The high photon energy allows to excite both, the exchange-split $n = 1$ and $n = 2$ image-potential states close to E_{vac}. The low intensity of the $n = 2$ compared to the $n = 1$ image-potential state indicates that the former is populated from initial states with very low electron occupation, *i.e.*, thermally excited electrons close above E_F. However, the positive spin polarization of the $n = 2$ image-potential state confirms the majority spin character of the initial Shockley state around E_F.

Binding energies and exchange splittings of the image-potential states are summarized in Table 6.1. From the fits in Figs. 6.2 and 6.5 we extract an exchange splitting of $\Delta E_1^{\uparrow\downarrow} = 14 \pm 3\,\text{meV}$ for the $n = 1$ image-potential state, which is very close to what we would expect from the following consideration: The energy of the image-potential states depends on the position of the *sp*-derived band-gap edges [Fauster and Steinmann, 1995]. Thus the exchange-split valence bands induce the exchange splitting of the image-potential states, which therefore is expected to scale with their bulk penetration. We calculated

Table 6.1: Binding energy $E - E_{\mathrm{vac}}$ and exchange splitting of the $n = 1$ and 2 image-potential states on the Ni(111) surface, reprinted from Ref. [II]. For the values measured by spin-resolved IPE (srIPE) we assume the most frequently observed work function of 5.25 eV. All previously derived energies were determined for Ni(111) single crystals.

n	$E_\uparrow$ (meV)	$E_\downarrow$ (meV)	$\Delta E_{\uparrow/\downarrow}(meV)$	Reference
1	736 ± 2	722 ± 2	14 ± 3	This work
	686.0 ± 1.8	667.8 ± 1.8	18.2 ± 2.5	srIPE [Passek and Donath, 1992]
	770 ± 30			2PPE [Link et al., 2001]
2	183 ± 15	171 ± 17	12 ± 12	This work
	250 ± 50			2PPE [Schuppler et al., 1990]
	270 ± 30			2PPE [Steinmann, 1989]

a bulk penetration of 5.7 % in a 1D-model of the image potential using the Ni band gap edges [Braun and Donath, 2002] for solving a two-band model of the bulk band-structure as described in Ref. [Fauster and Steinmann, 1995]. Given that at the Ni(111) surface only 5.7 % of the probability density of the $n = 1$ image-potential state reside within the crystal and that the valence bands of Ni are exchange split by about 300 meV [Braun et al., 1992] we estimate the $n = 1$ exchange splitting to 16 meV. This agrees well with the experimentally determined value.

Due to our low intensities in the $n = 2$ image-potential state we can only roughly estimate the exchange splitting to $\Delta E_2^{\uparrow\downarrow} = 12 \pm 12$ meV. Since $\Delta E_2^{\uparrow\downarrow}$ also scales with the bulk penetration ($\propto n^3$) it is expected to be smaller than $\Delta E_1^{\uparrow\downarrow}$ by a factor of 8. This scaling has been observed for 3 ML Fe on Cu(100) [Weinelt et al., 2007].

6.3.3 Lifetimes

Performing time-resolved 2PPE measurements with the electron analyzer tuned to the kinetic energy of the majority and minority $n = 1$ image-potential state, we can deduce the spin-dependent lifetimes of electrons excited to this state. The top part of Figure 6.6 shows such spin- and time-resolved 2PPE traces of the $n = 1$ image-potential states on a type A and a type B sample. For comparison, the cross correlation determined in parallel by 2PPE measurements of the occupied Shockley surface state on Cu(111) [Weinelt, 2002] is also shown. The temporal evolution of the $n = 1$ image-potential-state population on Ni(111) is identical to the shape of the cross correlation. This indicates that the lifetimes are small compared to the 110 fs full width at half maximum of the cross correlation. Nevertheless we observe a shift between the cross correlation measured on Cu(111) and the majority and minority image-potential-state signals of Ni(111) which is indicated in Figure 6.6 by the blue and red vertical lines offset with respect to the dashed line at zero pump-probe delay. It has been shown that this shift resembles the lifetime for systems with fast electronic decay measured with comparatively long laser pulses [Wolf, 1997].

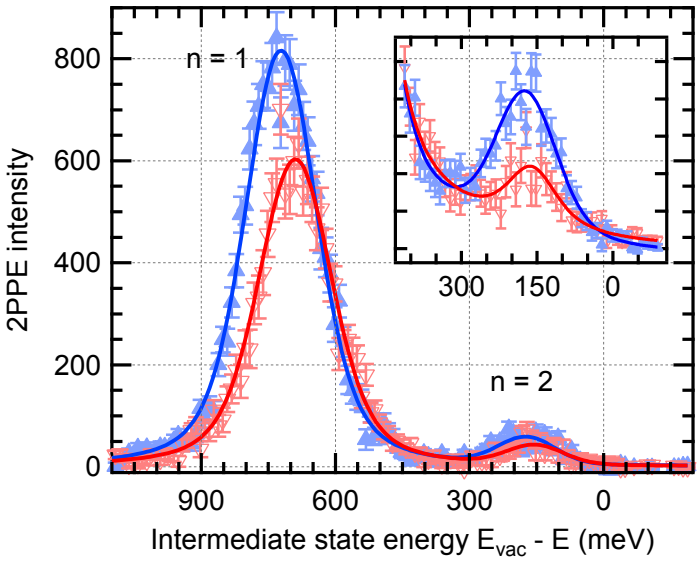

Figure 6.5: 2PPE spectrum of the $n = 1$ and $n = 2$ image-potential states at zero pump-probe delay, reprinted from Ref. [II]. The high photon energy ($3h\nu = 5.01\,\mathrm{eV}$) allows to populate the $n = 2$ image-potential state with electrons excited close above E_F. This leads to the significantly lower intensity compared to the $n = 1$ image-potential state populated from $S_d^\uparrow$.

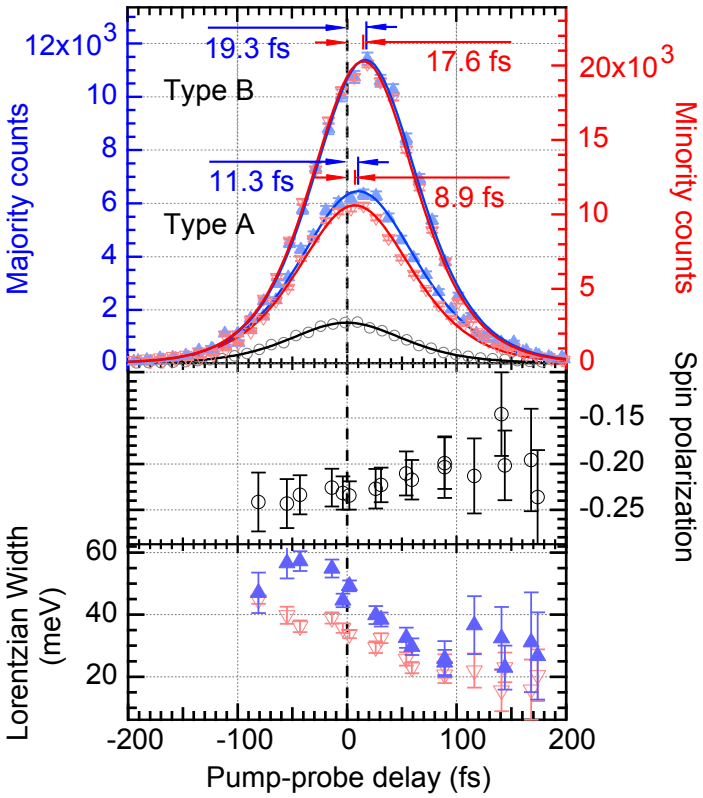

Figure 6.6: Top: Time- and spin-resolved measurement taken with the electron analyzer-energy tuned to the peak maximum of the majority and minority spin component of the $n = 1$ image-potential state. The two time-resolved traces stem from samples A and B and show distinct shifts with respect to delay zero. Up (blue) and down (red) triangles show the majority and minority spin contribution to the 2PPE intensity. The cross correlation is shown in black according to the majority intensity scale. The middle and bottom panels show the temporal evolution of the spin polarization and of the linewidth of the $n = 1$ image-potential states of the type A sample, respectively. All spectra were taken at a pump-photon energy of $3h\nu = 4.71\,\mathrm{eV}$. The figure is reprinted from Ref. [II]

Unlike the image-potential-state binding energies, their lifetimes do show a dependence on the annealing procedure. The lifetimes and spin asymmetries we determined for the two sample types are summarized in Table 6.2. The lifetimes found on the higher-work-function samples (type A) match the value of 7 ± 3 fs found in non-spin-resolved 2PPE [Link et al., 2001]. The lower-work-function (type B) samples show larger lifetimes. At first glance this is surprising, since scattering at defects is known to lead to a decrease of the image-potential-state lifetimes [Boger2004]. The increase of lifetime indicates a loss of decay channels.

In the relaxation process the unoccupied final states are populated by the image-potential-state electron and by the generation of a secondary electron-hole pair conserving energy and momentum. The Shockley surface state serves as prominent final state in electron-electron scattering due to the preferred large energy and small momentum transfer in inelastic electron-electron scattering [Chulkov et al., 1998]. Therefore we attribute the longer lifetimes to a partial quenching of the surface state near E_{F}.

A surface-quality-dependent change in the $n = 1$ image-potential-state lifetime has been observed before by Link et al. [2001]. They reported an increase in lifetime upon hydrogen adsorption accompanied by a quenching of the Shockley surface state. Fischer et al. [1990] observed the same effect in a decrease in linewidth of the $n = 1$ image-potential state. These observations corroborate that the Shockley surface state serves as a major decay channel for the electrons excited into the image-potential state. Note that in our measurements the increase of the lifetime from type A to type B samples is about 40 % of the type B lifetime, which resembles the contribution of the Shockley state to the $n = 1$ image-potential-state decay-rate calculated for the Cu(111) surface by Chulkov et al. [1998].

There is a small spin asymmetry in the lifetimes that is corroborated by the temporal evolution of the spin polarization shown in the mid part of Figure 6.6. The spin polarization is negative meaning that the initial state population excited to the image-potential state has minority spin character. With increasing pump-probe delay the polarization decreases by 20 % reflecting that the minority spin population is decaying faster than that of the majority spin electrons. The $n = 1$ image-potential-state lifetime-asymmetry $\tau^{\uparrow}/\tau^{\downarrow} = 1.27$ on Ni(111) is lower than on Fe (1.45) and Co (1.6) thin films on Cu(001) [Weinelt et al., 2007]. This supports the trend that has been predicted by Grechnev et al. [2007] for bulk states with slightly lower energies above the Fermi level. A recent calculation of hot electron lifetimes by Kaltenborn and Schneider [2014], which includes spin-orbit coupling and thus spin-mixing in the band structure, finds a different order for $\tau^{\uparrow}/\tau^{\downarrow}$ (Fe < Co < Ni).

With increasing lifetime from sample type A to sample type B the lifetime asymmetry decreases. This can also be attributed to a partial quenching of the Shockley surface state, which is completely unoccupied in the minority but partly occupied in the majority spin channel. Therefore it constitutes an additional spin-dependent decay channel, which is of importance due to the large spatial overlap of image-potential and Shockley surface state.

All literature values stem from measurements on single crystal surfaces [Fischer et al., 1990; Link et al., 2001]. As mentioned before in Sec. 6.1.1, in thin nickel films deposited on W(110) the formation of QWS is possible as has been observed by Nuber [2011]. These interface states could provide additional decay channels for the image-potential-state electrons.

Table 6.2: Comparison of work function, lifetimes and spin asymmetries of the $n = 1$ image-potential state for samples A and B, reprinted from Ref. [II].

Sample type	Work function (eV)	$\tau_{\uparrow}(fs)$	$\tau_{\downarrow}(fs)$	$\tau_{\uparrow/\downarrow}$
A	5.27 ± 0.03	11.3 ± 0.3	8.9 ± 0.5	1.27 ± 0.06
B	5.11 ± 0.03	19.3 ± 2.6	17.6 ± 2.5	1.10 ± 0.20

Despite the fact that the number of quantum-well states around the Fermi level is found to increase with the number of Ni layers, we have not observed any dependence of the image-potential-state lifetimes on the film thickness in the range from 7 to 14 ML. This corroborates our findings that the electronic structure of our films is characteristic for the Ni(111) surface and does not exhibit QWS.

6.3.4 Linewidths

The linewidths measured in 2PPE provide additional information about quasi-elastic scattering processes [Boger et al., 2002]. In 2PPE the laser field induces a superposition of electronic states. Scattering processes with an energy transfer lower than the experimental resolution (quasi-elastic) do not contribute to the electronic relaxation process but lead to a dephasing of this superposition, *i.e.*, the polarization. This results in a broadening of the spectral linewidth. A spin asymmetry in dephasing rates can be caused by electron-magnon scattering as it has been shown for 3 ML Fe/Cu(001) [Schmidt et al., 2005]. Here spin-wave emission leads to an additional linewidth broadening of the $n = 1$ minority image-potential state.

The lower part of Figure 6.6 shows the temporal evolution of the Lorentzian linewidth of the $n = 1$ image-potential state. The pure dephasing rate gives a constant offset to the linewidth. It can be observed at large positive pump-probe delays. For negative pump-probe delays the linewidth increases due to the decreasing overlap of the $h\nu$ probe and $3h\nu$ pump pulse as seen in Figure 6.6. Besides the laser pulse-widths an additional broadening may occur caused by a contribution of a particular initial state. We interpret the different linewidth for majority and minority $n = 1$ image-potential states at negative delay as an effect induced by different initial states for the two spin directions (see Fig. 6.2).

In the region of zero pump-probe delay where initial and image-potential states overlap in time, the linewidth of the 2PPE peak is decreasing until it reaches a constant value of 25 meV for large positive delays which is twice the pure dephasing rate. Unlike for the image-potential states on Fe/Cu(001) we cannot find a significant spin asymmetry in the dephasing rate for Ni/W(110). This corroborates the low probability of magnon emission predicted for Ni [Hong and Mills, 2000] leading to the low significance of spin-flip contributions to electronic decay [Zhukov et al., 2004]. The dephasing rate $\hbar\Gamma^{\star} \approx 12$ meV corresponds to the dephasing rate of the majority spin component of the $n = 1$ image-potential state on Fe/Cu(001) [Schmidt et al., 2005] which is likewise unaffected by magnon emission.

6.4 Conclusion

In summary our data collected with the superior surface sensitivity of 2PPE support the predictions from recent band structure calculations [Lobo-Checa et al., 2008; Ohwaki et al., 2006]. The majority spin component of the Shockley surface state is occupied with a binding energy of $\approx 150\,\mathrm{meV}$ at a sample temperature of 90 K. Its minority component is unoccupied and there is no sign of minority spin character around E_F. However, we clearly find a surface state with minority spin character at a binding energy $E_\mathrm{F} - 230\,\mathrm{meV}$. Since this state is derived from the d bands that are exchange split by about $160 - 250\,\mathrm{meV}$, [Kämper et al., 1990; Greber et al., 1997] we expect its majority counterpart at about $E_\mathrm{F} - 500\,\mathrm{meV}$. We give evidence for two majority surface states at 289 meV and at $\approx 500\,\mathrm{meV}$, as predicted in Refs. [Lobo-Checa et al., 2008; Ohwaki et al., 2006; Okuda et al., 2009].

For the image-potential states we determine binding energies lower than those measured in non-spin-resolved 2PPE but higher than those determined by inverse photoemission on Ni(111) single crystals. The exchange splitting of $14 \pm 3\,\mathrm{meV}$ for the $n = 1$ image-potential states is the smallest of the known values for the ferromagnetic surfaces of the $3d$-transition metals. Nevertheless, it agrees with the value of 16 meV expected from the bulk penetration of the image-potential state alone.

The small exchange splitting of valence and image-potential states is reflected in the low spin asymmetries of the inelastic as well as quasi-elastic scattering rates. The asymmetric spin-dependent DOS at the Fermi level effects the decay of the image-potential-state population much less than it has been predicted for hot bulk electrons by *ab initio* calculations [Grechnev et al., 2007; Zhukov et al., 2006]. We find the lifetime of majority spin electrons in the $n = 1$ image-potential state to be only a factor of $\tau_{\uparrow/\downarrow} = 1.27 \pm 0.06$ larger than that of the minority spin electrons. This ratio is even smaller for samples with lower work function. We attribute the latter to a partial quenching of the Shockley surface state, which constitutes an effective spin-dependent decay channel. Compared to the measured lifetime asymmetry theory predicts significantly larger values of $\tau_{\uparrow/\downarrow} \simeq 5$ [Hong and Mills, 2000; Zhukov et al., 2006; Grechnev et al., 2007]. Including spin mixing, recent calculations support lower lifetime asymmetries but still overestimate $\tau_{\uparrow/\downarrow} \simeq 2$ for nickel [Kaltenborn and Schneider, 2014]. The dephasing rate of the $n = 1$ image-potential state shows no spin dependence corroborating the minor role of magnon emission for electron scattering in nickel predicted by Hong and Mills [2000] and Zhukov et al. [2006].

In line with the experimentally observed low lifetime asymmetry of hot bulk electrons in nickel [Aeschlimann et al., 1997; Goris, 2010] the electron dynamics at the Ni(111) surface show a small spin-dependence. With no signature of magnon emission, low-energy spin-flip scattering seems to play a minor role. Furthermore, we observe a surface-state-enhanced spin-asymmetry of the lifetime. We therefore propose that also spin-dependent transmission barriers play a role for the highly spin-polarized electron emission in nickel hybrid-systems [Dedkov et al., 2008].

Chapter 7

Summary

This thesis investigates the ultrafast electron and spin dynamics on ferromagnetic surfaces. We applied spin-, time-, and angle-resolved direct and two-photon photoelectron spectroscopy (STARPES) to study the fundamentals of magnetism on the one hand as well as the spin dynamics relevant for technological applications on the other hand. The strength of our experiment is the combination of conventional laser photoemission with spin-resolution in pump-probe experiments. The former is able to investigate dynamic processes in electronic states near the Fermi level with low background from other energy ranges. The latter yields information about the magnetic order and the spin dependence of the triggered processes. Spin-resolving techniques continuously gain importance, since not only magnetic materials exhibit spin-polarized electronic states but also elements with a broken inversion symmetry or a lack of inversion symmetry at surfaces or interfaces like topological insulators or transition-metal dichalcogenites.

A part of this thesis was the installation of a new spin detector based on exchange scattering. This method is suited best to investigate nonmagnetic materials with spin-polarized electronic states. During the commissioning (described in Chapter 3), we showed that the count rates in the new detector improved by a factor of ten compared to the previously used SPLEED detector, while the Sherman function is slightly lower. Overall, the figure of merit was increased significantly. This advantage is exploited in the demagnetization experiment in Chapter 4, in which a high intensity per laser pulse was required. Amplification of the laser pulse comes at the expense of lower repetition rates, which also leads to a reduction in count rates. Another advantage of the new spin detector is the possibility to safely distinguish between spin polarization and magnetic dichroism as demonstrated by the example of an Fe(110) surface resonance in Chapter 5. The method of exchange scattering cancels the possibility of geometric asymmetries, since the spin polarization is resolved by switching the magnetization of the scattering target. This allows for spin resolution without changing the magnetization of the sample and thus allows to investigate dichroic effects with retained spin resolution as well as non-magnetic samples with spin-polarized states.

In Chapter 4, we performed the very first laser-induced demagnetization experiment by means of spin-, time-, and energy-resolved photoelectron spectroscopy. It yields the surprising result, that the exchange splitting and spin polarization of one electronic state

can show different time scales of demagnetization. In particular, we investigated the d_{z^2} surface state of Gd(0001), which is derived from the weakly localized d-bands mediating the exchange interaction in Gd. On a time scale of 0.6 ± 0.1 ps, the exchange splitting in the surface state breaks down, while the spin polarization is almost stable and decreases much slower with a time constant of 15 ± 8 ps.

Together with the ultrafast excitation of the electrons, the observed timescales explain the discrepancy between the results obtained by different methods in previous experiments. Magnetic second harmonic generation (MSHG) appears to be sensitive to the electronic temperature in terms of the population of the strongly spin-polarized surface state. The depopulation leads to a demagnetization at the surface, which is observed in MSHG. It thus shows an even faster time scale of < 0.1 ps. The d-band exchange splitting is reduced on the timescale of the thermalization of hot electrons and the lattice, as expected in Elliot-Yafet scattering. It thus leads to a demagnetization of the bulk, which is detected in the time-resolved magneto-optical Kerr effect (MOKE) and also in the X-ray magnetic circular dichroism (XMCD) at the M_5 edge. The magnetic moments of the $4f$ states is tilted on the much slower timescale observed in the magnetic linear dichroism (MLD) in photoemission from these states. The spin polarization of the surface state appears to stay aligned with the spins of the $4f$ electrons even when its exchange splitting is already reduced! This remarkable result shows that the indirect exchange coupling by the RKKY interaction can be described as proposed by Sandratskii [2014], [Sandratskii and Kübler, 1993]. The demagnetization of the $4f$ electrons is a spin-mixing process, for which the emission of magnons is a key ingredient, as introduced in Section 2.2.3. Furthermore, we found that the thermalized electrons in the Fermi function, which constitute the electronic temperature, neither show a significant spin polarization nor spin-dependent relaxation times. Spin-dependent electronic temperatures can thus be excluded as a cause driving the demagnetization on the timescales observed in Gd.

In Chapter 5, we proved that the electronic band dispersion of a surface state can be renormalized by the interaction with spin excitations, namely magnons. The renormalization was observed in a minority-spin surface resonance on Fe(110), similar to the work of Schäfer et al. [2004]. In contrast to the weak coupling ($\lambda = 0.20 \pm 0.04$) found by Schäfer et al. [2004], we find an extraordinarily large coupling factor of $\lambda = 4.0 \pm 0.8$. Renormalizations of that order of magnitude are also observed in de-Haas-van-Alphen measurements at the Fermi level of Fe [Lonzarich, 1984]. Furthermore, we observe the occurence of both the renormalized and the unperturbed peaks simultaneously in the photoemission spectra. This is in line with the photoemission spectra measured at band renormalizations in strongly correlated high-T_C superconductors [Lanzara et al., 2001], where coupling constants of the same order of magnitude can be found. The MLD that clearly appears in relation to the renormalization, confirms the magnetic character of the renormalization in Fe. We assign the MLD to be related to the asymmetric dispersion of the magnons along the $\overline{\Gamma\mathrm{H}}$ direction [Zakeri et al., 2010b].

Besides the remarkably strong magnon-induced renormalization of the surface resonance dispersion, the surface resonance itself has remarkable properties. It was predicted by Braun et al. [2002], that the different spin-orbit hybridization in the exchange-split bulk bands

can cause the existence of single majority- or minority-spin states, that do no longer appear in pairs. The minority-spin surface resonance appears in our spectra without any sign of a majority-spin partner. The corresponding majority-spin state is expected to appear above the Fermi level and disperse upwards in energy, which is contrasting the downwards dispersing minority-spin resonance. While this dispersion of the resonance was calculated for the $\overline{\Gamma\mathrm{N}}$ direction, where it had also been observed by Sánchez-Barriga et al. [2009], we confirm a similar dispersion of the resonance along the $\overline{\Gamma\mathrm{H}}$ direction.

In Chapter 6, we found several surface resonances near E_F on Ni(111). The minority-spin surface resonance at 230 meV, two majority-spin features at 289 and $\approx$ 500 meV, one of which is supposed to be the majority-spin partner of the minority-spin resonance, and the majority-spin part of the Shockley surface state below 150 meV. The binding energy of the latter is strongly temperature-dependent, which is in line with our observations. We found that the work function of Ni/W(110) is very sensitive to the temperature ramp rate during annealing. In analogy to clustered Fe films annealed to 800 K, the Ni films annealed at a higher ramp rate ($> 2\,\mathrm{Ks}^{-1}$) show a lower work function. In both cases, the image states don't change their binding energy on the fractured film, but remain at the same energy as on the properly annealed samples. This indicates the coexistence of islands, which still have the higher work function, and lower work function valleys giving rise to photoemission at lower kinetic energies. The image states on the broken nickel films show an increased lifetime with a decreased spin dependence, which we attribute to a quenching of the Shockley surface state as a dominant spin-dependent decay channel. The exchange splitting of the image states nicely agrees with our model view of the wave function overlap with the exchange-split valence bands. The spin-dependent lifetime asymmetry for nickel is low compared to Co and Fe. The dephasing rate shows no significant spin-dependence, indicating the low probability of magnon emission in nickel. Overall, there is a low spin dependence of the scattering rates in nickel, which is contradictory to theoretical predictions.

Appendix A

Additional Asymmetries in the Spin-Detection Process

During the characterization of the exchange-scattering spin-detector described in Chapter 3.1.1, it occurred in some test measurement that the spin-orbit-induced asymmetry as shown in Figure 3.6 deviated from zero. Such a scan through different scattering voltages is shown in the left panel of Figure A.1. The right panel shows the same measurement performed by Bertacco et al. [1999] for a thick ($> 3000\,\text{Å}$) Fe(001) film on a MgO(001) substrate for comparison. We find a similar behavior in our spin-orbit asymmetry (grey rectangles) as in Bertacco's A_{so} except for an offset of $\approx 12\,\%$. There is a small oscillation between 2 and 6 eV kinetic energy in both curves[1]. The additional spin-orbit asymmetry may be induced by the W(001) substrate, since the penetration depth in the regime of our scattering energies is beyond the thickness of the target Fe film (6 ML). W having a high Z number, shows significantly larger spin-orbit coupling effects than the Fe film itself. The effect of such a spin-orbit interaction with the W substrate could then vary between different target films due to variations of the evaporation rate unresolved by the flux monitor. Unfortunately, predictions for the spin-orbit-coupling-induced scattering asymmetry of W(001) are usually made for higher scattering energies and larger scattering angels – since W(001) is usually used in SPLEED – than we apply in our detector. Nevertheless, we would at least expect a few variations with scattering energy as they occur in the A_{so} of Fe(001) and also in the higher energy regime for W(001) [Kutnyakhov et al., 2015]. On the contrary, we find a nearly constant asymmetry in the whole range of 20 V. It thus seems unlikely that the measured asymmetry stems from a spin-orbit interaction with the W substrate. An asymmetry due to stray fields at the target may equally be excluded. This kind of asymmetry depends on the field applied to the scattering target, which cancels out in Equation (3.16).

Relying on the above-mentioned assumptions, we can rule out that the measured spin-orbit asymmetry is caused by our spin detector. The remaining causes are thus restricted to the sample and its vicinity. The magnetization dependence allows the effect to be either magnetic dichroism or a simple stray field of the sample holder. The magnetizing air-core

[1] Note that the pass energy of 1 eV has to be added to the bottom axis in the left panel.

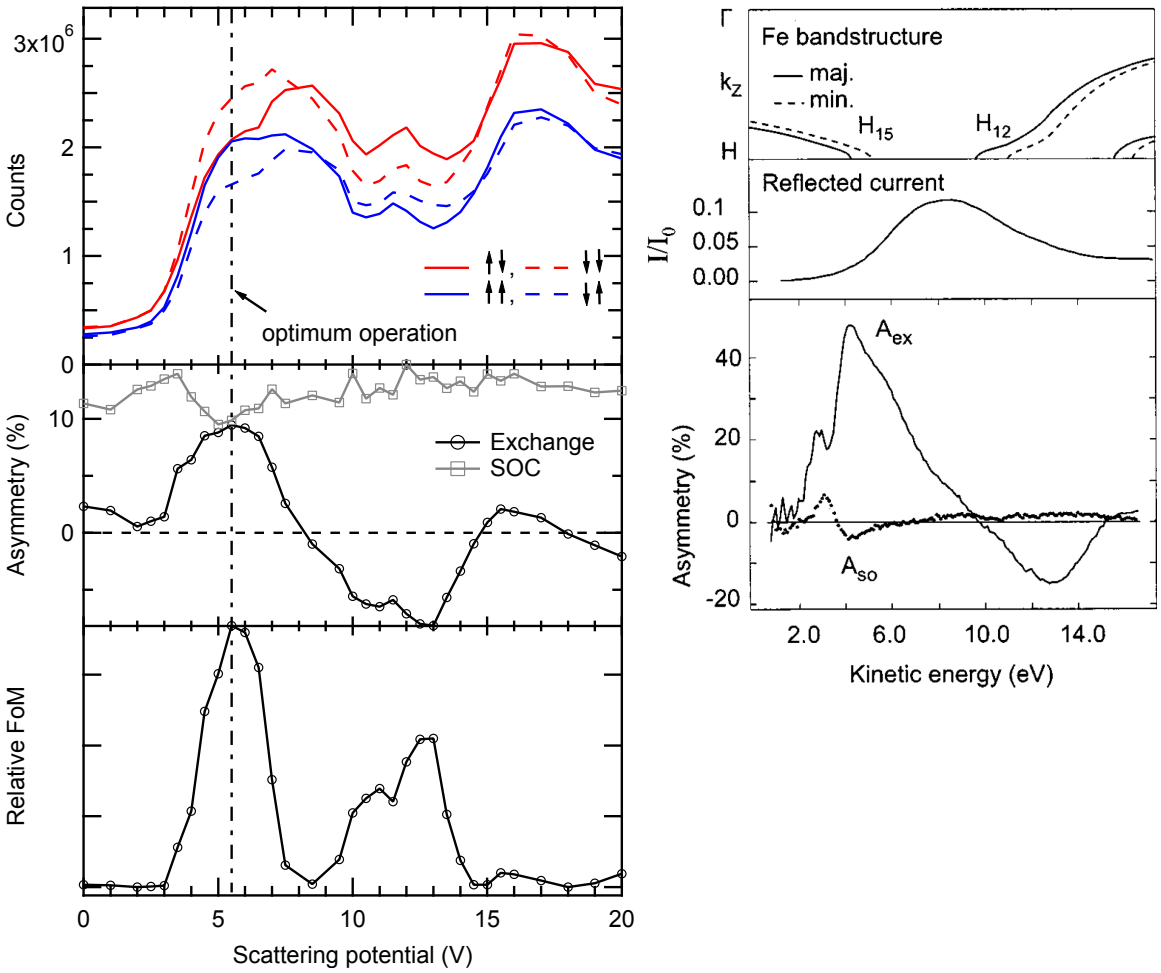

Figure A.1: Left: Magnetization-dependent count rates, resulting spin asymmetries, and figure of merit (FoM) for different scattering potentials. The arrows denote the direction of detector (first arrow) and sample (last arrow) magnetization direction. The exchange- and spin-orbit-induced asymmetries have been calculated using equations 3.15 and 3.16. The figure of merit (FoM) is given in Equation (3.7). Right: Same measurement performed by and reprinted from Bertacco et al. [1999] for a thick (> 3000 Å) Fe(001) film on a MgO(001) substrate.

coil has no remanent magnetization and is operated by a home-developed high-current power supply that has been carefully designed to avoid the occurrence of residual currents during the measurement. Although, a magnetic linear dichroic effect has been observed for the Gd surface state [Krupin, 2004], the effect can not explain an asymmetry as large as those we find (original spectra are shown in Fig. A.2). Furthermore, since it is significantly varying from one to the next sample – even without the preparation of a new detector target in between –, it is very likely to be a stray field of the sample holder. Parts of the sample holder may be contaminated with Gd during the growing of a new sample. This would lead to the occurrence of magnetic fields changing sign with the sample magnetization. This

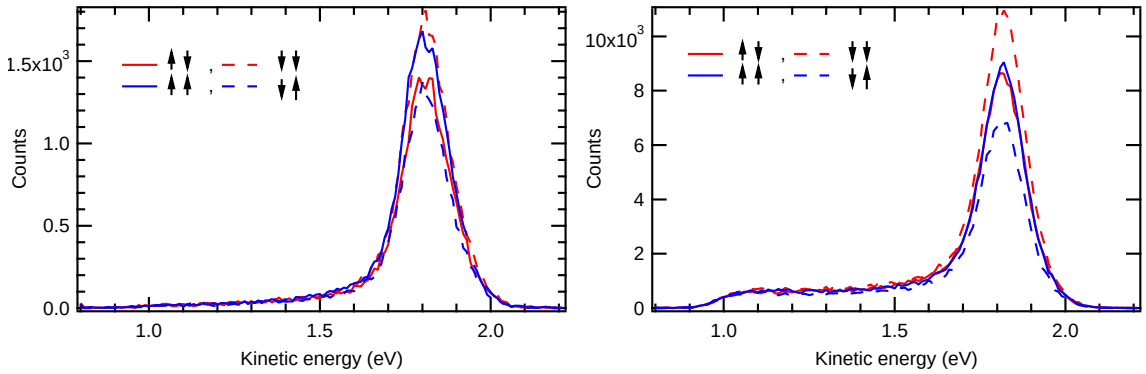

Figure A.2: Measured spectra of the Gd(0001) surface state for 5.5 V scattering potential. The spectra to the left and to the right have been measured on different samples but at the same conditions. The spectra shown in the left panel belong to the series of scattering energies shown in Chapter 3.1.1, Figure 3.6. The right panel belongs to the series shown in Figure A.1.

gives rise to a magnetization-dependent deflection of the electron trajectories and thus to a change of intensity as we observe it. Since the substrate is cleaned by flashing to a high temperature, the surroundings of the sample holder may equally desorb the contaminants, which also explains a reduction of the effect from one to the next sample.

Independent of the cause of our asymmetry, it is necessary to do a careful distinction of all observed asymmetry features in order to avoid mistaking them for real spin dependence. This is easily done in the case of simple spin-resolved measurements of magnetic samples, since the false spin-orbit asymmetry can be ruled out by using Equation (3.15). In the case of non-magnetic samples and in our spin-resolved measurements of magnetic dichroism, a full distinction of true and false asymmetries can not always be done. An additional measurement of unpolarized electrons can rule out stray field effects. Unfortunately, unpolarized electrons are not present in our setup, supposing the field to emerge from the sample growth process itself.

The only measurements in this work, that fall under the suspicion of being corrupted by additional asymmetries, are those regarding the magnetic linear dichroism of the Fe surface state in Chapter 5. Since the dichroic contrast changes sign within the spectra following the dispersion of the surface state, it is very unlikely that this effect is induced by a stray field. Also the Fe films under investigation are much thinner than the Gd films used for detector characterization. A contamination of the sample holder leading to stray fields is thus low compared to the investigations of Gd. We thus conclude that additional asymmetries observed in Chapter 5 are true magnetic linear dichroic effects.

Appendix B

Time Zero in the Laser-Induced Demagnetization of Gadolinium

In the spectra shown in Chapter 4, the time of zero pump-probe delay had been set to the center of the rise observed in the electron temperature. I'd like to show here that this is indeed the point of zero pump-probe delay.

In two-photon photoemission (2PPE), the time of zero pump-probe delay is usually determined by a measurement of an occupied state – *e.g.* the Shockley surface state on Cu(111) – in a two-photon process. The measured delay-dependent intensity is then a cross correlation of the two laser pulses providing us with time zero and the time resolution of the experiment.[1] 2PPE is of course only possible when photon energies below the work function of the sample are used and direct photoemission is avoided. Thus we had no means to measure the cross correlation using the 6.3 eV probe. To verify that the electron temperature increases at time zero within our time resolution, we performed the same experiment again, with a probe beam of 4.1 eV photon energy generated in the optical parametric amplifier and frequency-doubled. This photon energy is below the work function of Cu(111), so it is possible to measure a cross correlation in two-photon photoemission (2PPE) on our reference sample. The cross correlation measured in the Shockley surface state is shown as the solid line in Figure B.1. After time zero was determined as the peak of this cross correlation, we did the pump-probe experiment on Gd and found the temporal behavior of the electronic temperature, that is shown as gray dots in Figure B.1. The rise of the temperature exactly coincides with the cross correlation legitimizing our determination of time zero by fitting the electron temperature as it was done in Chapter 4.

Since the parameters of the experiment are different when 4.1-eV photon energy is used, I'd like to comment on the temperatures in Figure B.1. At a probe photon energy of 4.1 eV a reliable fitting of the Fermi function is compromised by the background spectrum photoemitted by the infrared (IR) pump beam in a three-photon process. The surface-state peak photoemitted by the IR appears 0.5 eV above that emitted by the probe beam, which causes additional intensities in the high-energy tail of the Fermi function. Instead of fitting

[1] If the photon energy is not accidentally resonant with the binding energy of an unoccupied state.

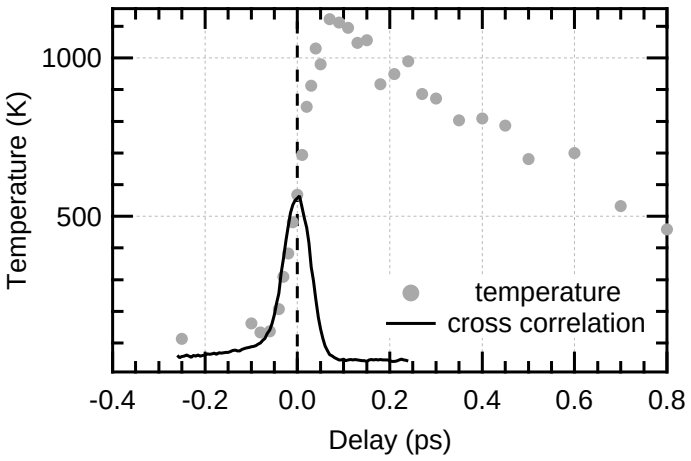

Figure B.1: Rising electronic temperature at zero pump-probe delay as obtained from the slope of the Fermi function (see text). The solid line shows the cross correlation of the laser pulses measured in two-photon photoemission of the Cu(111) Shockley surface state. The data was measured at a probe photon energy of 4.1 eV generated by an optical parametric amplifier (OPA) and then frequency-doubled. The pump fluence in that experiment was lower than in Chapter 4, since more power per pulse is needed to run the OPA compared to simple frequency quadrupling.

the Fermi function, we took the $\log_e$ of our spectra and evaluated the slope at the Fermi energy. Assuming a simple exponential decrease and comparing its slope to that of the Fermi function at the Fermi energy E_F, we find:

$$\frac{d}{dE}\ln\left(f(E,T)\right)\Big|_{E_F} = -\frac{1}{k_B b} \tag{B.1}$$

$$\Rightarrow b = 2T. \tag{B.2}$$

The slope of the logarithmized Fermi function devided by the Boltzmann constant k_B is thus twice the electron temperature at E_F. This evaluation yields the temperatures in Figure B.1, after subtracting the energy resolution of our experiment, which translates to a temperature of 90 K.

Appendix C

Space-Charge Effects in the Ulrafast Demagnetization of Gd

Space charge is a very well-known problem in photoelectron spectroscopy. Repulsive forces in a cloud of photoemitted electrons lead to acceleration or deceleration of individual electrons and thus to a broadened or distorted photoemission spectrum. Space charge has been found to effect not only the energies of the spectral components but also the spin polarization [Fognini et al., 2014b]. The intensity of space-charge effects depends on experimental parameters like the number of photons – translating to emitted electrons – per pulse and their distribution in the temporal and spatial profile of the light source [Hellmann et al., 2009, 2012; Graf et al., 2010]. Also the kinetic energies of the emitted electrons, electric fields surrounding sample and analyzer, and the angle of emission influence the space-charge effects [Hellmann et al., 2009, 2012; Graf et al., 2010]. Space-charge effects occur when pulsed radiation is used in XUV [Oloff et al., 2014], VUV [Fognini et al., 2014b; Hellmann et al., 2009, 2012], and UV [Graf et al., 2010] photoemission. It shall be clarified here, that space charge can be excluded as the source of the time-dependent effects shown in Chapter 4.

In our experiment, space-charge effects can be induced by the pump and the probe pulse. Figure C.1 shows spectra of the Gd(0001) surface state distorted by space-charge effects induced by the probe pulse. As the beam power in the fourth harmonic (UV) is too low for detection in a powermeter, the spectra are shown in dependence on the optical density (OD) of the filter[1] that was used to reduce the laser intensity. When a filter of OD$>$ 0.8 was used, we didn't observe any further shifts in the spectrum. We can thus assume, that the spectrum measured with OD$=$ 0.8 (violet line) is not effected by space charge. When the optical density of the filter is further reduced, we observe a broadening of the spectrum shifting the surface-state peak to higher energies. To avoid probe-induced space-charge effects, we measured a series of spectra in dependence on the probe-beam intensity (like that in Fig. C.1) every time the laser was readjusted. The intensity of the probe beam was then carefully set to the point, where the peak stopped shifting (in Fig. C.1 at OD$=$ 0.8).

An example for a strong pump-induced space-charge effect is shown in Figure C.2. Here

[1] This filter was placed before the frequency conversion, where the wavelength is still in the infrared regime.

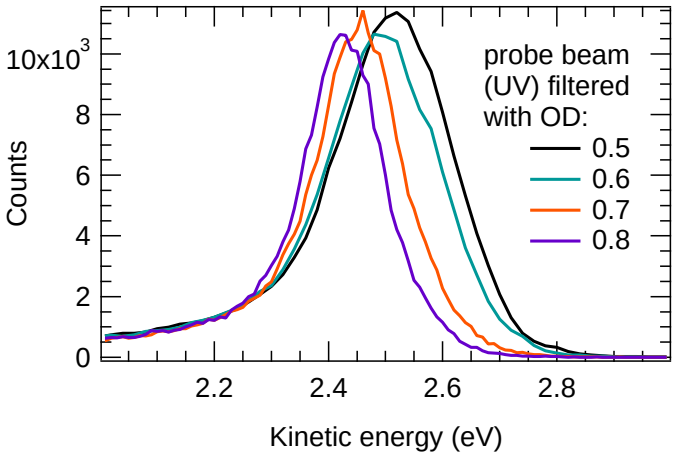

Figure C.1: Probe-pulse-induced space-charge effects on the spectrum of the Gd(0001) surface state. The spectra were measured with only the probe beam hitting the sample. The probe-beam intensity was reduced by placing a filter of the indicated optical density (OD) before the frequency conversion (see text). No space-charge-induced broadening or peak shift was observed for OD= 0.8. At higher intensities, the spectrum is gradually broadenend and the surface-state peak shifts to higher kinetic energies.

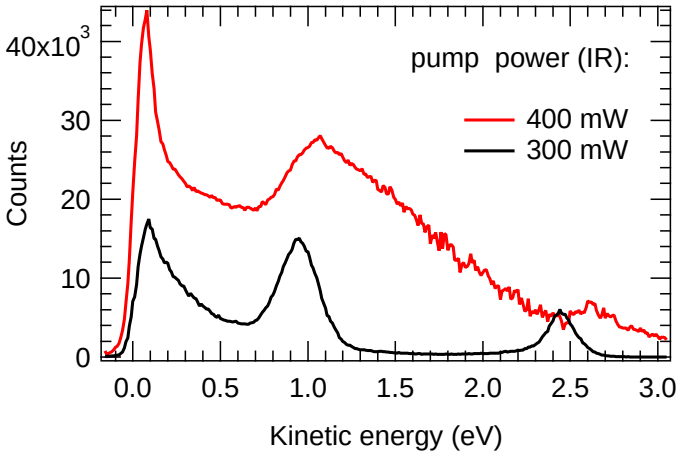

Figure C.2: Pump-pulse-induced space-charge effect measured at a pump-probe delay of -0.5 ps (see also Fig. 4.4). The red line shows a strongly distorted spectrum measured with the pump beam at its full power of 400 mW. When the pump intensity is reduced to 300 mW (by a filter with OD= 0.25), the space-charge-induced shift in the surface state is minimized (cf. Fig. C.3), while the pump fluence is still sufficient to demagnetize Gd.

two photoemission spectra are compared measured at a negative delay (-0.5 ps) with pump beams of different power. The probe intensity for both spectra was the same (OD= 0.8, see Fig. C.1). At our maximum pump power of 400 mW (red line), we find a strongly distorted spectrum compared to a pump beam with the power reduced to 300 mW (using an OD= 0.25 filter, black line in Fig. C.2). At 300 mW, the space-charge effects are minimized, while the pump fluence is still sufficient to demagnetize gadolinium. A comparably small shift of 16 meV still remained compared to the unpumped spectrum as shown in Figure C.3.

The time-dependence of space-charge effects in pump-probe photoemission has been studied by Oloff et al. [2014] and Frietsch [2015]. Pump-pulse-induced space-charge shifts can show a highly asymmetric dependence on pump-probe delay. This is the case, when X-ray photoemission is combined with laser-pump pulses [Oloff et al., 2014]. In such experiments, the fast electrons (several keV) emitted by the probe pulse travel through the slow electrons (eV) of the pump for positive delays. Thus pump-induced space charge can be observed for several hundreds of picoseconds (depending on the distance to the analyzer) in the direction of positive delays, while for negative delays the probe-emitted electrons quickly escape the

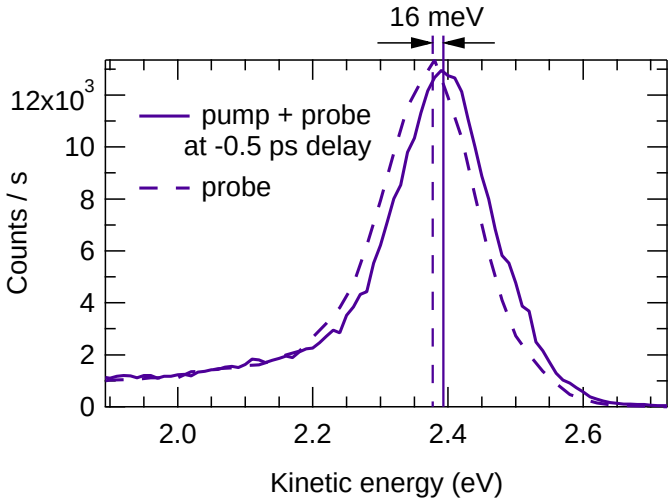

Figure C.3: Spectra showing the Gd(0001) surface-state peak with and without pump pulse. The dashed line shows the pure probe spectrum (violet line in Fig. C.1). The solid line shows the corresponding spectrum with pump beam at -0.5 ps pump-probe delay (black line in Fig. C.2). There is still a space-charge-induced shift of 16 meV occurring at negative delays. Comparing to the work of Frietsch [2015], we can assume that the temporal evolution of this shift contributes about 3 meV to the 80 meV shift, observed in Chapter 4.

following slow electrons emitted by the pump. This temporal asymmetry should be lifted, when the photon energies are similar. Nevertheless, in the recently published work of Frietsch [2015], a strongly asymmetric shift in the $4f$ photoemission peak of Gd was ascribed to a pump-induced space-charge effect.[2] Frietsch [2015] shows that the space-charge-induced additional shifts occurring at positive delays are small compared to the shift at negative pump-probe delay. He finds a delay-dependent shift of 50 meV in total on top of a 250 meV shift at negative pump-probe delay.

In Figure C.3, the pump-induced space charge at negative pump-probe delay shifts the surface-state peak to 16 meV higher energy without a measurable broadening of the spectrum. Comparing to the work of Frietsch, we can thus assume, that an additional delay-dependent space-charge-induced peak shift contributes about 3 meV to the shifts, we observe after pumping. This is included in the error bars in Chapter 4.

[2] In photoemission with a photon energy of 35 eV, Frietsch [2015] has access to the $4f$ states, which he assumes to show no energy shift due to the laser-induced demagnetization and thus only reflects the space-charge effects.

Bibliography

M. Aeschlimann, M. Bauer, S. Pawlik, W. Weber, R. Burgermeister, D. Oberli, and H. C. Siegmann. *Ultrafast Spin-Dependent Electron Dynamics in fcc Co.* Phys. Rev. Lett. **79** (25), 5158 (1997).

M. Albrecht, T. Furubayashi, M. Przybylski, J. Korecki, and U. Gradman. *Magnetic step anisotropies.* J. Magn. Magn. Mater. **113**(1-3), 207 (1992).

S. F. Alvarado and P. Renaud. *Observation of spin-polarized-electron tunneling from a ferromagnet into GaAs.* Phys. Rev. Lett. **68**, 1387 (1992).

S.F. Alvarado, R. Feder, H. Hopster, F. Ciccacci, and H. Pleyer. *Simultaneous probing of exchange and spin-orbit interaction in spin polarized low energy electron diffraction from magnetic surfaces.* Zeitschrift für Physik B Condensed Matter **49**(2), 129 (1982).

Beatrice Andres. *Spinauflösende Zwei-Photonen-Photoemission an der Gadolinium(0001)-Oberfläche.* Diploma thesis Freie Universität Berlin (2010).

S.I. Anisimov, B.L. Kapeliovich, and T.L. Perelman. *Electron emission from metal surfaces exposed to ultrashort laser pulses.* Zh. Eksp. Teor. Fiz **66**(2), 375 (1974).

Wilhelm Auwärter. *One monolayer of hexagonal boron nitride on Ni(111).* PhD thesis University of Zürich (2003).

M. Battiato, K. Carva, and P. M. Oppeneer. *Superdiffusive Spin Transport as a Mechanism of Ultrafast Demagnetization.* Phys. Rev. Lett. **105**(2), 027203 (2010).

M. Battiato, K. Carva, and P. M. Oppeneer. *Theory of laser-induced ultrafast superdiffusive spin transport in layered heterostructures.* Phys. Rev. B **86**, 024404 (2012).

E. Beaurepaire, J.-C. Merle, A. Daunois, and J.-Y. Bigot. *Ultrafast Spin Dynamics in Ferromagnetic Nickel.* Phys. Rev. Lett. **76**(22), 4250 (1996).

R. L. Benbow. *Dipole selection rules for the hexagonal-close-packed lattice.* Phys. Rev. B **22**, 3775 (1980).

P.J. Berlowitz, J.-W. He, and D.W. Goodman. *Overlayer growth and chemisorptve properties of ultra-thin Fe films on W(110) and W(100).* Surf. Sci. **231**(3), 315 (1990).

R. Bertacco and F. Ciccacci. *Oxygen-induced enhancement of the spin-dependent effects in electron spectroscopies of Fe(001).* Phys. Rev. B **59**(6), 4207 (1999).

R. Bertacco, D. Onofrio, and F. Ciccacci. *A novel electron spin-polarization detector with very large analyzing power.* Rev. Sci. Instrum. **70**(9), 3572 (1999).

H. Bethge, D. Heuer, Ch. Jensen, K. Reshöft, and U. Köhler. *Misfit-related effects in the epitaxial growth of iron on W (110).* Surf. Sci. **331**, 878 (1995).

J. Y. Bigot, M. Vomir, and E. Beaurepaire. *Coherent ultrafast magnetism induced by femtosecond laser pulses.* Nature Phys. **5**(7), 515 (2009).

M. Bode, M. Getzlaff, S. Heinze, R. Pascal, and R. Wiesendanger. *Magnetic exchange splitting of the Gd(0001) surface state studied by variable-temperature scanning tunneling spectroscopy.* Appl. Phys. A: Mater. Sci. Process. **66**(0), S121 (1998)a.

M. Bode, M. Getzlaff, and R. Wiesendanger. *Spin-Polarized Vacuum Tunneling into the Exchange-Split Surface State of Gd(0001).* Phys. Rev. Lett. **81**, 4256 (1998)b.

K. Boger, M. Roth, M. Weinelt, Th. Fauster, and P.-G. Reinhard. *Linewidths in energy-resolved two-photon photoemission spectroscopy.* Phys. Rev. B **65**, 075104 (2002).

G. Borstel, G. Thörner, M. Donath, V. Dose, and A. Goldmann. *Unoccupied and occupied surface states on Ni(111).* Solid State Commun. **55**(5), 469 (1985).

U. Bovensiepen. *Coherent and incoherent excitations of the Gd(0001) surface on ultrafast timescales.* J. Phys.: Condens. Matter **19**(8), 083201 (2007).

J. Braun and M. Donath. *Contest between surface resonances and surface states at 3 d ferromagnets.* EPL (Europhysics Letters) **59**(4), 592 (2002).

J. Braun, G. Borstel, and W. Nolting. *Theory of temperature-dependent photoemission in 3 d -band ferromagnets: Application to Ni(110) and Ni(111).* Phys. Rev. B **46**, 3510 (1992).

J. Braun, C. Math, A. Postnikov, and M. Donath. *Surface resonances versus surface states on Fe(110).* Phys. Rev. B **65**, 184412 (2002).

K.-F. Braun and K.-H. Rieder. *Ni(111) surface state observed with scanning tunneling microscopy.* Phys. Rev. B **77**, 245429 (2008).

P. Buczek, A. Ernst, and L. M. Sandratskii. *Different dimensionality trends in the Landau damping of magnons in iron, cobalt, and nickel: Time-dependent density functional study.* Phys. Rev. B **84**, 174418 (2011).

H. B. Callen. *Green Function Theory of Ferromagnetism.* Phys. Rev. **130**, 890 (1963).

R. Carley, K. Döbrich, B. Frietsch, C. Gahl, M. Teichmann, O. Schwarzkopf, P. Wernet, and M. Weinelt. *Femtosecond Laser Excitation Drives Ferromagnetic Gadolinium out of Magnetic Equilibrium.* Phys. Rev. Lett. **109**(5), 057401 (2012).

E. Carpene, E. Mancini, C. Dallera, M. Brenna, E. Puppin, and S. De Silvestri. *Dynamics of electron-magnon interaction and ultrafast demagnetization in thin iron films.* Phys. Rev. B **78**(17), 174422 (2008).

K. Carva, M. Battiato, and P. M. Oppeneer. *Ab Initio Investigation of the Elliott-Yafet Electron-Phonon Mechanism in Laser-Induced Ultrafast Demagnetization.* Phys. Rev. Lett. **107**(20), 207201 (2011).

G.-M. Choi, B.-C. Min, K.-J. Lee, and D. G. Cahill. *Spin current generated by thermally driven ultrafast demagnetization.* Nat. Comm. **5**, (2014).

Marc Christ. *A Spin Detector for time-resolved Two-Photon Photoemission - First measurement on bcc Fe(100).* Master's thesis Freie Universität Berlin (2014).

T.-H. Chuang, Kh. Zakeri, A. Ernst, L. M. Sandratskii, P. Buczek, Y. Zhang, H. J. Qin, W. Adeagbo, W. Hergert, and J. Kirschner. *Impact of Atomic Structure on the Magnon Dispersion Relation: A Comparison Between* Fe(111)/Au/**W**(110) *and* Fe(110)/**W**(110). Phys. Rev. Lett. **109**, 207201 (2012).

E.V. Chulkov, V.M. Silkin, and P.M. Echenique. *Image potential states on lithium, copper and silver surfaces.* Surf. Sci. **391**(1-3), L1217 (1997).

E.V. Chulkov, I. Sarria, V.M. Silkin, J.M. Pitarke, and P.M. Echenique. *Lifetimes of Image-Potential States on Copper Surfaces.* Phys. Rev. Lett. **80**, 4947 (1998).

E.V. Chulkov, V.M. Silkin, and P.M. Echenique. *Image potential states on metal surfaces: binding energies and wave functions.* Surf. Sci. **437**(3), 330 (1999).

E.V. Chulkov, A.G. Borisov, J.P. Gauyacq, D. Sánchez-Portal, V.M. Silkin, V.P. Zhukov, and P.M. Echenique. *Electronic excitations in metals and at metal surfaces.* Chem. Rev. **106**(10), 4160 (2006).

Operator's Manual: Legend-F Laser System, Kilohertz, Diode-Pumped, Ultrafast Ti:Sapphire Amplifier. Coherent, Inc. (2006).

X.Y. Cui, K. Shimada, M. Hoesch, Y. Sakisaka, H. Kato, Y. Aiura, M. Higashiguchi, Y. Miura, H. Namatame, and M. Taniguchi. *Angle-resolved photoemission spectroscopy study of Fe(1 1 0) single crystal: Many-body interactions between quasi-particles at the Fermi level.* Surf. Sci. **601**(18), 4010 (2007).

Yu. S. Dedkov, M. Fonin, and C. Laubschat. *A possible source of spin-polarized electrons: The inert graphene/Ni(111) system.* Appl. Phys. Lett. **92**(5), 052506 (2008).

D. G. Dempsey, Leonard Kleinman, and Ed Caruthers. *Energy bands of a (110) iron thin film.* Phys. Rev. B **13**, 1489 (1976).

Kristian M. Döbrich. *Bandstrukturen und Fermiflächen schwerer Lanthanidmetalle bei magnetischen Phasenübergängen.* PhD thesis Freie Universität Berlin (2007).

M. Donath, F. Passek, and V. Dose. *Surface State Contribution to the Magnetic Moment of Ni(111).* Phys. Rev. Lett. **70**(18), 2802 (1993).

M. Donath, B. Gubanka, and F. Passek. *Temperature-Dependent Spin Polarization of Magnetic Surface State at Gd(0001).* Phys. Rev. Lett. **77**, 5138 (1996).

M. Donath, C. Math, M. Pickel, A.B. Schmidt, and M. Weinelt. *Realization of a spin-polarized two-dimensional electron gas via image-potential-induced surface states.* Surf. Sci. **601**(24), 5701 (2007).

M. Donath, M. Pickel, A.B. Schmidt, and M. Weinelt. *Ferromagnetic Fe on Cu(001) throughout the fcc-like phase: arguing from the viewpoint of the electronic structure.* J. Phys.: Condens. Matter **21**(13), 134004 (2009).

V. Dose, W. Altmann, A. Goldmann, U. Kolac, and J. Rogozik. *Image-Potential States Observed by Inverse Photoemission.* Phys. Rev. Lett. **52**, 1919 (1984).

L. V. Dzemiantsova, M. Karolak, F. Lofink, A. Kubetzka, B. Sachs, K. von Bergmann, S. Hankemeier, T. O. Wehling, R. Frömter, H. P. Oepen, A. I. Lichtenstein, and R. Wiesendanger. *Multiscale magnetic study of Ni(111) and graphene on Ni(111).* Phys. Rev. B **84**, 205431 (2011).

D. E. Eastman, F. J. Himpsel, and J. A. Knapp. *Experimental Band Structure and Temperature-Dependent Magnetic Exchange Splitting of Nickel Using Angle-Resolved Photoemission.* Phys. Rev. Lett. **40**, 1514 (1978).

W. Eberhardt and F.J. Himpsel. *Dipole selection rules for optical transitions in the fcc and bcc lattices.* Phys. Rev. B **21**, 5572 (1980).

P.M. Echenique and J.B. Pendry. *The existence and detection of Rydberg states at surfaces.* J. Phys. C: Solid State Phys. **11**, 2065 (1978).

P.M. Echenique, J.M. Pitarke, E.V. Chulkov, and V.M. Silkin. *Image-potential-induced states at metal surfaces.* J. Electron Spectrosc. Relat. Phenom. **126**(1–3), 163 (2002).

P.M. Echenique, R. Berndt, E.V. Chulkov, Th. Fauster, A. Goldmann, and U. Höfer. *Decay of electronic excitations at metal surfaces.* Surf. Sci. Rep. **52**(7–8), 219 (2004).

C. Eickhoff, M. Teichmann, and M. Weinelt. *Two-State Double-Continuum Fano Resonance at the Si(100) Surface.* Phys. Rev. Lett. **107**, 176804 (2011).

R. J. Elliott. *Theory of the Effect of Spin-Orbit Coupling on Magnetic Resonance in Some Semiconductors.* Phys. Rev. **96**(2), 266 (1954).

A. Eschenlohr, M. Battiato, P. Maldonado, N. Pontius, T. Kachel, K. Holldack, R. Mitzner, A. Föhlisch, P. M. Oppeneer, and C. Stamm. *Ultrafast spin transport as key to femtosecond demagnetization.* Nat. Mater. **12**(4), 332 (2013).

M. Escher, N.B. Weber, M. Merkel, L. Plucinski, and C.M. Schneider. *FERRUM: A New Highly Efficient Spin Detector for Electron Spectroscopy.* e-Journal of Surface Science and Nanotechnology **9**, 340 (2011).

Thomas Fauster and Wulf Steinmann. *Two-photon photoemission spectroscopy of image states.* In P. Halevi, editor, *Electromagnetic Waves: Recent Developments in Research* volume Photonic Probes of Surfaceschapter 8, . Elsevier (1995).

A. V. Fedorov, T. Valla, F. Liu, P. D. Johnson, M. Weinert, and P. B. Allen. *Spin-resolved photoemission study of photohole lifetimes in ferromagnetic gadolinium.* Phys. Rev. B **65** (21), 212409 (2002).

N. Fischer, S. Schuppler, Th. Fauster, and W. Steinmann. *Intrinsic linewidths of image-potential states on Ni(111).* Phys. Rev. B **42**, 9717 (1990).

Focus SPLEED Technical Reference Manual. Focus, Omicron 1.2 edition (2003).

A. Fognini, T. U. Michlmayr, G. Salvatella, C. Wetli, U. Ramsperger, T. Bähler, F. Sorgenfrei, M. Beye, A. Eschenlohr, N. Pontius, C. Stamm, F. Hieke, M. Dell'Angela, S. de Jong, R. Kukreja, N. Gerasimova, V. Rybnikov, A. Al-Shemmary, H. Redlin, J. Raabe, A. Föhlisch, H. A. Dürr, W. Wurth, D. Pescia, A. Vaterlaus, and Y. Acremann. *Ultrafast reduction of the total magnetization in iron.* Appl. Phys. Lett. **104**(3), 032402 (2014)a.

A. Fognini, G. Salvatella, T.U. Michlmayr, C. Wetli, U. Ramsperger, T. Bähler, F. Sorgenfrei, M. Beye, A. Eschenlohr, N. Pontius, C. Stamm, F. Hieke, M. Dell'Angela, S. de Jong, R. Kukreja, N. Gerasimova, V. Rybnikov, H. Redlin, J. Raabe, A. Föhlisch, H. A. Dürr, W. Wurth, D. Pescia, A. Vaterlaus, and Y. Acremann. *The role of space charge in spin-resolved photoemission experiments.* New J. Phys. **16**(4), 043031 (2014)b.

A. Fognini, G. Salvatella, R. Gort, T. Michlmayr, A. Vaterlaus, and Y. Acremann. *The influence of the excitation pulse length on ultrafast magnetization dynamics in nickel.* Structural Dynamics **2**(2), 024501 (2015).

B. Frietsch, J. Bowlan, R. Carley, M. Teichmann, S. Wienholdt, D. Hinzke, U. Nowak, K. Carva, P. M. Oppeneer, and M. Weinelt. *Disparate ultrafast dynamics of itinerant and localized magnetic moments in gadolinium metal.* Nat. Comm. **6**, (2015).

Björn Frietsch. *Magnetization Dynamics of Itinerant and Localized Electrons in Lanthanide Metals.* PhD thesis Freie Universität Berlin (2015).

O. Fruchart, P.O. Jubert, M. Eleoui, F. Cheynis, B. Borca, P. David, V. Santonacci, A. Liénard, M. Hasegawa, and C. Meyer. *Growth modes of Fe(110) revisited: a contribution of self-assembly to magnetic materials.* J. Phys.: Condens. Matter **19**(5), 053001 (2007).

M. Getzlaff, M. Bode, S. Heinze, R. Pascal, and R. Wiesendanger. *Temperature-dependent exchange splitting of the magnetic Gd(0 0 0 1) surface state.* J. Magn. Magn. Mater. **184** (2), 155 (1998).

K. Giesen, F. Hage, F. J. Himpsel, H. J. Riess, and W. Steinmann. *Two-photon photoemission via image-potential states.* Phys. Rev. Lett. **55**, 300 (1985).

A. Goris, K. M. Döbrich, I. Panzer, A. B. Schmidt, M. Donath, and M. Weinelt. *Role of Spin-Flip Exchange Scattering for Hot-Electron Lifetimes in Cobalt.* Phys. Rev. Lett. **107** (1), 026601 (2011).

Andreas Goris. *Spinabhängige Lebensdauer heisser Elektronen in 3d-Ferromagneten.* PhD thesis Freie Universität Berlin (2010).

U. Gradmann and G. Waller. *Periodic lattice distortions in epitaxial films of Fe(110) on W(110).* Surf. Sci. **116**(3), 539 (1982).

U. Gradmann, J. Korecki, and G. Waller. *In-plane magnetic surface anisotropies in Fe (110).* Applied Physics A **39**(2), 101 (1986).

J. Graf, S. Hellmann, C. Jozwiak, C. L. Smallwood, Z. Hussain, R. A. Kaindl, L. Kipp, K. Rossnagel, and A. Lanzara. *Vacuum space charge effect in laser-based solid-state photoemission spectroscopy.* J. Appl. Phys. **107**(1), 014912 (2010).

T. Greber, T. J. Kreutz, and J. Osterwalder. *Photoemission above the Fermi Level: The Top of the Minority d Band in Nickel.* Phys. Rev. Lett. **79**(22), 4465 (1997).

A. Grechnev, I. Di Marco, M.I. Katsnelson, A.I. Lichtenstein, J. Wills, and O. Eriksson. *Theory of bulk and surface quasiparticle spectra for Fe, Co, and Ni.* Phys. Rev. B **76**(3), 035107 (2007).

M. Haag, C. Illg, and M. Fähnle. *Role of electron-magnon scatterings in ultrafast demagnetization.* Phys. Rev. B **90**, 014417 (2014).

S. Hellmann, K. Rossnagel, M. Marczynski-Bühlow, and L. Kipp. *Vacuum space-charge effects in solid-state photoemission.* Phys. Rev. B **79**, 035402 (2009).

S. Hellmann, T. Ott, L. Kipp, and K. Rossnagel. *Vacuum space-charge effects in nano-ARPES.* Phys. Rev. B **85**, 075109 (2012).

J. Henk, T. Scheunemann, S.V. Halilov, and R. Feder. *Magnetic dichroism and electron spin polarization in photoemission: analytical results.* J. Phys.: Condens. Matter **8**(1), 47 (1996).

J. Hermanson. *Final-state symmetry and polarization effects in angle-resolved photoemission spectroscopy.* Solid State Communications **22**(1), 9 (1977).

G. Herzog, S. Krause, and R. Wiesendanger. *Heat assisted spin torque switching of quasistable nanomagnets across a vacuum gap.* Appl. Phys. Lett. **96**(10), 102505 (2010).

S. Hüfner. *Photoelectron Spectroscopy.* Springer (2003).

M. Higashiguchi, K. Shimada, M. Arita, Y. Miura, N. Tobita, X. Cui, Y. Aiura, H. Namatame, and M. Taniguchi. *High-resolution angle-resolved photoemission study of Ni(1 1 1) surface state.* Surf. Sci. **601**(18), 4005 (2007).

F. J. Himpsel. *Exchange Splitting of epitaxial fcc Fe/Cu(100) versus bcc Fe/Ag(100).* Phys. Rev. Lett. **67**, 2363 (1991).

F. J. Himpsel and D. E. Eastman. *Observation of a Λ_1-Symmetry Surface State on Ni(111).* Phys. Rev. Lett. **41**, 507 (1978).

F. J. Himpsel and D. E. Eastman. *Experimental energy-band dispersions and magnetic exchange splitting for cobalt.* Phys. Rev. B **21**, 3207 (1980).

J. Hong and D. L. Mills. *Spin dependence of the inelastic electron mean free path in Fe and Ni: Explicit calculations and implications.* Phys. Rev. B **62**(9), 5589 (2000).

Arthur Hotzel. *Femtosekunden-Elektronendynamik der Adsorbat-bedeckten Cu(111)-Oberfläche.* PhD thesis Freie Universität Berlin (1999).

H. Ibach and H. Lüth. *Festkörperphysik.* Springer (2009).

C. Illg, M. Haag, and M. Fähnle. *Ultrafast demagnetization after laser irradiation in transition metals: Ab initio calculations of the spin-flip electron-phonon scattering with reduced exchange splitting.* Phys. Rev. B **88**, 214404 (2013).

C. Jensen, K. Reshöft, and U. Köhler. *Direct observation of strain relaxation in iron layers on W(110) by time-resolved STM.* **62**(3), 217 (1996).

S. Kaltenborn and H.C. Schneider. *Spin-orbit coupling effects on spin-dependent inelastic electronic lifetimes in ferromagnets.* Phys. Rev. B **90**, 201104 (2014).

K.-P. Kämper, W. Schmitt, G. Güntherodt, and H. Kuhlenbeck. *Thickness dependence of the electronic structure of ultrathin, epitaxial Ni(111)/W(110) layers.* Phys. Rev. B **38** (14), 9451 (1988).

K.-P. Kämper, W. Schmitt, and G. Güntherodt. *Temperature and wave-vector dependence of the spin-split band structure of Ni(111) along the* Γ- *L line.* Phys. Rev. B **42**, 10696 (1990).

T. Kampfrath, M. Battiato, P. Maldonado, G. Eilers, J. Notzold, S. Mahrlein, V. Zbarsky, F. Freimuth, Y. Mokrousov, S. Blügel, M. Wolf, I. Radu, P.M. Oppeneer, and M. Münzenberg. *Terahertz spin current pulses controlled by magnetic heterostructures.* Nat Nano **8** (4), 256 (2013).

T. Kasuya. *A Theory Of Metallic Ferromagnetism And Antiferromagnetism On Zeners Model.* Progress of Theoretical Physics **16**(1), 45 (1956).

J. Kirschner. *Direct and Exchange Contributions in Inelastic Scattering of Spin-Polarized Electrons from Iron.* Phys. Rev. Lett. **55**, 973 (1985).

J. Kirschner. *Sources and Detectors for Polarized Electrons*chapter 5, . WORLD SCIENTIFIC (1986).

R. Knorren, G. Bouzerar, and K. H. Bennemann. *Theory for the dynamics of excited electrons in noble and transition metals.* J. Phys.: Condens. Matter **14**, R739 (2002).

J. Koĺaczkiewicz and E. Bauer. *V and Fe on the W(110) face.* Surf. Sci. **450**(1-2), 106 (2000).

B. Koopmans, H.H.J.E. Kicken, M. van Kampen, and W.J.M. de Jonge. *Microscopic model for femtosecond magnetization dynamics.* J. Magn. Magn. Mater. **286**, 271 (2005)a.

B. Koopmans, J. J. M. Ruigrok, F. Dalla Longa, and W. J. M. de Jonge. *Unifying Ultrafast Magnetization Dynamics.* Phys. Rev. Lett. **95**(26), 267207 (2005)b.

B. Koopmans, G. Malinowski, F. Dalla Longa, D. Steiauf, M. Fahnle, T. Roth, M. Cinchetti, and M. Aeschlimann. *Explaining the paradoxical diversity of ultrafast laser-induced demagnetization.* Nat. Mater. **9**(3), 259 (2010).

M. Krauß, T. Roth, S. Alebrand, D. Steil, M. Cinchetti, M. Aeschlimann, and H.C. Schneider. *Ultrafast demagnetization of ferromagnetic transition metals: The role of the Coulomb interaction.* Phys. Rev. B **80**, 180407 (2009).

A. Krönlein, J. Kemmer, P.-J. Hsu, and M. Bode. *Quasiparticle interference scattering of spin-polarized Shockley-like surface state electrons: Ni(111).* Phys. Rev. B **89**, 155413 (2014).

Oleg Krupin. *Dichroism and Rashba effect at magnetic crystal surfaces of rare-earth metals.* PhD thesis Freie Universität Berlin (2004).

André Kubetzka. *Spinpolarisierte Rastertunnelmikroskopie an magnetischen Nanostrukturen: Fe/W(110).* PhD thesis Fachbereichs Physik der Universität Hamburg (2002).

W. Kuch and C.M. Schneider. *Magnetic dichroism in valence band photoemission.* Reports on Progress in Physics **64**(2), 147 (2001).

P. Kurz, G. Bihlmayer, and S. Bluegel. *Magnetism and electronic structure of hcp Gd and the Gd (0001) surface.* Journal of Physics Condensed Matter **14**(25), 6353 (2002).

D. Kutnyakhov, H. J. Elmers, G. Schönhense, C. Tusche, S. Borek, J. Braun, J. Minár, and H. Ebert. *Specular reflection of spin-polarized electrons from the W(001) spin-filter crystal in a large range of scattering energies and angles.* Phys. Rev. B **91**, 014416 (2015).

J. Kutzner, R. Paucksch, C. Jabs, H. Zacharias, and J. Braun. *High-resolution photoelectron emission spectroscopy of surface states on Ni(111).* Phys. Rev. B **56**(24), 16003 (1997).

A. Lanzara, P. V. Bogdanov, X. J. Zhou, S. A. Kellar, D. L. Feng, E. D. Lu, T. Yoshida, H. Eisaki, A. Fujimori, K. Kishio, J.-I. Shimoyama, T. Noda, S. Uchida, Z. Hussain, and Z.-X. Shen. *Evidence for ubiquitous strong electron-phonon coupling in high-temperature superconductors.* Nature **412**(6846), 510 (2001).

K. O. Legg, F. Jona, D. W. Jepsen, and P. M. Marcus. *Early stages of oxidation of the Fe001 surface: Atomic structure of the first monolayer.* Phys. Rev. B **16**, 5271 (1977).

T. C. Leung, C. L. Kao, W. S. Su, Y. J. Feng, and C. T. Chan. *Relationship between surface dipole, work function and charge transfer: Some exceptions to an established rule.* Phys. Rev. B **68**, 195408 (2003).

D. Li, J. Pearson, S.D. Bader, D.N. McIlroy, C. Waldfried, and P.A. Dowben. *Spin-polarized photoemission studies of the exchange splitting of the Gd 5d electrons near the Curie temperature.* Phys. Rev. B **51**(19), 13895 (1995).

L. Liebermann, J. Clinton, D. M. Edwards, and J. Mathon. *"Dead" Layers in Ferromagnetic Transition Metals.* Phys. Rev. Lett. **25**, 232 (1970).

S. Link, J. Sievers, H.A. Dürr, and W. Eberhardt. *Lifetimes of image-potential states on the clean and hydrogen-covered Ni(111) surface.* J. Electron Spectrosc. Relat. Phenom. **114–116**(0), 351 (2001).

M. Lisowski, P. A. Loukakos, A. Melnikov, I. Radu, L. Ungureanu, M. Wolf, and U. Bovensiepen. *Femtosecond Electron and Spin Dynamics in Gd(0001) Studied by Time-Resolved Photoemission and Magneto-optics.* Phys. Rev. Lett. **95**(13), 137402 (2005).

Martin Lisowski. *Elektronen- und Magnetisierungsdynamik in Metallen untersucht mit zeitaufgelöster Photoemission.* PhD thesis Freie Universität Berlin (2005).

J. Lobo-Checa, T. Okuda, M. Hengsberger, L. Patthey, Th. Greber, P. Blaha, and J. Osterwalder. *Hidden surface states on pristine and H-passivated Ni(111): Angle-resolved photoemission and density-functional calculations.* Phys. Rev. B **77**, 075415 (2008).

G.G. Lonzarich. *Band structure and magnetic fluctuations in ferromagnetic or nearly ferromagnetic metals.* J. Magn. Magn. Mater. **45**(1), 43 (1984).

C.-K. Loong, J. M. Carpenter, J. W. Lynn, R. A. Robinson, and H. A. Mook. *Neutron scattering study of the magnetic excitations in ferromagnetic iron at high energy transfers.* J. Appl. Phys. **55**(6), 1895 (1984).

P. A. Loukakos, M. Lisowski, G. Bihlmayer, S. Blügel, M. Wolf, and U. Bovensiepen. *Dynamics of the Self-Energy of the Gd(0001) Surface State Probed by Femtosecond Photoemission Spectroscopy.* Phys. Rev. Lett. **98**, 097401 (2007).

O. Madelung. *Festkörpertheorie I.* Springer - Verlag (1972).

K. Maiti, M. C. Malagoli, A. Dallmeyer, and C. Carbone. *Finite Temperature Magnetism in Gd: Evidence against a Stoner Behavior.* Phys. Rev. Lett. **88**(16), 167205 (2002).

A. Melnikov, I. Radu, U. Bovensiepen, O. Krupin, K. Starke, E. Matthias, and M. Wolf. *Coherent Optical Phonons and Parametrically Coupled Magnons Induced by Femtosecond Laser Excitation of the Gd(0001) Surface.* Phys. Rev. Lett. **91**(22), 227403 (2003).

A. Melnikov, H. Prima-Garcia, M. Lisowski, T. Giessel, R. Weber, R. Schmidt, C. Gahl, N. M. Bulgakova, U. Bovensiepen, and M. Weinelt. *Nonequilibrium Magnetization Dynamics of Gadolinium Studied by Magnetic Linear Dichroism in Time-Resolved 4f Core-Level Photoemission.* Phys. Rev. Lett. **100**(10), (2008)a.

A. Melnikov, I. Radu, A. Povolotskiy, T. Wehling, A. Lichtenstein, and U. Bovensiepen. *Ultrafast dynamics at lanthanide surfaces: microscopic interaction of the charge, lattice and spin subsystems.* Journal Of Physics D-Applied Physics **41**(16), 164004 (2008)b.

H. A. Mook, J. W. Lynn, and R. M. Nicklow. *Temperature Dependence of the Magnetic Excitations in Nickel.* Phys. Rev. Lett. **30**, 556 (1973).

N. F. Mott. *The Scattering of Fast Electrons by Atomic Nuclei.* Proceedings of the Royal Society of London A: Mathematical, Physical and Engineering Sciences **124**(794), 425 (1929).

N. F. Mott. *The Polarisation of Electrons by Double Scattering.* Proceedings of the Royal Society of London A: Mathematical, Physical and Engineering Sciences **135**(827), 429 (1932).

B. Y. Mueller and B. Rethfeld. *Thermodynamic μT model of ultrafast magnetization dynamics.* Phys. Rev. B **90**, 144420 (2014).

B. Y. Mueller, A. Baral, S. Vollmar, M. Cinchetti, M. Aeschlimann, H. C. Schneider, and B. Rethfeld. *Feedback Effect during Ultrafast Demagnetization Dynamics in Ferromagnets.* Phys. Rev. Lett. **111**, 167204 (2013).

T.-U. Nahm and R. Gomer. *The adsorption of Fe on W(110) and of O and H on Fe-covered W(110).* Surface Science **373**(2-3), 237 (1997)a.

T.-U. Nahm and R. Gomer. *The conversion of Fe on W(110) from the low temperature to the high temperature form.* Surface Science **380**(1), 52 (1997)b.

M. Nekovee and J.E. Inglesfield. *Theory of image states at magnetic surfaces.* Prog. Surf. Sci. **50**(1), 149 (1995).

Y. Nishimura, M. Kakeya, M. Higashiguchi, A. Kimura, M. Taniguchi, H. Narita, Y. Cui, M. Nakatake, K. Shimada, and H. Namatame. *Surface electronic structures of ferromagnetic Ni(111) studied by STM and angle-resolved photoemission.* Phys. Rev. B **79**, 245402 (2009).

W. Nolting, S. Rex, and S. Mathi Jaya. *Magnetism and electronic structure of a local moment ferromagnet.* J. Phys.: Condens. Matter **9**(6), 1301 (1997).

Andreas Nuber. *Intrinsische und extrinsische Einflüsse auf zweidimensionale elektronische Zustände.* PhD thesis University of Würzburg (2011).

T. Ohwaki, D. Wortmann, H. Ishida, S. Blügel, and K. Terakura. *Spin-polarized field emission from Ni(001) and Ni(111) surfaces.* Phys. Rev. B **73**, 235424 (2006).

T. Okuda, Y. Takeichi, Y. Maeda, A. Harasawa, I. Matsuda, T. Kinoshita, and A. Kakizaki. *A new spin-polarized photoemission spectrometer with very high efficiency and energy resolution.* Rev. Sci. Instrum. **79**(12), 123117 (2008).

T. Okuda, J. Lobo-Checa, W. Auwärter, M. Morscher, M. Hoesch, V. N. Petrov, M. Hengsberger, A. Tamai, A. Dolocan, C. Cirelli, M. Corso, M. Muntwiler, M. Klöckner, M. Roos, J. Osterwalder, and T. Greber. *Exchange splitting of the three Gamma -bar surface states of Ni(111) from three-dimensional spin- and angle-resolved photoemission spectroscopy.* Phys. Rev. B **80**(18), 180404 (2009).

L.-P. Oloff, M. Oura, K. Rossnagel, A. Chainani, M. Matsunami, R. Eguchi, T. Kiss, Y. Nakatani, T. Yamaguchi, J. Miyawaki, M. Taguchi, K. Yamagami, T. Togashi, T. Katayama, K. Ogawa, M. Yabashi, and T. Ishikawa. *Time-resolved HAXPES at SACLA: probe and pump pulse-induced space-charge effects.* New J. Phys. **16**(12), 123045 (2014).

F. Passek and M. Donath. *Spin-split image-potential-induced surface state on Ni(111).* Phys. Rev. Lett. **69**, 1101 (1992).

Boris Peev. *Modellierung von Bildpotentialzuständen an Metalloberflächen.* Master's thesis Freie Universität Berlin (2013).

T. G. Perring, A. T. Boothroyd, D. McK. Paul, A. D. Taylor, R. Osborn, R. J. Newport, J. A. Blackman, and H. A. Mook. *High-energy spin waves in bcc iron.* J. Appl. Phys. **69** (8), 6219 (1991).

L. G. Petersson, R. Melander, D. P. Spears, and S. B. M. Hagström. *Density of states of ferromagnetic and paramagnetic Ni and Fe studied by photoelectron spectroscopy with 21.2- and 40.8-eV photon energies.* Phys. Rev. B **14**, 4177 (1976).

J.P. Petrakian, N.A. Mokhtar, and R. Fraisse. *Optical constants of gadolinium at various temperatures from polarimetric measurements. (Magnetic ordering effects).* Journal of Physics F: Metal Physics **7**(11), 2431 (1977).

D. Y. Petrovykh, K. N. Altmann, H. Höchst, M. Laubscher, S. Maat, G. J. Mankey, and F. J. Himpsel. *Spin-dependent band structure, Fermi surface, and carrier lifetime of permalloy.* Appl. Phys. Lett. **73**(23), 3459 (1998).

M. Pickel, A.B. Schmidt, M. Donath, and M. Weinelt. *A two-photon photoemission study of spin-dependent electron dynamics.* Surface Science **600**(18), 4176 (2006).

M. Pickel, A. B. Schmidt, F. Giesen, J. Braun, J. Minár, H. Ebert, M. Donath, and M. Weinelt. *Spin-Orbit Hybridization Points in the Face-Centered-Cubic Cobalt Band Structure.* Phys. Rev. Lett. **101**(6), 066402 (2008).

M. Pickel, A. B. Schmidt, M. Weinelt, and M. Donath. *Magnetic Exchange Splitting in Fe above the Curie Temperature.* Phys. Rev. Lett. **104**(23), 237204 (2010).

Martin Pickel. *Image-potential states as a sensor for magnetism.* PhD thesis Freie Universität Berlin (2007).

E. W. Plummer and W. Eberhardt. *Magnetic surface states on Ni(100).* Phys. Rev. B **20**, 1444 (1979).

M. Przybylski, U. Gradmann, and J. Korecki. *Magnetic hyperfine fields near the W(110)/Fe(110)-interface.* J. Magn. Magn. Mater. **69**(2), 199 (1987).

I. Radu, K. Vahaplar, C Stamm, T. Kachel, N. Pontius, H. A. Dürr, T. A. Ostler, J. Barker, R. F. L. Evans, R. W. Chantrell, A. Tsukamoto, A. Itoh, A. Kirilyuk, Th. Rasing, and A. V. Kimel. *Transient ferromagnetic-like state mediating ultrafast reversal of antiferromagnetically coupled spins.* Nature **472**, 205 (2011).

A. Rampe, G. Güntherodt, D. Hartmann, J. Henk, T. Scheunemann, and R. Feder. *Magnetic linear dichroism in valence-band photoemission: Experimental and theoretical study of Fe(110).* Phys. Rev. B **57**, 14370 (1998).

B. Reihl. *Streuung spinpolarisierter Elektronen an Au(110).* Zeitschrift für Physik B Condensed Matter **41**(1), 21 (1981).

S. Rex, V. Eyert, and W. Nolting. *Temperature-dependent quasiparticle bandstructure of ferromagnetic gadolinium.* J. Magn. Magn. Mater. **192**(3), 529 (1999).

H.-S. Rhie, H. A. Dürr, and W. Eberhardt. *Femtosecond Electron and Spin Dynamics in $Ni/W(110)$ Films.* Phys. Rev. Lett. **90**(24), 247201 (2003).

J.S. Risley. *Design Parameters for the Cylindrical Mirror Energy Analyzer.* Rev. Sci. Instrum. **43**(1), 95 (1972).

M. Roth, M. Pickel, M. Weinelt, and T. Fauster. *Dynamics of image-potential states on stepped Cu(001) surfaces.* Appl. Phys. A **78**(2), 149 (2003).

M. A. Ruderman and C. Kittel. *Indirect exchange coupling of nuclear magnetic moments by conduction electrons.* Phys. Rev. **96**, 99 (1954).

M. Rybicki, I. Zasada, K. Freindl, N. Spiridis, and J. Korecki. *A {LEED} study of surface relaxation in Fe(1 1 0) epitaxial film on W(1 1 0).* Applied Surface Science **286**, 66 (2013).

Y. Sakisaka, Thor Rhodin, and D. Mueller. *Angle-resolved photoemission from Fe(110): Determination of E(k).* Solid State Communications **53**(9), 793 (1985).

J. Sánchez-Barriga, J. Fink, V. Boni, I. Di Marco, J. Braun, J. Minár, A. Varykhalov, O. Rader, V. Bellini, F. Manghi, H. Ebert, M. I. Katsnelson, A. I. Lichtenstein, O. Eriksson, W. Eberhardt, and H. A. Dürr. *Strength of Correlation Effects in the Electronic Structure of Iron.* Phys. Rev. Lett. **103**, 267203 (2009).

J. Sánchez-Barriga, J. Braun, J. Minár, J.r, I. Di Marco, A. Varykhalov, O. Rader, V. Boni, V. Bellini, F. Manghi, H. Ebert, M. I. Katsnelson, A. I. Lichtenstein, O. Eriksson, W. Eberhardt, H. A. Dürr, and J. Fink. *Effects of spin-dependent quasiparticle renormalization in Fe, Co, and Ni photoemission spectra:An experimental and theoretical study.* Phys. Rev. B **85**(20), 205109 (2012).

L. M. Sandratskii. *Exchange splitting of surface and bulk electronic states in excited magnetic states of Gd: First-principles study.* Phys. Rev. B **90**(18), 184406 (2014).

L. M. Sandratskii and J. Kübler. *Local Magnetic Moment of Conduction Electrons in Gadolinium.* Europhys. Lett. **23**, 661 (1993).

C. Santos, V. Eyert, and W. Nolting. *Ferromagnetism and temperature-dependent electronic structure of HCP gadolinium.* J. Magn. Magn. Mater. **272-276**(Supplement 1), E371 (2004).

E.D. Schaefer, S.V. Chernov, A.A. Sapozhnik, D.M. Kostyuk, A.V. Zaporozhchenko, S.I. Protsenko, M.Bode, S.A. Nepijko, H.-J. Elmers, and G. Schönhense. *Morphological and magnetic analysis of Fe nanostructures on W(110) by using scanning tunneling microscopy and Lorentz microscopy.* Japanese Journal of Applied Physics **55**(2S), 02BC11 (2016).

J. Schäfer, D. Schrupp, Eli Rotenberg, K. Rossnagel, H. Koh, P. Blaha, and R. Claessen. *Electronic Quasiparticle Renormalization on the Spin Wave Energy Scale.* Phys. Rev. Lett. **92**(9), 097205 (2004).

J Schäfer, M Hoinkis, Eli Rotenberg, P Blaha, and R Claessen. *Fermi surface and electron correlation effects of ferromagnetic iron.* Phys. Rev. B **72**(15), 155115 (2005).

A. J. Schellekens, K. C. Kuiper, R.R.J.C. de Wit, and B Koopmans. *Ultrafast spin-transfer torque driven by femtosecond pulsed-laser excitation.* Nat. Commun. **5**, (2014).

A. Schlenhoff, S. Krause, A. Sonntag, and R. Wiesendanger. *Individual Atomic-Scale Magnets Interacting with Spin-Polarized Field-Emitted Electrons.* Phys. Rev. Lett. **109**, 097602 (2012).

A. B. Schmidt, M. Pickel, M. Wiemhofer, M. Donath, and M. Weinelt. *Spin-dependent electron dynamics in front of a ferromagnetic surface.* Phys. Rev. Lett. **95**, 107402(4) (2005).

A. B. Schmidt, M. Pickel, T. Allmers, M. Budke, J. Braun, M. Weinelt, and M. Donath. *Surface electronic structure of fcc Co films: a combined spin-resolved one- and two-photon-photoemission study.* J. Phys. D: Appl. Phys. **41**, 164003 (2008).

A.B. Schmidt, M. Pickel, M. Donath, and M. Weinelt. *Ultrafast spin-dependent electron dynamics at the surface of ferromagnetic thin films.* J. Magn. Magn. Mater. **310**(2, Part 3), 2330 (2007).

A.B. Schmidt, M. Pickel, M. Donath, P. Buczek, A. Ernst, V.P. Zhukov, P.M. Echenique, L.M. Sandratskii, E.V. Chulkov, and M. Weinelt. *Ultrafast Magnon Generation in an Fe Film on Cu(100).* Phys. Rev. Lett. **105**, 197401 (2010).

Anke B. Schmidt. *Spin-dependent electron dynamics in front of ferromagnetic surfaces.* PhD thesis Freie Universität Berlin (2007).

A. Scholl, L. Baumgarten, R. Jacquemin, and W. Eberhardt. *Ultrafast spin dynamics of ferromagnetic thin films observed by fs spin-resolved two-photon photoemission.* Phys. Rev. Lett. **79**, 5146 (1997).

K. Schroeder. *A1 Atomarer Magnetismus und Austauschwechselwirkung.* In *30. IFF - Ferienschule "Magnetische Schichtsysteme".* Forschungszentrum Jülich GmbH (1999).

S. Schuppler, N. Fischer, W. Steinmann, R. Schneider, and E. Bertel. *Image-potential states on Ni(111): A two-photon-photoemission study.* Phys. Rev. B **42**, 9403 (1990).

C. G. Shull, C. T. Chase, and F. E. Myers. *Electron Polarization.* Phys. Rev. **63**, 29 (1943).

J. C. Slater. *The Ferromagnetism of Nickel.* Phys. Rev. **49**, 537 (1936)a.

J. C. Slater. *The Ferromagnetism of Nickel. II. Temperature Effects.* Phys. Rev. **49**, 931 (1936)b.

M. Slezak, T. Giela, D. Wilgocka-Slezak, A. Koziol,-Rachwal,, T. Slezak, R. Zdyb, N. Spiridis, C. Quitmann, J. Raabe, N. Pilet, and J. Korecki. *X-ray photoemission electron microscopy study of the in-plane spin reorientation transitions in epitaxial Fe films on W(110).* J. Magn. Magn. Mater. **348**, 101 (2013).

N. V. Smith. *Phase analysis of image states and surface states associated with nearly-free-electron band gaps.* Phys. Rev. B **32**, 3549 (1985).

R. Smoluchowski. *Anisotropy of the Electronic Work Function of Metals.* Phys. Rev. **60**, 661 (1941).

A. Sonntag, J. Hermenau, A. Schlenhoff, J. Friedlein, S. Krause, and R. Wiesendanger. *Electric-Field-Induced Magnetic Anisotropy in a Nanomagnet Investigated on the Atomic Scale.* Phys. Rev. Lett. **112**, 017204 (2014).

C. Stamm, T. Kachel, N. Pontius, R. Mitzner, T. Quast, K. Holldack, S. Khan, C. Lupulescu, E. F. Aziz, M. Wietstruk, H. A. Durr, and W. Eberhardt. *Femtosecond modification of electron localization and transfer of angular momentum in nickel.* Nat. Mater. **6**(10), 740 (2007).

D. Steiauf and M. Fähnle. *Elliott-Yafet mechanism and the discussion of femtosecond magnetization dynamics.* Phys. Rev. B **79**(14), 140401 (2009).

W. Steinmann. *Spectroscopy of image-potential states by two-photon photoemission.* Appl. Phys. A **49**(4), 365 (1989).

S. D. Stolwijk, A. B. Schmidt, and M. Donath. *Surface state with d_{z^2} symmetry at Y(0001): A combined direct and inverse photoemission study.* Phys. Rev. B **82**, 201412 (2010).

E.C. Stoner. *Collective Electron Specific Heat and Spin Paramagnetism in Metals.* Proceedings of the Royal Society of London. Series A, Mathematical and Physical Sciences **154** (883), pp. 656 (1936).

E.C. Stoner. *Collective Electron Ferromagnetism.* Proceedings of the Royal Society of London. Series A, Mathematical and Physical Sciences **165**(922), pp. 372 (1938).

D. Straub and F. J. Himpsel. *Identification of Image-Potential Surface States on Metals.* Phys. Rev. Lett. **52**, 1922 (1984).

M. Sultan, A. Melnikov, and U. Bovensiepen. *Ultrafast magnetization dynamics of Gd(0001): Bulk versus surface.* Phys. Status Solidi B **248**(10), 2323 (2011).

M. Sultan, U. Atxitia, A. Melnikov, O. Chubykalo-Fesenko, and U. Bovensiepen. *Electron- and phonon-mediated ultrafast magnetization dynamics of Gd(0001).* Phys. Rev. B **85**, 184407 (2012).

E. Tamura and R. Feder. *Theory of Spin-Polarized Secondary-Electron Emission from Ferromagnets.* Phys. Rev. Lett. **57**, 759 (1986).

W. X. Tang, Y. Zhang, I. Tudosa, J. Prokop, M. Etzkorn, and J. Kirschner. *Large Wave Vector Spin Waves and Dispersion in Two Monolayer Fe on W*(110). Phys. Rev. Lett. **99**, 087202 (2007).

M. Teichmann, B. Frietsch, K. Döbrich, R. Carley, and M. Weinelt. *Transient band structures in the ultrafast demagnetization of ferromagnetic gadolinium and terbium.* Phys. Rev. B **91**, 014425 (2015).

U. Thomann, I. L. Shumay, M. Weinelt, and Th. Fauster. *Spin Splitting of Image-Potential States on fcc Fe/Cu(100).* Appl. Phys. B: Lasers and Optics **68**, 531 (1999).

U. Thomann, Ch. Reuß, Th. Fauster, F. Passek, and M. Donath. *Image-potential states on bcc (110) surfaces of iron and tungsten.* Phys. Rev. B **61**(23), 16163 (2000).

L. Udvardi and L. Szunyogh. *Chiral Asymmetry of the Spin-Wave Spectra in Ultrathin Magnetic Films.* Phys. Rev. Lett. **102**, 207204 (2009).

A. Vaterlaus, T. Beutler, and F. Meier. *Spin-lattice relaxation time of ferromagnetic gadolinium determined with time-resolved spin-polarized photoemission.* Phys. Rev. Lett. **67**(23), 3314 (1991).

E. Vescovo, C. Carbone, W. Eberhardt, O. Rader, T. Kachel, and W. Gudat. *Spin-resolved photoemission study of the clean and oxygen-covered Fe(110) surface.* Phys. Rev. B **48**, 285 (1993).

C. von Korff Schmising, B. Pfau, M. Schneider, C. M. Günther, M. Giovannella, J. Perron, B. Vodungbo, L. Müller, F. Capotondi, E. Pedersoli, N. Mahne, J. Lüning, and S. Eisebitt. *Imaging Ultrafast Demagnetization Dynamics after a Spatially Localized Optical Excitation.* Phys. Rev. Lett. **112**, 217203 (2014).

Alexander von Reppert and Azize Koc. *Private Communication* (2015).

A.L. Walter, J.D. Riley, and O. Rader. *Theoretical limitations to the determination of bandwidth and electron mass renormalization: the case of ferromagnetic iron.* New J. Phys. **12**(1), 013007 (2010).

A. Weber, F. Pressacco, S. Günther, E. Mancini, P. M. Oppeneer, and C. H. Back. *Ultrafast demagnetization dynamics of thin Fe/W(110) films: Comparison of time- and spin-resolved photoemission with time-resolved magneto-optic experiments.* Phys. Rev. B **84**(13), 132412 (2011).

D. Wegner, A. Bauer, and G. Kaindl. *Magnon-broadening of exchange-split surface states on lanthanide metals.* Phys. Rev. B **73**, 165415 (2006).

M. Weinelt. *Time-resolved two-photon photoemission from metal surfaces.* J. Phys.: Condens. Matter **14**(43), R1099 (2002).

M. Weinelt, A.B. Schmidt, M. Pickel, and M. Donath. *Spin-polarized image-potential-state electrons as ultrafast magnetic sensors in front of ferromagnetic surfaces.* Progress in Surface Science **82**, 388 (2007).

Paul Weiss. *Spin- and Time-Resolved Photoemission on Thin Ni(111) Films.* Master's thesis Freie Universität Berlin (2013).

E. Weschke and G. Kaindl. *Magnetic exchange splitting in lanthanide metals.* J. Phys.: Condens. Matter **13**(49), 11133 (2001).

E. Weschke, C. Schüssler-Langeheine, R. Meier, A. V. Fedorov, K. Starke, F. Hübinger, and G. Kaindl. *Temperature Dependence of the Exchange Splitting of the Surface State on Gd(0001): Evidence against Spin-Mixing Behavior.* Phys. Rev. Lett. **77**(16), 3415 (1996).

S. Wienholdt, D. Hinzke, K. Carva, P. Oppeneer, and U. Nowak. *Orbital-resolved spin model for thermal magnetization switching in rare-earth-based ferrimagnets.* Phys. Rev. B **88**, 020406 (2013).

M. Wietstruk, A. Melnikov, C. Stamm, T. Kachel, N. Pontius, M. Sultan, C. Gahl, M. Weinelt, H.A. Dürr, and U. Bovensiepen. *Hot-Electron-Driven Enhancement of Spin-Lattice Coupling in Gd and Tb 4f Ferromagnets Observed by Femtosecond X-Ray Magnetic Circular Dichroism.* Phys. Rev. Lett. **106**(12), 127401 (2011).

Marko Wietstruk. *Ultraschnelle Magnetisierungsdynamik in itineranten und Heisenberg-Ferromagneten.* PhD thesis Technische Universität Berlin (2010).

A. Winkelmann, D. Hartung, H. Engelhard, C.-T. Chiang, and J. Kirschner. *High efficiency electron spin polarization analyzer based on exchange scattering at Fe/W(001).* Rev. Sci. Instrum. **79**(8), 083303 (2008).

E. P. Wohlfahrt. *Bändermodell von Ferromagnetismus.* In *Magnetismus Struktur und Eigenschaften magnetischer Festkörper.* VEB Deutscher Verlag für Grundstoffindustrie (1967).

Martin Wolf. *Femtosecond dynamics of electronic excitations at metal surfaces.* Surface Science **377-379**, 343 (1997).

Henry Wortelen. *Wachstum und elektronische Struktur von ultradünnen Nickelfilmen auf Wolfram(110).* Diplomarbeit Westfälische Wilhelms-Universität Münster (2011).

Y. Yafet. *g Factors and Spin-Lattice Relaxation of Conduction Electrons* volume 14. Academic New York (1963).

K. Yosida. *Magnetic Properties of Cu-Mn Alloys.* Phys. Rev. **106**(5) (1957).

D. Yu, C. Math, M. Meier, M. Escher, G. Rangelov, and M. Donath. *Characterisation and application of a SPLEED-based spin polarisation analyser.* Surf. Sci. **601**(24), 5803 (2007).

Kh. Zakeri. *Elementary spin excitations in ultrathin itinerant magnets.* Physics Reports **545**(2), 47 (2014).

Kh. Zakeri, T.R.F. Peixoto, Y. Zhang, J. Prokop, and J. Kirschner. *On the preparation of clean tungsten single crystals.* Surf. Sci. **604**(2), L1 (2010)a.

Kh. Zakeri, Y. Zhang, J. Prokop, T.-H. Chuang, N. Sakr, W. X. Tang, and J. Kirschner. *Asymmetric Spin-Wave Dispersion on Fe(110): Direct Evidence of the Dzyaloshinskii-Moriya Interaction.* Phys. Rev. Lett. **104**, 137203 (2010)b.

Kh. Zakeri, Y. Zhang, and J. Kirschner. *Surface magnons probed by spin-polarized electron energy loss spectroscopy.* J. Electron Spectrosc. Relat. Phenom. **189**, 157 (2013).

G. P. Zhang and W. Hübner. *Laser-Induced Ultrafast Demagnetization in Ferromagnetic Metals.* Phys. Rev. Lett. **85**(14), 3025 (2000).

G. P. Zhang, W. Hubner, G. Lefkidis, Y. H. Bai, and T. F. George. *Paradigm of the time-resolved magneto-optical Kerr effect for femtosecond magnetism.* Nature Phys. **5**(7), 499 (2009).

Y. Zhang, P. Buczek, L. Sandratskii, W. X. Tang, J. Prokop, I. Tudosa, T. R. F. Peixoto, Kh. Zakeri, and J. Kirschner. *Nonmonotonic thickness dependence of spin wave energy in ultrathin Fe films: Experiment and theory.* Phys. Rev. B **81**, 094438 (2010).

V. P. Zhukov and E. V. Chulkov. *The femtosecond dynamics of electrons in metals.* Physics-Uspekhi **52**(2), 105 (2009).

V. P. Zhukov, E. V. Chulkov, and P. M. Echenique. *Lifetimes of Excited Electrons in Fe and Ni: First-Principles GW and the T-Matrix Theory.* Phys. Rev. Lett. **93**(9), 096401 (2004).

V. P. Zhukov, E. V. Chulkov, and P. M. Echenique. *GW+T theory of excited electron lifetimes in metals.* Phys. Rev. B **72**(15), 155109 (2005).

V. P. Zhukov, E. V. Chulkov, and P. M. Echenique. *Lifetimes and inelastic mean free path of low-energy excited electrons in Fe, Ni, Pt, and Au: Ab initio GW+T calculations.* Phys. Rev. B **73**(12), 125105 (2006).

Deutsche Kurzfassung

Die vorliegende Arbeit beschäftigt sich mit der ultraschnellen Elektronen- und Spindynamik in ferromagnetischen dünnen Filmen. Spin-, zeit- und winkelauflösende Photoelektronenspektroskopie (STARPES) wurde genutzt, um sowohl Grundzüge des Magnetismus als auch die für technische Anwendungen relevante Spindynamik zu untersuchen. Dies beinhaltet sowohl die Wechselwirkungen der Elektronen untereinander als auch mit den anderen Subsystemen des Materials wie dem Kristallgitter oder den magnetischen Freiheitsgraden. Das Verständnis der Spinabhängigkeit derartiger Wechselwirkungen ist ein vielversprechender Baustein für den technologischen Fortschritt. Die bisherige Nutzung spinabhängiger Effekte ist jedoch stark eingeschränkt.

In STARPES-Experimenten nutzen wir eine, der eigentlichen Messung vorangehende, Laseranregung, um das zu untersuchende System aus seinem thermodynamischen Gleichgewicht auszulenken. Dabei werden die Elektronen des Systems in Zustände höherer Energie gebracht, in denen wir dann ihr dynamisches Verhalten untersuchen können. Durch die energetische Relaxation der Elektronen, wird Energie in andere Systeme transferiert, was bei hohen Anregungsdichten zu Phasenübergängen und neuartigen Zuständen des Materials führen kann.

In dieser Arbeit ist ein solcher laserinduzierter magnetischer Phasenübergang in Gadolinium untersucht worden. Hier ist erstmalig eine Studie zur laserinduzierten Entmagnetisierung mittels STARPES geglückt. Die Ergebnisse unterstreichen die Wichtigkeit spin- und energieauflösender Experimente, denn sie zeigen, dass verschiedene für den Magnetismus charakteristische Größen wie die Austauschaufspaltung und die Spinpolarisation desselben Zustands in der Magnetisierungsdynamik unterschiedlich schnell reagieren. Dieses Ergebnis liefert nun auch eine Erklärung für die unterschiedlichen Entmagnetisierungszeiten, die zuvor unter Verwendung verschiedener experimenteller Techniken beobachtet wurden. Die Realisierung dieses Entmagnetisierungsexperiments erforderte zunächst die Installation eines neuen Spindetektors, der auf dem Prinzip der Austauschstreuung basiert. Neben einer erhöhten Zählrate hat die Nutzung der Austauschstreuung den Vorteil, dass sie bestens geeignet ist um auch nichtmagnetische Probensysteme spinaufgelöst zu untersuchen, welche ebenso interessante und nützliche spinabhängige Phänomene aufweisen wie magnetische Systeme.

Ein weiterer Vorteil des neuen Detektors ist die Möglichkeit Spinabhängigkeiten und magnetischen Lineardichroismus voneinander zu trennen. Dies wurde in der vorliegenden Arbeit genutzt, um die Elektron-Magnon-Wechselwirkung an einer Oberflächenresonanz mit Minoritätsspincharakter in Eisen zu untersuchen. Die beobachtete ausgeprägte Energierenormalisierung der Bandstruktur belegt, dass die Wechselwirkung zwischen Elektronen und Magnonen deutlich stärker sein kann als bisher beobachtet wurde und sogar mit der Stärke der Elektron-Phonon- und der Elektron-Elektron-Wechselwirkung vergleichbar ist. Der magnetische Charakter der Renormalisierung spiegelt sich in einem starken dichroischen Kontrast wieder, der zuvor im Zusammenhang mit derartigen Phänomenen noch nicht beobachtet werden konnte.

Auch in Nickel wurde der Emission von Magnonen bisher eine wichtige Rolle in der Streuung von Elektronen zugeordnet. In einem dritten STARPES Experiment wurden die elektronischen Oberflächenzustände der Ni(111)-Oberfläche untersucht. In den Streuraten der angeregten Elektronen in den unbesetzten Bildladungszuständen dieser Oberfläche zeigten sich jedoch vergleichsweise geringe Spinanhängigkeiten, die unter anderem auf einen sehr geringen Beitrag der Magnonenemission zu den Streuraten in Nickel schließen lässt. Dies steht aktuell im Widerspruch zu theoretischen Vorhersagen für die Streuraten heißer Elektronen, die von hoher Relevanz für die Nutzung spinpolarisierter Ströme sind.

Abstract

This work is a spin-, time- and angle-resolved photoemission (STARPES) study of ultrafast electron and spin dynamics in ferromagnetic thin films. The experimental studies address fundamentals of magnetism as well as spin dynamics relevant for technological application. The latter are determined by the interactions of electrons near the Fermi energy and their spin dependence. The utilization of such spin dependencies is a promising way towards technological innovation.

In STARPES experiments we use a laser excitation preceding the actual measurement to drive the sample system out of equilibrium by exciting electrons into energetically higher states, where we investigate their dynamic behavior. The relaxation of the excited electrons transfers energy to the lattice and spin system. At high excitation densities this can lead to phase transitions and create novel states in the material.

In this work a laser-induced magnetic phase transition in gadolinium has been investigated. It is the first successful study of a laser-induced demagnetization by means of STARPES. It yields the surprising result, that two fundamental magnetic properties of the same electronic state, exchange splitting and spin polarization, show different response times upon demagnetization. This underlines the importance of spin- and energy-resolved measurements. The result can furthermore explain the various demagnetization times found by different experimental techniques. To realize such a demagnetization experiment, it was necessary to install a new spin detector based on exchange scattering. Besides an increase in count rate, the great advantage of exchange scattering is that it is also suited to study nonmagnetic systems, which show spin-dependent phenomena just as fascinating and useful as the ones in magnetic systems.

A further advantage of the new spin detector is the possibility to distinguish between spin dependence and magnetic linear dichroism in the photoemission intensity. We made use of this advantage to investigate the electron-magnon interaction of a minority-spin surface resonance in iron. A pronounced energy renormalization in this resonance revealed that the electron-magnon interaction can in fact be much stronger than previously observed. We find a coupling strength on the order of electron-phonon and electron-electron interaction. The magnetic character of the renormalization is reflected in a strong dichroic contrast, which has up to now not been observed in this context.

Another system, in which magnonic contributions have been proposed to play an important role in electron-spin-flip scattering processes, is nickel. In a third STARPES experiment, we studied the electronic surface states of Ni(111). The scattering rates of excited electrons in the unoccupied image-potential states at this surface show an unexpectedly low spin dependence. This proves a minor contribution of magnon emission to the electronic scattering rates in nickel. The low magnonic contribution contradicts theoretical predictions for the scattering rates of hot electrons, which are highly relevant for the utilization of spin-polarized currents.

Acknowledgements

Ich danke Martin Weinelt, dem Vater des Spinner-Projektes, dafür, dass er ein netter und umgänglicher Chef ist, der mir die Arbeit in seiner Gruppe bisher ermöglicht hat und weiterhin ermöglicht und immer genügend Sach- und Personalmittel dafür übrig hatte. Ich weiß, dass sich nicht jeder Professor die Zeit nimmt, sich zu seinen Doktoranden an den Schreibtisch zu setzen und Messergebnisse zu diskutieren, doch bei Martin kann man das jederzeit einfordern und dafür bin ich sehr dankbar.

Ich danke auch Marko Wietstruk, der mir über die vergangenen fünf Jahre ein fürsorglicher Postdoc war, der bei jedem Umbau im Labor mit Rat und Tat dabei war, gerne smarte Projektpläne aufstellte und ebenso offen für Korrekturlesungen und Auswertediskussionen war. Zudem erstellte er das Messprogramm für Tony Stark, unseren Austauschstreu-Spindetektor, und passte es auch während meiner Messzeiten jederzeit auf neue Bedürfnisse an, was ein echter Luxus war. Außerdem bin ich Marko für die Nachhilfe in Berlinerisch zu Dank verpflichtet, welchet ick inzwischen fast fließend beherrsche.

Schon an dritter Stelle möchte ich Dominic Lawrenz danken, der meine Arbeit nicht nur als Lebensgefährte, sondern auch als Wissenschaftler unterstützt hat. Mit den in seiner Masterarbeit erworbenen Kenntnissen des hier genutzten verstärkten Titan-Saphir-Lasersystems, trug er einiges zur Entstehung der gezeigten Gadolinium- und Eisenspektren bei. Auch beim Schreiben konnte ich bei Diskussionen und beim Korrekturlesen immer auf ihn zählen. Ich bin ihm für all das und das frisch gekochte Essen in der einen oder anderen langen Messnacht sehr dankbar.

Ich danke Marc Christ und Paul Weiss, die zwei großartige Masterstudenten waren und damit maßgeblich zum Entstehen dieser Arbeit beigetragen haben. Auch wenn bei einem Laborumzug und einem Detektorwechsel wahrscheinlich immer eine Menge schiefgeht, hat es viel Spaß gemacht, mit euch zu arbeiten.

Meinem Diplomanden, Thomas Odebrecht, danke ich für die Möglichkeit, mich als Betreuerin das erste Mal auszuprobieren. Ich muss leider zugeben, dass ich an dieser Zusammenarbeit grandios gescheitert bin. Trotzdem habe ich auch von Thomas einiges dazu gelernt und bin ihm dafür dankbar.

Aus einer Idee von Cornelius Gahl kam Boris Peev in unser Büro und wurde nach und nach auch (theoretisch) zum Spinner. Wie wir nach einigen Diskussionen bemerkten, passte das Thema seiner Bachelorarbeit perfekt zu meiner Doktorarbeit und ist in der einen oder anderen Abbildung weiterverarbeitet worden. Dafür, für die gute Unterhaltung im Büro und für die Wiederaufbereitung des Image-States-In-Gaps-Programms möchte ich Boris vielmals

danken.

Meinen Eltern, meiner Schwester und meiner Oma möchte ich dafür danken, dass sie tapfere Kämpfer sind und sich super umeinander kümmern. Sie haben mir damit ermöglicht, viel Zeit in diese Arbeit zu stecken und mir vielerlei Lasten und Sorgen so gut es ging abgenommen.

Ebenso danke ich Anne und Simon, Anne-Christin, Becci, Cid, Jörn, Julle, Manu, Michi, Tine und Wolfgang und Viola, die alle immer wieder dafür sorgen, dass ich auch mal etwas anderes tue als arbeiten.

Eine besondere Erwähnung hat auch Daniel Brete verdient, von dem ich einiges über Verdampfer und über die Software von Eurotherm PID-Reglern lernen durfte.

Zu guter letzt möchte ich mich bei der gesamten AG Weinelt bedanken. Ich höre oft, dass es schlecht für den Lebenslauf sein soll, für mehrere Abschlussarbeiten in derselben Gruppe zu bleiben, doch wenn ich an all das denke, was ich in der Doktorarbeit noch dazu gelernt habe, an all die Leute, die ich kennengelernt habe und all den Spaß, den wir zusammen hatten, bereue ich nicht eine einzige Minute. Vielen vielen Dank an Andi, Basti, Björn, Boris, Christian, Corni, Daniel B., Daniel Pschue, Dietgard, Dom, Jan B., Jan W., Janos, Jens, John, Kamil, Kristian, Kristof, Larissa, Malte, Marc, Marko, Markus, den kleinen Martin, den großen Martin, Marvin, Paul, Robert, Roman, Sabine, Soph, Stefan, Steffi, Thea, Thomas, Thomo, TKU, Trabbi junior, Trabbi senior, Uwe und Wibke!

List of Publications

[I] Beatrice Andres, Marc Christ, Cornelius Gahl, Jürgen Kirschner, Marko Wietstruk, and Martin Weinelt *Separating Exchange Splitting from Spin Mixing in Gadolinium by Femtosecond Laser Excitation*, Phys. Rev. Lett. **115**, 207404 (2015), doi:10.1103/PhysRevLett.115.207404

[II] Beatrice Andres, Paul Weiss, Marko Wietstruk, and Martin Weinelt, *Spin-Dependent Lifetimes and Exchange Splittings of Surface States on Ni(111)*, J. Phys.: Condens. Matter **27**, 015503 (2015), doi:10.1088/0953-8984/27/1/015503

[III] Beatrice Andres, Cornelius Gahl, Jürgen Kirschner, Marko Wietstruk, and Martin Weinelt, *Spin dependence of relaxation processes in the laser-driven demagnetization of Gd*, accepted for publication in Ultrafast Magnetism II (J.-Y. Bigot, W. Hübner, T. Rasing and R. Chantrell, eds.), Springer Proceedings in Physics

Conference contributions

I presented this work on the following conferences:

Talk "Spin dependence of relaxation processes in the laser-driven demagnetization of Gd" *Ultrafast Magnetism Conference*, Nijmegen (2015)

Poster "Orbital-resolved ultrafast magnetization dynamics of gadolinium" *XIV. Research Course on X-Ray Sciences*, DESY Hamburg (2015)

Talk "Constant spin polarization of the Gd(0001) surface state during laser-induced demagnetization" *DPG Spring Meeting*, Berlin (2015)

Poster "Surface states on Fe(110) – exploring their spin, decay rates and magnetic linear dichroism" *DPG Spring Meeting*, Berlin (2015)

Talk "Ultrafast magnetization dynamics in Gadolinium – Analyzing the transient spin polarization" *5th Winterschool on Ultrafast Processes in Condensed Matter*, Reit im Winkl (2015)

Talk "Magnetization dynamics in Gadolinium – Part II: Analyzing the transient spin polarization" *Young Investigators Workshop on Ultrafast Dynamics*, Reit im Winkl (2015)

Poster "Image-Potential States on close-packed Magnetic Surfaces" *DPG Spring Meeting*, Dresden (2014)

Poster "Temporal Evolution of Excited Electrons in the Ni(111) Image-Potential States" *DPG Spring Meeting*, Regensburg (2013)

Talk "Temporal evolution of excited electrons in the Ni(111) image-potential states" *4th Winterschool on Ultrafast Processes in Condensed Matter*, Reit im Winkl (2013)

Poster "Surface and Image-Potential States of Ni(111) Investigated with Spin- and Time-Resolved 2PPE" *DPG Spring Meeting*, Berlin (2012)

Poster "Spin-Resolved Investigations of the Exchange-Split Gd Surface and Image-Potential States" *Würzburg Fall School*, Würzburg (2011)

Talk "Spin-Resolved Investigations of the Exchange-Split Gd Surface and Image-Potential States" *DPG Spring Meeting*, Dresden (2011)

Bachelor and Master Students

During this PhD work I was cosupervising the following Bachelor, Master, and Diploma students:

1. Thomas Odebrecht, *Spinauflösende Zwei-Photonen-Photoemission an der Ni(111)/W(110)-Oberfläche*, Diplomarbeit, Freie Universität Berlin (05/2012)

2. Paul Weiss, *Spin- and Time-Resolved Photoemission on Thin Ni(111) Films*, Master Thesis, Freie Universität Berlin (06/2013)

3. Marc Christ, *A Spin Detector for time-resolved Two-Photon Photoemission - First measurement on bcc Fe(110)*, Master Thesis, Freie Universität Berlin (06/2014)

4. Boris Peev, *Modellierung von Bildpotentialzuständen an Metalloberflächen*, Bachelor Thesis, FU Berlin (08/2013)